

2014-06-20

Theoretical and Experimental Development of an Array of Droopy Bowties with Integrated Baluns

Angelo Puzella

Worcester Polytechnic Institute

Follow this and additional works at: <https://digitalcommons.wpi.edu/etd-dissertations>

Repository Citation

Puzella, A. (2014). *Theoretical and Experimental Development of an Array of Droopy Bowties with Integrated Baluns*. Retrieved from <https://digitalcommons.wpi.edu/etd-dissertations/313>

This dissertation is brought to you for free and open access by [Digital WPI](#). It has been accepted for inclusion in Doctoral Dissertations (All Dissertations, All Years) by an authorized administrator of Digital WPI. For more information, please contact wpi-etd@wpi.edu.

**Theoretical and Experimental Development of an Array of Droopy Bowties with Integrated
Baluns**

by

Angelo Puzella

A Dissertation

Submitted to the Faculty

of the

WORCESTER POLYTECHNIC INSTITUTE

In partial fulfillment of the requirements for the

Degree of Doctor of Philosophy

in

Electrical and Computer Engineering

May 2014

APPROVED

Dr. Sergey Makarov
Worcester Polytechnic Institute



Dr. Hans Steyskal
US Air Force, Consultant

Dr. Reinhold Ludwig
Worcester Polytechnic Institute

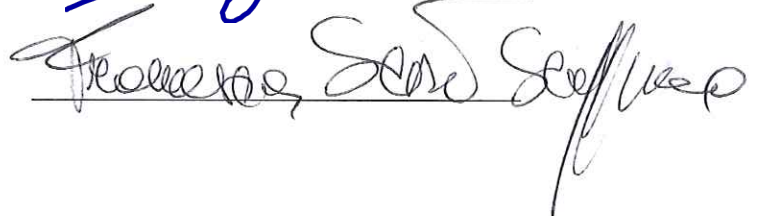
Dr. Sara Louie
ANSYS, Inc.

Dr. Francesca Sciré-Scappuzzo
Metamagnetics, Inc.







To my wife, Anna

Abstract

Theoretical modeling, design, assembly, and measurement of a novel integrated phased array radiator are presented. The droopy bowtie turnstile radiator with quad line feed meets challenging radar requirements and uses low cost manufacturing and assembly techniques.

- 1) This thesis develops the complete theoretical model (antenna, balun, feeding network) of a broadband phased array radiator: the droopy bowtie turnstile radiator. A novel quad line balun feed is developed that provides a low loss, high isolation, and coincident phase-center feeding network for the droopy bowtie. The radiator and feed design combines broadband RF performance and high-isolation dual-linear polarization in a low profile, compact package that enables wide scan volume performance versus frequency.
- 2) This thesis develops low-cost manufacturing and assembly techniques applied to the droopy bowtie radiator with the quad line feed. The new radiator design would utilize low cost fabrication techniques such as injection molding and 3-D printing, and also leverages automated assembly techniques.
- 3) Measurement prototypes and array prototypes of droopy bowtie radiators with the quad line feed are developed for L- and X-bands. The measurements demonstrate broadband RF performance in a low profile compact package viable for wide-scale phased array applications.

Acknowledgment

I believe in continual learning. When Prof. Makarov suggested that I go for the PhD, I thought “I really enjoy learning, but this is crazy!” However, Prof. Makarov is very good at persuading, so I took the leap. My real goal was to learn more about my field, to help contribute more at work with an eye towards teaching others what I have learned through the years.

One of the greatest gifts that one can give is the gift of teaching; and, throughout this PhD process, I have learned a great deal from the following people:

Thank you Prof. Sergey Makarov for being my thesis advisor; for your confidence in me, support and dedication as a teacher. I will always be indebted to your teaching ability, kindness and scholarship and I will always look to you as a role model.

Thank you Prof. Reinhold Ludwig for the honor of having you on my thesis committee.

Thank you Dr. Francesca Scire-Scappuzzo for your dedication and help in achieving my goal.

Thank you Dr. Hans Steyskal – your exceptional insights, experience and patience helped me focus on the important aspects of my thesis – and I learned a great deal from your questions.

Thank you Dr. Sara Louis of ANSYS, Inc. for your generous time and expertise.

Finally, thank you to Mr. Rome Pozgay of Raytheon (retired). Rome and I collaborated over the last few years of his career at Raytheon and this collaboration has continued into his retirement. It is a great gift when someone opens their home to you and gives you their time, patience and wisdom. And a special thank you to Rome’s wife, Ann, who generously gave me so much of Rome’s time.

Table of Contents

| | |
|---|------|
| Abstract | iii |
| Acknowledgment | iv |
| Table of Contents | v |
| List of Figures | viii |
| List of Tables | xiv |
| List of Published Papers and Patents | xv |
| Chapter 1 – Introduction to Non-finite and Finite Phased Arrays | 1 |
| 1.0 Theoretical Background of Phased Array Design | 1 |
| 1.1 The Array Factor | 4 |
| 1.1.1 Linear Phase Taper for Electronic Scan..... | 5 |
| 1.1.2 Uniformly Excited Linear Array..... | 6 |
| 1.2 Element Pattern | 8 |
| 1.3 Beamwidth | 9 |
| 1.4 Linear Array Factor Examples | 9 |
| 1.4.1 Linear Array of $N = 2$ Isotropic Radiators..... | 9 |
| 1.4.2 Linear Array of $N = 16$ Isotropic Radiators..... | 13 |
| 1.4.3 Linear Array of $N = 16$ Isotropic Radiators with $\cos(\theta)$ Element Pattern..... | 16 |
| 1.5 Instantaneous Bandwidth | 18 |
| 1.6 Planar Phased Array Array Factor: Rectangular Lattice..... | 20 |
| 1.6.1 Grating Lobes..... | 21 |
| 1.6.2 Grating Lobe Plots | 22 |
| 1.7 Planar Array Patterns | 25 |
| 1.7.1 19x19 Planar Array Patterns: $dx = 0.5\lambda$ $dy = 0.5\lambda$ | 26 |
| 1.8 Summary | 36 |
| Chapter 2 – Floquet Analysis Applied to Phased Arrays | 38 |
| 2.0 Introduction..... | 38 |
| 2.1 Mutual Coupling in Phased Arrays: An Analytical Approach..... | 38 |
| 2.2 The Floquet Modal Approach | 40 |
| 2.2.1 The Floquet Series Expansion of a Periodic Function..... | 41 |
| 2.3 Two–Dimensional Floquet Source Excitation of Strip Dipole Elements | 49 |
| 2.4 Fourier Transform of Current Expansion..... | 51 |
| 2.5 Radiated Electric Field and Scan Impedance of Printed Dipole Array..... | 56 |

| | | |
|---|--|-----|
| 2.6 | Scan Impedance of Printed Dipole Array: Effect of a Ground Plane | 59 |
| 2.7 | Scan Impedance of Printed Dipole Array: Comparison with Hansen’s Formulas..... | 61 |
| 2.8 | On the Difference between HFSS and Analytical Formulation Results | 66 |
| 2.8.1 | Comparison between the Analytical approach ^{2.1} and HFSS..... | 67 |
| 2.9 | Multimodal Floquet Approach..... | 70 |
| 2.10 | A Simplified Model for Multimode Solution Expansion..... | 81 |
| 2.11 | Summary | 88 |
| Chapter 3 – Droopy Bowtie Radiator with Integrated Balun: Theory | | 90 |
| 3.0 | Introduction..... | 90 |
| 3.1 | Phased Array Radiator Selection | 91 |
| 3.2 | Droopy Bowtie Radiator Model..... | 93 |
| 3.2.1 | Droopy Bowtie Radiator Model: Infinite Array Modeled Results | 95 |
| 3.2.1.1 | Infinite Array Simulation Performance: Scan Impedance and Return Loss | 96 |
| 3.2.1.2 | Isolated Element Pattern Performance | 100 |
| 3.2.1.3 | Isolated Element Input Impedance and Return Loss Performance | 101 |
| 3.3 | Cross-Polarization Performance..... | 102 |
| 3.3.1 | Axial Ratio for Circular Polarization..... | 104 |
| 3.4 | Feed and Balun..... | 104 |
| 3.4.1 | Dyson Balun..... | 105 |
| 3.4.2 | Vertical Balun Column: The Quad line RF Transmission Line | 105 |
| 3.4.3 | Transmission Line Parameters of the Quad Line Model | 107 |
| 3.4.4 | Mode Isolation of the Quad Line | 109 |
| 3.5 | Complete Antenna-Transmission Line Model..... | 111 |
| 3.5.1 | Built-in Hybrid..... | 112 |
| 3.5.2 | Antenna-Balun Transmission Line Model..... | 112 |
| 3.5.3 | Power Divider Design..... | 116 |
| 3.6 | Summary | 116 |
| Chapter 4 – Practical Realization and Applications of Droopy Bowtie for Finite Arrays | | 118 |
| 4.0 | Introduction..... | 118 |
| 4.1 | Droopy Bowtie Radiator with Quad Line Feed: Manufacturing Approach..... | 118 |
| 4.1.1 | Approach..... | 118 |
| 4.1.2 | Injection Molded Radiator | 119 |
| 4.1.3 | The Quad Line Feed Assembly..... | 124 |
| 4.1.3.1 | Quad Line Feed Assembly Process..... | 125 |

| | | |
|---------|--|-----|
| 4.1.3.2 | Unit Cell Assembly Concept..... | 128 |
| 4.2 | Array Assembly..... | 128 |
| | Array Assembly Summary | 135 |
| 4.3 | HFSS Model: Gen 1.0 | 135 |
| 4.3.1 | HFSS Model: Gen 2.0..... | 137 |
| 4.4 | HFSS Infinite Array Simulation Results..... | 143 |
| 4.5 | L-Band Prototype Droopy Bowtie Turnstile with Quad Line Feed..... | 146 |
| 4.5.1 | Measurement Set-up | 147 |
| 4.5.2 | Measurements | 148 |
| 4.5.3 | Discussion: L-Band Prototype | 149 |
| 4.6 | X-Band Prototype Gen 1.0 Droopy Bowtie Turnstile with Quad Line Feed..... | 149 |
| 4.6.1 | Gen 1.0 Return Loss Measurement..... | 150 |
| 4.6.2 | Gen 1.0 Far-field Element Patterns..... | 152 |
| 4.6.3 | Gen 2.0 RF Measurements..... | 156 |
| 4.7 | Summary | 157 |
| | Conclusions..... | 161 |
| | Appendix A: Time Domain Approach to Characterizing Antenna Radiation | 165 |
| | References..... | 174 |

List of Figures

| | |
|---|----|
| Figure 1-1. Linear phased array antenna of 8 isotropic radiators: Scan to $\theta=0^\circ$ | 2 |
| Figure 1-2. Linear phased array antenna of 8 isotropic radiators: Scan to θ | 3 |
| Figure 1-3. Linear phased array antenna of N isotropic radiators | 4 |
| Figure 1-4. Linear array factor for $N = 2$ | 10 |
| Figure 1-5. Polar plot: $N=2$ array, $d_x = \lambda/2$ | 11 |
| Figure 1-6. Polar plot: $N=2$ array, $d_x = \lambda/2$ | 12 |
| Figure 1-7. Polar plot: $N=2$ array, $d_x = \lambda$ | 13 |
| Figure 1-8. Linear array factor: $N = 16$ isotropic radiators. Un-normalized (left); normalized (right) | 14 |
| Figure 1-9. Linear array factor: $N = 16$ isotropic radiators. 3dB beamwidth | 14 |
| Figure 1-10. Linear array factor: $N = 16$ isotropic radiators, beamwidth vs. scan | 15 |
| Figure 1-11. Linear array factor: $N = 16$ isotropic radiators, beamwidth vs. scan | 15 |
| Figure 1-12. Linear array factor: $N = 16$ radiators with $\cos^{0.5}(\theta)$ element pattern | 16 |
| Figure 1-13. Linear array factor: $N = 16$ radiators with $\cos^{1.4}(\theta)$ element pattern | 17 |
| Figure 1-14. Phased array beam steering. Phase shift (left) and time delay shift (right)..... | 18 |
| Figure 1-15. Main beam squint versus frequency..... | 19 |
| Figure 1-16. Planar, rectangular array | 20 |
| Figure 1-17. Case 1. Rectangular lattice with $d_x = d_y = \lambda/2$ | 23 |
| Figure 1-18. Case 2. Rectangular lattice with $d_x = d_y = \lambda$ | 23 |
| Figure 1-19. Case 2. Rectangular lattice with $d_x = d_y = \lambda$. main beam scanned to $u=0.321$, $v=0.117$ | 24 |
| Figure 1-20. Case 3. Rectangular lattice with $d_x = d_y = 5\lambda/4$ | 25 |
| Figure 1-21. 19 x 19 array; scan angle: $u = 0, v = 0; \cos^{0.0}(\theta)$ | 26 |
| Figure 1-22. 19 x 19 array; scan angle: $u = 0.5, v = 0; \cos^{0.0}(\theta)$ | 27 |
| Figure 1-23. 19 x 19 array; scan angle: $u = 0.5, v = 0; \cos^{1.5}(\theta)$ | 27 |
| Figure 1-24. 19 x 19 array; scan angle: $u = 0.71, v = 0; \cos^{0.0}(\theta)$ | 28 |
| Figure 1-25. 19 x 19 array; scan angle: $u = 0.71, v = 0; \cos^{1.5}(\theta)$ | 28 |
| Figure 1-26. 19 x 19 array; scan angle: $u = 0.87, v = 0; \cos^{0.0}(\theta)$ | 29 |
| Figure 1-27. 19 x 19 array; scan angle: $u = 0.87, v = 0; \cos^{1.5}(\theta)$ | 29 |
| Figure 1-28. 19 x 19 array; scan angle: $u = 0, v = 0.5; \cos^{0.0}(\theta)$ | 30 |

| | |
|---|----|
| Figure 1-29. 19 x 19 array; scan angle: $u = 0, v = 0.5; \cos^{1.5}(\theta)$ | 30 |
| Figure 1-30. 19 x 19 array; scan angle: $u = 0, v = 0.71; \cos^{0.0}(\theta)$ | 31 |
| Figure 1-31. 19 x 19 array; scan angle: $u = 0, v = 0.71; \cos^{1.5}(\theta)$ | 31 |
| Figure 1-32. 19 x 19 array; scan angle: $u = 0, v = 0.87; \cos^{0.0}(\theta)$ | 32 |
| Figure 1-33. 19 x 19 array; scan angle: $u = 0, v = 0.87; \cos^{1.5}(\theta)$ | 32 |
| Figure 1-34. 19 x 19 array; scan angle: $u = 0.61, v = 0.5; \cos^{0.0}(\theta)$ | 33 |
| Figure 1-35. 19 x 19 array; scan angle: $u = 0.61, v = 0.5; \cos^{1.5}(\theta)$ | 33 |
| Figure 1-36. 19 x 19 array; scan angle: $u = 0.5, v = 0.71; \cos^{0.0}(\theta)$ | 34 |
| Figure 1-37. 19 x 19 array; scan angle: $u = 0.5, v = 0.71; \cos^{1.5}(\theta)$ | 34 |
| Figure 1-38. 19 x 19 array; scan angle: $u = 0.35, v = 0.87; \cos^{0.0}(\theta)$ | 35 |
| Figure 1-39. 19 x 19 array; scan angle: $u = 0.35, v = 0.87; \cos^{1.5}(\theta)$ | 35 |
| Figure 2-1. One-dimensional infinite array of y-axis directed current elements | 44 |
| Figure 2-2. The geometry of the infinite array with strip-dipole elements (single polarization) | 50 |
| Figure 2-3. Scan resistance/reactance as a function of scan angle θ_0 ; solid curves: Hansen's plots ^{2,6} ; dashed curves: Reference 2.1 | 64 |
| Figure 2-4. The electric current distribution along the metal strip | 66 |
| Figure 2-5. Scan impedance (scan resistance- top; scan reactance- bottom) 0.5λ array lattice; 0.480λ dipole length; $h=0.25\lambda$ | 67 |
| Figure 2-6. Scan impedance (scan resistance- top; scan reactance-bottom) 0.5λ array lattice; 0.495λ dipole length; $h=0.25\lambda$ | 67 |
| Figure 2-7. Figure 35 from Microwave Scanning Antennas, Ch. 3, pg. 286..... | 68 |
| Figure 2-8. Scan impedance (scan resistance- top; scan reactance- bottom) 0.7λ array lattice; 0.495λ dipole length; $h=0.25\lambda$ | 69 |
| Figure 2-9. Scan impedance (scan resistance- top; scan reactance- bottom) 0.7λ array lattice; 0.480λ dipole length; $h=0.25\lambda$ | 69 |
| Figure 2-10. Single dipole configuration: an infinite dipole..... | 72 |
| Figure 2-11. A collinear dipole array with feeding gaps equal to spacing gaps..... | 73 |
| Figure 2-12. Distribution of the periodic current component, $I(x)$, for the half-lambda collinear array in echelon (no ground plane) at two different scan angles from zenith - 0 deg and 37 deg, respectively. Array parameters: $d_x=\lambda/2$, $ka=0.08$, $g/a=0.61$. a) – scan angle 0 deg, exact solution; b) – scan angle 37 deg, exact solution; c) – scan angle 37 deg, averaged gap current is used through the gap. | 75 |
| Figure 2-13. A planar dipole array with feeding gaps equal to spacing gaps..... | 76 |

| | |
|---|-----|
| Figure 2-14. Scan impedance in the E-plane. Scan resistance is marked red; reactance – blue Thick curves - theory model; crosses - the Ansoft HFSS v.11 solution; thin curves - the CST solution | 77 |
| Figure 2-15. Scan impedance in the D-plane. Scan resistance is marked red; reactance – blue Thick curves - theory model; crosses - the Ansoft HFSS v.11 solution; thin curves - the CST solution | 78 |
| Figure 2-16. Scan impedance in the H-plane. Scan resistance is marked red; reactance – blue Thick curves - theory model; crosses - the Ansoft HFSS v.11 solution; thin curves - the CST solution | 79 |
| Figure 2-17. Surface current distribution in the D-plane at 75 degree scan angle for the dipole with $ka=0.08$, $g/a=0.5$ - Ansoft HFSS v. 11. Note longitudinal asymmetry of current distribution and angular asymmetry in the current distribution a) E-plane; b) D-plane ($\phi=45$ deg); c) H-plane | 80 |
| Figure 2-18. Strip dipole current approximated by sinusoidal current over each section | 81 |
| Figure 3-1. Model of the center-fed droopy bowtie turnstile radiator in Ansoft HFSS. Left: Full model; Right: Radiator block..... | 94 |
| Figure 3-2. Parametric model of radiator block. Left: Side view of dimensioned droopy bowtie radiator. Right: Top view showing lumped port excitation. | 95 |
| Figure 3-3. Baseline X-Band droopy bowtie radiator simulation a) Scan impedance, b) Scan reactance, c) Scan return loss. Dimensionless convexity factor $\Delta/b= 0.0$ | 97 |
| Figure 3-4. Baseline X-Band droopy bowtie radiator simulation a) Scan impedance, b) Scan reactance, c) Scan return loss. Dimensionless convexity factor $\Delta/b= +0.06$ | 98 |
| Figure 3-5. Baseline X-Band droopy bowtie radiator simulation a) Scan impedance, b) Scan reactance, c) Scan return loss. Dimensionless convexity factor $\Delta/b= -0.06$ | 99 |
| Figure 3-6. Total directivity of an isolated element over infinite ground plane –one bowtie pair is excited; radiator geometry is given in Table 3-2. a) E-plane; b) D-plane ($\phi=45$ deg); c) H-plane. Dimensionless convexity factor $\Delta/b= 0.0$ | 100 |
| Figure 3-7. Input impedance (a) and return loss (b) for an isolated droopy bowtie over infinite ground plane. Dimensionless convexity factor $\Delta/b= 0.0$ | 101 |
| Figure 3-8. Cross polarization of droopy bowtie turnstile array radiators versus a dipole array and a “bunny-ear” array..... | 103 |
| Figure 3-9. Dyson balun for single polarized dipole antenna..... | 105 |
| Figure 3-10. Quad line concept..... | 106 |
| Figure 3-11. Bowtie wing to quad line to printed wiring board assembly | 107 |

| | |
|---|-----|
| Figure 3-12. Calculation of odd mode characteristic impedance and propagation constant using the method of images over a PEC ground plane. | 108 |
| Figure 3-13. HFSS model of quad line (left); high isolation quad line (right) | 109 |
| Figure 3-14. Isolation between parallel plate waveguides: HFSS calculated S-parameters..... | 110 |
| Figure 3-15. Differential-mode results for the terminated four-port quad line column..... | 111 |
| Figure 3-16. Complete Dyson balun-based antenna radiator with a symmetric antenna load. The balun for only one antenna element is shown..... | 113 |
| Figure 3-17. Antenna-balun transmission line model for the droopy bowtie turnstile radiator with quad line feed | 114 |
| Figure 3-18. Four-port model of one section for the standard Wilkinson power divider..... | 115 |
| Figure 4-1. Injection Molded, 8 x 16 droopy bowtie turnstile radiator array: Top: rectangular lattice; Bottom: triangular lattice | 119 |
| Figure 4-2. Injection Molded, Gen 1.0 droopy bowtie turnstile radiator array: Left: 2x6 drawing; Right: injection molded prototypes | 120 |
| Figure 4-3. Right: injection molded, copper plated Gen 1.0 droopy bowtie radiator Left: Gen 1.0 droopy bowtie radiator after laser etch..... | 120 |
| Figure 4-4. Injection molded, plated Gen 2.0 droopy bowtie radiator model | 121 |
| Figure 4-5. Injection molded, silver epoxy spray plated Gen 2.0 droopy bowtie radiator | 122 |
| Figure 4-6. Close-up: injection molded, silver epoxy spray plated Gen 2.0 droopy bowtie radiator | 122 |
| Figure 4-7. Microstrip line insertion loss: silver epoxy spray vs copper and aluminum..... | 123 |
| Figure 4-8. Dipole efficiency: silver epoxy spray vs copper | 124 |
| Figure 4-9. Quad line feed assembly concept..... | 125 |
| Figure 4-10. Quad line feed assembly | 125 |
| Figure 4-11. Printed wiring board array of quad line strips..... | 126 |
| Figure 4-12. Semi-automated quad line feed assembly | 127 |
| Figure 4-13. Batch process: quad line feed assembly..... | 127 |
| Figure 4-14. Droopy bowtie with quad line feed: unit cell assembly concept | 128 |
| Figure 4-15. Pick-and-place robot | 129 |
| Figure 4-16. 2x6 Printed wiring board-radiator side | 130 |
| Figure 4-17. 2x6 Printed wiring board-connector side | 131 |
| Figure 4-18. Quad line feed assembly process | 131 |
| Figure 4-19. 2x6 eggcrate assembly | 132 |
| Figure 4-20. 2x6 eggcrate assembled to pwb carrier | 132 |
| Figure 4-21. Droopy bowtie assembled to eggcrate unit cell | 133 |

| | |
|---|-----|
| Figure 4-22. 2x6 Gen 2.0 X-Band droopy bowtie radiator with quad line feed | 133 |
| Figure 4-23. Assembly steps 1 - 4 | 134 |
| Figure 4-24. Assembly steps 5 – 6..... | 134 |
| Figure 4-25. Gen 1.0 HFSS model..... | 136 |
| Figure 4-26. Gen 1.0 radiator and quad line feed assembly. Left: Pro-E model showing quad line; Right: fabricated 2x6 X-Band array | 137 |
| Figure 4-27. Gen 2.0 HFSS model..... | 138 |
| Figure 4-28. X-Band droopy bowtie subassembly: side view, unplated | 138 |
| Figure 4-29. X-Band droopy bowtie subassembly: top view, unplated. Dimensions of openings in mold..... | 139 |
| Figure 4-30. X-Band droopy bowtie subassembly: top view, plated. Left: topside plated wings; Right: bottom side plated wings..... | 139 |
| Figure 4-31. X-Band quad line, side view | 140 |
| Figure 4-32. X-Band quad line, top view | 140 |
| Figure 4-33. X-Band eggcrate subassembly, side view | 141 |
| Figure 4-34. X-Band eggcrate subassembly, top view | 141 |
| Figure 4-35. X-Band PWB subassembly, side view..... | 142 |
| Figure 4-36. X-Band PWB subassembly, top view of coplanar line | 142 |
| Figure 4-37. X-Band PWB subassembly. Detail of coplanar Line..... | 143 |
| Figure 4-38. Gen 2.0 radiator and feed: return loss | 144 |
| Figure 4-39. Gen 2.0 lattice grating lobe plot: 0.440in square lattice. Left: 12GHz; Right: 15GHz..... | 144 |
| Figure 4-40. Gen 2.0 radiator and feed: infinite array embedded element patterns | 145 |
| Figure 4-41. Droopy bowtie electric field polarization | 145 |
| Figure 4-42. L-Band prototype assembly | 146 |
| Figure 4-43. L-Band test measurement set up | 147 |
| Figure 4-44. L-Band prototype. Measured isolation between the two prototype antennas setup (left); measured results (right)..... | 148 |
| Figure 4-45. L-Band prototype. Measured return loss..... | 149 |
| Figure 4-46. X-Band return loss measurement set up..... | 150 |
| Figure 4-47. X-Band Gen 1.0 droopy bowtie turnstile radiator and quad line feed | 150 |
| Figure 4-48. Unit under test..... | 151 |
| Figure 4-49. Return loss. Vertical polarization (left) and horizontal polarization (right) | 151 |
| Figure 4-50. Far-field pattern test measurement set up | 152 |

| | |
|--|-----|
| Figure 4-51. Unit under test in the far-field anechoic chamber | 152 |
| Figure 4-52. E-plane pattern cuts | 153 |
| Figure 4-53. D-plane pattern cuts | 154 |
| Figure 4-54. H-plane pattern cuts | 155 |
| Figure 4-55. Gen 2.0 X-Band droopy bowtie radiator with quad line feed: Return loss for vertical and horizontal polarization for a single element (measurement) and an embedded array element at boresite (simulation)..... | 156 |
| Figure 4-56. Gen 2.0 X-Band droopy bowtie radiator with quad line feed: isolation between vertical and horizontal polarization for a single element (measurement) and embedded array element at boresite (simulation). | 157 |
| Figure A-1. Linear system block diagram | 165 |
| Figure A-2. Impulse response for $ r =0.9$ | 168 |
| Figure A-3. Single unit cell bowtie surface currents | 169 |
| Figure A-4. Impulse response $ H(\omega) $ for $ r = 0.05$; $n = 3$ | 169 |
| Figure A-5. Single unit cell bowtie surface currents | 170 |
| Figure A-6. Impulse response $ H(\omega) $ for $ r = 0.035$; $n = 3$ | 170 |
| Figure A-7. Single unit cell bowtie surface currents | 171 |
| Figure A-8. Impulse response $ H(\omega) $ for $ r = 0.06$; $n = 3$ | 171 |
| Figure A-9. Single unit cell bowtie surface currents | 172 |
| Figure A-10. Impulse response $ H(\omega) $ for $ r = 0.1$; $n = 3$ | 172 |

List of Tables

| | |
|--|-----|
| Table 1-1. 19x19 Planar array cases | 26 |
| Table 3-1. Phased array radiator requirement..... | 91 |
| Table 3-2. Bowtie radiator vs. phased array radiator requirement | 92 |
| Table 3-3. Bowtie radiator design challenges vs. approach..... | 93 |
| Table 3-4. Baseline X-band droopy bowtie radiator dimensions | 95 |
| Table 3-5. Quad line features..... | 106 |
| Table 4-1. Silver epoxy technical specifications | 123 |

List of Published Papers and Patents

1. Puzella, A., Palevsky, A., “Electromagnetic Dispersion of a Coaxial Waveguide with an Arbitrary Radial Dielectric Profile”, IEEE Transactions on Electron Devices, Vol. 35, No. 11, November, 1988, pg. 2048-2051.
2. S. N. Makarov, A. Puzella, “Scan Impedance for An Infinite Dipole Array: Hansen’s Formulas Compared with Ansoft HFSS Simulations”, IEEE Antennas and Propagation Magazine, Vol. 49, No. 4, August 2007, pg. 143-156.
3. S. N. Makarov, A. Puzella, “Insertion Loss for Two Microstrip Ports Coupled by Proximity Slots”, IEEE Antennas and Propagation Society International Symposium, Honolulu, HI, 2007, pg. 505-508.
4. A. Puzella, R. Alm, “Air-Cooled, Active Transmit/Receive Panel Array”, IEEE Radar Conference, Vol. 35, No. 11, Rome, Italy, May, 2008, pg. 421-26.
5. Puzella, M. Sarcione, “Technology Trends for Future Low Cost Phased Arrays”, Microwave Symposium Digest (MTT), 2010 IEEE MTT-S International, Baltimore, MD, May 23-28, 2010, pg. 688-690.
6. Puzella, F. Sciré-Scappuzzo, S. N. Makarov, “Design and Manufacturing of an Injection-Molded Dual-Polarized X-Band Low-Cost Scanning Array”, Antenna Applications Symposium, Allerton, Illinois, September 17, 2013, pg. 1-28.
7. U.S. Patent. Puzella, Angelo, Fernando Beltran; 2003; Slot Coupled, Polarized, Egg-Crate Radiator; 6,624,787; October 1, 2001; September 23, 2003.
8. U.S. Patent. Puzella, Angelo, Crowder, Joseph; Dupuis, Patricia and Fallica, Michael, 2004; Multilayer Stripline Radio Frequency Circuits and Interconnections Methods; 6,731,189; June 27, 2002; May 4, 2004.
9. U.S. Patent. Puzella, Angelo, Komisarek, Kenneth; Crowder, Joseph; Dupuis, Patricia and Kingston, Gary, 2003; Embedded Planar Circulator; 6,611,180; April 16, 2002; August 26, 2003.
10. U.S. Patent. Puzella, Angelo, Crowder, Joseph; Dupuis, Patricia; Fallica, Michael; Francis, John and Licciardello, Joseph, 2008; Tile Sub-Array And Related Circuits And Techniques; 7,348,932; September 21, 2006; March 25, 2008.

11. U.S. Patent. Puzella, Angelo, Crowder, Joseph; Dupuis, Patricia; Fallica, Michael; Francis, John and Licciardello, Joseph, 2010; Radio Frequency Interconnect Circuits and Techniques; 7,671,696; November 9, 2006; March 2, 2010.
12. U.S. Patent. Puzella, Angelo, Licciardello, Joseph; Dupuis, Patricia; Francis, John; Komisarek, Kenneth; Bozza, Donald; Alm, Roberto ,2012; Panel Array; 8,279,131; June 15, 2009; October 2, 2012.
13. U.S. Patent. Puzella, Angelo, Licciardello, Joseph; Pereira, Stephen and Ellsworth, Joseph, 2010; Method and Apparatus for Thermal Management of a Radio Frequency System; 7,859,835; June 10, 2009; December 28, 2010.
14. U.S. Patent. Puzella, Angelo, Makarov, Sergey and Morrison, Patrick; 2013; “Droopy bowtie Radiator with Integrated Balun”; 8,581,801; June 1, 2010; November 12, 2013.
15. U.S. Patent Application No. 12/694,450; Published On May 27, 2010; (Filing Date January 27, 2010); (Angelo Puzella, Joseph Crowder; Patricia Dupuis; Michael Fallica; John B. Francis and Joseph Licciardello, Applicant); Entitled: Radio Frequency Interconnect Circuits and Techniques.
16. U.S. Patent Application No. 13/295,437; Published On December 13, 2012; (Filing Date November 14, 2011); (Angelo Puzella, Patricia Dupuis; Craig Lemmler; Donald Bozza; Kassam Bellahrossi; James Robbins; and John Francis , Applicant); Entitled: An Active Electronically Scanned Array (AESA) Card.
17. U.S. Patent Application No. 13/267,193; Published On April 24, 2014; (Filing Date October 6, 2011); (Angelo Puzella, Tunglin Tsai; John Francis; Donald Bozza; Kathe Scott; and Patricia Dupuis, Applicant); Entitled: Scalable, Analog Monopulse Network.
18. U.S. Patent Application No. 14/072,949; Published On April 11, 2013; (Filing Date November 6, 2013); (Angelo Puzella, Jeffrey Upton; Arsenio Vargas; Steven Nguyen; and Kassam Bellahrossi, Applicant); Entitled: Calibration System and Technique for A Scalable, Analog Monopulse Network.

Introduction

Thesis Goal

Radar requirements are driving towards higher range resolution to track smaller, stealthier targets which drives RF bandwidth and low cross-polarization of radiator designs for Active Electronically Scanned Antenna's (AESA). In addition to broadband RF performance, AESA designs also demand polarization diversity and stable scan element pattern gain across the operating frequency band.

Therefore, the main objective of this thesis has been to develop a

- i. low profile
- ii. wideband and
- iii. polarization diverse

radiator for advanced phased array applications with the goal of using low cost manufacturing and assembly techniques from the commercial sector. Ideally, the new radiator design would utilize low cost fabrication techniques such as injection molding and/ or 3-D printing, and also leverage automated assembly techniques.

The thesis is organized into four chapters and two appendices, which are briefly reviewed below.

Chapter 1. Introduction to Non-finite and Finite Phased Arrays

Chapter 1 reviews basic phased array concepts and introduces the array factor formulation. Finite array patterns are plotted using the array factor to demonstrate basic characteristics of the array pattern as the number of radiating elements are increased and as the array is scanned; the effect of the element pattern on the array pattern is introduced to show the reality that as the array is scanned off boresite the gain of the array is reduced by the element pattern shape. However, the array patterns at this stage do not include the important effect of mutual coupling and the effect mutual coupling has on the array pattern as the pattern is scanned.

Chapter 2. Floquet Analysis for Phased Array Antennas

Chapter 2 is based on my paper "Scan Impedance for An Infinite Dipole Array: Hansen's Formulas Compared with Ansoft HFSS Simulations"^{2.1} and introduces the Floquet Modal approach as applied to linear phased arrays with a periodic amplitude and phase excitation. The array scan

impedance for an infinite array of strip-dipole is derived and includes the effect of mutual coupling. The analytical scan impedance results are compared with the scan impedance computed by the infinite array solver HFSS; the section concludes with an approach of extending the analytical single mode Floquet expansion to multimode current expansion on the dipole.

In addition, a multimodal Floquet approach based on the paper “Scan Impedance for An Infinite Dipole Array: Accurate Theoretical Model Versus Numerical Software”^{2.10} is also discussed. The paper extends the analytical formulation for the scan impedance of an infinite dipole array by extending the original theoretical model of VanKoughnett and Yen for the infinite, planar dipole array.

The Floquet modal expansion approach provides an elegant mathematical method to initially analyze the scan performance of a phased array of dipoles (or slots) and gives the designer an appreciation for the parameters that greatly influence the scan impedance. The value of the analytical Floquet approach is that it provides a rapid estimation of antenna array performance over a frequency band of interest; the value of the numerical simulation tool HFSS is to make final adjustments to the model for optimal performance.

Chapter 2 concludes by recognizing the need for a new tool to analyze finite arrays that combines the versatility and power of an electromagnetic solver like HFSS with the speed of an analytical formulation that enables the engineer in industry to rigorously and efficiently model a finite array of any size comprised of radiators of virtually any complexity.

Chapter 3. Droopy Bowtie Radiator with Integrated Balun: Theory

Chapter 3 presents the theoretical model of a new phased array element: the droopy bowtie turnstile radiator with quad line feed. Chapter 3 is based on my paper “Design and Manufacturing of an Injection-Molded Dual-Polarized X-Band Low-Cost Scanning Array”^{3.1} and US Patent “Droopy bowtie Radiator with Integrated Balun”^{3.2}.

A droopy bowtie radiator was selected as baseline element to investigate how it meets the phased array system requirements outlined in Chapter 3. The bowtie element is also amenable to an integrated packaging approach using injection molded parts and plating techniques and automated assembly. A novel quad line balun feed is developed that provides a low loss, high isolation feed for the droopy bowtie. Finally, the overall antenna-transmission line model theory is presented that

integrates the bowtie radiator, quad line and the hybrid feed circuit. In Chapter 4, this antenna-transmission line is realized in hardware based on a detailed HFSS model incorporating an injection-molded droopy bowtie radiator; RF measurements of an X-Band prototype will be presented.

Chapter 4. Practical Realization and Applications of Droopy Bowtie for Finite Arrays

Chapter 4 presents low cost manufacturing and assembly techniques applied to the droopy bowtie radiator with the quad line feed developed in Chapter 3. RF measurements are presented for a prototype L-Band and X-Band droopy bowtie radiator with the quad line feed demonstrating a viable, broadband and compact radiator and feed architecture for phased arrays.

Injection molding and pattern plating are introduced as a low cost manufacturing approach for the droopy bowtie. An automated step by step assembly concept using commercially available robots is presented that shows how the printed wiring board carrier is first assembled with an eggcrate base; then, the quad line feeds are inserted into each unit cell; finally, the droopy bowtie subassemblies are mounted over each quad line; the entire assembly uses solder-jetted paste applied at the critical RF and mechanical joints and a reflow oven to bond together the final assembly.

Chapter 4 concludes that the droopy bowtie turnstile radiator with quad line feed RF measurements of the L-Band prototype and X-Band prototypes were encouraging- although the measurements were not in a phased array environment:

- L-Band prototype achieved a 2:1 RF bandwidth;
- X-Band prototype achieved a 14% RF bandwidth.

Future measurements at X-Band will be performed on an array of droopy bowtie turnstile radiator with quad line feed elements.

Overall, the goal of “Practical Realization and Application” of the droopy bowtie turnstile radiator with quad line feed was achieved with the first prototypes.

Appendix A. Time Domain Approach to Characterizing Antenna Radiation

Appendix A is analyzing the time domain impulse response of a bowtie antenna. It provides an insightful method to analyze the relationship between bandwidth and radiation efficiency.

Chapter 1 – Introduction to Non-finite and Finite Phased Arrays

1.0 Theoretical Background of Phased Array Design

Chapter 1 is an introductory chapter that reviews basic phased array concepts and establishes terminology that will aid the understanding the development of the droopy bowtie radiator and, later, the new method to analyze finite planar arrays. Section 1.1 introduces the array factor. For an array with uniform spacing, the array factor is shown to have the same form as a complex Fourier series for the uniform arrangement of isotropic radiators. Section 1.2 introduces the element pattern into the array factor expression. Section 1.3 discusses the array pattern main beam width. Section 1.4 presents examples of array factor calculations for a linear array of 2 isotropic radiators and a linear array of 16 isotropic radiators. Section 1.5 extends the linear array factor to the planar array factor. The grating lobe series is derived and examples of grating lobes plots are given for several element spacing's. Section 1.6 presents the instantaneous bandwidth expression for a phased array. Section 1.7 presents planar array patterns for a 19x19 array. Section 1.8 summarizes Chapter 1.

Introduction

A practical phased array antenna is complex system. However, at its most basic level, a phased array antenna is a spatial arrangement of antennas, electrically combined to form a directional antenna pattern and pattern shape. For example:

Figure 1-1 shows a linear array of 8 isotropic radiators; the total complex electric field can be described by destructive and constructive interference in the far-field:

- A zero electric field is at a point where the complex (magnitude and phase) electric fields from the isotropic point sources perfectly cancel;
- At all other points in the far-field, the total complex electric field is non-zero; the relative magnitude of the field depends on the relative phase shift from each point source;
 - In the example below, the total electric field is a maximum at boresite; boresite is defined as the direction normal to the axis of the linear array and denoted by the spherical polar angle θ ;

As shown in Figure 1-1, the fields from the isotropic radiators interfere constructively and destructively in the space beyond the array; at any one point in the far-field, the field strength depends upon the complex superposition of the amplitude and phase of the received electric field due to each source; the relative phases depend on the difference in distance from the field point to the individual point sources and on any phase delay applied at the point source.

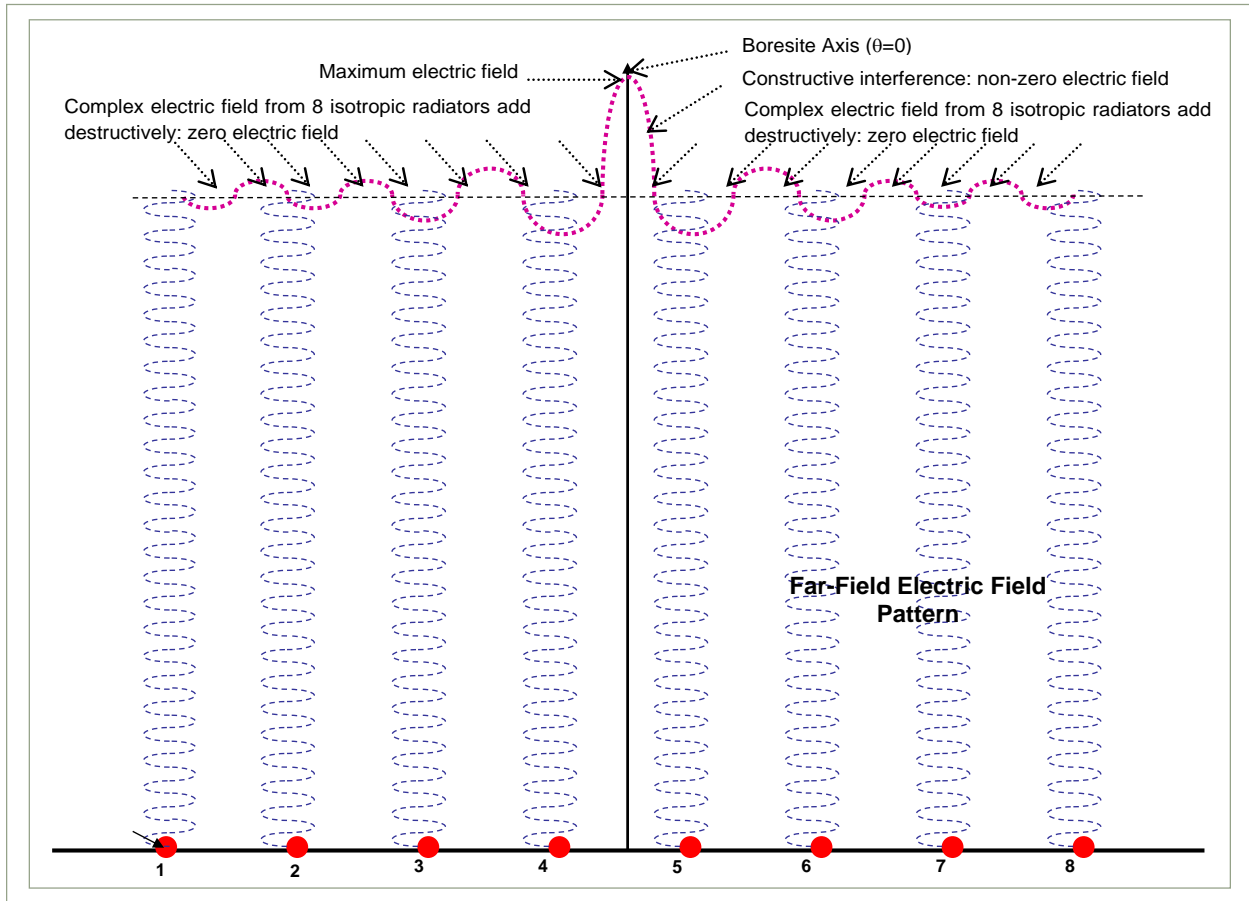


Figure 1-1. Linear phased array antenna of 8 isotropic radiators: Scan to $\theta=0^\circ$

Figure 1-2 illustrates the concept of steering the main beam off of boresite; a periodic phase delay is applied from right (point source #8) to left (point source #1). The greater the phase delay between adjacent elements, the greater the scan angle θ off of boresite. At each element, the phase delay can be accomplished with a “true time delay” or with a phase shifter (Section 1.1.1).

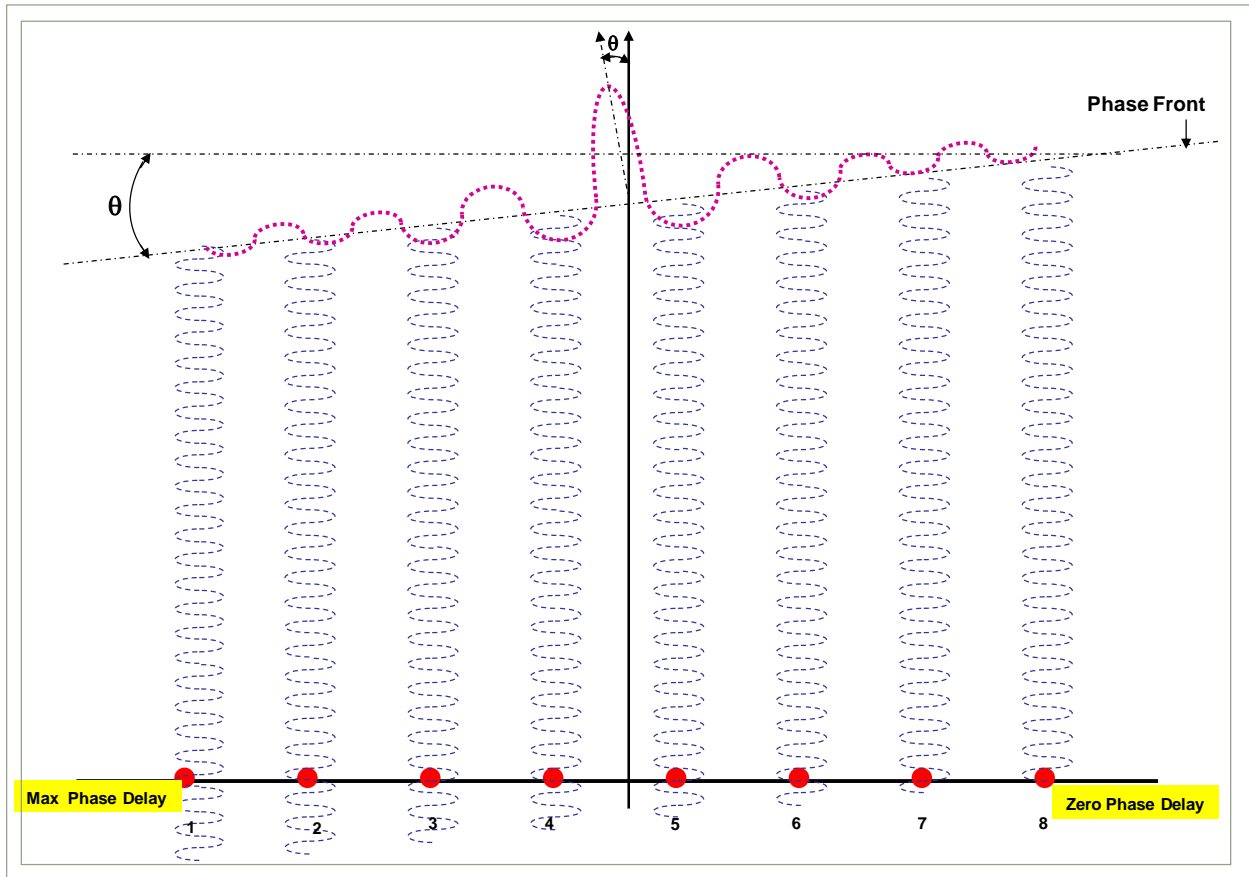


Figure 1-2. Linear phased array antenna of 8 isotropic radiators: Scan to θ

1.1 The Array Factor

Section 1.1 develops the array factor for a linear array; extension of the array factor to a two-dimensional planar array is presented in Section 1.5. The discussion that follows assumes a receive array; but, the mathematical expressions also apply to a transmit array.

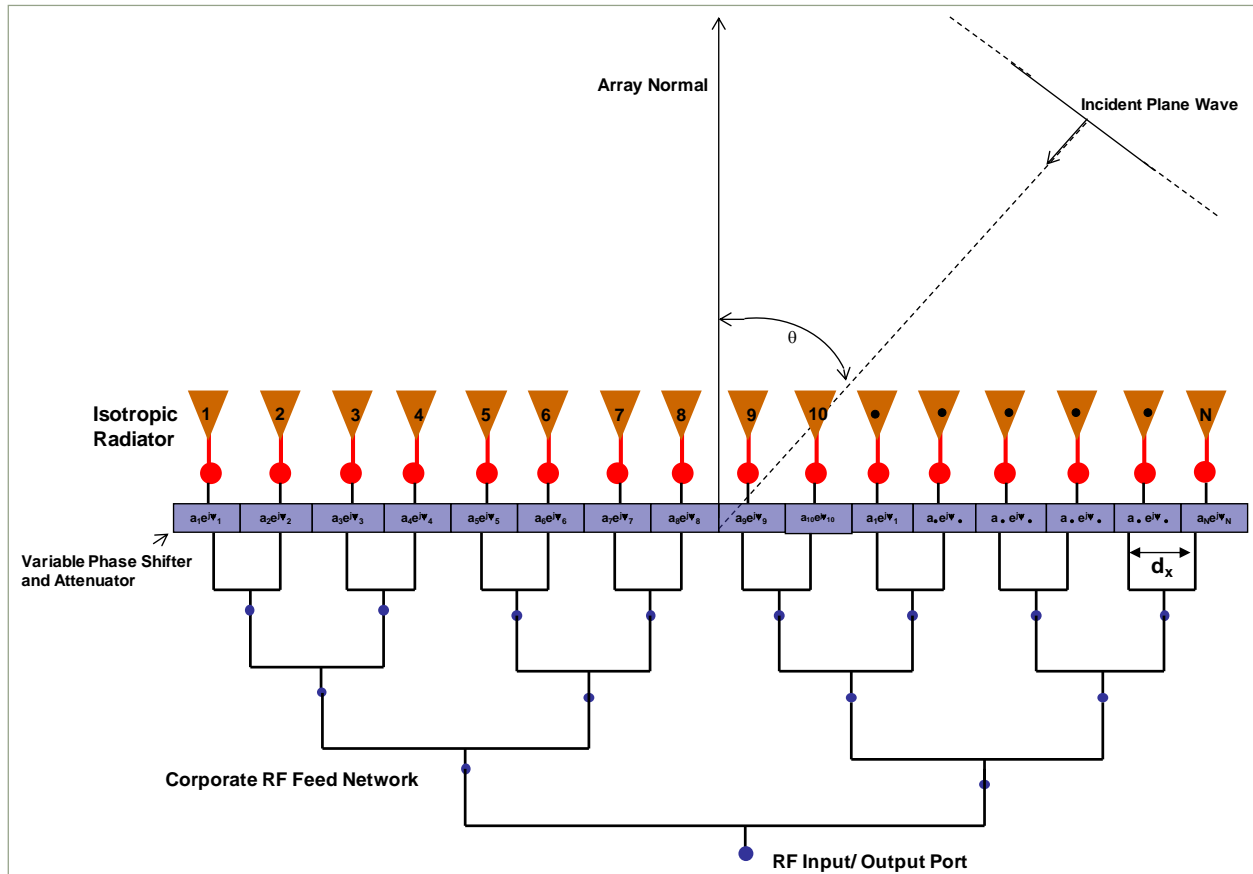


Figure 1-3. Linear phased array antenna of N isotropic radiators

Consider a one-dimensional array of N isotropic radiators shown in Figure 1-3; the isotropic radiators are electrically connected by an RF corporate feed network; the RF corporate feed is based on 3dB power splitters arranged in a parallel architecture:

The position of each isotropic radiator, a_n , is expressed as: $a_n = (n - 0.5(N+1)) * d_x$, $n = 1, 2, \dots, N$. In addition, each radiator has a variable phase shifter and attenuator which enables the array pattern to be shaped and scanned as will be shown in Sections 1.4 and 1.7.

For an incident plane wave at angle θ with respect to the array normal and referenced to the geometrical center of the array, the complex weighted voltage at each element output is written as:

$$A_n = a_n e^{j\frac{2\pi}{\lambda}x_n \sin\theta} \quad (1.1.1)$$

where a_n is the complex voltage weighting at the n^{th} element. The sum of complex voltages given in expression 1.1.1 is called the Array Factor (AF) which mathematically expresses the spatial response of an array of isotropic sources:

$$AF = \sum_{n=1}^N A_n = \sum_{n=1}^N a_n e^{j\frac{2\pi}{\lambda}x_n \sin\theta} \quad (1.1.2)$$

The array factor is the normalized radiation pattern of an array of isotropic radiators. The array factor expression in 1.1.2 is a complex Fourier series that relates physical space- the spatial distribution of point sources x_n , to the array pattern in angle space; in angle space, the response at each angle θ represents the total contribution (complex summation) of all point sources of the array at θ . Summarizing, the array factor is the radiation pattern produced by an array of N isotropic radiators:

- Function of element position;
- Does not include the effects of mutual coupling;
- Function of frequency and scan angle θ .

1.1.1 Linear Phase Taper for Electronic Scan

In Figure 1-1, each radiator has a variable phase shifter and attenuator; this section will show how the array main beam is scanned in the array factor expression.

The linear array main beam is scanned by the complex voltage weighting of the n^{th} element, a_n :

$$a_n = \alpha_n e^{j\psi_n} \quad (1.1.3)$$

Inserting expression 1.1.3 into expression 1.1.2:

$$AF = \sum_{n=1}^N a_n e^{j\frac{2\pi}{\lambda}x_n \sin\theta} = \sum_{n=1}^N \alpha_n e^{j\psi_n} e^{j\frac{2\pi}{\lambda}x_n \sin\theta} \quad (1.1.4)$$

The array scan angle θ_0 is determined by the inter-element phase shift given by expression 1.1.5:

$$\psi_n = -\frac{2\pi}{\lambda}x_n \sin\theta_0 \quad (1.1.5)$$

Inserting expression 1.1.5 into expression 1.1.4:

$$AF = \sum_{n=1}^N \alpha_n e^{j\psi_n} e^{j\frac{2\pi}{\lambda} x_n \sin\theta} = \sum_{n=1}^N \alpha_n e^{j\frac{2\pi}{\lambda} x_n (\sin\theta - \sin\theta_0)} \quad (1.1.6)$$

The array factor in expression 1.1.6 is the basis for scanning the main beam of a phased array. Electronic scan can be achieved through phase shifter steering or time delay steering. For phase shifter steering, the expression 1.1.6 is written^{1.1}:

$$AF = \sum_{n=1}^N \alpha_n e^{jx_n \left(\frac{2\pi}{\lambda} \sin\theta - \frac{2\pi}{\lambda_0} \sin\theta_0 \right)} \quad (1.1.7)$$

For time delay steering:

$$AF = \sum_{n=1}^N \alpha_n e^{j\frac{2\pi}{\lambda} x_n (\sin\theta - \sin\theta_0)} \quad (1.1.8)$$

Expression 1.1.7 shows that the peak of the scanned beam moves in angle space when $f \neq f_0$ ($\lambda \neq \lambda_0$); for “true time delay” steering, expression 1.1.8 shows that the beam peak at θ_0 remains the same for any frequency f . Phase shifter and time delay steering will be further discussed in Section 1.6.

1.1.2 Uniformly Excited Linear Array

For the uniformly excited linear array, the magnitude of the complex voltage weighting for each element is identical:

$$|a_1| = |a_2| = \dots = |a_N| \Rightarrow |\alpha_1| = |\alpha_2| = \dots = |\alpha_N|, \text{ for } n = 1, 2, \dots, N. \quad (1.1.9)$$

The array factor for the phase shifter case is:

$$AF = \sum_{n=1}^N \alpha_n e^{jx_n \left(\frac{2\pi}{\lambda} \sin\theta - \frac{2\pi}{\lambda_0} \sin\theta_0 \right)} = \alpha \sum_{n=1}^N e^{jx_n \left(\frac{2\pi}{\lambda} \sin\theta - \frac{2\pi}{\lambda_0} \sin\theta_0 \right)} \quad (1.1.10)$$

Substituting for element position x_n :

$$AF = \sum_{n=1}^N \alpha_n e^{j \left(n - \frac{N+1}{2} \right) \left(\frac{2\pi}{\lambda} \sin\theta - \frac{2\pi}{\lambda_0} \sin\theta_0 \right) d} = \alpha \sum_{n=1}^N e^{j\psi \left(n - \frac{N+1}{2} \right)} \quad (1.1.11)$$

where:

$$\psi = \left(\frac{2\pi}{\lambda} \sin \theta - \frac{2\pi}{\lambda_0} \sin \theta_0 \right) d \quad (1.1.12)$$

Writing out the terms for the array factor:

$$AF = \alpha \sum_{n=1}^N e^{j\psi(n-\frac{N+1}{2})} = \left[e^{j\psi(\frac{1-N}{2})} + e^{j\psi(\frac{3-N}{2})} + \dots + e^{j\psi(\frac{N-1}{2})} \right] \quad (1.1.13)$$

Now, multiply both sides by $e^{j\psi}$:

$$e^{j\psi} AF = \alpha \left[e^{j\psi(\frac{3-N}{2})} + e^{j\psi(\frac{5-N}{2})} + \dots + e^{j\psi(\frac{N+1}{2})} \right] \quad (1.1.14)$$

Subtracting the last two equations:

$$\begin{aligned} AF - e^{j\psi} AF &= AF(1 - e^{j\psi}) = \alpha \left[e^{j\psi(\frac{1-N}{2})} - e^{j\psi(\frac{1+N}{2})} \right] \\ AF &= \frac{\alpha \left[e^{j\psi(\frac{1-N}{2})} - e^{j\psi(\frac{1+N}{2})} \right]}{(1 - e^{j\psi})} = \frac{\alpha \left[e^{-j\psi\frac{N}{2}} - e^{j\psi\frac{N}{2}} \right]}{e^{-j\psi\frac{N}{2}}(1 - e^{j\psi})} \end{aligned} \quad (1.1.15)$$

The array factor for a uniformly excited linear array is:

$$AF = \alpha \left[\frac{\sin(\frac{N\psi}{2})}{\sin(\frac{\psi}{2})} \right] \quad (1.1.16)$$

The array factor is a maximum for $\Psi=0^\circ$:

$$AF = \alpha[1+1+\dots+1] = \alpha N \quad (1.1.17)$$

Normalizing to the maximum value of the array factor:

$$AF = \left[\frac{\sin(\frac{N\psi}{2})}{N \sin(\frac{\psi}{2})} \right] \quad (1.1.18)$$

Expression 1.1.18 is the normalized array factor for a linear array of N isotropic radiators. The mathematical form of expression 1.1.18 is the same as that for a single slit diffraction pattern^{1,2}; phased array antenna pattern theory is based on the theory developed for diffraction gratings.

General observations on the array factor for a uniform illumination steered to boresite^{1,3}:

1. As the number of elements, N , increases the main antenna beam narrows;
2. In one 2π period of Ψ , the number of lobes equals $N-1$;
3. Width of minor lobes: $2\pi/N$;
4. Width of major lobes: $4\pi/N$;

1.2 Element Pattern

The element pattern is critical to the scan performance of a phased array: the element pattern determines the loss in gain as the array is scanned off boresite.

There are many types of antenna elements that can be used in a phased array: patch radiator, slot cut in a ground plane, dipole, helix, bowtie, etc.; what they all have in common is the element pattern for any antenna element multiplies the array factor.

Next, the element pattern of each element is considered. If N is large, the total array pattern can be written as a product of the array factor and element pattern; that is, we can assume that all the element patterns are identical across the array with negligible error:

$$P(\theta)_{array} = \sum_{n=1}^N (p_{en}(\theta)) a_n e^{j\frac{2\pi}{\lambda} x_n \sin\theta} \approx p_e(\theta) \sum_{n=1}^N a_n e^{j\frac{2\pi}{\lambda} x_n \sin\theta} = p_e(\theta) * AF \quad (1.2.1)$$

where p_{en} is the element pattern of the n^{th} element and p_e is the element pattern for all elements. This last equation is termed “pattern multiplication” and is the result of the large array approximation:

All elements in the array are assumed to have identical element patterns in all angle space;
 angle space: $0^\circ \leq \theta \leq 90^\circ, 0^\circ \leq \varphi \leq 360^\circ$

Expression 1.2.1 is the fundamental expression, and key approximation, for phased arrays:

All element patterns are identical

This approximation is justified for “large” arrays- that is, arrays that have a small percentage of “edge” elements.

Examples of the linear array factor for different N are presented in Section 1.4 to show how a directional beam is formed and how the beam can move for different complex weightings applied at the isotropic radiator; in addition, the effect of the element pattern as the main beam is scanned is shown in Section 1.4.3.

1.3 Beamwidth

The array main beamwidth is a function of the length of the array, L , and the scan angle θ . The array main beam width is the angular extent between the points on the main beam where power drops to 3dB (i.e., the half-power beamwidth). The general expression for the beamwidth scanned to θ_0 is^{1.4}:

$$\theta_{BW} = \frac{k\lambda}{L \cos \theta_0} \quad (1.3.1)$$

where $k \equiv$ beamwidth factor which is a function of the array aperture weighting. For example, for a uniformly illuminated aperture $k = 0.866$. Expression 1.3.1 for the beamwidth is valid for phase shifter and time delay beamsteering.

1.4 Linear Array Factor Examples

Linear array factor examples are presented for 1) linear array of 2 isotropic radiators and 2) linear array of 16 isotropic radiators. Sections 1.4.1 and 1.4.2 show array factor for N=2 and N=16, respectively. Section 1.4.3 introduces the element pattern in the array factor calculation for N=16.

1.4.1 Linear Array of N = 2 Isotropic Radiators

Case 1. Identical amplitude/ phase weighting; spacing $d_x = \lambda/2$ as shown in Figure 1-4.

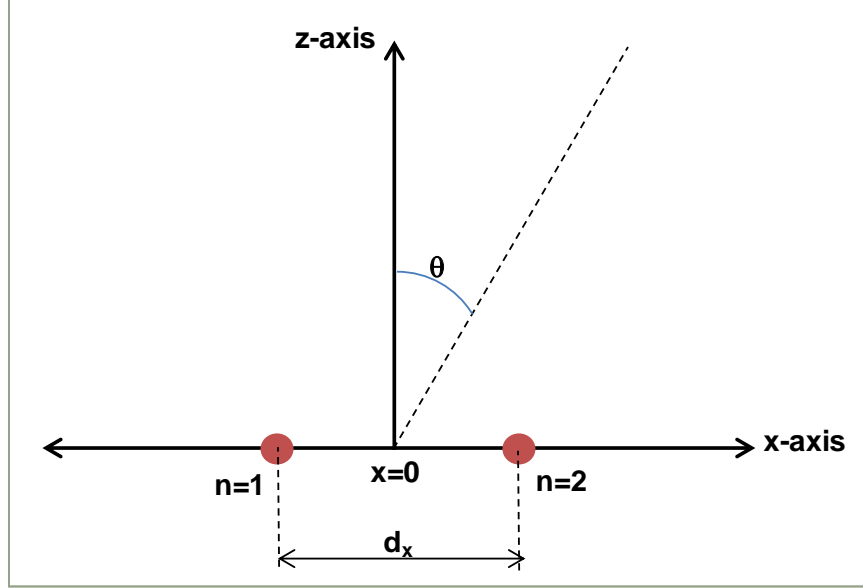


Figure 1-4. Linear array factor for $N = 2$

Now, $x_n = (n - 0.5(2+1))*d_x = (n - 3/2)*d_x$; $x_1 = -d_x/2$ and $x_2 = d_x/2$. From array factor expression 1.1.2:

$$AF = \sum_{n=1}^2 a_n e^{j\frac{2\pi}{\lambda} x_n \sin \theta} = \sum_{n=1}^2 (1) e^{j\frac{2\pi}{\lambda} x_n \sin \theta} = e^{j\frac{2\pi}{\lambda} x_1 \sin \theta} + e^{j\frac{2\pi}{\lambda} x_2 \sin \theta} = e^{j\frac{2\pi}{\lambda} (-d_x/2) \sin \theta} + e^{j\frac{2\pi}{\lambda} (d_x/2) \sin \theta}$$

$$AF = e^{-j\frac{\pi}{\lambda} d_x \sin \theta} + e^{j\frac{\pi}{\lambda} d_x \sin \theta} = e^{-j\frac{\pi}{\lambda} (\lambda/2) \sin \theta} + e^{j\frac{\pi}{\lambda} (\lambda/2) \sin \theta} = e^{-j\frac{\pi}{2} \sin \theta} + e^{j\frac{\pi}{2} \sin \theta} = 2 \cos\left(\frac{\pi}{2} \sin \theta\right)$$

$$AF = 2 \cos\left(\frac{\pi}{2} \sin \theta\right)$$

The polar plot of the normalized array factor is shown in Figure 1-5; the maxima are at $\theta = 0^\circ$, 180° and the minima are at $\theta = 90^\circ$, 270° .

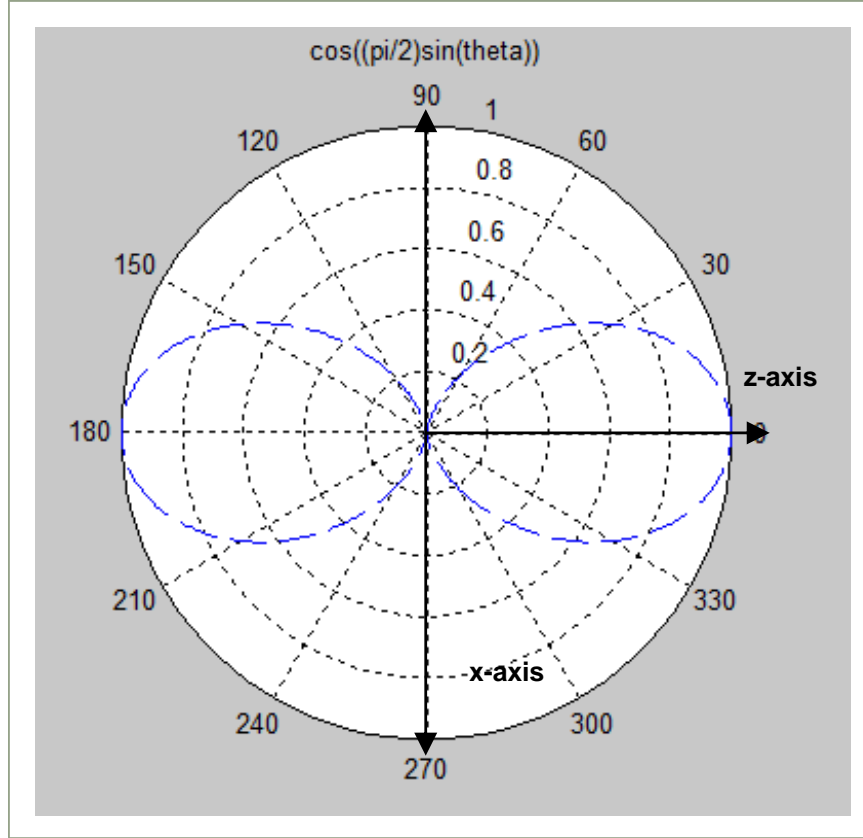


Figure 1-5. Polar plot: $N=2$ array, $d_x = \lambda/2$

Case 2. Identical amplitude; 180° phase difference; spacing $d_x = \lambda/2$

$$AF = \sum_{n=1}^2 a_n e^{j\frac{2\pi}{\lambda} x_n \sin \theta} = (-1)e^{j\frac{2\pi}{\lambda} x_1 \sin \theta} + (1)e^{j\frac{2\pi}{\lambda} x_2 \sin \theta} = -e^{j\frac{2\pi}{\lambda} (-d_x/2) \sin \theta} + e^{j\frac{2\pi}{\lambda} (d_x/2) \sin \theta}$$

$$AF = -e^{-j\frac{\pi}{\lambda} d_x \sin \theta} + e^{j\frac{\pi}{\lambda} d_x \sin \theta} = -e^{-j\frac{\pi}{\lambda} (\lambda/2) \sin \theta} + e^{j\frac{\pi}{\lambda} (\lambda/2) \sin \theta} = -e^{-j\frac{\pi}{2} \sin \theta} + e^{j\frac{\pi}{2} \sin \theta} = 2j \sin\left(\frac{\pi}{2} \sin \theta\right)$$

$$AF = 2j \sin\left(\frac{\pi}{2} \sin \theta\right)$$

The normalized array factor for a linear array of two isotropic radiators spaced $d_x = \lambda/2$ with equal amplitude and phase weighting is given by:

$$AF = \sin\left(\frac{\pi}{2} \sin \theta\right)$$

The polar plot of the array factor is shown in Figure 1-6; the maxima are now at $\theta = 90^\circ, 270^\circ$ and the minima are at $\theta = 0^\circ, 180^\circ$.

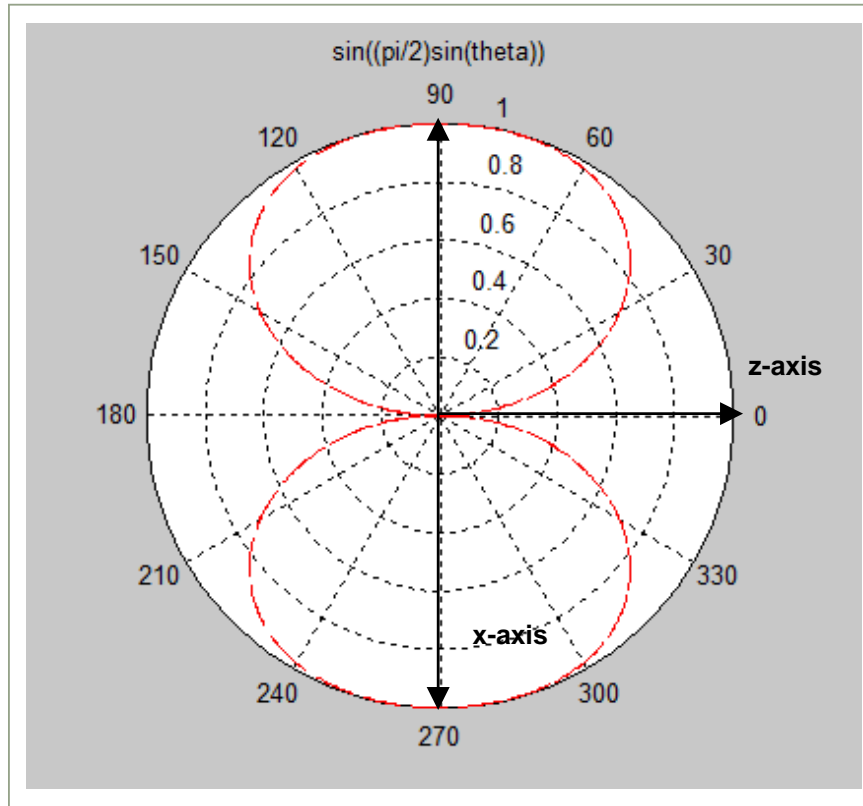


Figure 1-6. Polar plot: $N=2$ array, $d_x = \lambda/2$

Case 3. Identical amplitude and phase weighting; spacing $d_x = \lambda$.

$$AF = \sum_{n=1}^2 a_n e^{j\frac{2\pi}{\lambda} x_n \sin \theta} = \sum_{n=1}^2 (1) e^{j\frac{2\pi}{\lambda} x_n \sin \theta} = e^{j\frac{2\pi}{\lambda} x_1 \sin \theta} + e^{j\frac{2\pi}{\lambda} x_2 \sin \theta} = e^{j\frac{2\pi}{\lambda} (-d_x/2) \sin \theta} + e^{j\frac{2\pi}{\lambda} (d_x/2) \sin \theta}$$

$$AF = e^{-j\frac{\pi}{\lambda} d_x \sin \theta} + e^{j\frac{\pi}{\lambda} d_x \sin \theta} = e^{-j\frac{\pi}{\lambda} (\lambda) \sin \theta} + e^{j\frac{\pi}{\lambda} (\lambda) \sin \theta} = e^{-j\pi \sin \theta} + e^{j\pi \sin \theta} = 2 \cos(\pi \sin \theta)$$

$$AF = 2 \cos\left(\frac{\pi}{2} \sin \theta\right)$$

The normalized array factor for a linear array of two isotropic radiators spaced $d_x = \lambda/2$ with equal amplitude and phase weighting is given by:

$$AF = \cos(\pi \sin \theta)$$

Figure 1-7 now shows four lobes: the main antenna lobes at $\theta = 0^\circ, 180^\circ$ and two additional lobes called *grating lobes* at $\theta = 90^\circ, 270^\circ$. Grating lobes will be discussed in Section 1.5.1.

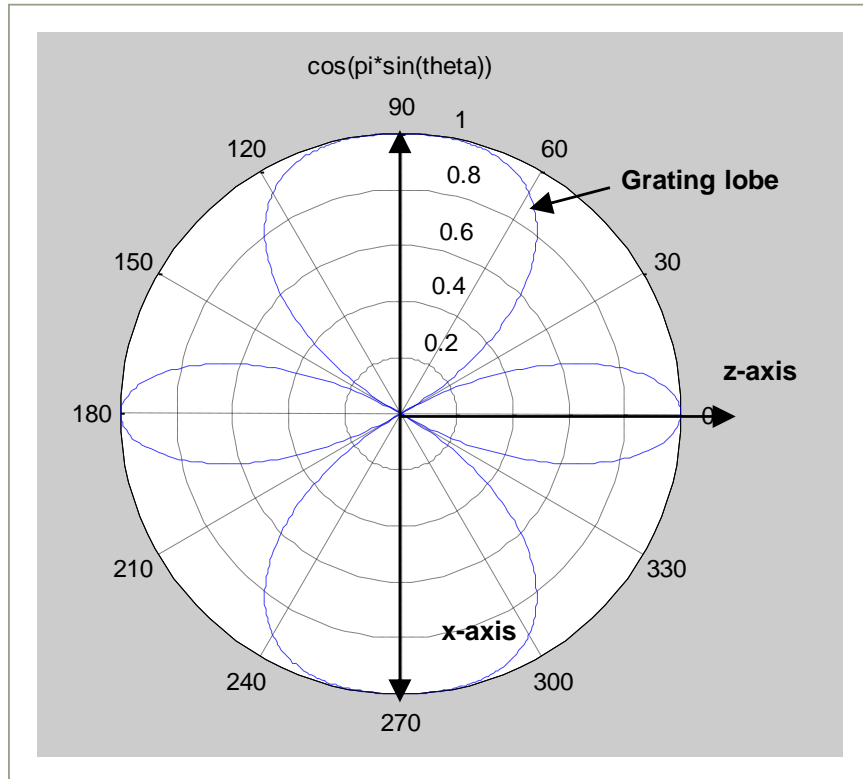


Figure 1-7. Polar plot: $N=2$ array, $d_x = \lambda$

1.4.2 Linear Array of $N = 16$ Isotropic Radiators

Case 4. Identical amplitude weighting; spacing $d_x = \lambda/2$. The rectangular plot in Figure 1-8 is of the array factor only. Calculating the 3dB beamwidth for the uniformly weighted linear array at $\theta_0 = 0^\circ$:

$$\theta_{BW} = \frac{k\lambda}{L \cos \theta_0} = \frac{0.866\lambda}{(16\lambda/2) \cos(0)} = 0.108 \text{ rad} = 6.2 \text{ deg}$$

where $k = 0.866$ for uniform weighting. The rectangular plot in Figure 1-9 zooms in on the array factor pattern to show the 3dB beamwidth; the calculated 3dB beamwidth of 6.2 degrees agrees with the array factor simulation of 6.2 degrees.

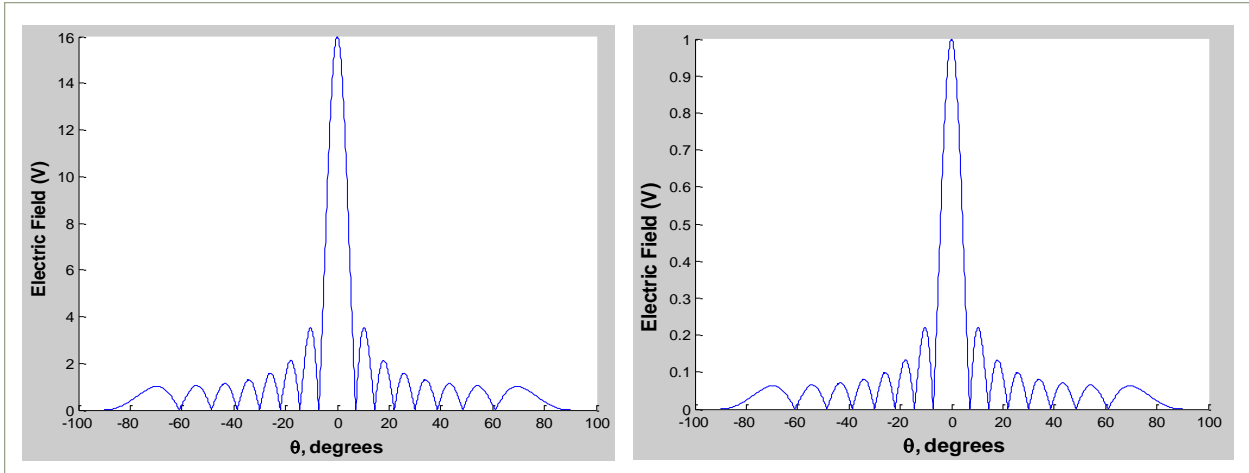


Figure 1-8. Linear array factor: $N = 16$ isotropic radiators. Un-normalized (left); normalized (right)

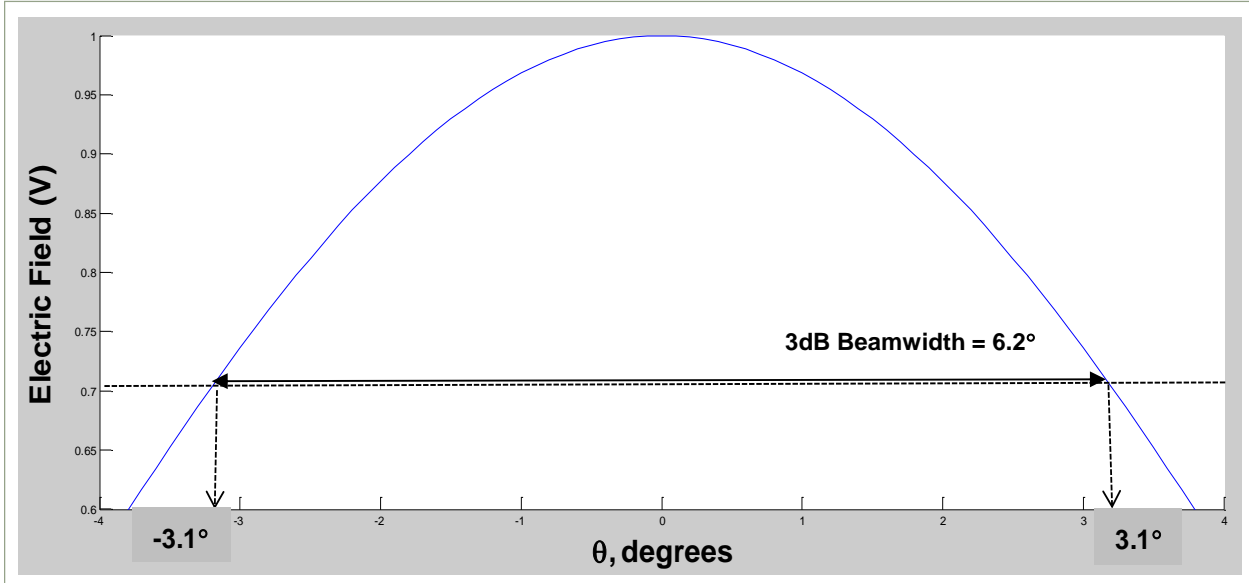


Figure 1-9. Linear array factor: $N = 16$ isotropic radiators. 3dB beamwidth

Case 4 (continued). Figure 1-10 shows the 3dB beamwidth increasing with scan angle Figure 1-11 zooms in on the beam peaks.

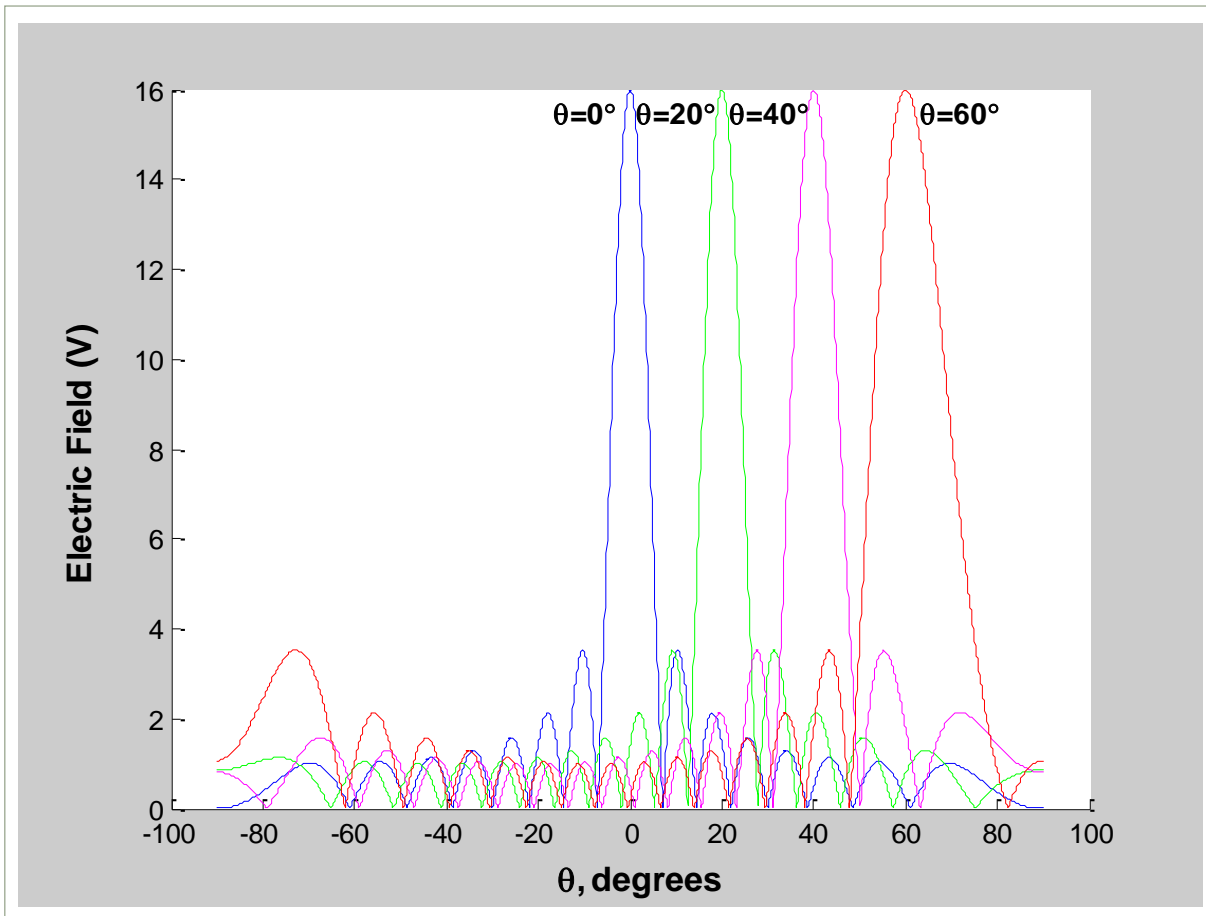


Figure 1-10. Linear array factor: $N = 16$ isotropic radiators, beamwidth vs. scan

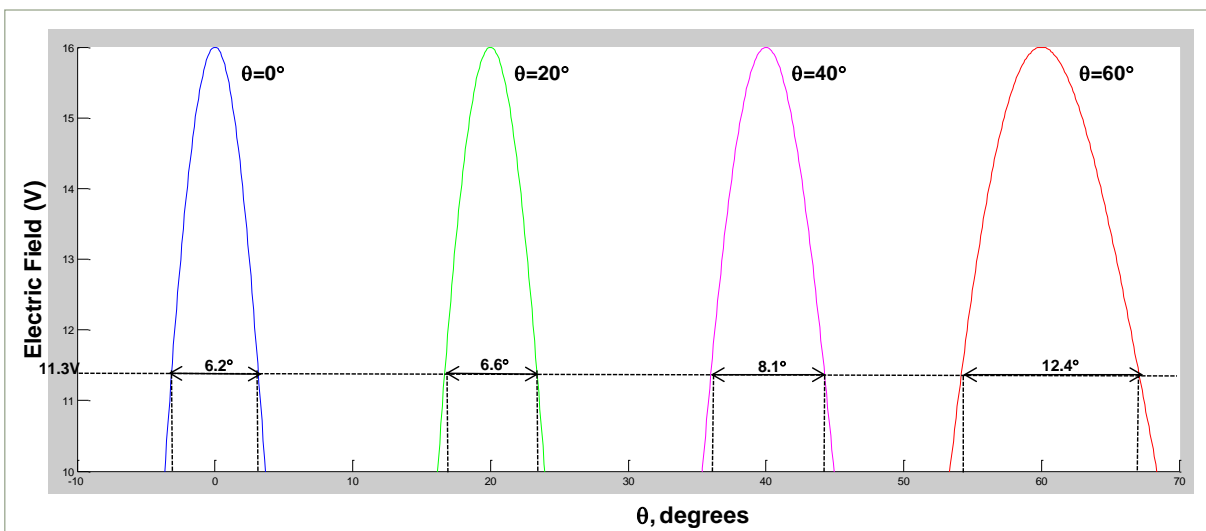


Figure 1-11. Linear array factor: $N = 16$ isotropic radiators, beamwidth vs. scan

1.4.3 Linear Array of $N = 16$ Isotropic Radiators with $\cos(\theta)$ Element Pattern

Case 5. Identical amplitude weighting; spacing $d_x = \lambda/2$; $\cos^n(\theta)$ element pattern.

The scan element pattern (also known as the active element pattern) is the radiation pattern of a single element excited in an array environment with all the other elements terminated in their characteristic impedance^{1.5}; element pattern roll-off is a function of lattice spacing and mutual coupling between all elements in the array^{1.6}. The scan element pattern is modeled as a cosine function raised to a power^{1.7}, n : $\cos^n(\theta)$.

Suppose $n = 0.5$ for the linear array of $N = 16$ isotropic radiators: The scan loss, in volts, at each angle relative to the voltage peak of 16V at $\theta=0^\circ$ is computed as follows:

$$\theta=20^\circ: \quad \sqrt{\cos(20^\circ)} = 0.97 \Rightarrow 0.97 * 16V = 15.5V$$

$$\theta=40^\circ: \quad \sqrt{\cos(40^\circ)} = 0.87 \Rightarrow 0.87 * 16V = 14V$$

$$\theta=60^\circ: \quad \sqrt{\cos(60^\circ)} = 0.707 \Rightarrow 0.707 * 16V = 11.3V$$

The computed values agree with the scan loss plot in Figure 1-12. Again, note that the 3dB beamwidth increasing with scan angle.

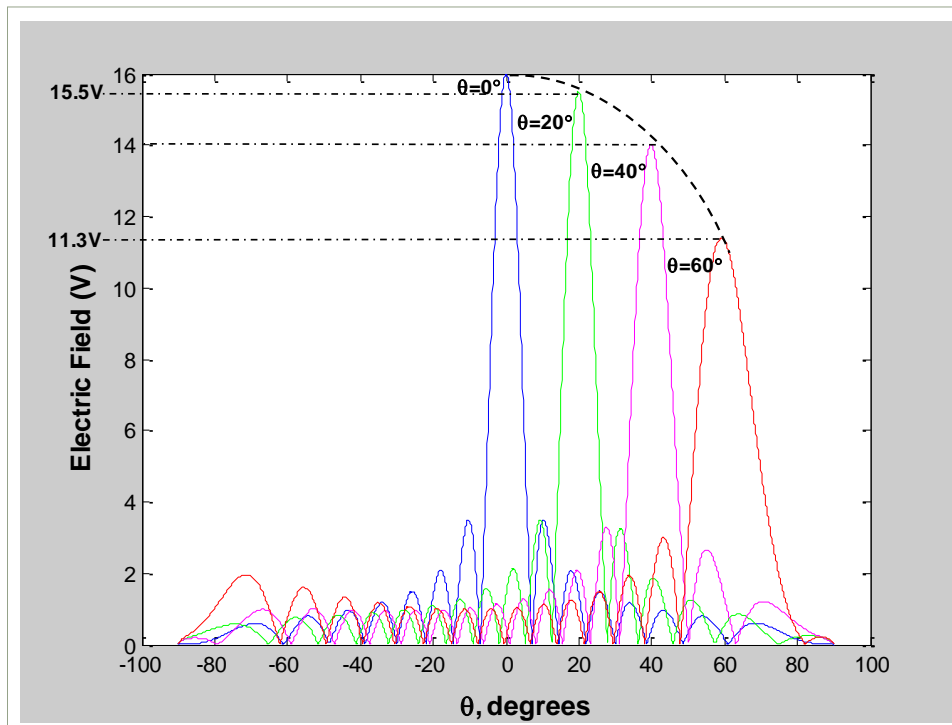


Figure 1-12. Linear array factor: $N = 16$ radiators with $\cos^{0.5}(\theta)$ element pattern

Case 6. Linear Array of N = 16 Radiators with $\cos^{1.4}(\theta)$ Element Pattern

Case 6. Identical amplitude weighting; spacing $d_x = \lambda/2$; $\cos^{1.4}(\theta)$ element pattern.

The scan loss, in volts, at each angle relative to the voltage peak of 16V at $\theta=0^\circ$ is computed as follows:

$$\theta=20^\circ: \quad \sqrt[1.4]{\cos(20^\circ)} = 0.96 \Rightarrow 0.96 * 16V = 15.3V$$

$$\theta=40^\circ: \quad \sqrt[1.4]{\cos(40^\circ)} = 0.83 \Rightarrow 0.83 * 16V = 13.3V$$

$$\theta=60^\circ: \quad \sqrt[1.4]{\cos(60^\circ)} = 0.62 \Rightarrow 0.62 * 16V = 9.8V$$

The computed values agree with the values given in Figure 1-13. Comparing Figure 1-13 with Figure 1-12, scan loss is significantly higher for a $\cos^{1.4}(\theta)$ element pattern versus a $\cos^{0.5}(\theta)$ element pattern since the $\cos^{1.4}(\theta)$ element pattern has a faster roll-off versus scan angle θ .

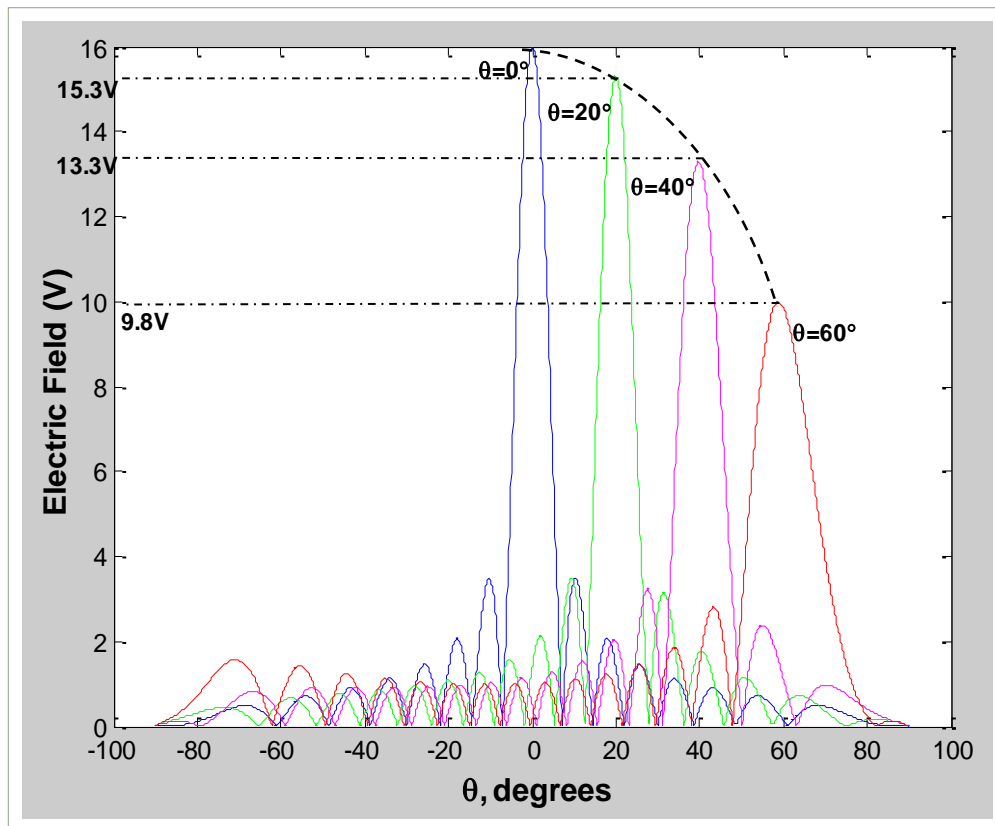


Figure 1-13. Linear array factor: N = 16 radiators with $\cos^{1.4}(\theta)$ element pattern

1.5 Instantaneous Bandwidth

The instantaneous bandwidth is a function of the length of the array, L , and the scan angle θ . For phase shifter based phased arrays, the instantaneous bandwidth is limited by the acceptable pattern loss due to beam squint loss; that is, the instantaneous bandwidth is the range of frequencies over which the beam squint loss is acceptable.

The instantaneous bandwidth for a phase shifter steered array is a function of the length of the array, L , and maximum scan angle θ_{max} ^{1.8}:

$$BW_{inst} = \frac{kc}{L \sin \theta_{max}} \quad (1.5.1)$$

where $k \equiv 3\text{dB}$ beamwidth factor which is a function of the array aperture weighting, $c \equiv$ speed of light in vacuum. For a uniformly illuminated aperture, $k = 0.866$.

As discussed in expressions 1.1.7 and 1.1.8, the array beam can be steering using phase shifter steering or time delay steering; Figure 1-14 shows a schematic of each approach:

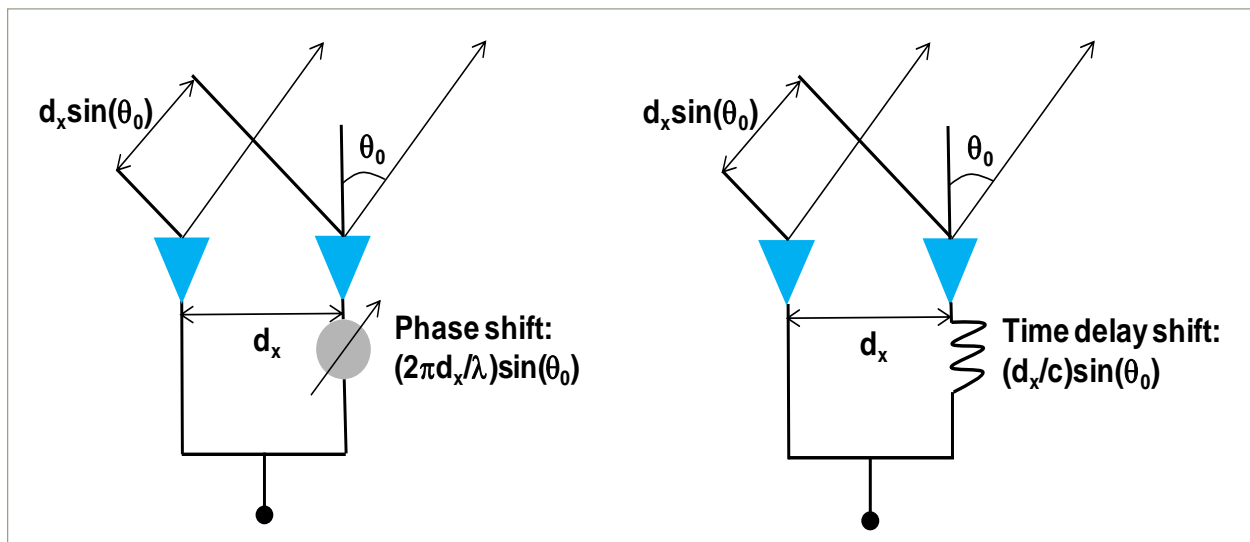


Figure 1-14. Phased array beam steering. Phase shift (left) and time delay shift (right)

Typically, large arrays (large L) have a narrow beamwidth and narrow instantaneous bandwidth; ideally, time delay at the element level would eliminate beam-squint (i.e., array beam peak moving in angle space as the frequency is varied). True time delay is accomplished with a piece of non-dispersive transmission line like a coaxial line; the transmission line can be many wavelengths long. In principle, with true time delay, the instantaneous bandwidth of an array would not be

limited by the dimensions of the array nor the scan angle as written in expression 1.5.1. However, time delay steering typically requires switched sections of coaxial transmission line; presently, implementing time delay steering at RF at the element level is prohibitive: it is costly, bulky and has relatively high RF loss.

Modern digital phase shifters are the key to beam agility. Modern digital phase shifter can switch on the order of microseconds and enables radars to simultaneously detect and track a number of targets. Modern digital phase shifters change phase primarily by changing the path length; that is, using diode phase shifters to switch in different path lengths- however, digital phase shifters are typically limited to 355 degrees of total phase shift.

Phase shifter based arrays limit the bandwidth of phased arrays because phase shifting is frequency dependent; time delay steering is frequency independent (i.e., dispersion-less). Thus, for phase shifter based arrays, the main beam peak is scanned to the desired scan angle at one given frequency; if the radar waveform is composed of many frequencies, then the main beam “squints”.

Figure 1-15 illustrates main beam squint as a function of frequency using a phase shifter; the figure on the left shows how the phase front is “tilted” as the frequency of operation is changed from the center frequency f_0 to a lower frequency f ; the figure on the right illustrates how the main beam of the array is scanned to a higher angle or lower angle as the frequency is changed from f_{min} to f_{max} , respectively.

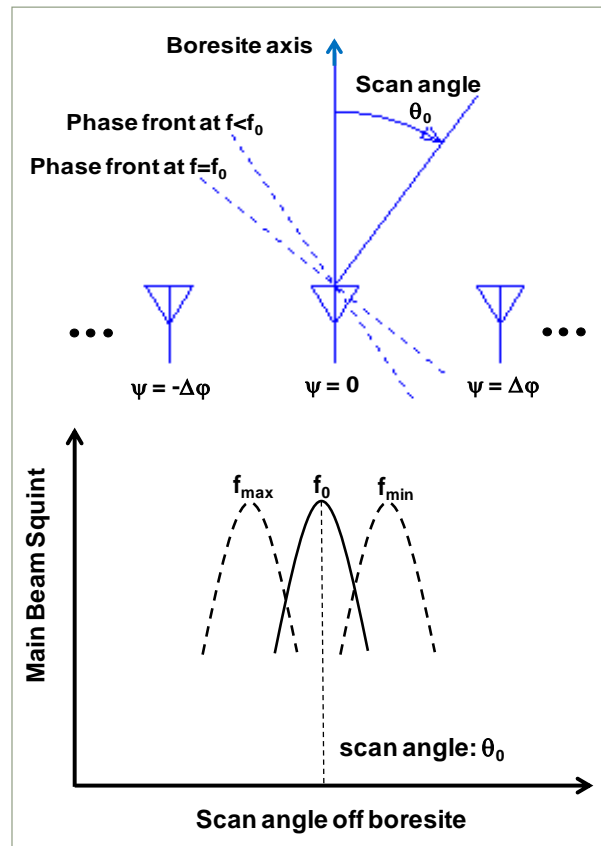


Figure 1-15. Main beam squint versus frequency

1.6 Planar Phased Array Array Factor: Rectangular Lattice

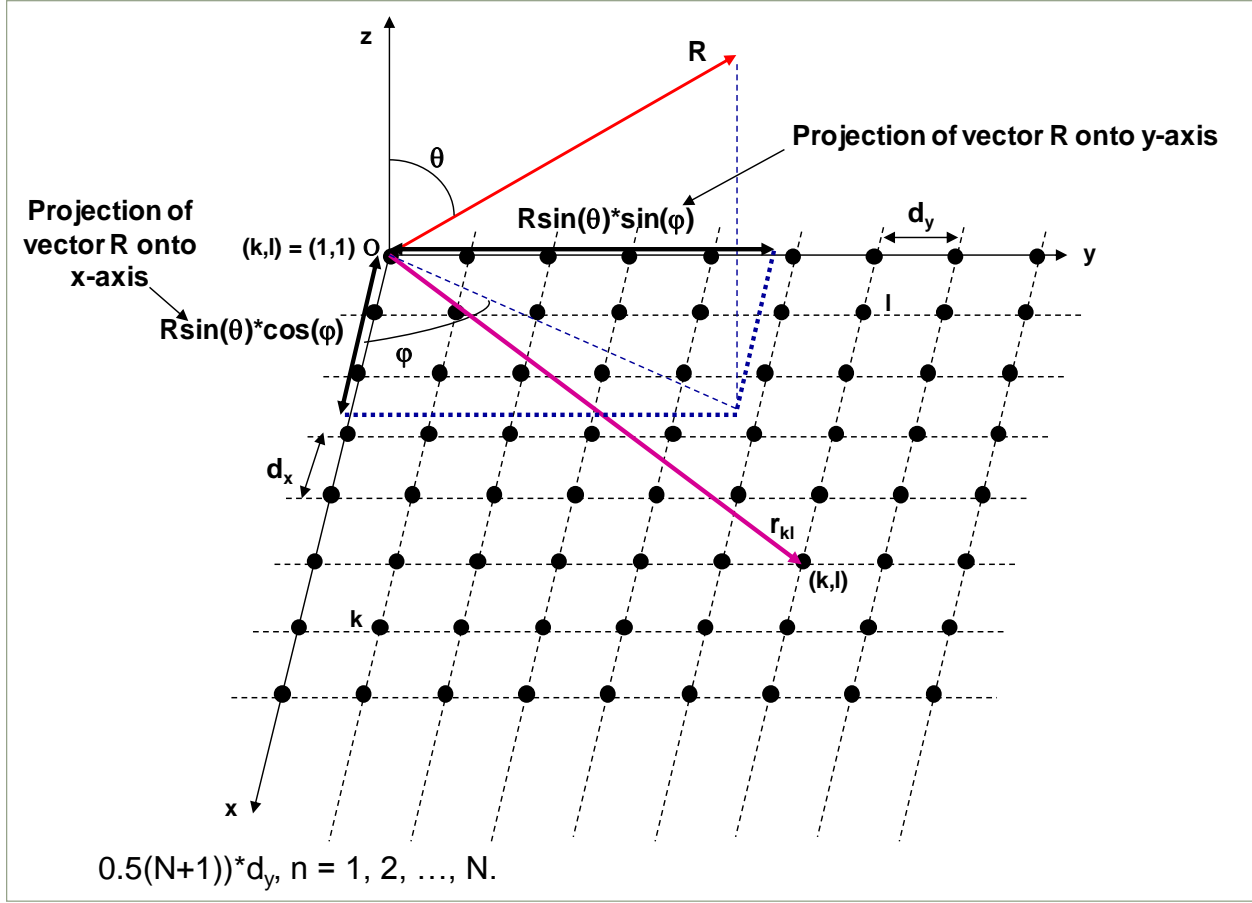


Figure 1-16. Planar, rectangular array

The two dimensional array factor for a rectangular aperture is linear array of linear arrays; that is, the planar array factor is written as the product of the linear array factor in the x-direction and the linear array factor in the y-direction. The x and y element positions for an MxN planar array is shown in Figure 1-16; the element positions (x_m, y_m) are given by the coordinates: $x_m = (m - 0.5(M+1))d_x$, $m = 1, 2, \dots, M$ and $y_m = (n - 0.5(N+1))d_y$, $n = 1, 2, \dots, N$.

The expressions for the linear array factors in the x-direction and in the y-direction are written:

$$AF_x = \sum_{m=1}^M (\alpha_m e^{j\psi_m}) e^{j\frac{2\pi}{\lambda} x_m \sin\theta \cos\phi} \quad \text{and} \quad AF_y = \sum_{n=1}^N (\beta_n e^{j\psi_n}) e^{j\frac{2\pi}{\lambda} y_n \sin\theta \sin\phi} \quad (1.6.1)$$

where the complex weighting along the x-axis is $a_m = \alpha_m e^{j\psi_m}$ and the complex weighting along the y-axis is $b_n = \beta_n e^{j\psi_n}$.

For planar arrays, we may assume separable weightings a_m and b_n along the x- and y- axes, respectively. The product of linear array factors produces the planar array factor:

$$AF_{xy} = \sum_{m=1}^M (\alpha_m e^{j\psi_m}) e^{j\frac{2\pi}{\lambda} x_m \sin\theta \cos\varphi} \sum_{n=1}^N (\beta_n e^{j\psi_n}) e^{j\frac{2\pi}{\lambda} y_n \sin\theta \sin\varphi} \quad (1.6.2)$$

The element level phase shifts along the x-axis and along the y-axis are, respectively:

$$\psi_m = -\frac{2\pi}{\lambda} x_m \sin\theta \cos\varphi \quad \psi_n = -\frac{2\pi}{\lambda} y_n \sin\theta \sin\varphi \quad (1.6.3)$$

Inserting expression 1.6.3 into 1.6.2:

$$AF_{xy} = \sum_{m=1}^M \alpha_m e^{j\frac{2\pi}{\lambda} x_m (\sin\theta \cos\varphi - \sin\theta_0 \cos\varphi_0)} \sum_{n=1}^N \beta_n e^{j\frac{2\pi}{\lambda} y_n (\sin\theta \sin\varphi - \sin\theta_0 \sin\varphi_0)} \quad (1.6.4)$$

The spatial coordinate representation typically used for electronically scanned phased arrays is “sine space”; the direction cosines are:

$$u = \sin\theta \cos\varphi, -1 \leq u \leq 1 \quad v = \sin\theta \sin\varphi, -1 \leq v \leq 1 \quad (1.6.5)$$

where θ and φ are the sine space angular coordinates. Using expression 1.6.5, the planar array factor in expression 1.6.4:

$$AF_{xy} = \sum_{m=1}^M \alpha_m e^{j\frac{2\pi}{\lambda} x_m (u-u_0)} \sum_{n=1}^N \beta_n e^{j\frac{2\pi}{\lambda} y_n (v-v_0)} = \sum_{m=1}^M \sum_{n=1}^N c_{mn} e^{j\frac{2\pi}{\lambda} [x_m (u-u_0) + y_n (v-v_0)]} \quad (1.6.6)$$

where $c_{mn} \equiv \alpha_m \beta_n$ is the complex weight at element position (m, n).

1.6.1 Grating Lobes

The phased array can be viewed as a “sampling” of a continuous aperture. In Section 1.1, it was noted that the array factor is a Fourier series expansion; it is a periodic function of complex, weighted samples from the phased array. From signal processing theory, the Nyquist theorem states that if a periodic function is not properly sampled, aliasing occurs; that is, the periodic copying of the original signal occurs. For phased arrays, the periodic copy of the array main beam is called a “grating lobe”. A grating lobe in real space is undesired: loss in power in the desired array main beam, interference and potential damage from undesired reflections are some of the consequences of having a grating lobe in addition to the desired, main array beam.

Grating lobes are generated when the argument of the array factor is an integer multiple of 2π . The maxima of expression 1.6.7 below occur when the argument of the complex exponential is an integer multiple of 2π :

$$(2\pi/\lambda)(u - u_0)md_x + (2\pi/\lambda)(v - v_0)nd_y = (2\pi)s \quad (1.6.7)$$

where s is an integer and $x_m = md_x$ and $y_m = nd_y$. Simplifying:

$$(d_x/\lambda)(u - u_0)m + (d_y/\lambda)(v - v_0)n = s \quad (1.6.8)$$

Expression 1.6.8 is satisfied only if each term on the left hand side is an integer:

$$(u - u_0) = p\lambda/d_x \Rightarrow u = u_0 + p\lambda/d_x \quad (1.6.9)$$

$$(v - v_0) = q\lambda/d_y \Rightarrow v = v_0 + q\lambda/d_y \quad (1.6.10)$$

where p, q are integers.

The expressions for u and v are known as the grating lobe series; each (u, v) coordinate in sine space represents a grating lobe at the center of a circle with radius equal to 1. The array main beam is defined by the coordinates (u_0, v_0) ; as the main beam is scanned by varying θ_0 and φ_0 , the (u, v) coordinate also scans in the same direction.

1.6.2 Grating Lobe Plots

The following grating lobe plots are for a planar array with the following x- and y- coordinate spacing:

- Case 1: $d_x = d_y = \lambda/2$;
- Case 2: $d_x = d_y = \lambda$;
- Case 3: $d_x = d_y = 5\lambda/4$.

Case 1. $d_x = d_y = \lambda/2$

In this case, the array can be scanned anywhere within visible space up to $u=\pm 1$ and $v=\pm 1$ before a higher order ($p \neq 0, q \neq 0$) propagating Floquet mode (“Grating Lobe”) just touches visible space. Note that the fundamental propagating Floquet mode ($p=q=0$) is at boresite (the array main beam). Note: The scan volume (in pink) is defined by $\theta_{AZ} = 60^\circ$ and $\theta_{EL} = 60^\circ$ in radar coordinates.

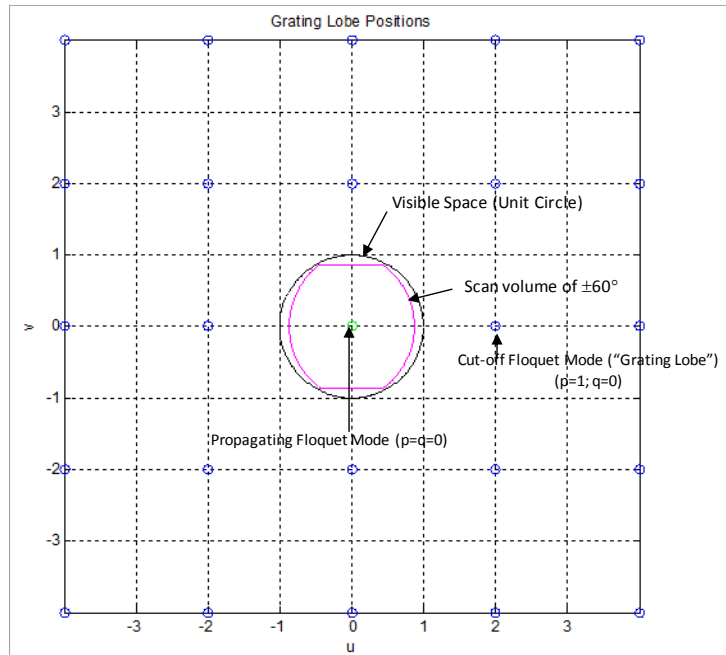


Figure 1-17. Case 1. Rectangular lattice with $d_x = d_y = \lambda/2$

Case 2. $d_x = d_y = \lambda$

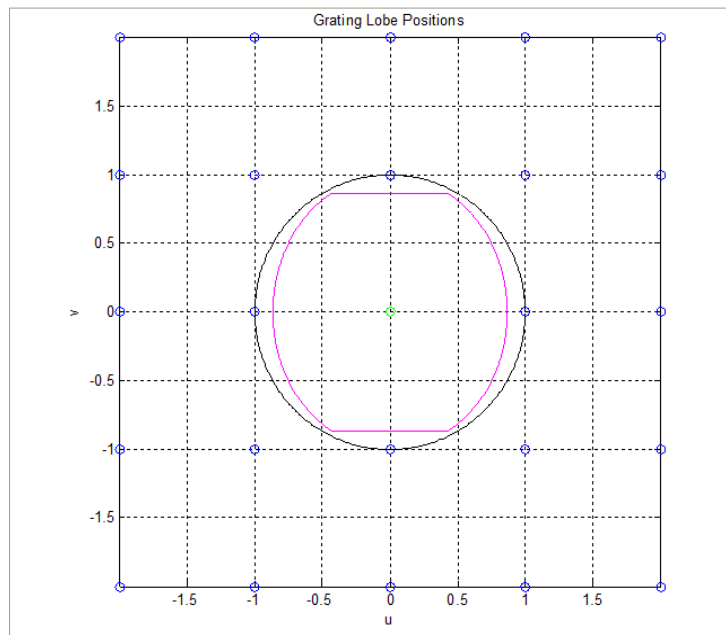


Figure 1-18. Case 2. Rectangular lattice with $d_x = d_y = \lambda$

The higher order Floquet modes are already at the edge of visible space with the fundamental propagating Floquet mode at boresite (the array main beam). As the propagating mode is scanned, the higher order Floquet modes also scan in the same (u, v) direction.

Suppose the main beam is scanned to $u=0.321$, $v=0.117$ (corresponding to spherical polar angles $\theta=20^\circ$ and $\varphi=20^\circ$). All the Floquet modes (an infinite number) move in the same (u, v) direction. However, there are 3 beams propagating (radiating) as shown in the figure.

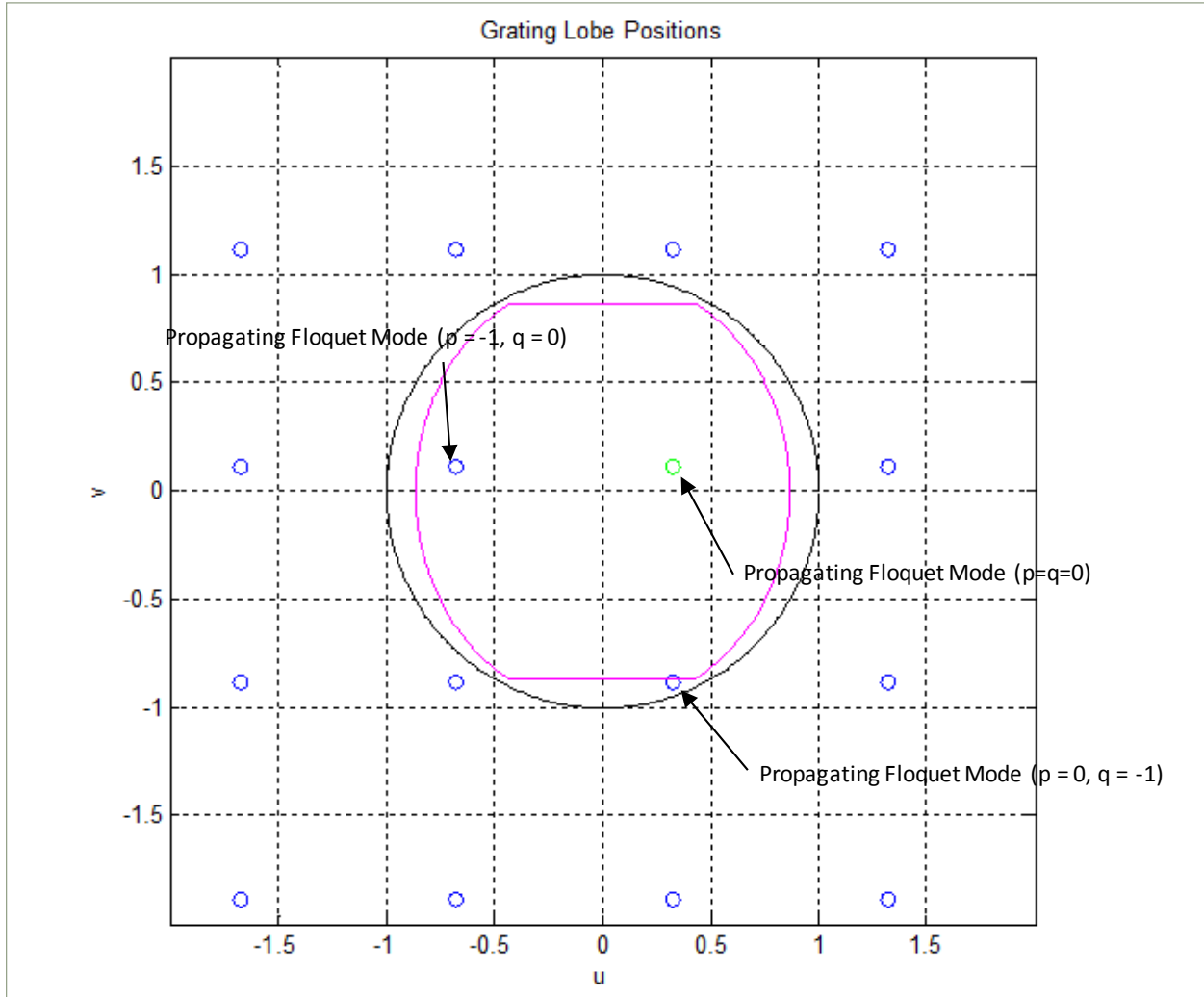


Figure 1-19. Case 2. Rectangular lattice with $d_x = d_y = \lambda$. main beam scanned to $u=0.321$, $v=0.117$

Case 3. $d_x = d_y = 5\lambda/4$

In this case, there are already 4 higher order Floquet modes in real space including the fundamental propagating Floquet mode at boresite. Therefore, 5 beams will be radiating with the array commanded to boresite scan.

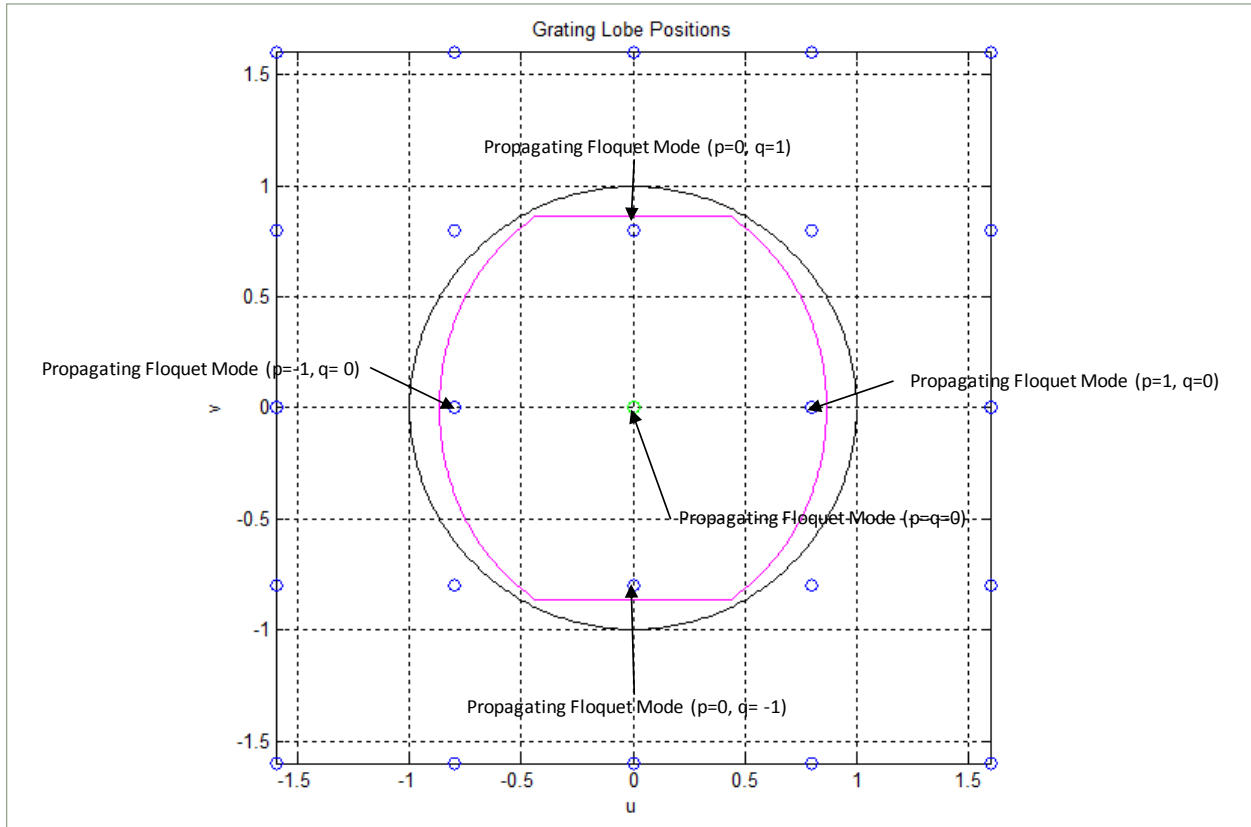


Figure 1-20. Case 3. Rectangular lattice with $d_x = d_y = 5\lambda/4$

1.7 Planar Array Patterns

Most practical phased arrays scan in two-dimensions and are designed to have a grating lobe free scan volume; hence, the x- and y- axis lattice spacing is typically one-half free space wavelength ($\lambda/2$).

Table 1-1 lists the planar array patterns presented in Section 1.7.1. The scan angles are presented in u, v direction cosine coordinates. The effects of element pattern scan loss is shown with a $\cos^{1.5}(\theta)$ element pattern where $n = 1.5$ is a typical array element pattern loss factor; $n = 0$ represents the array factor pattern only without element pattern loss. Note: the patterns do not include the effects of mutual coupling.

Table 1-1. 19x19 Planar array cases

| Rectangular Lattice | | Scan Angle | | $\cos^n(\theta)$ | | Sidelobe Weighting | |
|---------------------|--------------|------------|---------|------------------|-----|--------------------|--------------|
| dx/λ | dy/λ | u (deg) | v (deg) | 0.0 | 1.5 | X-coordinate | Y-coordinate |
| 0.5 | 0.5 | 0.00 | 0.00 | 0.0 | 1.5 | Uniform | Uniform |
| | | 0.50 | 0.00 | 0.0 | 1.5 | Uniform | Uniform |
| | | 0.71 | 0.00 | 0.0 | 1.5 | Uniform | Uniform |
| | | 0.87 | 0.00 | 0.0 | 1.5 | Uniform | Uniform |
| | | 0.00 | 0.50 | 0.0 | 1.5 | Uniform | Uniform |
| | | 0.00 | 0.71 | 0.0 | 1.5 | Uniform | Uniform |
| | | 0.00 | 0.87 | 0.0 | 1.5 | Uniform | Uniform |
| | | 0.61 | 0.50 | 0.0 | 1.5 | Uniform | Uniform |
| | | 0.50 | 0.71 | 0.0 | 1.5 | Uniform | Uniform |
| | | 0.35 | 0.87 | 0.0 | 1.5 | Uniform | Uniform |

1.7.1 19x19 Planar Array Patterns: $dx = 0.5\lambda$ $dy = 0.5\lambda$

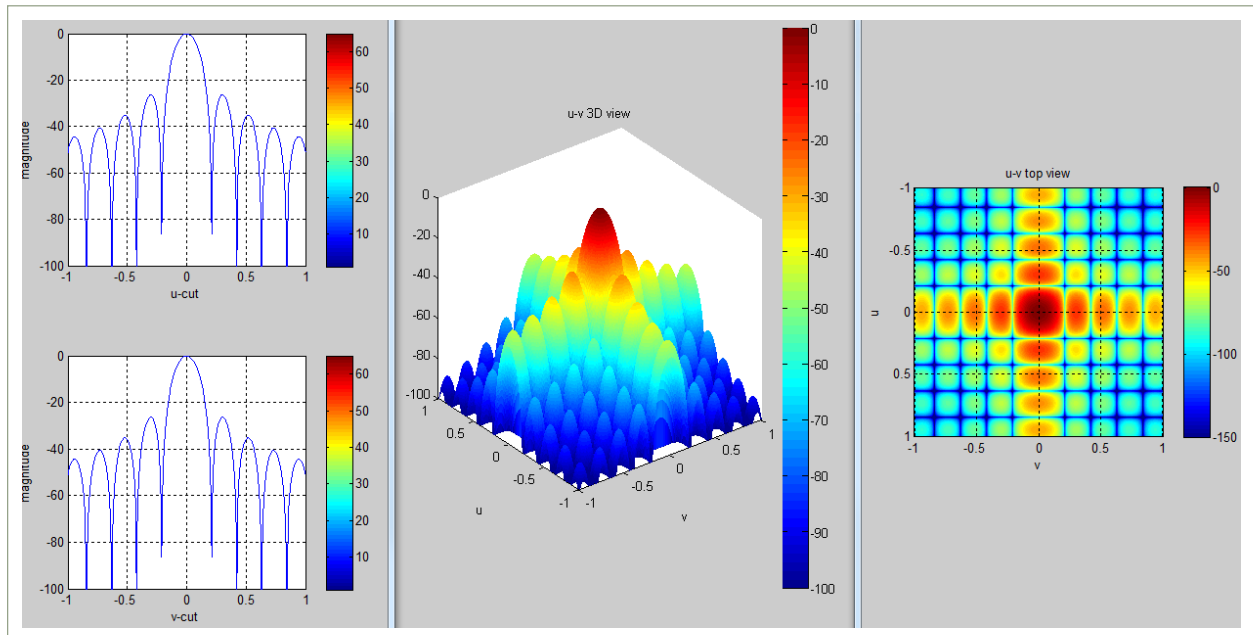


Figure 1-21. 19 x 19 array; scan angle: $u = 0, v = 0; \cos^{0.0}(\theta)$

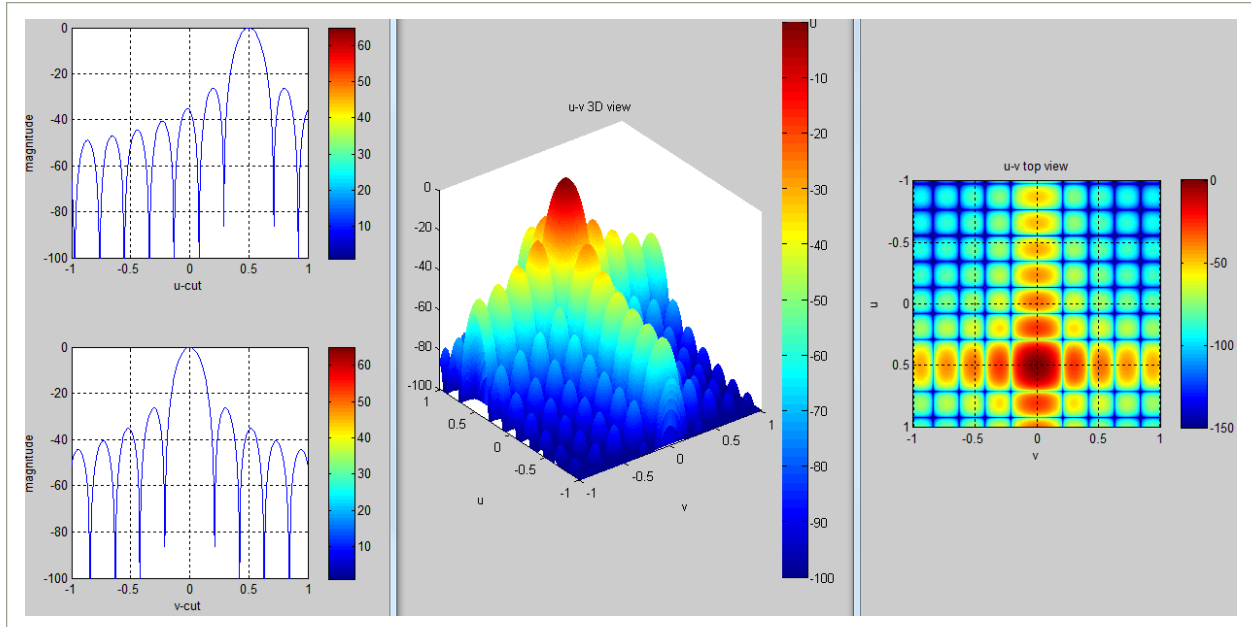


Figure 1-22. 19 x 19 array; scan angle: $u = 0.5, v = 0; \cos^{0.0}(\theta)$

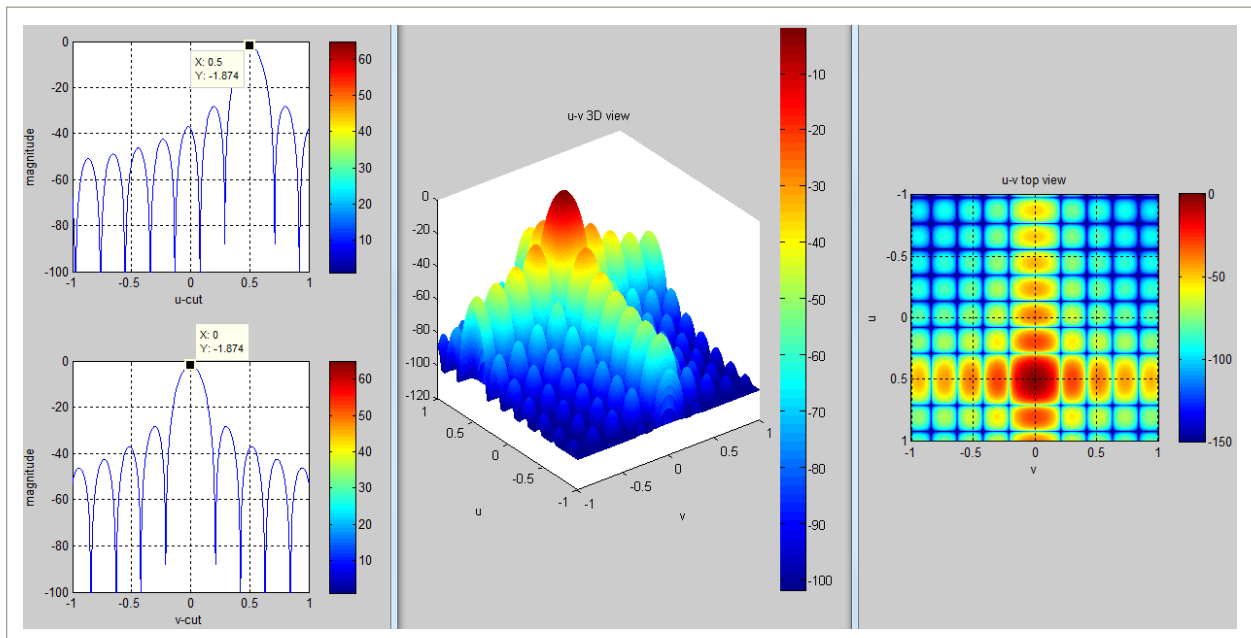


Figure 1-23. 19 x 19 array; scan angle: $u = 0.5, v = 0; \cos^{1.5}(\theta)$

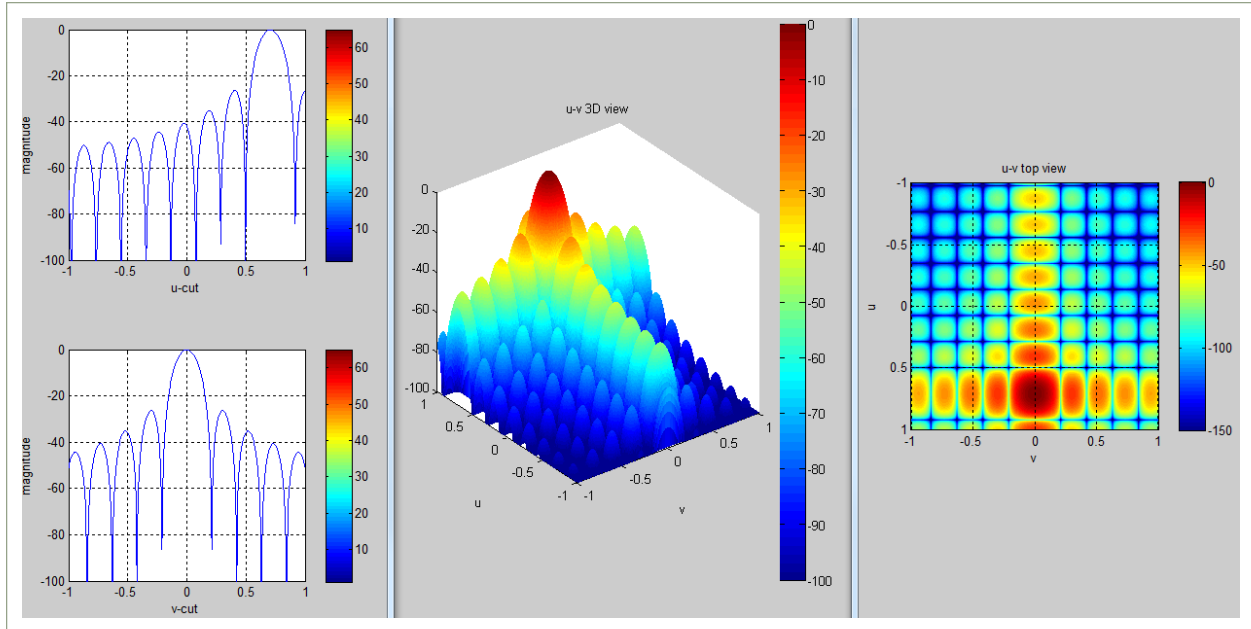


Figure 1-24. 19 x 19 array; scan angle: $u = 0.71, v = 0; \cos^{0.0}(\theta)$

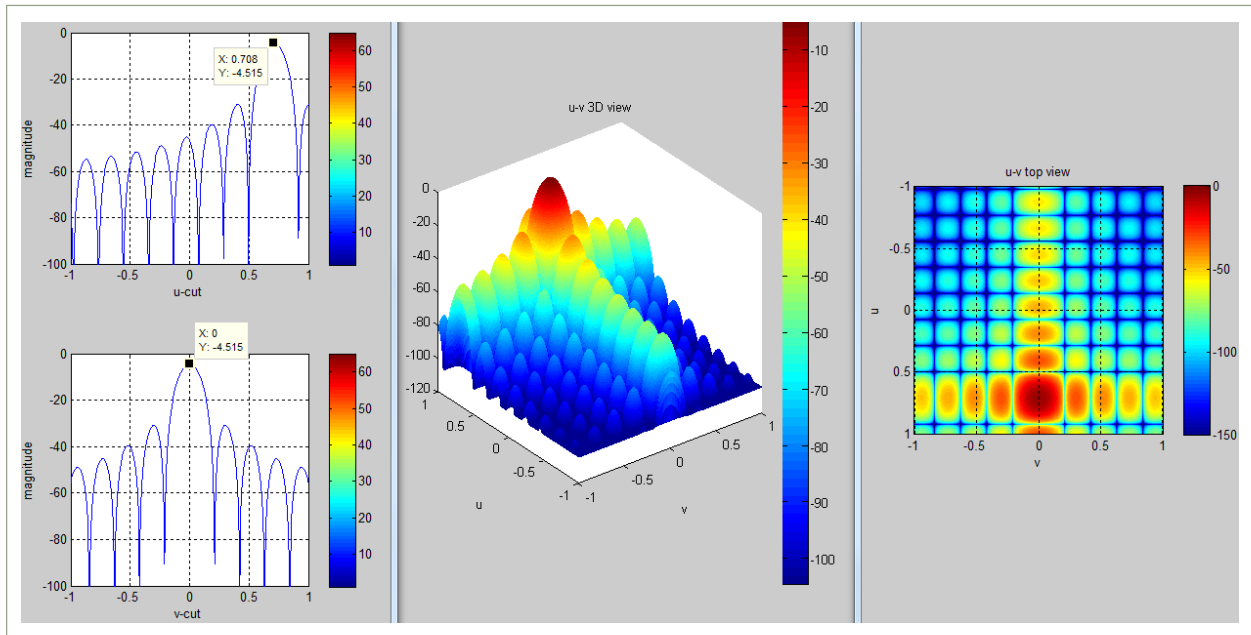


Figure 1-25. 19 x 19 array; scan angle: $u = 0.71, v = 0; \cos^{1.5}(\theta)$

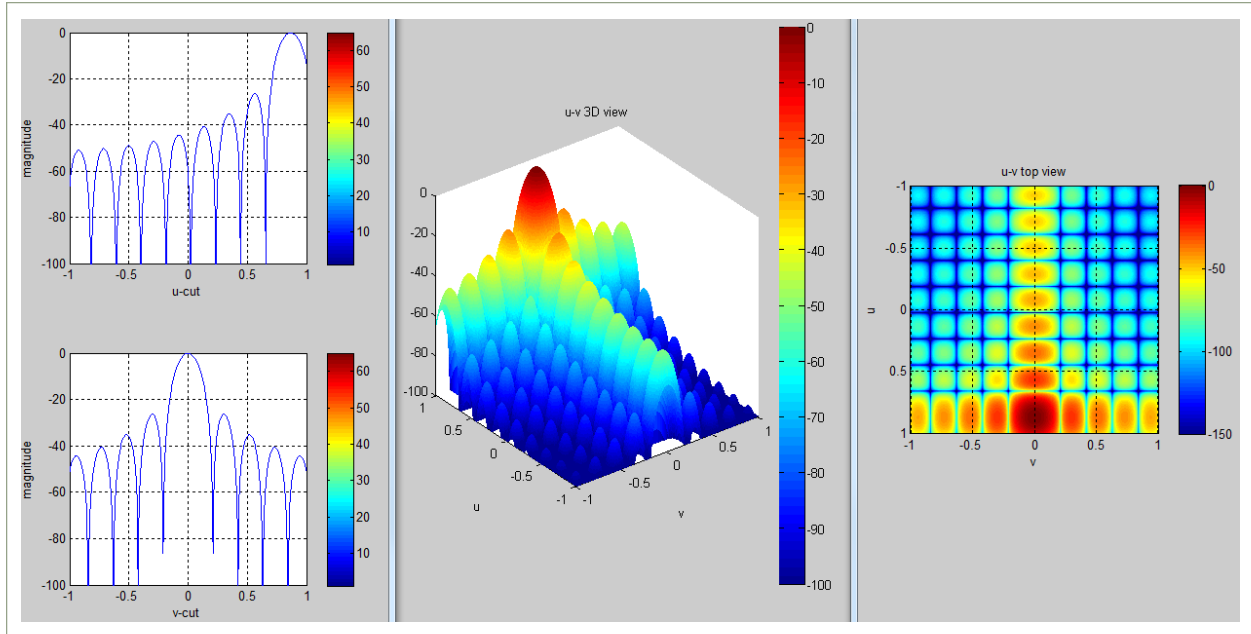


Figure 1-26. 19 x 19 array; scan angle: $u = 0.87, v = 0; \cos^{0.0}(\theta)$

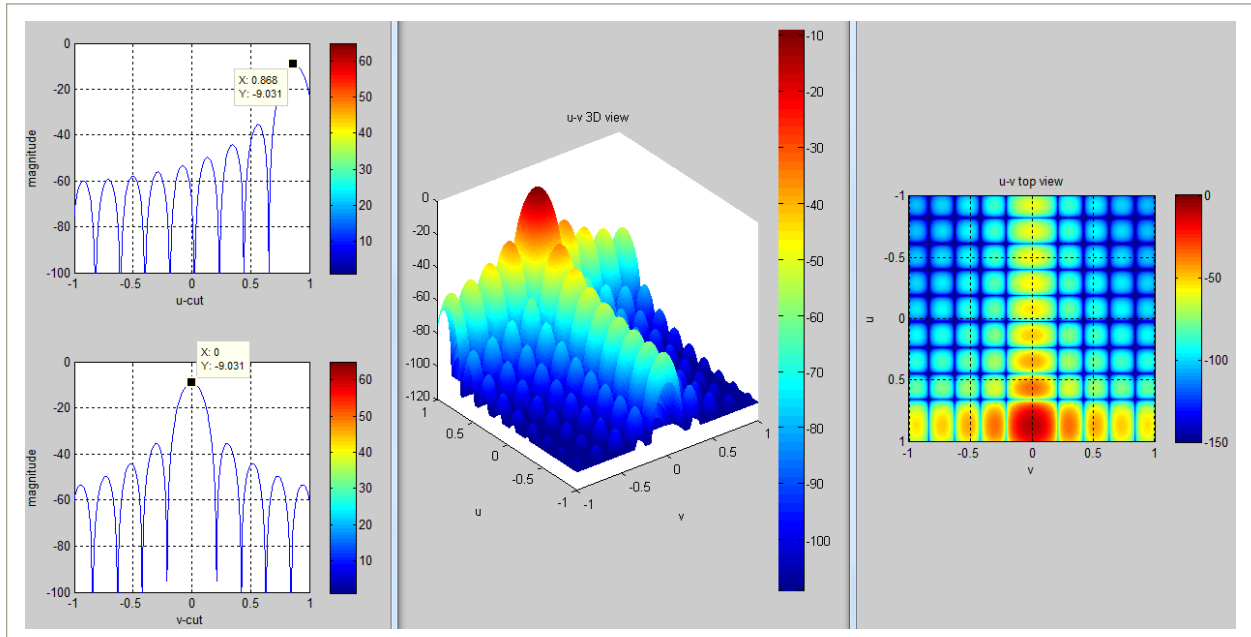


Figure 1-27. 19 x 19 array; scan angle: $u = 0.87, v = 0; \cos^{1.5}(\theta)$

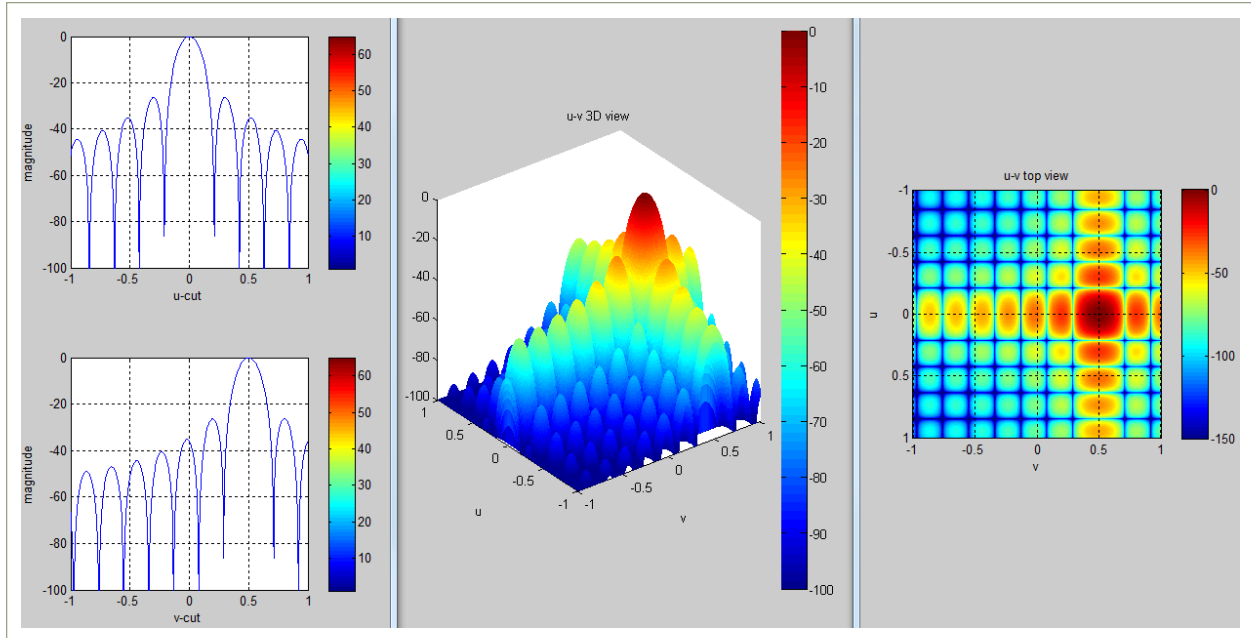


Figure 1-28. 19 x 19 array; scan angle: $u = 0, v = 0.5; \cos^{0.0}(\theta)$

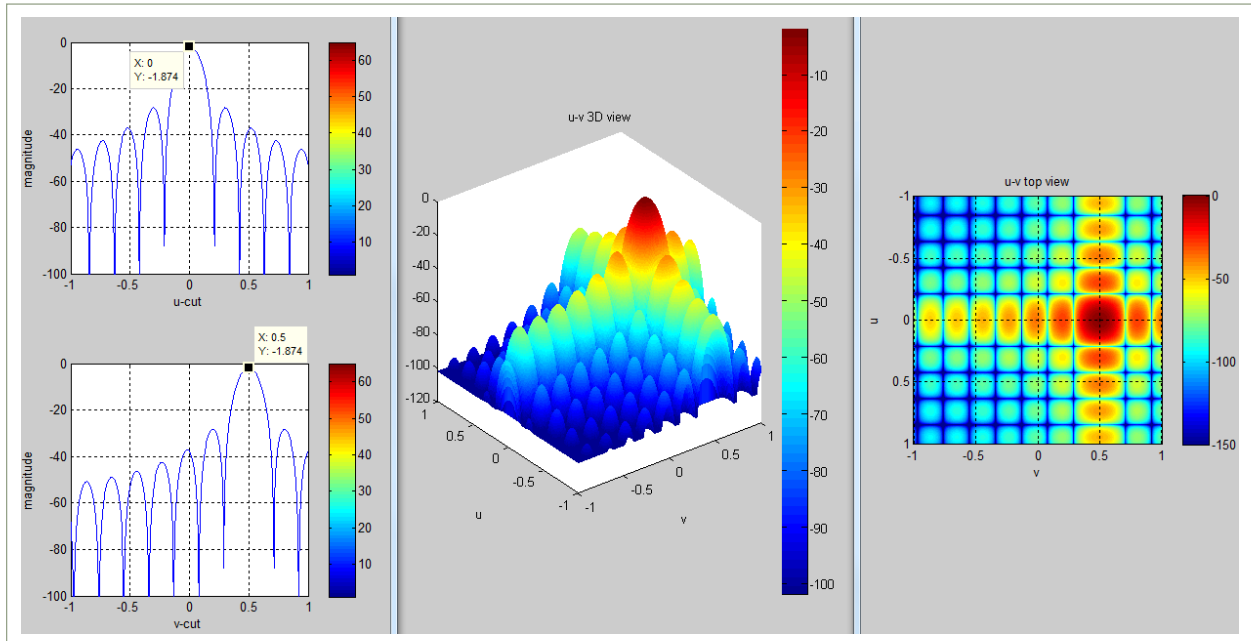


Figure 1-29. 19 x 19 array; scan angle: $u = 0, v = 0.5; \cos^{1.5}(\theta)$

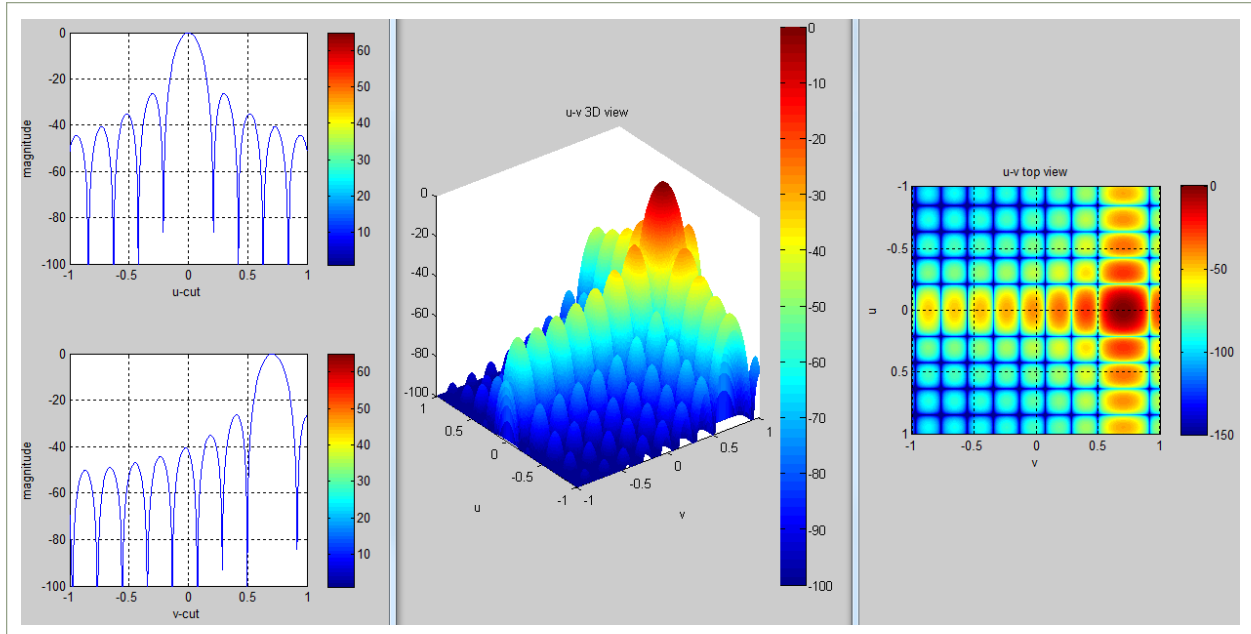


Figure 1-30. 19 x 19 array; scan angle: $u = 0, v = 0.71; \cos^{0.0}(\theta)$

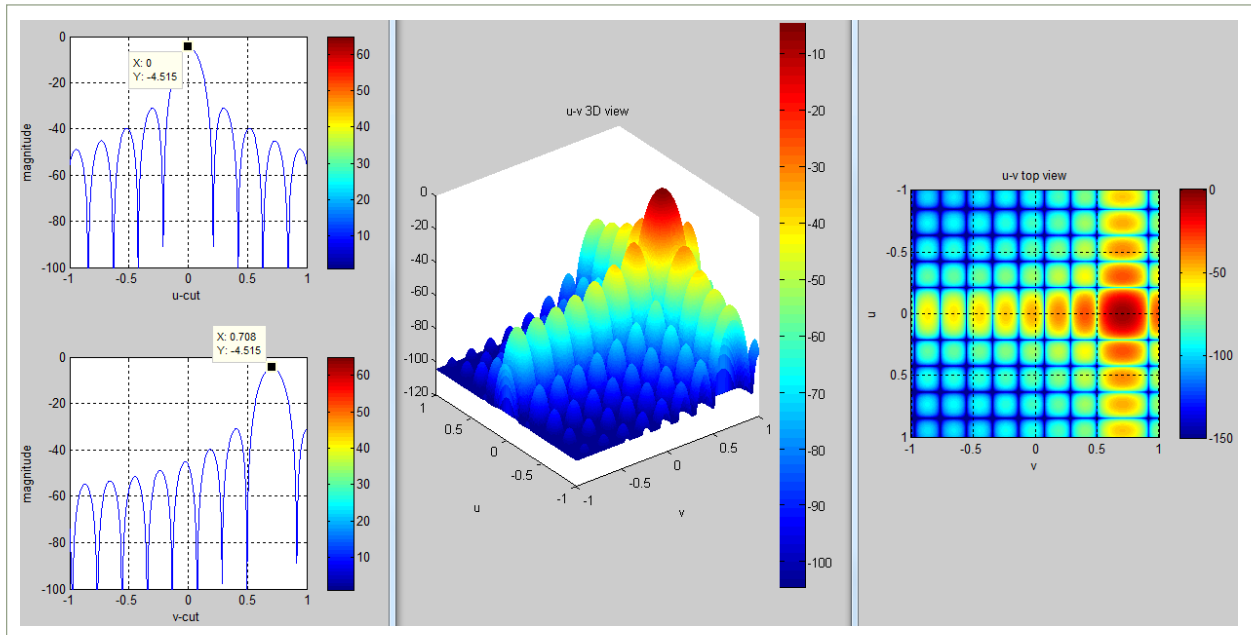


Figure 1-31. 19 x 19 array; scan angle: $u = 0, v = 0.71; \cos^{1.5}(\theta)$

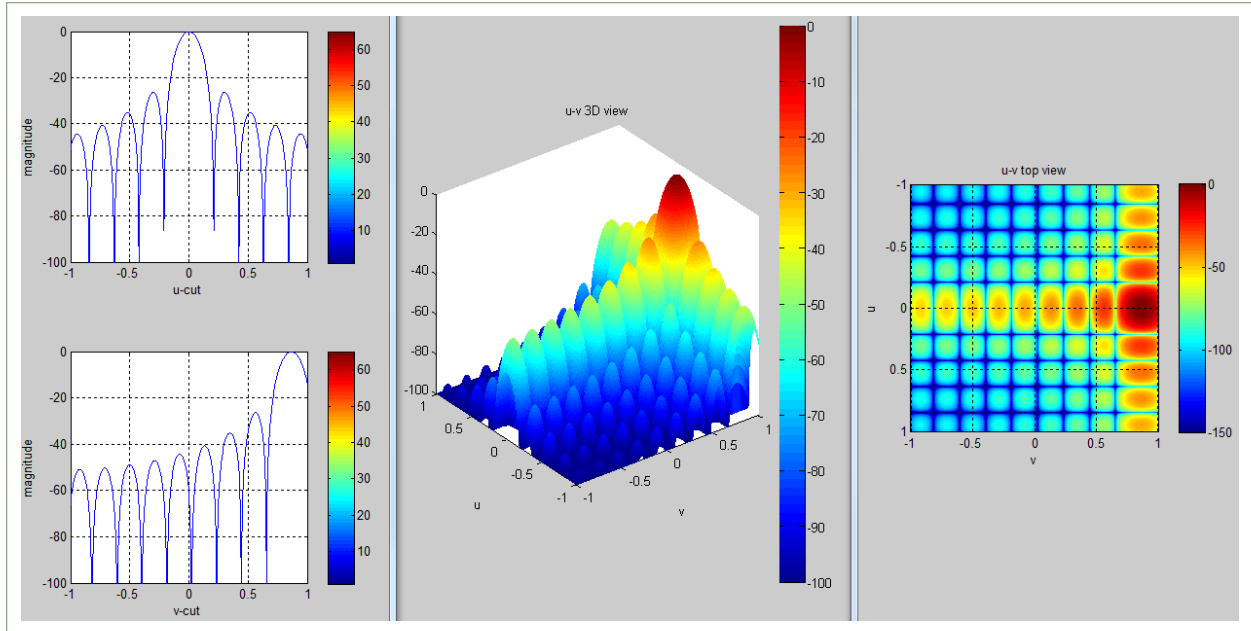


Figure 1-32. 19×19 array; scan angle: $u = 0, v = 0.87; \cos^{0.0}(\theta)$

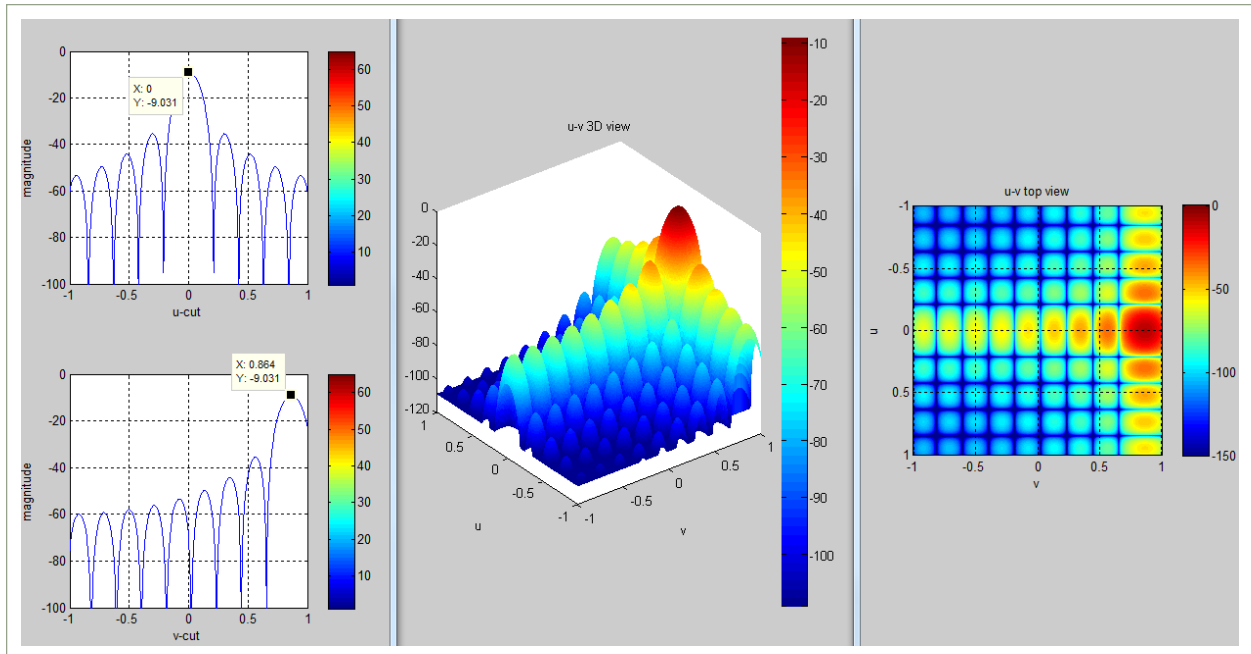


Figure 1-33. 19×19 array; scan angle: $u = 0, v = 0.87; \cos^{1.5}(\theta)$

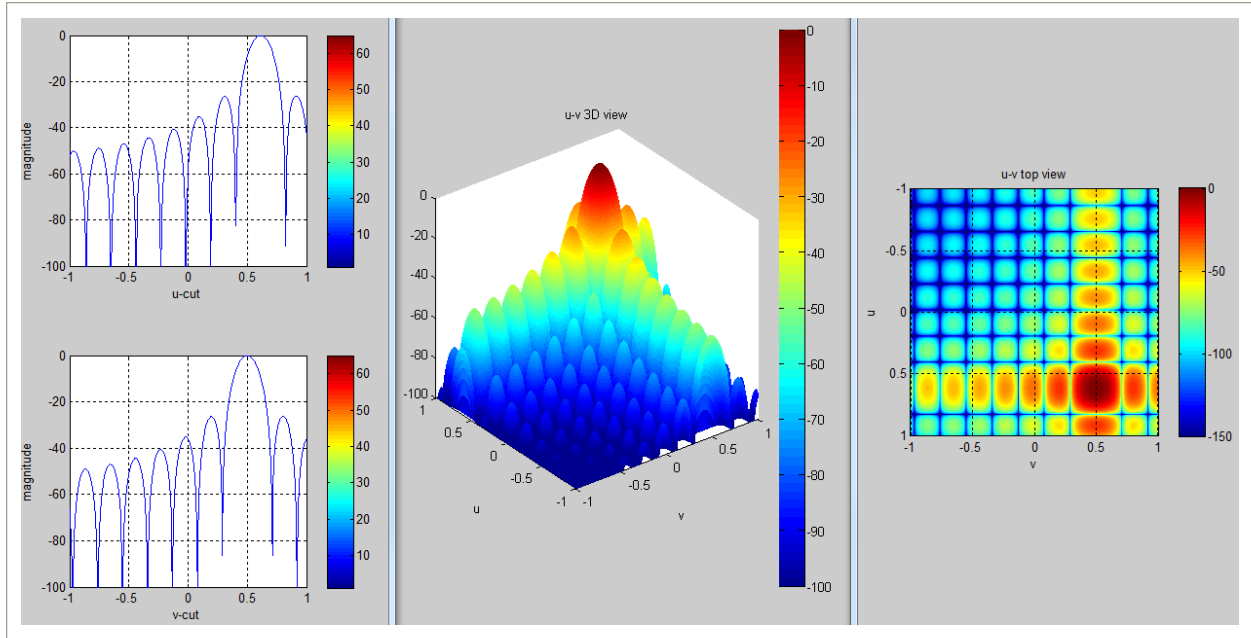


Figure 1-34. 19 x 19 array; scan angle: $u = 0.61, v = 0.5; \cos^{0.0}(\theta)$

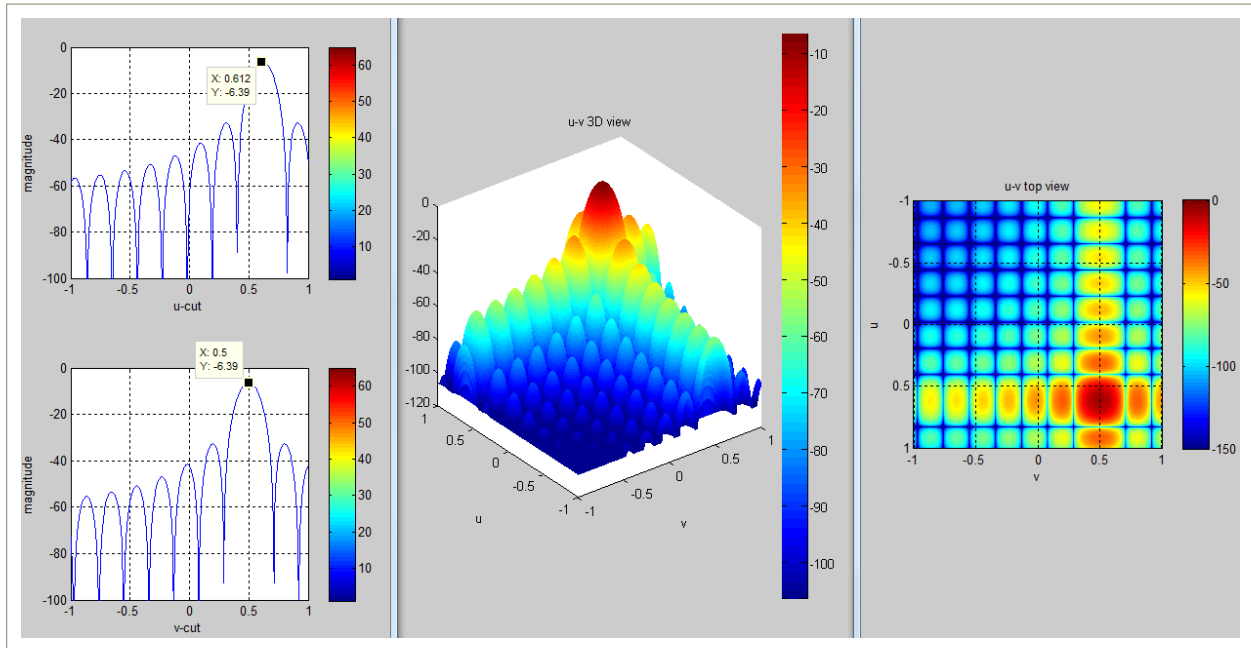


Figure 1-35. 19 x 19 array; scan angle: $u = 0.61, v = 0.5; \cos^{1.5}(\theta)$

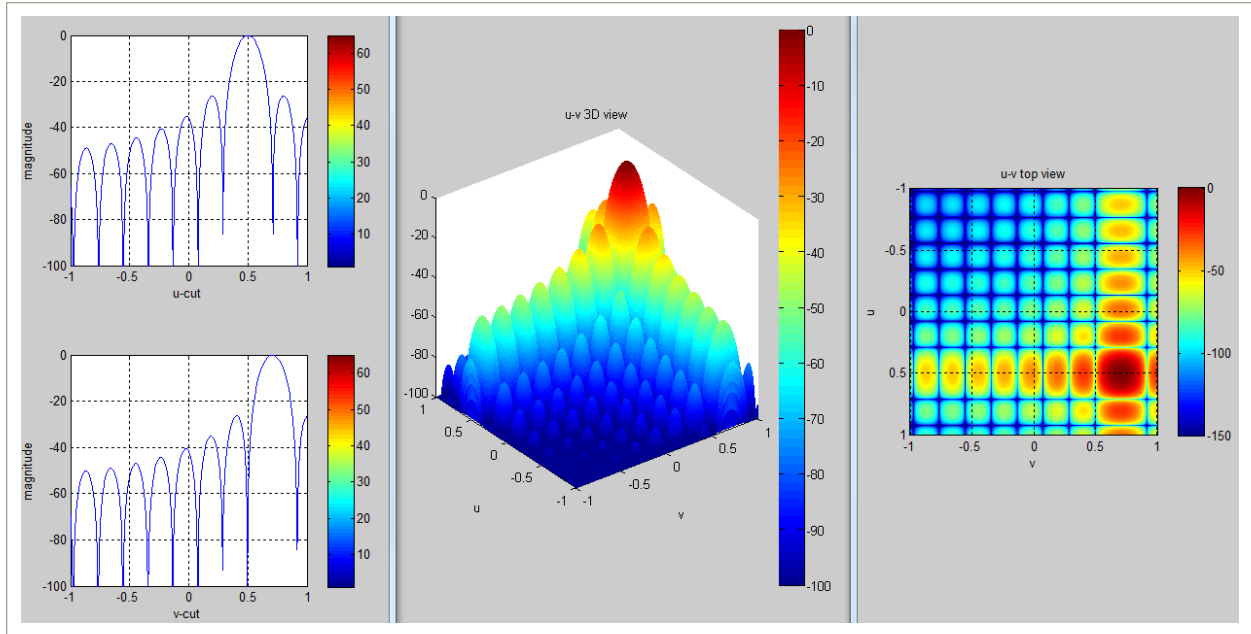


Figure 1-36. 19 x 19 array; scan angle: $u = 0.5, v = 0.71; \cos^{0.0}(\theta)$

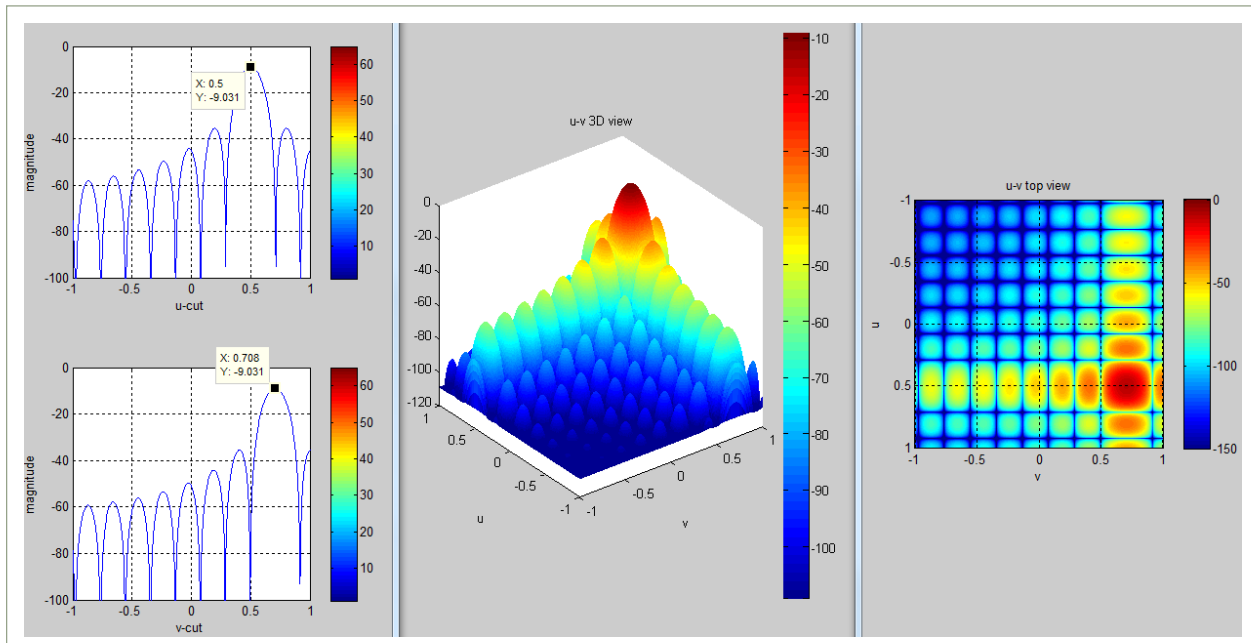


Figure 1-37. 19 x 19 array; scan angle: $u = 0.5, v = 0.71; \cos^{1.5}(\theta)$

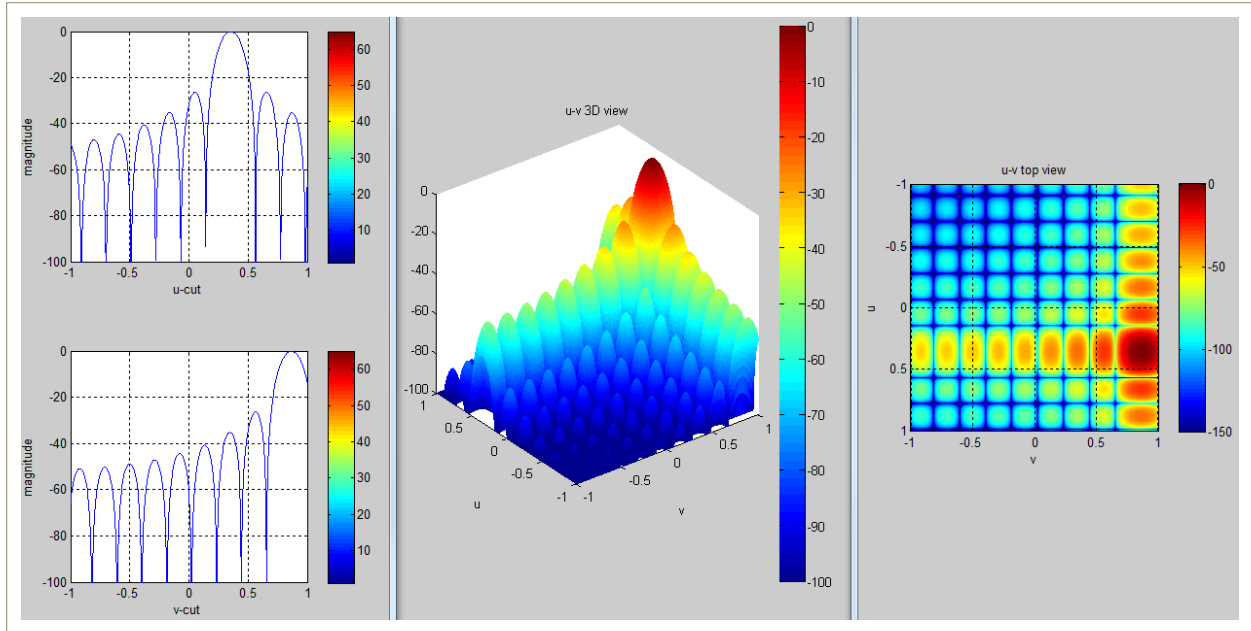


Figure 1-38. 19 x 19 array; scan angle: $u = 0.35$, $v = 0.87$; $\cos^{0.0}(\theta)$

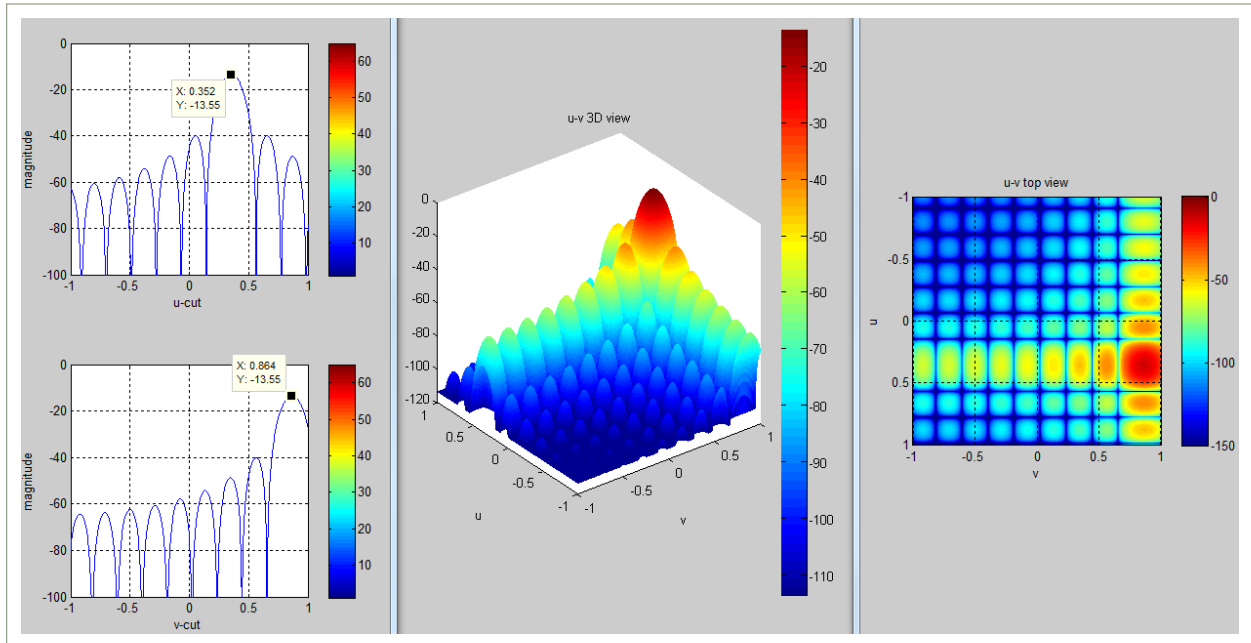


Figure 1-39. 19 x 19 array; scan angle: $u = 0.35$, $v = 0.87$; $\cos^{1.5}(\theta)$

1.8 Summary

Chapter 1 has presented basic phased array theory and plotted finite array patterns that show the basic characteristics of the array pattern as the number of radiating elements are increased and as the array is scanned; the effect of the element pattern was introduced to the array factor pattern to illustrate the real array pattern characteristics: as the array is scanned off boresite the gain of the array is reduced by the element pattern shape.

Although the concepts presented in Chapter 1 are basic and straightforward, the examples given on forming an array pattern are important to understanding practical phased arrays:

- Section 1.1 introduced the array factor and Section 1.2 added the element pattern to the array factor summation;
- Section 1.3 gave the expression for the main beam 3dB beamwidth as a function of array length and scan angle θ_0 ;
- Section 1.4 presented simple array patterns based on two isotropic radiators;
 - The effect on the array pattern on the relative amplitude and phase weighting was changed as well as the relative spacing between elements- this is a very important concept regardless of the complexity of the array;
 - Next, then number of isotropic radiators was increased to 16 to show the effect on main beam width and sidelobes;
 - The element pattern was added to the array factor summation; the effect on array scan loss directly depends on the element pattern roll-off with scan θ ;
- Section 1.5 gave an overview was given on the limitations to array instantaneous bandwidth;
- Section 1.6 introduced the rectangular, planar array geometry
 - The two dimensional array factor was derived;
 - The concept of viewing a phased array as a “spatial sampling” of a continuous aperture was presented and how “extra beam” or “grating lobes” can be formed when the phased array of elements is “under-sampled” in physical space; that is, when the spacing between elements exceeds a certain fraction of a free-space wavelength; several examples were given in Section 1.6.1;

- Finally, Section 1.7 plotted patterns for a 19x19 planar array as a function of scan angle and for two different element patterns to show the effect of scan loss as the array is scanned.

Chapter 1 presented the important concepts and mathematical expressions to calculate simple phased array patterns and predict their shape as the beam was scanned; however, the patterns did not include the important effect of mutual coupling and the effect mutual coupling has on the array pattern as the pattern is scanned.

The next chapter will introduce the effect of mutual coupling by discussing the analytical approach based on a Floquet modal expansion of an array of printed dipoles to derive the infinite array scan impedance characteristics as a function of scan angle.

Chapter 2 – Floquet Analysis Applied to Phased Arrays

2.0 Introduction

Chapter 2 is based on the paper “Scan Impedance for An Infinite Dipole Array: Hansen’s Formulas Compared with Ansoft HFSS Simulations”^{2.1} and introduces the Floquet Modal approach as applied to linear phased arrays with a periodic amplitude and phase excitation. The array scan impedance for an infinite array of strip-dipole is derived and includes the effect of mutual coupling. The analytical scan impedance results are compared with the scan impedance computed by the infinite array solver HFSS; the section concludes with an approach of extending the analytical single mode Floquet expansion to multimode current expansion on the dipole.

2.1 Mutual Coupling in Phased Arrays: An Analytical Approach

In the array factor development presented in Chapter 1, the element pattern was taken outside the summation- the assumption was that mutual coupling effects between elements could be ignored. The assumption that the element pattern is identical for all elements in the array is true only for an infinite array of identical elements; this assumption is not true for finite arrays and may result in a large error in pattern performance if a common element pattern is assumed.

Mutual coupling is an electromagnetic interaction between antenna elements in an antenna array: antennas in close proximity interact through free-space coupling; the effect of this coupling changes the amplitude and phase of the currents on the antennas. The active impedance of a given element in a phased array is the input impedance of the element (self-impedance) and the mutual impedance between it and all the other elements in the array and the excitation on the other elements in the array. Thus, as the amplitude and phase excitation across the array changes the effect on the active impedance of each element changes. Specifically, mutual coupling affects array performance in the following manner^{2.2}:

1. Change in the element active impedance;
2. Change in the array radiation pattern: pattern nulls filling in; beam-pointing error; higher RMS sidelobe levels.

Therefore, in order to characterize the scan and pattern performance of a phased array, it is critical that mutual coupling effects be taken into account.

The radar system designer has to achieve the following objectives within the constraints of cost and schedule:

- Maximize the power incident on the target;
- Maximize the received power reflected by the target;
- Minimize the amount of un-wanted received power referred to as “clutter”;
- Minimize the noise generated within the radar;
- Minimize the RF losses within the radar;

One of the key subsystems of modern radar is the phased array. The phased array is the antenna, or transducer, between free-space and a constrained transmission lines that connect a transmit/receive chain with the phased array. The design of the phased array antenna impacts all of the above radar design objectives: the phased array is the key to maximizing radar sensitivity and to reducing cost.

The objective of the phased array designer is to minimize antenna loss with scan angle over the frequency band of interest; understanding the scan impedance of the array is important in order to minimize antenna loss and maximize radar sensitivity. Array scan impedance versus scan angle provides the information required to estimate scan loss due to mismatch and potentially catastrophic mismatches leading to “scan blindness” where considerable damage may be done to the radar.

Phased array design, development and testing is typically an expensive and time consuming effort, and an early estimation of the scan impedance between different proposed array architectures is critical to reducing the risk of investing time and money on a design where issues may come to light only after an expensive phased array is fielded.

Section 2.2 presents an analytical approach based on Floquet modal expansion to derive the scan (or active) impedance of an array of strip-dipole elements on a dielectric slab^{2,1}; the analytical results are compared with the infinite array solver HFSS in Section 2.8.

Section 2.9 presents the Multimodal Floquet Approach based on the paper “Scan Impedance for An Infinite Dipole Array: Accurate Theoretical Model Versus Numerical Software”. The paper extends the analytical formulation for the scan impedance of an infinite dipole array by extending the original theoretical model of VanKoughnett and Yen for the infinite, planar dipole array.

Section 2.10 extends the single mode Floquet modal expansion to a piecewise modal expansion across the strip-dipole element. Section 2.11 summarizes Chapter 2.

2.2 The Floquet Modal Approach

Section 2.2 introduces the Floquet Modal Approach as applied to a linear phased array with a periodic amplitude and phase excitation^{2,3}; Section 1.8.2 extends the approach to a two-dimensional array. We begin by stating Floquet's Theorem: Any planar periodic function can be expanded as an infinite superposition of Floquet Harmonics. Hansen adds^{2,4}: "Floquet's theorem for arrays states that an infinite regular periodic structure will have the same fields in each cell except for a progressive exponential multiplier".

First, we present an example that derives the spatial Floquet Harmonics for a one-dimensional periodic structure. Suppose we have an infinite periodic grating of period "t" along the x-axis and let $h(x)$ represent a plane wave incident on the grating. The geometry of the grating produces the following spatial relationship for the function $h(x)$:

$$h(x+t) = \alpha h(x), \text{ where } \alpha \equiv \text{complex constant}; \quad (2.2.1)$$

$h(x+2t) = \alpha h(x+t)$, $h(x+3t) = \alpha h(x+2t)$, $h(x+4t) = \alpha h(x+3t)$, ..., $h(x+nt) = \alpha h(x+(n-1)t) = \alpha^n h(x)$,
for $n = \pm\infty$.

Let $\alpha = e^{jkt}$, where k is a complex constant. Now, let us define a periodic function $T(x) = e^{-jkx} h(x)$

. For $x = x+t$:

$$T(x+t) = e^{-jk(x+t)} h(x+t) = e^{-jk(x+t)} \alpha h(x) = e^{-jk(x+t)} e^{jkt} h(x) = e^{-jkx} h(x) = T(x) \quad (2.2.2)$$

We can write the expression $T(x)$ as a periodic function in x with period "t"; we express $T(x)$ as a Fourier series expansion:

$$T(x) = \sum_{n=-\infty}^{\infty} b_n e^{j \frac{2\pi n}{t} x} \quad (2.2.3)$$

But, $T(x) = e^{-jkx} h(x)$:

$$\begin{aligned}
T(x) &= e^{-jkx} h(x) = \sum_{n=-\infty}^{\infty} b_n e^{j\frac{2\pi n}{t}x} \\
h(x) &= \sum_{n=-\infty}^{\infty} (b_n e^{jkx}) e^{j\frac{2\pi n}{t}x} = \sum_{n=-\infty}^{\infty} b_n e^{jk_{x_n}x}
\end{aligned} \tag{2.2.4}$$

where $k_{x_n} = k + \frac{2\pi n}{t}$.

We note: Each term in the infinite series representation of $h(x)$ is a spatial Floquet Harmonic:

The term $b_n e^{jkx}$ represents the complex amplitude of the n^{th} Floquet Harmonic;

The term $e^{j\frac{2\pi n}{t}x}$ represents the phase of the n^{th} Floquet Harmonic.

Thus, any planar periodic function $h(x)$ can be represented by an infinite sum of Floquet harmonics. Next, we derive the general expression for the Floquet series expansion of a function with periodic amplitude and phase shift. The Floquet series for the source function is derived for an infinite, one dimensional surface current excitation; the radiated E and H fields are given by the magnetic vector potential and Maxwell's equations.

2.2.1 The Floquet Series Expansion of a Periodic Function

An infinite phased array is modeled as an array of infinite source functions. Consider a function with the following periodic amplitude and phase shift^{2,3}:

$$h(x) = \sum_{n=-\infty}^{\infty} f(x - na) e^{-jn\varphi} \tag{2.2.5}$$

where $f(x) \equiv$ complex function of a real variable x and $\varphi \equiv$ real constant. The function $h(x)$ has periodicity “ a ”:

$$\begin{aligned}
h(x+a) &= h(x)e^{-j\varphi} \\
&\vdots \\
h(x+na) &= h(x)e^{-jn\varphi}
\end{aligned} \tag{2.2.6}$$

We may express $h(x)$ in a Fourier series type expansion; taking the Fourier transform of expression 2.2.5:

$$\tilde{h}(k_x) = (2\pi)^{-1} \int_{-\infty}^{\infty} \left[\sum_{n=-\infty}^{\infty} f(x-na) e^{-jn\varphi} e^{+jk_x x} dx \right]$$

$$\tilde{h}(k_x) = (2\pi)^{-1} \sum_{n=-\infty}^{\infty} e^{-jn\varphi} \int_{-\infty}^{\infty} f(x-na) e^{+jk_x x} dx \quad (2.2.7)$$

Make the variable substitution $x' = x-na$ in expression 2.2.7:

$$\tilde{h}(k_x) = (2\pi)^{-1} \sum_{n=-\infty}^{\infty} e^{-jn\varphi} \int_{-\infty}^{\infty} f(x') e^{+jk_x(x'+na)} dx'$$

$$\tilde{h}(k_x) = (2\pi)^{-1} \sum_{n=-\infty}^{\infty} e^{-jn\varphi} e^{-jk_x na} \int_{-\infty}^{\infty} f(x') e^{+jk_x x'} dx' \quad (2.2.8)$$

We recognize the Fourier Transform of $f(x')$:

$$\tilde{f}(k_x) = (2\pi)^{-1} \int_{-\infty}^{\infty} f(x') e^{+jk_x x'} dx'$$

Therefore, expression 2.2.8 becomes:

$$\tilde{h}(k_x) = \tilde{f}(k_x) \sum_{n=-\infty}^{\infty} e^{jn(k_x a - \varphi)} \quad (2.2.9)$$

Using the Poisson Sum Formula^{2.1.3}:

$$\sum_{n=-\infty}^{\infty} e^{jnk_x a} = \frac{2\pi}{a} \sum_{n=-\infty}^{\infty} \delta\left(k_x - \frac{2n\pi}{a}\right)$$

$$\sum_{n=-\infty}^{\infty} e^{jn(k_x a - \varphi)} = \frac{2\pi}{a} \sum_{n=-\infty}^{\infty} \delta\left(k_x - \frac{2n\pi}{a} - \frac{\varphi}{a}\right) \quad (2.2.10)$$

Substituting expression 2.2.10 into expression 2.2.9:

$$\tilde{h}(k_x) = \frac{2\pi}{a} \tilde{f}(k_x) \sum_{n=-\infty}^{\infty} \delta\left(k_x - \frac{2n\pi}{a} - \frac{\varphi}{a}\right) \quad (2.2.11)$$

The function $h(x)$ can be recovered from the inverse Fourier Transform of $\tilde{h}(k_x)$:

$$\begin{aligned}
h(x) &= \int_{-\infty}^{\infty} \tilde{h}(k_x) e^{-jk_x x'} dk_x \\
h(x) &= \frac{2\pi}{a} \int_{-\infty}^{\infty} \tilde{f}(k_x) \left[\sum_{n=-\infty}^{\infty} \delta\left(k_x - \frac{2n\pi}{a} - \frac{\varphi}{a}\right) e^{-jk_x x'} dk_x \right] \\
h(x) &= \frac{2\pi}{a} \sum_{n=-\infty}^{\infty} \left[\int_{-\infty}^{\infty} \tilde{f}(k_x) \delta\left(k_x - \frac{2n\pi}{a} - \frac{\varphi}{a}\right) e^{-jk_x x'} dk_x \right] \\
h(x) &= \frac{2\pi}{a} \sum_{n=-\infty}^{\infty} \left[\tilde{f}\left(\frac{2n\pi}{a} + \frac{\varphi}{a}\right) e^{-j\left(\frac{2n\pi}{a} + \frac{\varphi}{a}\right)x} \right]
\end{aligned} \tag{2.2.12}$$

Expression 2.2.12 represents the Floquet Series expansion of the source excitation; that is, we have transformed an element by element representation of $h(x)$ from the “spatial domain” (expression 2.2.5) to the “spectral domain” (expression 2.2.12):

- $\tilde{f}\left(\frac{2n\pi}{a} + \frac{\varphi}{a}\right)$ represents the Floquet complex amplitude coefficient,
- $e^{-j\left(\frac{2n\pi}{a} + \frac{\varphi}{a}\right)x}$ represents the Floquet harmonic function.

In summary, a Floquet series expansion for an array of source functions, as represented in expression 2.2.5, the amplitude and phase are periodic but may have different periods. In contrast, the complex amplitude and phase have the same period in the Fourier series representation.

We examine the case of the infinite, one-dimensional surface current excitation and derive the electric field produced by the array. Suppose we have an infinite, linear array of y – directed surface current elements in the $x - y$ plane located at $z = 0$ as shown in Figure 2-1:

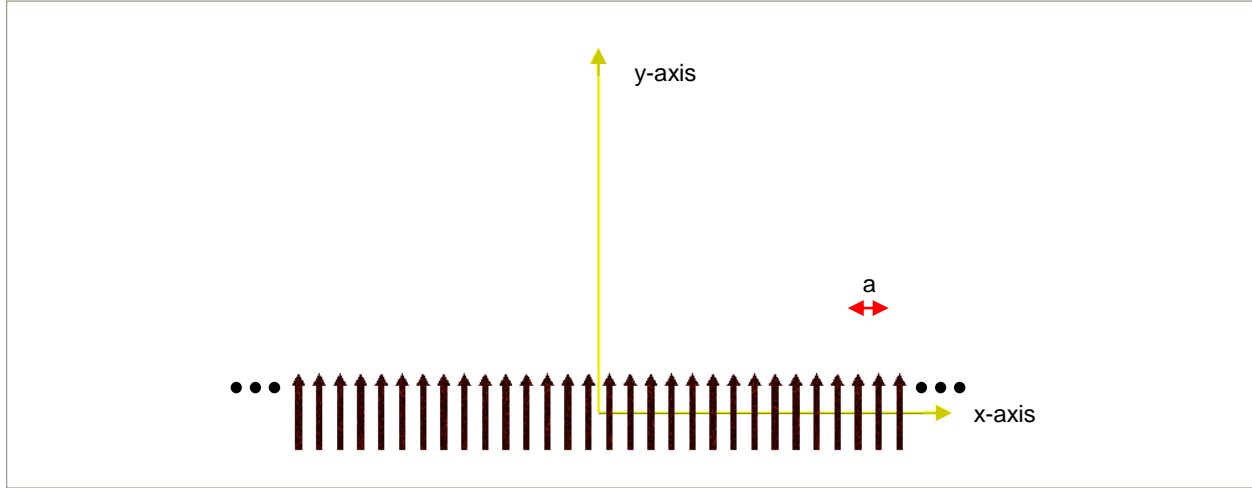


Figure 2-1. One-dimensional infinite array of y -axis directed current elements

The surface current excitation is represented as:

$$\vec{J} = \hat{y}h(x) = \hat{y} \sum_{n=-\infty}^{\infty} f(x - na)e^{-jn\phi} \quad (2.2.13)$$

For this example, the current \vec{J} is in the \hat{y} direction and thus will generate a magnetic vector potential \vec{A} in the \hat{y} direction:

$$\vec{A} = \hat{y}A_y \quad (2.2.14)$$

The fundamental expression equating the source excitation and the modal spectrum of electromagnetic plane waves for an infinite periodic structure is the vector Helmholtz' equation:

$$\nabla^2 \vec{A} + k_0^2 \vec{A} = -\vec{J} \quad (2.2.15)$$

where

$\vec{A} \equiv$ magnetic vector potential

$\vec{J} \equiv$ source volume current element (A/m^2)

$k_0^2 \equiv \omega^2 \mu_0 \epsilon_0$ is the free space wave-number.

We wish to show that for an infinite periodic structure the source excitation, \vec{J} , generates a solution \vec{A} that produces electromagnetic fields represented by an infinite sum of Floquet Modal functions (plane wave functions). Based on the spatial excitation given in expression 2.2.13, the vector Helmholtz equation is reduced to a second order, inhomogeneous partial differential equation in the \hat{y} direction:

$$\nabla^2 A_y + k_0^2 A_y = -J_y \quad (2.2.16)$$

Substituting expression 2.2.13 for J_y into equation 2.2.12:

$$\nabla^2 A_y + k_0^2 A_y = - \sum_{n=-\infty}^{\infty} f(x-na) e^{-jn\varphi} \quad (2.2.17)$$

Substituting the series expansion from expression 2.2.12 for the right – hand side of expression 2.2.17:

$$\nabla^2 A_y + k_0^2 A_y = - \frac{2\pi}{a} \sum_{n=-\infty}^{\infty} \left[\tilde{f} \left(\frac{2n\pi}{a} + \frac{\varphi}{a} \right) e^{-j \left(\frac{2n\pi}{a} + \frac{\varphi}{a} \right) x} \right] \quad (2.2.18)$$

Expression 2.2.18 is an inhomogeneous partial differential equation; we pose a solution, A_y , as a Fourier-Series like expansion using the characteristic solutions of the scalar Helmholtz equation:

$$A_y = \sum_{n=-\infty}^{\infty} \left[F_n(n) e^{-j \left(\frac{2n\pi}{a} + \frac{\varphi}{a} \right) x} \right] \quad (2.2.19)$$

The next task is to determine the coefficients, $F_n(n)$, of the expansion in expression 2.2.18.

Substitute expression 2.2.19 into expression 2.2.18:

$$\nabla^2 \sum_{n=-\infty}^{\infty} F_n(n) e^{-j \left(\frac{2n\pi}{a} + \frac{\varphi}{a} \right) x} + k_0^2 \sum_{n=-\infty}^{\infty} F_n(n) e^{-j \left(\frac{2n\pi}{a} + \frac{\varphi}{a} \right) x} = - \frac{2\pi}{a} \sum_{n=-\infty}^{\infty} \left[\tilde{f} \left(\frac{2n\pi}{a} + \frac{\varphi}{a} \right) e^{-j \left(\frac{2n\pi}{a} + \frac{\varphi}{a} \right) x} \right] \quad (2.2.20)$$

Expanding expression 2.2.20:

$$\left(\frac{\partial^2}{\partial x^2} + \frac{\partial^2}{\partial y^2} + \frac{\partial^2}{\partial z^2} \right) \sum_{n=-\infty}^{\infty} F_n(n) e^{-j \left(\frac{2n\pi}{a} + \frac{\varphi}{a} \right) x} + k_0^2 \sum_{n=-\infty}^{\infty} F_n(n) e^{-j \left(\frac{2n\pi}{a} + \frac{\varphi}{a} \right) x} = - \frac{2\pi}{a} \sum_{n=-\infty}^{\infty} \left[\tilde{f} \left(\frac{2n\pi}{a} + \frac{\varphi}{a} \right) e^{-j \left(\frac{2n\pi}{a} + \frac{\varphi}{a} \right) x} \right]$$

$$\sum_{n=-\infty}^{\infty} \left(-\left(\frac{2n\pi + \varphi}{a}\right)^2 F_n(n) + 0 + \frac{\partial^2 F_n(n)}{\partial z^2} \right) e^{-j\left(\frac{2n\pi + \varphi}{a}\right)x} + k_0^2 \sum_{n=-\infty}^{\infty} F_n(n) e^{-j\left(\frac{2n\pi + \varphi}{a}\right)x} = -\frac{2\pi}{a} \sum_{n=-\infty}^{\infty} \left[\tilde{f}\left(\frac{2n\pi}{a} + \frac{\varphi}{a}\right) e^{-j\left(\frac{2n\pi + \varphi}{a}\right)x} \right]$$

$$\sum_{n=-\infty}^{\infty} \left(-\left(\frac{2n\pi + \varphi}{a}\right)^2 F_n(n) \right) e^{-j\left(\frac{2n\pi + \varphi}{a}\right)x} + \sum_{n=-\infty}^{\infty} \frac{\partial^2 F_n(n)}{\partial z^2} e^{-j\left(\frac{2n\pi + \varphi}{a}\right)x} + k_0^2 \sum_{n=-\infty}^{\infty} F_n(n) e^{-j\left(\frac{2n\pi + \varphi}{a}\right)x} = -\frac{2\pi}{a} \sum_{n=-\infty}^{\infty} \left[\tilde{f}\left(\frac{2n\pi}{a} + \frac{\varphi}{a}\right) e^{-j\left(\frac{2n\pi + \varphi}{a}\right)x} \right] \quad (2.2.21)$$

where the wave-number $k_{zn} \equiv \frac{2n\pi + \varphi}{a}$. Comparing each term on both sides of the series expansion in expression 2.2.21, and defining the dispersion relation $k_{zn}^2 = k_0^2 - k_{zn}^2$, we obtain:

$$\frac{\partial^2 F_n(n)}{\partial z^2} + k_{zn}^2 F_n(n) = -\frac{2\pi}{a} \tilde{f}(k_{zn}), \text{ for each } n. \quad (2.2.22)$$

Expression 2.2.22 relates the expansion coefficients $F_n(n)$ for A_y and the complex expansion coefficients of the source excitation, $\tilde{f}(k_{zn})$.

For the region $z > 0$, expression 2.2.22 becomes a homogeneous equation:

$$\frac{\partial^2 F_n(n)}{\partial z^2} + k_{zn}^2 F_n(n) = 0 \quad (2.2.23)$$

Expression 2.2.23 is satisfied by the following spectral representation of $F_n(n)$:

$$F_n(n) = \frac{\pi}{jak_{zn}} \tilde{f}(k_{zn}) e^{-jk_{zn}z} \quad (2.2.24)$$

Substituting Expression 2.2.24 into Expression 2.2.23:

$$\frac{\partial^2}{\partial z^2} \left(\frac{\pi}{jak_{zn}} \tilde{f}(k_{zn}) e^{-jk_{zn}z} \right) + \frac{k_{zn}^2 \pi}{jak_{zn}} \tilde{f}(k_{zn}) e^{-jk_{zn}z} = 0$$

$$\frac{-k_{zn}^2 \pi}{jak_{zn}} \tilde{f}(k_{zn}) e^{-jk_{zn}z} + \frac{k_{zn}^2 \pi}{jak_{zn}} \tilde{f}(k_{zn}) e^{-jk_{zn}z} = 0$$

$$0 = 0$$

Thus, for the region $z > 0$ the y – directed magnetic vector potential A_y becomes:

$$A_y = \frac{\pi}{ja} \sum_{n=-\infty}^{\infty} \left[\frac{\tilde{f}(k_{xn})}{k_{zn}} e^{-j(k_{xn}x+k_{zn}z)} \right] \quad (2.2.25)$$

Having determined the expansion for the magnetic vector potential A_y , we now generate the fields from Maxwell's equations. The magnetic field \vec{H} is found from the curl of the magnetic vector potential \vec{A} :

$$\vec{H} = \nabla \times \vec{A}, \quad \vec{H} = \nabla \times \hat{y}A_y \quad (2.2.26)$$

Performing the curl in rectangular coordinates:

$$\vec{H} = \hat{x} \frac{\pi}{a} \sum_{n=-\infty}^{\infty} \left[\frac{k_{zn} \tilde{f}(k_{xn})}{k_{zn}} e^{-j(k_{xn}x+k_{zn}z)} \right] - \hat{z} \frac{\pi}{a} \sum_{n=-\infty}^{\infty} \left[\frac{k_{xn} \tilde{f}(k_{xn})}{k_{zn}} e^{-j(k_{xn}x+k_{zn}z)} \right] \quad (2.2.27)$$

Thus,

$$H_x = \hat{x} \frac{\pi}{a} \sum_{n=-\infty}^{\infty} \left[\tilde{f}(k_{xn}) e^{-j(k_{xn}x+k_{zn}z)} \right] \quad (2.2.28)$$

$$H_z = -\hat{z} \frac{\pi}{a} \sum_{n=-\infty}^{\infty} \left[\frac{k_{xn} \tilde{f}(k_{xn})}{k_{zn}} e^{-j(k_{xn}x+k_{zn}z)} \right] \quad (2.2.29)$$

From Maxwell's equations, Ampere's Law determines the radiated electric field \vec{E} :

$$\vec{E} = \frac{1}{j\omega\epsilon_0} \nabla \times \vec{H}, \quad \vec{J} = 0 \quad (2.2.30)$$

Performing the curl in rectangular coordinates:

$$\vec{E} = \frac{1}{j\omega\epsilon_0} \left[\hat{x} \frac{\partial H_z}{\partial y} - \hat{y} \left(\frac{\partial H_z}{\partial x} - \frac{\partial H_x}{\partial z} \right) - \hat{z} \frac{\partial H_x}{\partial y} \right] \quad (2.2.31)$$

But, $\frac{\partial H_z}{\partial y} = 0$ and $\frac{\partial H_x}{\partial y} = 0$; substituting for H_x and H_y from expressions 2.2.28 and 2.2.29:

$$\left(\frac{\partial H_z}{\partial x} - \frac{\partial H_x}{\partial z} \right) = \frac{-j\pi}{a} \left[\sum_{n=-\infty}^{\infty} \left[\frac{k_{xn}^2 \tilde{f}(k_{xn})}{k_{zn}} e^{-j(k_{xn}x+k_{zn}z)} \right] + \sum_{n=-\infty}^{\infty} \left[k_{zn} \tilde{f}(k_{xn}) e^{-j(k_{xn}x+k_{zn}z)} \right] \right]$$

$$\begin{aligned} \left(\frac{\partial H_z}{\partial x} - \frac{\partial H_x}{\partial z} \right) &= \frac{-j\pi}{a} \sum_{n=-\infty}^{\infty} \tilde{f}(k_{xn}) \left(\frac{k_{xn}^2}{k_{zn}} + k_{zn} \right) e^{-j(k_{xn}x + k_{zn}z)} \\ \left(\frac{\partial H_z}{\partial x} - \frac{\partial H_x}{\partial z} \right) &= \frac{-j\pi k_0^2}{a} \sum_{n=-\infty}^{\infty} \frac{\tilde{f}(k_{xn})}{k_{zn}} e^{-j(k_{xn}x + k_{zn}z)} \\ \text{since } \left(\frac{k_{xn}^2}{k_{zn}} + k_{zn} \right) &= \left(\frac{k_{xn}^2 + k_{zn}^2}{k_{zn}} \right) \end{aligned} \quad (2.2.32)$$

For the region $z > 0$ and in the plane $y=0$, the electric field \vec{E} is given by:

$$\begin{aligned} \vec{E} &= \hat{y}E_y = \left(\frac{1}{j\omega\epsilon_0} \right) \left(\frac{-j\pi k_0^2}{a} \right) \sum_{n=-\infty}^{\infty} \frac{\tilde{f}(k_{xn})}{k_{zn}} e^{-j(k_{xn}x + k_{zn}z)} \\ \vec{E} &= \hat{y}E_y = \hat{y} \left(\frac{-\pi\omega\mu_0}{a} \right) \sum_{n=-\infty}^{\infty} \frac{\tilde{f}(k_{xn})}{k_{zn}} e^{-j(k_{xn}x + k_{zn}z)} \end{aligned} \quad (2.2.33)$$

Observations from expression 2.2.33 for the electric field \vec{E} :

- \vec{E} is the radiated (transmitted) electric field of the periodic structure due to the source excitation \vec{J} ;
- Each harmonic of \vec{E} must satisfy the wave equation;
- \vec{E} is polarized along the y-axis and is a function of the x coordinate ($-\infty < x < +\infty$) and z coordinate ($z > 0$);
- The complex electric field \vec{E} is represented by an infinite summation of plane waves:
- Each plane wave is given by $\hat{y} \left(\frac{-\pi\omega\mu_0}{a} \right) \frac{\tilde{f}(k_{xn})}{k_{zn}} e^{-j(k_{xn}x + k_{zn}z)}$;
- $\frac{\tilde{f}(k_{xn})}{k_{zn}}$ is the complex amplitude of each mode. Note that $\tilde{f}(k_{xn})$ is determined by the source excitation $f(x - na)$;
- The direction of propagation of the n^{th} mode is given by $\vec{p}_n = \hat{x}k_{xn} + \hat{z}k_{zn}$

Re-writing expression 2.2.12 using $k_{xn} = \frac{2n\pi + \varphi}{a}$:

$$h(x) = \frac{2\pi}{a} \sum_{n=-\infty}^{\infty} [\tilde{f}(k_{xn}) e^{-jk_{xn}x}] \quad (2.2.34)$$

Comparing the exponential terms in expressions 2.2.33 and 2.2.34, we recognize that the exponential wavenumber dependency for the field vectors, k_{xn} , has exactly the same exponential wavenumber dependency as the source excitation $h(x)$. This is not surprising given that Floquet's theorem states that all observables (e.g., the electromagnetic field) will have the same periodicity as the structure and a unit cell to unit cell phase shift that is equal to the source unit cell phase shift. Now, suppose we have a Floquet mode (plane wave) incident on an infinite, one – dimensional phased array; we can think of this situation as the array in “receive mode”. The Floquet mode will excite a signal at the output of each port of the infinite, one – dimensional phased array with the same polarization and phase shift.

The relationship between the source excitation and a plane-wave spectrum representation will be presented in Section 2.3 for the two – dimensional Floquet source excitation of strip dipole elements. Section 2.3 will present the expansion of the printed (or strip) dipole array and derive the scan impedance.

2.3 Two–Dimensional Floquet Source Excitation of Strip Dipole Elements

Section 2.3 extends the infinite one–dimensional Floquet Source excitation to an infinite, two–dimensional Source Excitation. Section 2.3 will derive the Fourier coefficients used in the electric field expressions derived in Section 2.2; then, in Section 2.5, the scan impedance is derived from the radiated electric fields.

The Floquet series representation for the current distribution given in Figure 2-2^{2.1} is first developed; the radiated electric field is then derived.

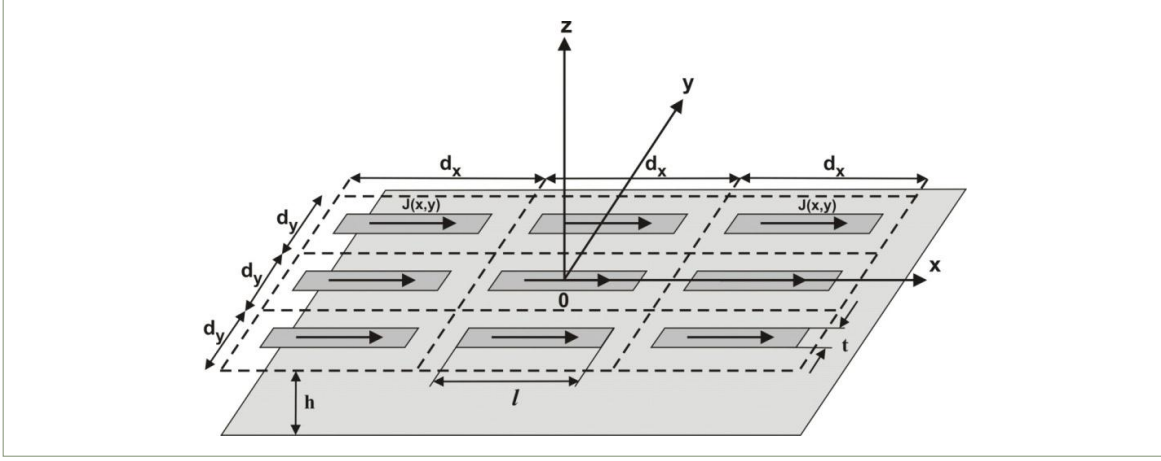


Figure 2-2. The geometry of the infinite array with strip-dipole elements (single polarization)

The spatial current distribution is given by:

$$\vec{J}(x, y, z) = \vec{x} J_0 \delta(z) \sum_{m=-\infty}^{m=+\infty} \sum_{n=-\infty}^{n=+\infty} f(x - x_{mn}) g(y - y_{mn}) \exp(-jk_{x0}x_{mn} - jk_{y0}y_{mn}) \quad (2.3.1)$$

Focusing on the double infinite summation:

$$\vec{J}(x, y, z) = \vec{x} \sum_{m=-\infty}^{m=+\infty} \sum_{n=-\infty}^{n=+\infty} f(x - x_{mn}) g(y - y_{mn}) e^{(-jk_{x0}x_{mn} - jk_{y0}y_{mn})} \quad (2.3.2)$$

where the element coordinates are given by $x_{mn} = md_x$, $y_{mn} = nd_y$, $m, n = 0, \pm 1, \pm 2, \dots, \pm\infty$. Following the mathematical approach outlined in Section 2.2, the Floquet Series expansion for expression 2.3.2 is written by inspection:

$$\vec{J}(x, y, z) = \vec{x} \frac{4\pi^2}{d_x d_y} J_0 \delta(z) \sum_{m=-\infty}^{m=+\infty} \sum_{n=-\infty}^{n=+\infty} \tilde{f}(k_{xmn}) \tilde{g}(k_{ymn}) e^{(-jk_{xmn}x - jk_{ymn}y)} \quad (2.3.3)$$

where the wavenumbers in the $x - y$ plane are given by:

$$k_{xmn} = k_{x0} + \frac{2m\pi}{d_x} \quad \text{and} \quad k_{ymn} = k_{y0} + \frac{2n\pi}{d_y}. \quad (2.3.4)$$

The radiated fields are again determined by the Helmholtz equation for the magnetic vector potential A_x :

$$\nabla^2 A_x + k_0^2 A_x = -J_x(x, y, z) \quad (2.3.5)$$

Following the procedure outlined in Section 2.2:

1. Find the magnetic field, \bar{H} , from the curl of A_x ;
2. Find the radiated electric field, \bar{E} , in the region $z > 0$ from Maxwell's (Faraday) equation:

$$\begin{aligned}
 E_x &= -\hat{x} \frac{2\pi^2 J_0}{d_x d_y \omega \epsilon_0} \sum_m \sum_n \frac{k_0^2 - k_{xmn}^2}{k_{zmn}} \tilde{f}(k_{xmn}) \tilde{g}(k_{ymn}) e^{(-jk_{xmn}x - jk_{ymn}y - jk_{zmn}z)} \\
 E_y &= \hat{y} \frac{2\pi^2 J_0}{d_x d_y \omega \epsilon_0} \sum_m \sum_n \frac{k_{xmn} k_{ymn}}{k_{zmn}} \tilde{f}(k_{xmn}) \tilde{g}(k_{ymn}) e^{(-jk_{xmn}x - jk_{ymn}y - jk_{zmn}z)} \\
 E_z &= \hat{z} \frac{2\pi^2 J_0}{d_x d_y \omega \epsilon_0} \sum_m \sum_n k_{ymn} \tilde{f}(k_{xmn}) \tilde{g}(k_{ymn}) e^{(-jk_{xmn}x - jk_{ymn}y - jk_{zmn}z)}
 \end{aligned} \tag{2.3.6}$$

We note the following in expression 2.3.6:

- In the k_{xmn}, k_{ymn} plane, the source excitation $\bar{J}(x, y, z)$ has exactly the same exponential dependency, $e^{(-jk_{xmn}x - jk_{ymn}y)}$, as the exponential dependency for the field vectors;
- The coefficients $\tilde{f}(k_{xmn})$ and $\tilde{g}(k_{ymn})$ are independent of z since the source and geometry are independent of z .

2.4 Fourier Transform of Current Expansion

Mathematically representing the array source distribution as a Floquet Series expansion requires taking the Fourier Transform of the element source distribution. In Section 2.3, the Fourier Transform of the current distributions given in reference^{2.1} will be derived.

For the infinite array of strip-dipole elements, the current expansion is written^{2.1}:

$$\bar{J}(x, y) = \bar{x} J_0 f(x) g(y)$$

$$\bar{J}(x, y) = \bar{x} J_0 f(x) g(y), \quad f(x) = \begin{cases} \Pi\left(\frac{x}{l}\right) & \text{case A} \\ \sin\left(k_0 \left[\frac{l}{2} - |x|\right]\right) & \text{case B, } g(y) = \Pi\left(\frac{y}{t}\right) \\ \cos(k_0 x) & \text{case C} \end{cases} \tag{2.4.1}$$

The spatial Fourier transform (denoted by superscript “~”) of the surface/volume current distribution in expression 2.4.1 is mathematically given by:

$$\tilde{J}(k_x, k_y) \equiv \bar{x} J_0 \tilde{f}(k_x) \tilde{g}(k_y) \quad (2.4.2)$$

$$\tilde{f}(k_x) = \frac{1}{2\pi} \int_{-\infty}^{+\infty} f(x) \exp(jk_x x) dx \quad (2.4.3)$$

$$\tilde{g}(k_y) = \frac{1}{2\pi} \int_{-\infty}^{+\infty} g(y) \exp(jk_y y) dy \quad (2.4.4)$$

We begin with the spatial Fourier Transform of $g(y)$; from expressions 2.4.1 and 2.4.4:

$$g(y) = \Pi\left(\frac{y}{t}\right)$$

$$\tilde{g}(k_y) = \frac{1}{2\pi} \int_{-\infty}^{+\infty} g(y) \exp(jk_y y) dy = \frac{1}{2\pi} \int_{-\frac{t}{2}}^{+\frac{t}{2}} \exp(jk_y y) dy = \frac{1}{j2\pi k_y} \left[\exp(jk_y \frac{t}{2}) - \exp(jk_y \frac{t}{2}) \right]$$

$$\tilde{g}(k_y) = \frac{2j}{j2\pi k_y} \left[\sin(k_y \frac{t}{2}) \right] \left(\frac{t/2}{2} \right)$$

$$\tilde{g}(k_y) = \frac{t}{2\pi} \left[\sin c(k_y \frac{t}{2}) \right] \tag{2.4.5}$$

Case A. From expressions 2.4.1, Case A and 2.4.3:

$$f(x) = \Pi\left(\frac{x}{l}\right)$$

$$\tilde{f}(k_x) = \frac{1}{2\pi} \int_{-\infty}^{+\infty} f(x) \exp(jk_x x) dx = \frac{1}{2\pi} \int_{-\frac{l}{2}}^{+\frac{l}{2}} \exp(jk_x x) dx = \frac{1}{j2\pi k_x} \left[\exp(jk_x \frac{l}{2}) - \exp(jk_x \frac{l}{2}) \right]$$

$$\tilde{f}(k_x) = \frac{2j}{j2\pi k_x} \left[\sin(k_x \frac{l}{2}) \right] \left(\frac{l/2}{2} \right)$$

$$\tilde{f}(k_x) = \frac{l}{2\pi} \left[\sin c(k_x \frac{l}{2}) \right] \tag{2.4.6}$$

Case B. From expressions 2.4.1, Case B and 2.4.3:

$$f(x) = \sin\left(k_0 \left[\frac{l}{2} - |x| \right]\right)$$

$$\begin{aligned} \tilde{f}(k_x) &= \frac{1}{2\pi} \int_{-\infty}^{+\infty} f(x) \exp(jk_x x) dx \\ &= \frac{1}{2\pi} \left\{ \int_{-\frac{l}{2}}^0 \sin\left(k_0 \left[\frac{l}{2} + x \right]\right) \exp(jk_x x) dx + \int_0^{\frac{l}{2}} \sin\left(k_0 \left[\frac{l}{2} - x \right]\right) \exp(jk_x x) dx \right\} \\ \tilde{f}(k_x) &= \frac{1}{2\pi} \left\{ \int_0^{\frac{l}{2}} \sin\left(k_0 \left[\frac{l}{2} - x \right]\right) \exp(-jk_x x) dx + \int_0^{\frac{l}{2}} \sin\left(k_0 \left[\frac{l}{2} - x \right]\right) \exp(jk_x x) dx \right\} \\ &= \frac{1}{2\pi} \left\{ \int_0^{\frac{l}{2}} \sin\left(k_0 \left[\frac{l}{2} - x \right]\right) (\exp(-jk_x x) + \exp(jk_x x)) dx \right\} \\ &= \frac{2}{2\pi} \left\{ \int_0^{\frac{l}{2}} \sin\left(k_0 \left[\frac{l}{2} - x \right]\right) \cos(k_x x) dx \right\} \\ &= \frac{1}{2\pi} \left\{ \int_0^{\frac{l}{2}} \sin\left[\left(k_0 \frac{l}{2}\right) + (k_x - k_0)x\right] dx + \int_0^{\frac{l}{2}} \sin\left[\left(k_0 \frac{l}{2}\right) - (k_x + k_0)x\right] dx \right\} \\ &= \frac{1}{2\pi} \left\{ \frac{1}{(k_x - k_0)} \left[-\cos\left(k_x \frac{l}{2}\right) + \cos\left(k_0 \frac{l}{2}\right) \right] - \frac{1}{(k_0 + k_x)} \left[-\cos\left(k_x \frac{l}{2}\right) + \cos\left(k_0 \frac{l}{2}\right) \right] \right\} \\ &= \frac{2k_0}{2\pi(k_x^2 - k_0^2)} \left[\cos\left(k_0 \frac{l}{2}\right) - \cos\left(k_x \frac{l}{2}\right) \right] \end{aligned}$$

$$\tilde{f}(k_x) = \frac{2k_0}{2\pi(k_x^2 - k_0^2)} \left[\cos\left(k_0 \frac{l}{2}\right) - \cos\left(k_x \frac{l}{2}\right) \right]$$

(2.4.7)

Case C. From expressions 2.4.1, Case C and 2.4.3:

$$f(x) = \cos(k_0 x)$$

$$\begin{aligned} \tilde{f}(k_x) &= \frac{1}{2\pi} \int_{-\infty}^{+\infty} f(x) \exp(jk_x x) dx = \frac{1}{2\pi} \int_{-\infty}^{+\infty} \cos(k_0 x) \exp(jk_x x) dx \\ &= \frac{2}{2\pi} \left\{ \int_{-\frac{l}{2}}^{\frac{l}{2}} [\exp(jk_0 x) + \exp(-jk_0 x)] \exp(jk_x x) dx \right\} \\ &= \frac{1}{\pi} \left\{ \int_{-\frac{l}{2}}^{\frac{l}{2}} [\exp(j(k_0 + k_x)x) + \exp(j(k_x + k_0)x)] dx \right\} \\ &= \frac{1}{\pi} \left[\frac{1}{j(k_0 + k_x)} \left(\exp(j(k_0 + k_x)\frac{l}{2}) - \exp(-j(k_x + k_0)\frac{l}{2}) \right) + \right. \\ &\quad \left. \frac{1}{j(k_0 - k_x)} \left(\exp(j(k_0 - k_x)\frac{l}{2}) - \exp(-j(k_x - k_0)\frac{l}{2}) \right) \right] \\ &= \frac{1}{\pi} \left[\frac{2j \sin[(k_0 + k_x)\frac{l}{2}]}{j(k_0 + k_x)} + \frac{2j \sin[(k_x - k_0)\frac{l}{2}]}{j(k_x - k_0)} \right] \end{aligned}$$

$$\tilde{f}(k_x) = \frac{2}{\pi} \left[\frac{\sin[(k_0 + k_x)\frac{l}{2}]}{(k_0 + k_x)} + \frac{\sin[(k_x - k_0)\frac{l}{2}]}{(k_x - k_0)} \right]$$

(2.4.8)

2.5 Radiated Electric Field and Scan Impedance of Printed Dipole Array

Section 2.5 details the derivation of the scan impedance Z_s ; we begin by computing the complex power over the unit cell^{2.5}:

$$Z_s \equiv \frac{P}{I_0 J_0^*} \equiv \frac{- \iint_{\text{unitcell}} \vec{E} \cdot \vec{J}^* ds}{|I_0|^2} = - \frac{\iint_{\text{unitcell}} E_x(x, y, z=0) \cdot J_x^*(x, y) dx dy}{I_0^2} \quad (2.5.1)$$

The expressions for $E_x(x, y, z)$ and $J_x(x, y)$ are given by expressions 2.3.6 and 2.3.3, respectively:

$$E_x(x, y, z) = - \frac{2\pi^2}{d_x d_y \omega \epsilon_0} J_0 \sum_{m=-\infty}^{m=+\infty} \sum_{n=-\infty}^{n=+\infty} \frac{k_0^2 - k_{xmn}^2}{k_{zmn}} \tilde{f}(k_{xmn}) \tilde{g}(k_{ymn}) e^{-jk_{xmn}x - jk_{ymn}y - jk_{zmn}z} \quad (2.5.2)$$

$$J_x(x, y) = \frac{4\pi^2}{d_x d_y} J_0 \sum_{m=-\infty}^{m=+\infty} \sum_{n=-\infty}^{n=+\infty} \tilde{f}(k_{xmn}) \tilde{g}(k_{ymn}) e^{-jk_{xmn}x - jk_{ymn}y} \quad (2.5.3)$$

Substituting for $E_x(x, y, z)$ and $J_x(x, y)$ for Z_s at $z=0$:

$$Z_s = \frac{1}{I_0^2} \iint_{\text{unitcell}} \frac{2\pi^2 J_0}{d_x d_y \omega \epsilon_0} \left(\sum_{m=-\infty}^{m=+\infty} \sum_{n=-\infty}^{n=+\infty} \frac{k_0^2 - k_{xmn}^2}{k_{zmn}} \tilde{f}(k_{xmn}) \tilde{g}(k_{ymn}) e^{-jk_{xmn}x - jk_{ymn}y} \right) \cdot \left(\frac{4\pi^2 J_0}{d_x d_y} \sum_{m'=-\infty}^{m'=+\infty} \sum_{n'=-\infty}^{n'=+\infty} \tilde{f}(k_{xm'n'}) \tilde{g}(k_{ym'n'}) e^{-jk_{xm'n'}x - jk_{ym'n'}y} \right)^* dx dy \quad (2.5.4)$$

where “*” denotes complex conjugate. Exchanging the order of summation and integration:

$$Z_s = \frac{8\pi^4 J_0^2}{(d_x d_y)^2 \omega \epsilon_0^2 I_0^2} \sum_{\substack{m=-\infty \\ m'=+\infty}}^{\substack{m=+\infty \\ m'=-\infty}} \sum_{\substack{n=-\infty \\ n'=+\infty}}^{\substack{n=+\infty \\ n'=-\infty}} \frac{k_0^2 - k_{xmn}^2}{k_{zmn}} \tilde{f}(k_{xmn}) \tilde{g}(k_{ymn}) \tilde{f}^*(k_{xm'n'}) \tilde{g}^*(k_{ym'n'}) \iint_{\text{unitcell}} e^{j(k_{xm'n'} - k_{xmn})x + j(k_{ym'n'} - k_{ymn})y} dx dy \quad (2.5.5)$$

There are two cases for the integration over the unit cell:

Case 1: $m \neq m'$ and $n \neq n'$

Performing the integration over dx :

$$\int_{\frac{-dx}{2}}^{\frac{dx}{2}} e^{j(k_{xm'n'} - k_{xmn})x} dx = \int_{\frac{-dx}{2}}^{\frac{dx}{2}} e^{j\left[\left(k_{x0} + \frac{2\pi m'}{d_x}\right) - \left(k_{x0} + \frac{2\pi m}{d_x}\right)\right]x} dx = \int_{\frac{-dx}{2}}^{\frac{dx}{2}} e^{j\frac{2\pi}{d_x}(m' - m)x} dx = \frac{1}{j\frac{2\pi}{d_x}(m' - m)} \left[e^{j\frac{2\pi}{d_x}(m' - m)\frac{dx}{2}} - e^{-j\frac{2\pi}{d_x}(m' - m)\frac{dx}{2}} \right] = 0 \quad (2.5.6)$$

Similarly, $\int_{\frac{-dy}{2}}^{\frac{dy}{2}} e^{j(k_{ym'n'} - k_{ymn})y} dy = 0$.

Therefore, for $m \neq m'$ and $n \neq n'$:

$$\iint_{\text{unitcell}} e^{j(k_{xm'n'} - k_{xmn})x + j(k_{ym'n'} - k_{ymn})y} dx dy = 0 \quad (2.5.7)$$

Case 2: $m = m'$ and $n = n'$

Performing the integration over dx :

$$\int_{\frac{-dx}{2}}^{\frac{dx}{2}} e^{j(k_{xm'n'} - k_{xmn})x} dx = \int_{\frac{-dx}{2}}^{\frac{dx}{2}} e^{j\left[\left(k_{x0} + \frac{2\pi m'}{d_x}\right) - \left(k_{x0} + \frac{2\pi m}{d_x}\right)\right]x} dx = \int_{\frac{-dx}{2}}^{\frac{dx}{2}} e^{j\frac{2\pi}{d_x}(m' - m)x} dx = \int_{\frac{-dx}{2}}^{\frac{dx}{2}} (1) dx = d_x \quad (2.5.8)$$

Similarly, $\int_{\frac{-dy}{2}}^{\frac{dy}{2}} e^{j(k_{ym'n'} - k_{ymn})y} dy = d_y$.

Therefore, for $m = m'$ and $n = n'$:

$$\iint_{\text{unitcell}} e^{j(k_{xm'n'} - k_{xmn})x + j(k_{ym'n'} - k_{ymn})y} dx dy = d_x d_y \quad (2.5.9)$$

The expression for Z_s for $m = m'$ and $n = n'$ simplifies to:

$$\begin{aligned}
Z_s &= \frac{8\pi^4 J_0^2}{(d_x d_y)^2 \omega \varepsilon_0 I_0^2} \sum_{m=-\infty}^{m=+\infty} \sum_{n=-\infty}^{n=+\infty} \frac{k_0^2 - k_{xmn}^2}{k_{zmn}} |\tilde{f}(k_{xmn})|^2 |\tilde{g}(k_{ymn})|^2 (d_x d_y) \\
&= \frac{8\pi^4}{t^2 (d_x d_y) \omega \varepsilon_0} \sum_{m=-\infty}^{m=+\infty} \sum_{n=-\infty}^{n=+\infty} \frac{k_0^2 - k_{xmn}^2}{k_{zmn}} |\tilde{f}(k_{xmn})|^2 |\tilde{g}(k_{ymn})|^2, \text{ where } I_0 = J_0 t
\end{aligned} \tag{2.5.10}$$

We make the substitution: $D_x = d_x / \lambda_0$; $D_y = d_y / \lambda_0$

$$\begin{aligned}
Z_s &= \frac{8\pi^4}{t^2 (D_x D_y) \lambda_0^2 \omega \varepsilon_0} \sum_{m=-\infty}^{m=+\infty} \sum_{n=-\infty}^{n=+\infty} \frac{k_0^2 - k_{xmn}^2}{k_{zmn}} |\tilde{f}(k_{xmn})|^2 |\tilde{g}(k_{ymn})|^2 \\
&= \frac{2\pi^2 k_0^2}{t^2 (D_x D_y) \omega \varepsilon_0} \sum_{m=-\infty}^{m=+\infty} \sum_{n=-\infty}^{n=+\infty} \frac{k_0^2 - k_{xmn}^2}{k_{zmn}} |\tilde{f}(k_{xmn})|^2 |\tilde{g}(k_{ymn})|^2
\end{aligned} \tag{2.5.11}$$

Further simplifying Z_s and using $k_0^2 = \omega^2 \mu_0 \varepsilon_0$:

$$\begin{aligned}
Z_s &= \frac{2\pi^2 k_0^2 k_0^2}{t^2 (D_x D_y) \omega \varepsilon_0} \sum_{m=-\infty}^{m=+\infty} \sum_{n=-\infty}^{n=+\infty} \left(\frac{1 - \frac{k_{xmn}^2}{k_0^2}}{k_{zmn}} \right) |\tilde{f}(k_{xmn})|^2 |\tilde{g}(k_{ymn})|^2 \\
&= \frac{2\pi^2 k_0^2 k_0^2}{t^2 (D_x D_y) \omega \varepsilon_0 k_0^4} \sum_{m=-\infty}^{m=+\infty} \sum_{n=-\infty}^{n=+\infty} \left(\frac{1 - \frac{k_{xmn}^2}{k_0^2}}{k_{zmn}} \right) |k_0 \tilde{f}(k_{xmn})|^2 |k_0 \tilde{g}(k_{ymn})|^2 \\
&= \frac{2\pi^2}{t^2 (D_x D_y) \omega \varepsilon_0} \sum_{m=-\infty}^{m=+\infty} \sum_{n=-\infty}^{n=+\infty} \left(\frac{1 - \frac{k_{xmn}^2}{k_0^2}}{k_{zmn}} \right) |k_0 \tilde{f}(k_{xmn})|^2 |k_0 \tilde{g}(k_{ymn})|^2 \\
&= \frac{2\pi^2}{t^2 (D_x D_y) k_0} \sqrt{\frac{\mu_0}{\varepsilon_0}} \sum_{m=-\infty}^{m=+\infty} \sum_{n=-\infty}^{n=+\infty} \left(\frac{1 - \frac{k_{xmn}^2}{k_0^2}}{k_{zmn}} \right) |k_0 \tilde{f}(k_{xmn})|^2 |k_0 \tilde{g}(k_{ymn})|^2 \\
&= \frac{2\pi^2 \eta}{t^2 (D_x D_y) k_0^2} \sum_{m=-\infty}^{m=+\infty} \sum_{n=-\infty}^{n=+\infty} \left(\frac{1 - \frac{k_{xmn}^2}{k_0^2}}{\frac{k_{zmn}}{k_0}} \right) |k_0 \tilde{f}(k_{xmn})|^2 |k_0 \tilde{g}(k_{ymn})|^2
\end{aligned} \tag{2.5.12}$$

Thus, the final form for the scan impedance of the infinite array of strip dipole elements, Z_s , is given by:

$$Z_s = \frac{2\pi^2\eta}{t^2(D_x D_y)k_0^2} \sum_{m=-\infty}^{m=+\infty} \sum_{n=-\infty}^{n=+\infty} \frac{\left(1 - \frac{k_{xmn}^2}{k_0^2}\right)}{\frac{k_{zmn}}{k_0}} |k_0 \tilde{f}(k_{xmn})|^2 |k_0 \tilde{g}(k_{ymn})|^2 \quad (2.5.13)$$

Note that Z_s contains the complex spectral terms $\tilde{f}(k_{xmn})$ and $\tilde{g}(k_{ymn})$ which are due to the current distribution on the dipole; Z_s is also:

- Inversely proportional to the square of the dipole width; that is, the thinner the dipole, the higher the scan impedance;
- Inversely proportional to the normalized variables D_x and D_y ; that is, the larger the unit cell dimensions with respect to the free space wavelength λ_s the lower Z_s .

2.6 Scan Impedance of Printed Dipole Array: Effect of a Ground Plane

Section 2.6 derives the scan impedance that includes the effect of the ground plane.

For a perfect electric conductor a distance $z = -h$, the electric field for every Floquet mode is the incident field plus the reflected field^{2.1}:

$$E_x \rightarrow E_x + E_x[-e^{-jk_{zmn}2h}] \quad (2.6.1)$$

Using E_x from expression 2.3.6 in 2.6.1:

$$E_x(x, y, z) = -\frac{2\pi^2}{dxdy\omega\epsilon_0} J_0 \sum_{m=-\infty}^{m=+\infty} \sum_{n=-\infty}^{n=+\infty} \frac{k_0^2 - k_{xmn}^2}{k_{zmn}} \tilde{f}(k_{xmn}) \tilde{g}(k_{ymn}) e^{-jk_{xmn}x - jk_{ymn}y - jk_{zmn}z} (1 - e^{-jk_{zmn}2h}) \quad (2.6.2)$$

The derivation of the scan impedance Z_s follows Section 2.5 using the expression 2.6.2 for E_x ; the result is written:

$$Z_s = \frac{2\eta\pi^2}{t^2 D_x D_y k_0^2} \sum_{m=-\infty}^{m=+\infty} \sum_{n=-\infty}^{n=+\infty} \frac{1 - k_{xmn}^2 / k_0^2}{k_{zmn} / k_0} |k_0 \tilde{f}(k_{xmn})|^2 |k_0 \tilde{g}(k_{ymn})|^2 (1 - e^{-jk_{zmn}2h}) \quad (2.6.3)$$

There are 3 cases for Z_s based on the 3 electric current distributions:

Case A

$$\tilde{f}(k_{xmn})\tilde{g}(k_{ymn}) = \frac{l}{2\pi} \operatorname{sinc}\left(\frac{k_{xmn}l}{2}\right) \frac{t}{2\pi} \operatorname{sinc}\left(\frac{k_{ymn}t}{2}\right) = \frac{lt}{(2\pi)^2} \operatorname{sinc}\left(\frac{k_{xmn}l}{2}\right) \operatorname{sinc}\left(\frac{k_{ymn}t}{2}\right) \quad (2.6.4)$$

Define:

$$P(k_{xmn}, k_{ymn}) \equiv \frac{tlk_0^2}{4\pi^2} \operatorname{sinc}\left(\frac{k_{xmn}l}{2}\right) \operatorname{sinc}\left(\frac{k_{ymn}t}{2}\right) \quad (2.6.5)$$

Case B

$$\begin{aligned} \tilde{f}(k_{xmn})\tilde{g}(k_{ymn}) &= \frac{l^2k_0}{8\pi} \operatorname{sinc}\left(\frac{(k_x+k_0)l}{4}\right) \operatorname{sinc}\left(\frac{(k_x-k_0)l}{4}\right) \frac{t}{2\pi} \operatorname{sinc}\left(\frac{k_{ymn}t}{2}\right) \\ &= \frac{l^2k_0t}{16\pi^2} \operatorname{sinc}\left(\frac{(k_x+k_0)l}{4}\right) \operatorname{sinc}\left(\frac{(k_x-k_0)l}{4}\right) \operatorname{sinc}\left(\frac{k_{ymn}t}{2}\right) \end{aligned} \quad (2.6.6)$$

Define:

$$P(k_{xmn}, k_{ymn}) \equiv \frac{tl^2k_0^3}{16\pi^2} \operatorname{sinc}\left(\frac{(k_{xmn}+k_0)l}{4}\right) \operatorname{sinc}\left(\frac{(k_{xmn}-k_0)l}{4}\right) \operatorname{sinc}\left(\frac{k_{ymn}t}{2}\right) \quad (2.6.7)$$

Case C

$$\begin{aligned} \tilde{f}(k_{xmn})\tilde{g}(k_{ymn}) &= \frac{1}{\pi k_0} \operatorname{cosec}\left(\frac{k_{xmn}l}{2\pi}\right) \frac{t}{2\pi} \operatorname{sinc}\left(\frac{k_{ymn}t}{2}\right) \\ &= \frac{t}{2\pi^2 k_0} \operatorname{cosec}\left(\frac{k_{xmn}l}{2\pi}\right) \operatorname{sinc}\left(\frac{k_{ymn}t}{2}\right) \end{aligned} \quad (2.6.8)$$

Define:

$$P(k_{xmn}, k_{ymn}) \equiv \frac{tk_0}{2\pi^2} \operatorname{cosec}\left(\frac{k_{xmn}l}{2\pi}\right) \operatorname{sinc}\left(\frac{k_{ymn}t}{2}\right) \quad (2.6.9)$$

2.7 Scan Impedance of Printed Dipole Array: Comparison with Hansen's Formulas

We now consider the case for the resonant dipole (Case C)^{2.1} to compare the results with Hansen's formulas^{2.4}; we re-write the scan impedance Z_s that explicitly shows the contributions due to the fundamental propagating Floquet Mode and higher order cut-off Floquet Modes. We begin by deriving the expressions for H_{00} and H_{mn} :

Fundamental propagating Floquet Mode, $m = n = 0$:

$$H_{00} = \frac{1 - k_{x00}^2 / k_0^2}{k_{z00} / k_0} \quad (2.7.1)$$

To scan in the direction θ_0, φ_0 in spherical coordinates:

$$k_{x0} = k_0 \sin \theta_0 \cos \varphi_0, \quad k_{y0} = k_0 \sin \theta_0 \sin \varphi_0 \quad (2.7.2)$$

$$k_{zmn} = \begin{cases} +\sqrt{k_0^2 - k_{xmn}^2 - k_{ymn}^2} & \text{for } k_0^2 - k_{xmn}^2 - k_{ymn}^2 > 0 \\ -j\sqrt{k_{xmn}^2 + k_{ymn}^2 - k_0^2} & \text{for } k_0^2 - k_{xmn}^2 - k_{ymn}^2 < 0 \end{cases} \quad (2.7.3)$$

Now, k_{z00} is given by:

$$\begin{aligned} k_{zmn} &= \sqrt{k_0^2 - k_{x0}^2 - k_{y0}^2} \quad \text{for } k_0^2 - k_{xmn}^2 - k_{ymn}^2 > 0 \\ &= k_0 \sqrt{1 - \sin^2 \theta_0 \cos^2 \varphi_0 - \sin^2 \theta_0 \sin^2 \varphi_0} = k_0 \sqrt{1 - \sin^2 \theta_0} = k_0 \cos \theta_0 \end{aligned} \quad (2.7.4)$$

Thus,

$$H_{00} = \frac{1 - k_{x00}^2 / k_0^2}{k_{z00} / k_0} = \frac{1 - k_0^2 (\sin \theta_0 \cos \varphi_0)^2 / k_0^2}{k_0 \cos \theta_0 / k_0} = \frac{1 - \sin^2 \theta_0 \cos^2 \varphi_0}{\cos \theta_0} \quad (2.7.5)$$

For most practical phased arrays, there is only one propagating mode ($m = n = 0$); therefore for $m \neq 0, n \neq 0$, the Floquet Modes are cutoff (non-propagating):

$$H_{mn} = j \frac{1 - k_{xmn}^2 / k_0^2}{k_{zmn} / k_0} \quad (2.7.6)$$

where:

$$k_{xmn} = k_{x0} + \frac{2\pi m}{d_x}, \quad k_{ymn} = k_{y0} + \frac{2\pi n}{d_y} \quad (2.7.7)$$

We have previously defined the parameters D_x and D_y : $D_x = d_x / \lambda_0$; $D_y = d_y / \lambda_0$

The generalized wavenumbers are re-written:

$$k_{xmn} = k_0 \left(\sin \theta_0 \cos \varphi_0 + \frac{m}{D_x} \right), \quad k_{ymn} = k_0 \left(\sin \theta_0 \sin \varphi_0 + \frac{n}{D_y} \right) \quad (2.7.8)$$

For cut-off Floquet Modes, $k_0^2 - k_{xmn}^2 - k_{ymn}^2 < 0$:

$$k_{zmn} = -jk_0 \sqrt{\left(\sin \theta_0 \cos \varphi_0 + \frac{m}{D_x} \right)^2 + \left(\sin \theta_0 \sin \varphi_0 + \frac{n}{D_y} \right)^2 - 1} \quad (2.7.9)$$

$$\begin{aligned} H_{mn} &= j \frac{1 - k_0^2 \left(\sin \theta_0 \cos \varphi_0 + \frac{m}{D_x} \right)^2 / k_0^2 / k_0^2}{-jk_0 \sqrt{\left(\sin \theta_0 \cos \varphi_0 + \frac{m}{D_x} \right)^2 + \left(\sin \theta_0 \sin \varphi_0 + \frac{n}{D_y} \right)^2 - 1} / k_0} \\ &= \frac{\left(\sin \theta_0 \cos \varphi_0 + \frac{m}{D_x} \right)^2 - 1}{\sqrt{\left(\sin \theta_0 \cos \varphi_0 + \frac{m}{D_x} \right)^2 + \left(\sin \theta_0 \sin \varphi_0 + \frac{n}{D_y} \right)^2 - 1}} \end{aligned} \quad (2.7.10)$$

The complex scan impedance is expressed as: $Z_s = R_s + j X_s$.

The scan resistance, R_s , for Case C is given by the term $m = n = 0$:

$$R_s = \frac{\eta / \pi}{\pi D_x D_y} H_{00} \text{cosec}^2 \left(\frac{k_{x00} l}{2\pi} \right) \text{sinc}^2 \left(\frac{k_{y00} t}{2} \right) \sin^2 k_{z00} h \quad (2.7.11)$$

where we have used the result:

$$\begin{aligned} 1 + [-\exp(-jk_{zmn} 2h)] &= 1 - [\cos(k_{zmn} 2h) - j \sin(k_{zmn} 2h)] \\ &= 1 - [1 - 2 \sin^2(k_{zmn} h) - 2j \sin(k_{zmn} h) \cos(k_{zmn} 2h)] \\ &= 2 \sin^2(k_{zmn} h) + 2j \sin(k_{zmn} 2h) \cos(k_{zmn} 2h) \end{aligned} \quad (2.7.12)$$

The reactive part of the scan resistance, X_s , is given by:

$$X_s = \frac{0.5\eta / \pi}{\pi D_x D_y} \left[H_{00} \text{cosec}^2 \left(\frac{k_{x00} l}{2\pi} \right) \text{sinc}^2 \left(\frac{k_{y00} t}{2} \right) \sin(2k_{z00} h) - \sum_{N^2 \cap [m=0, n=0]} H_{mn} \text{cosec}^2 \left(\frac{k_{xmn} l}{2\pi} \right) \text{sinc}^2 \left(\frac{k_{ymn} t}{2} \right) \right] \quad (2.7.13)$$

where we have used $\sin(2k_{z00} h)$ in the expansion of $1 + [-e^{-jk_{zmn} 2h}]$. Note: the $m = n = 0$ term is explicitly taken out of the double infinite summation to emphasize the contribution of the fundamental propagating Floquet mode to the reactive part of the scan impedance.

The scan resistance and scan reactance given by Hansen^{2,4} are written:

$$R_s = \frac{480a_s^2}{\pi d_x d_y \lambda^2} \cos^2 c^2 \frac{k_{x0} a_s}{2} \sin^2 c^2 \frac{k_{y0} b_s}{2} \sin^2(k_{z0} h) H_{00} \quad (2.7.14)$$

$$X_s = \frac{240a_s^2}{\pi d_x d_y \lambda^2} \left[\cos^2 c^2 \frac{k_{x0} a_s}{2} \sin^2 c^2 \frac{k_{y0} b_s}{2} \sin^2(k_{z0} h) H_{00} \right] - \sum \sum \cos^2 c^2 \frac{k_{xm} a_s}{2} \sin^2 c^2 \frac{k_{ym} b_s}{2} \sin^2(k_{z0} h) H_{nm}$$

Equations 2.7.11 and 2.7.13 should be equivalent to Hansen's equations given in 2.7.14. Noting that $\eta \approx 120\pi$, we make the following corrections^{2.1}:

- A factor of π is missing in the denominator of the argument of the csc function. This circumstance does not affect the scan resistance in the H plane ($k_{x00} = 0$);
- A sine of the double argument should be used instead of the sine squared in the first term for the scan reactance.

With the above corrections made to equation 2.7.14, the scan impedances as a function of θ_0 are plotted in Figure 2-3^{2.1}; $D_x = D_y = 0.5$, $l = 0.5\lambda_0$ and $h = 0.25\lambda_0$:

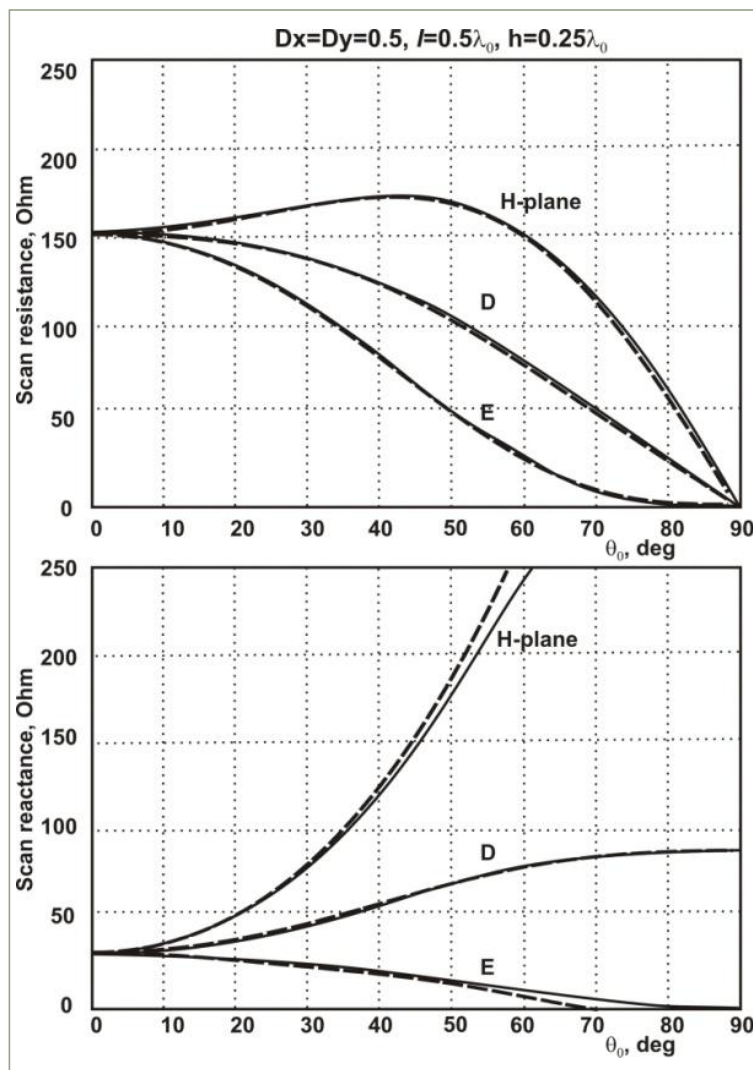


Figure 2-3. Scan resistance/reactance as a function of scan angle θ_0 ; solid curves: Hansen's plots^{2.6}; dashed curves: Reference 2.1

Figure 2-3 shows slight disagreement between the two sets of results for scan reactance for scan angles beyond 40 degrees in the H-Plane and beyond 50 degrees in the E-Plane. This discrepancy is probably due to the simplified treatment of the ground plane in equations 2.7.11 and 2.7.13.

The exponential term in equation 17^{2.1} is significant only for the fundamental $m = n = 0$ terms; equation 17 is re-written:

$$E_x \rightarrow E_x + E_x[-\exp(-jk_{zmn}2h)] \quad (2.7.15)$$

Hansen^{2.7} notes that for a ground plane spacing of $\lambda/4$, higher order unit-cell evanescent modes are significantly attenuated; for example, suppose $m = 0$ and $n = 1$:

$$\begin{aligned} k_{z01} &= -jk_0 \sqrt{(\sin \theta_0 \cos \varphi_0)^2 + \left(\sin \theta_0 \sin \varphi_0 + \frac{1}{D_y} \right)^2} - 1 \\ &= -jk_0 \sqrt{(\sin \theta_0 \cos \varphi_0)^2 + \left(\sin \theta_0 \sin \varphi_0 + \frac{\lambda_0}{d_y} \right)^2} - 1 \\ &= -jk_0 \sqrt{(\sin \theta_0 \cos \varphi_0)^2 + (\sin \theta_0 \sin \varphi_0 + 2)^2} - 1, \text{ for } D_y = \frac{d_y}{\lambda_0} \text{ and } d_y = \frac{\lambda_0}{2} \end{aligned} \quad (2.7.16)$$

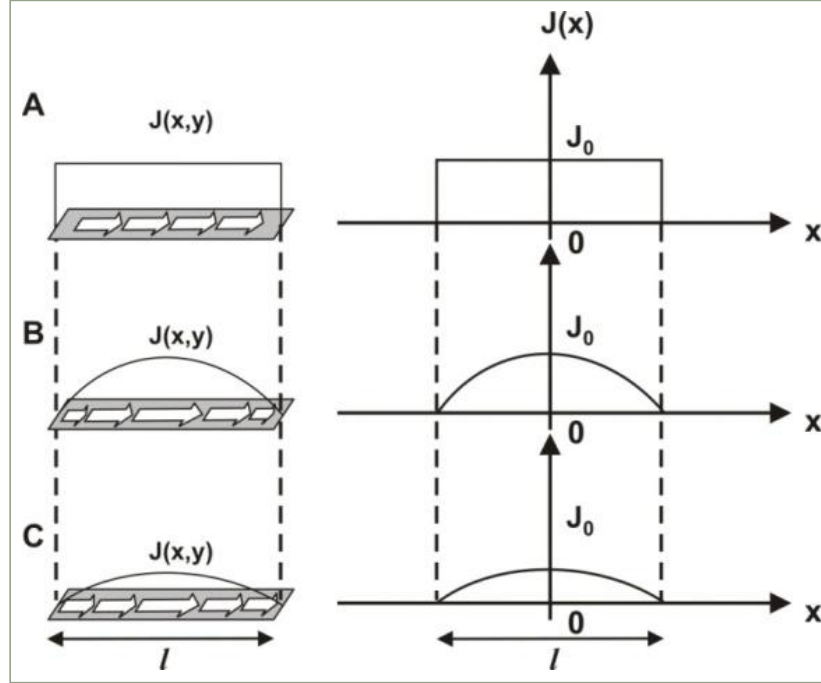
Upon substituting for k_{01} in the exponential expression and $h = \lambda_0/4$, we have:

$$\begin{aligned} |\exp(-jk_{zmn}2h)| &= |\exp(-jk_{z01}2h)| = |\exp(-j(-jk_0\sqrt{3})2h)| \leq \left| \exp(-j(-j\frac{2\pi}{\lambda_0}\sqrt{3})2\frac{\lambda_0}{4}) \right| \\ &|\exp(-jk_{zmn}2h)| \leq |\exp(-\pi\sqrt{3})| \approx 0.004 \end{aligned} \quad (2.7.17)$$

Summarizing: for $m = 0$ and $n = 1$, the magnitude of the electric field attenuates to just 0.4% of its original value in going from the dipole to the ground plane and back to the dipole; the same result would be obtained for $m = 1$ and $n = 0$. Higher order Floquet modes attenuate faster; thus, the reflections from higher order terms can be neglected.

2.8 On the Difference between HFSS and Analytical Formulation Results

The analytical formulation was based on a three assumed current distributions denoted by “Case A”, “Case B”, and “Case C” and re-written below²⁻¹:



$$\vec{J}(x, y) = \vec{x}J_0 f(x)g(y), \quad f(x) = \begin{cases} \Pi\left(\frac{x}{l}\right) & \text{case A} \\ \sin\left(k_0\left[\frac{l}{2} - |x|\right]\right) & \text{case B, } g(y) = \Pi\left(\frac{y}{t}\right) \\ \cos(k_0 x) & \text{case C} \end{cases}$$

Figure 2-4. The electric current distribution along the metal strip

Note: Case B current distribution is reduced to the resonant dipole (Case C) when $\lambda_0 = 2\pi / k_0 = l / 2$; that is:

$$\sin\left(k_0\left[\frac{l}{2} - |x|\right]\right) = \sin\left(k_0\left[\frac{\lambda_0/2}{2} - |x|\right]\right) = \sin\left(\left[\frac{\pi}{2} - k_0|x|\right]\right) = \cos(k_0 x) \quad (2.8.1)$$

upon applying the double angle trigonometric formula $\sin(A-B) = \sin(A)\cos(B) - \sin(B)\cos(A)$. In each case, the mathematical distributions were “single” mode expansions- this is the key in

explaining the differences between the analytical Floquet approach and the finite element numerical method used in HFSS. That is, on a real dipole the current distribution varies as the array is scanned; a single current mode cannot accurately model the varying current distribution as the array is scanned off boresite.

2.8.1 Comparison between the Analytical approach^{2.1} and HFSS

Figure 2-5 and Figure 2-6 are for the scan impedance (scan resistance and scan reactance) for two different dipole lengths, l , for a lattice spacing $Dx = Dy = 0.5$ (solid curves- analytical solution; dashed curves- HFSS)^{2.1}:

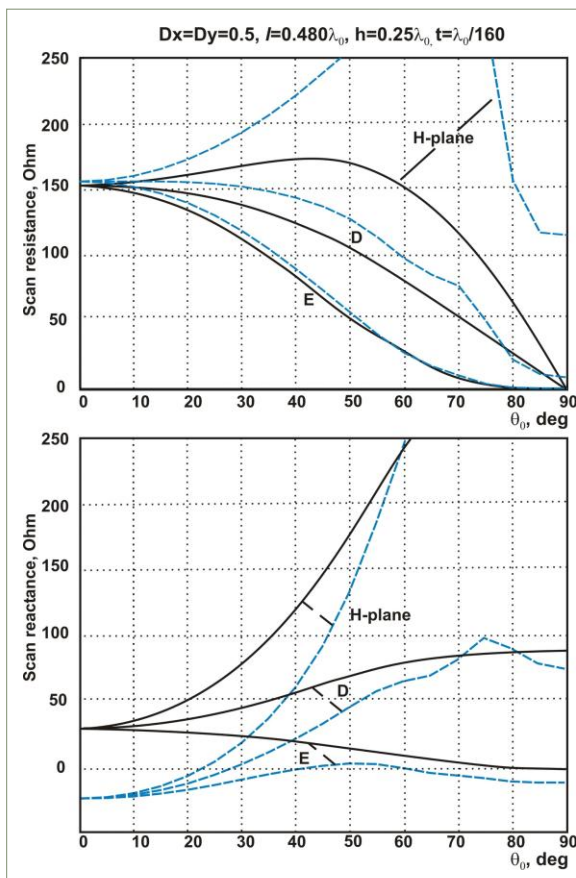


Figure 2-5. Scan impedance (scan resistance- top; scan reactance- bottom) 0.5λ array lattice; 0.480λ dipole length; $h=0.25\lambda$

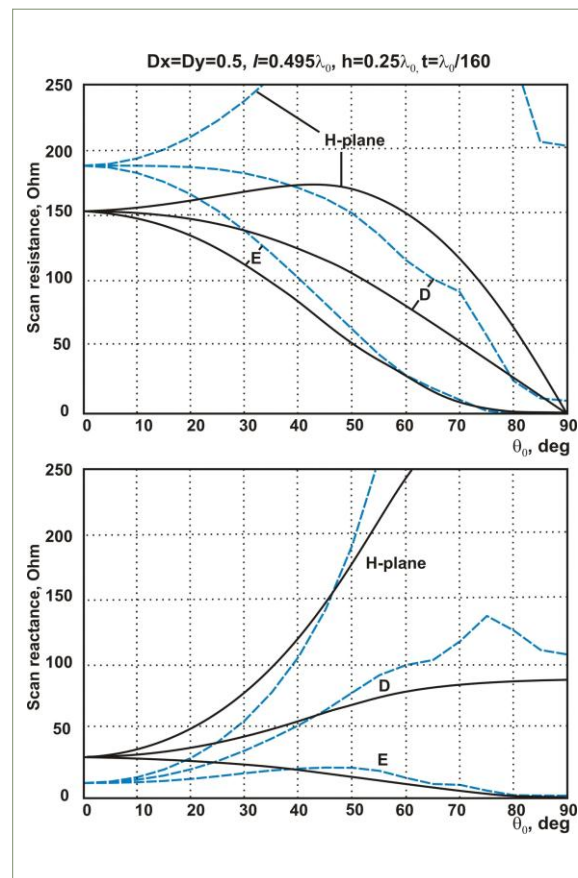


Figure 2-6. Scan impedance (scan resistance- top; scan reactance- bottom) 0.5λ array lattice; 0.495λ dipole length; $h=0.25\lambda$

Insight into the discrepancy between the HFSS results and the single mode Floquet series expansion for the scan reactance in Figure 2-5 and Figure 2-6 above is given in Figure 2-7^{2.6}; we note in Figure 2-7:

- Unit cell spacing: $0.5\lambda \times 0.5\lambda$;
- Height $h = 0.25\lambda$ above the ground plane;
- 65 by 149 element array;

Note the large discrepancy between a single mode “periodic structure” (Floquet expansion) and the “element-by-element sums” approach described by Hansen^{2,7}. For one mode, there is a large difference between the two methods for both the E and H plane scans. As the number of terms is increased in the “periodic structure” approach, agreement between both methods rapidly converges.

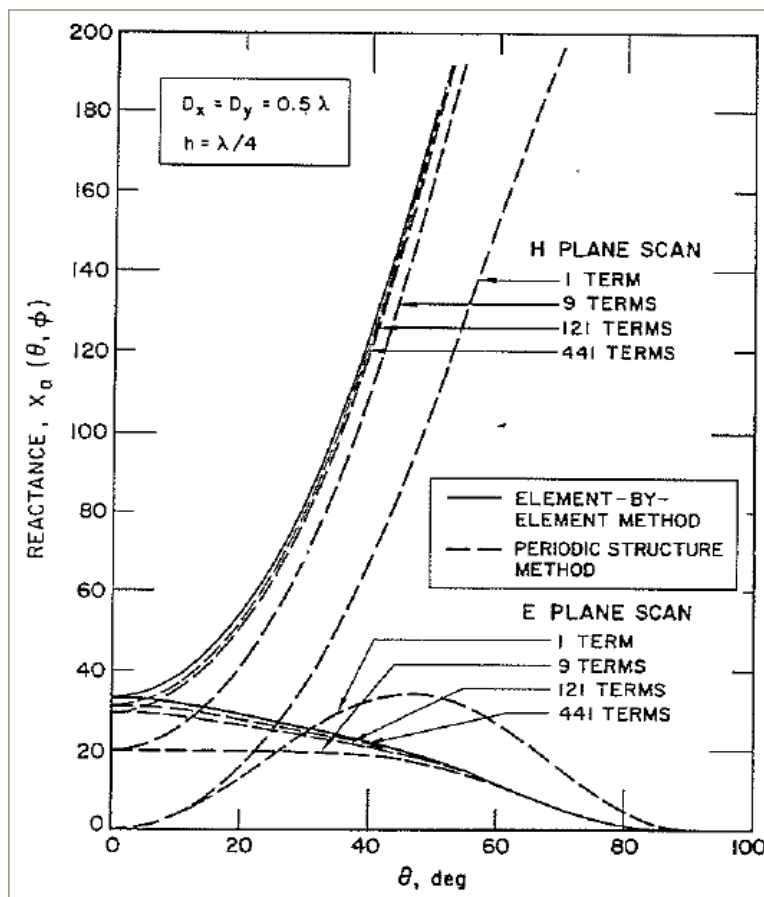


Figure 2-7. Figure 35 from *Microwave Scanning Antennas*, Ch. 3, pg. 286

Figure 2-8 and Figure 2-9 are for the scan impedance (scan resistance and scan reactance) for two different dipole lengths, l , for a lattice spacing $D_x = D_y = 0.7$ (solid curves- analytical solution; dashed curves- HFSS) ^{2.1}:

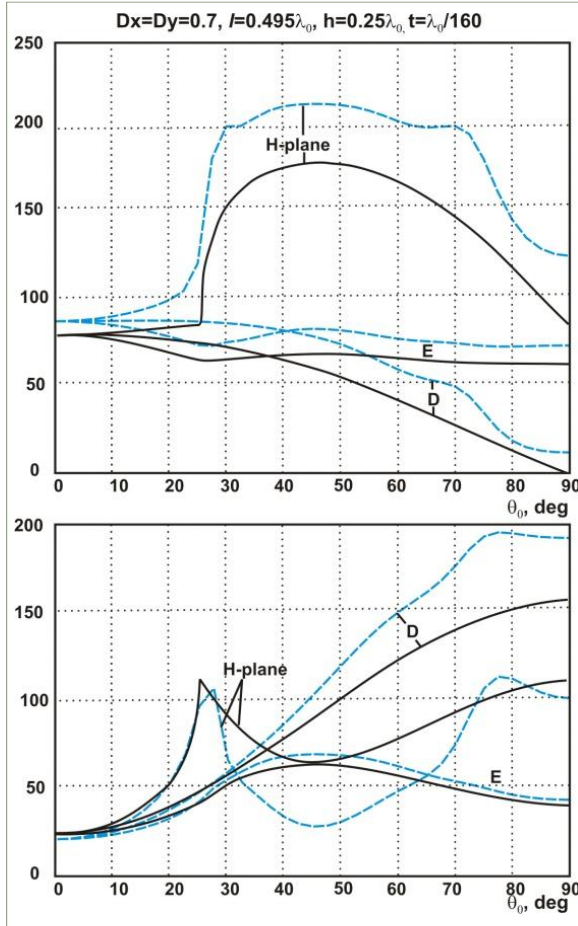


Figure 2-8. Scan impedance (scan resistance- top; scan reactance- bottom) 0.7λ array lattice; 0.495λ dipole length; $h=0.25\lambda$

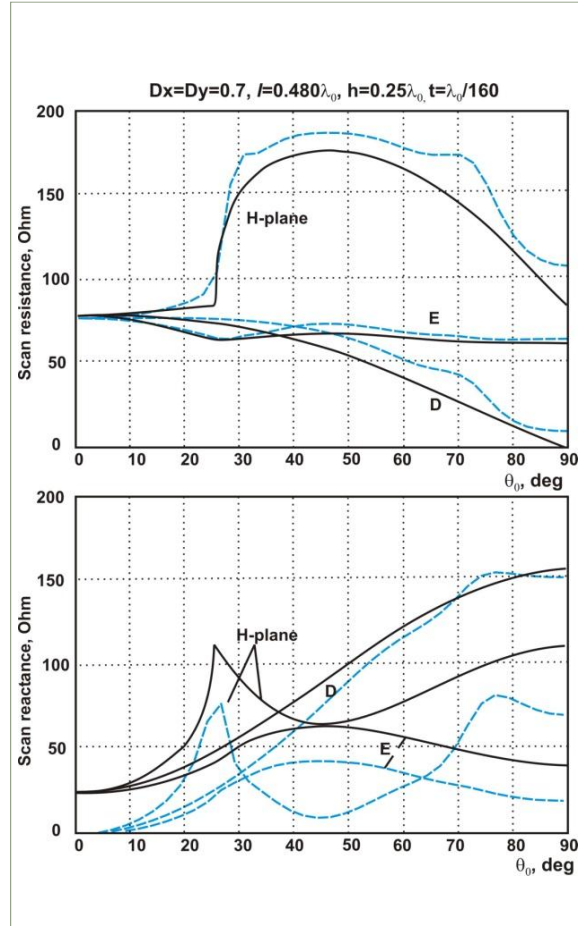


Figure 2-9. Scan impedance (scan resistance- top; scan reactance- bottom) 0.7λ array lattice; 0.480λ dipole length; $h=0.25\lambda$

Figure 2-8 and Figure 2-9 show a greater deviation between HFSS predicted results and single mode Floquet series expansion for the larger array lattice spacing $0.7\lambda \times 0.7\lambda$ and height 0.25λ above the ground plane. As the element spacing increases, the grating lobes move closer to real space; proximity of the array scan to the grating lobe accelerates the divergence between the scan impedance in the E and H planes. The reactive term in the scan impedance is more sensitive to the height above the ground plane as a function of scan angle:

- The height, h , of the dipole array above the ground plane enters the expression for the real part of the scan impedance in a multiplicative manner; the height enters the expression for the imaginary part of the scan impedance in an additive manner^{2.8}.

2.9 Multimodal Floquet Approach

The limitations of the sinusoidal current model discussed in Sections 2.3 through 2.9, and based on Reference 2.1, were the key motivation for the paper “Scan Impedance for An Infinite Dipole Array: Accurate Theoretical Model Versus Numerical Software”^{2.10}. In reference 2.10, the authors extend the analytical formulation for the scan impedance of an infinite dipole array using a fresh approach on extending the original theoretical model of VanKoughnett and Yen for the infinite, planar dipole array.

The paper by A. VanKoughnett and J. Yen from 1967^{2.11} develops a full-wave analytical model for a planar array of cylindrical dipoles has been developed based on Pocklington integral equation. The authors then replace the collinear dipole array in echelon by one infinitely long dipole with multiple periodic feeds; the gaps are treated as extra feeds with a priori unknown voltages. This approach enabled VanKoughnett and Yen to simplify the mathematics and use an analytical model for an infinitely long cylindrical dipole^{2.12-2.28} that distills the solution to coupled Pocklington equations to a simple Fourier series with the known coefficients.

Makarov and Iyer have two basic objectives in this paper^{2.29}:

- 1 Extend VanKoughnett and Yen’s full-wave analytical solution using delta-gap feeds and infinitesimally small dipole gaps, to the case of dipole feeds and gaps of finite width;
- 2 Compare the new, full-wave analytical solution with Ansoft HFSS v.11 and- CST Microwave Studio results for three scan planes.

Analytical Formulation

The authors extend the VanKoughnett and Yen model for cylindrical dipoles in order to avoid difficulties with field singularities and to compute more accurate scan impedance versus scan plan curves compared to numerical analysis tools.

Following VanKoughnett and Yen, the authors apply Pocklington's integral equation to an infinitely long dipole with multiple feeds; this reduced the coupled Pocklington's equation to a Fourier series with known coefficients^{2.29}.

The problem is broken up into a number of steps:

The integral equation approach is an established method in analyzing boundary value problems. The general expression for Pocklington's integral equation is given by^{2.30}:

$$-E^i(z) = \int I(z')K(z, z')dz' \quad (2.9.1)$$

In antenna radiation problems, the integral equation approach places the unknown current the current distribution, $I(z')$, within the integrand; the current on the antenna element is "convolved" with a kernel, $K(z, z')$, (or, "Greens Function").

In Section 1.2, the authors derive the exact solution to the Pocklington's integral equation^{2.31}:

$$E_x(x) = \frac{Z_0}{jk} \left(\frac{\partial^2}{\partial x^2} + k^2 \right) \int_{-\infty}^{+\infty} I(x')G(x-x')dx' \quad (2.9.2)$$

To find the current $I(x')$, we need to determine E_x in the antenna feed- this is the key to the formulation of the new analytical solution for the scan impedance that the authors will explore.

In Section 2.1 of reference 2.1.10, the first approximation is made: an infinite cylindrical dipole antenna. This then allows use of the 1-D spatial Fourier transform applied to expression 2.9.2:

$$\tilde{E}_x(k_x) = \frac{2\pi Z_0}{jk} (k^2 - k_x^2) \tilde{I}(k_x) \tilde{G}(k_x) \quad (2.9.3)$$

Solving for the antenna current distribution:

$$\tilde{I}(k_x) = \frac{jk \tilde{E}_x(k_x)}{2\pi Z_0 (k^2 - k_x^2) \tilde{G}(k_x)}, \quad I(x) = \int_{-\infty}^{+\infty} \tilde{I}(k_x) \exp(-jk_x x) dk_x \quad (2.9.4)$$

Next, in Section 2.2 the critical feed model is introduced; the authors examined three feed models for the gap, $2g$, shown in Figure 2-10^{2.32}:

1. infinitesimally short voltage gap:

$$a. \quad E_x(x) = -V_0 \delta(x), \quad \tilde{E}_x(k_x) = \frac{-V_0}{2\pi} \quad (2.9.5)$$

2. finite gap with the width of $2g$ and for the uniform field in the gap:

$$a. E_x(x) = -V_0 \Pi(x/2g), \quad \tilde{E}_x(k_x) = \frac{-V_0}{2\pi} \text{sinc}\left(\frac{k_x g}{\pi}\right) \quad (2.9.6)$$

3. non-uniform electric field in the gap of width $2g$ (the “square root” model):

$$a. E_x(x) = -\frac{V_0}{\pi} (g^2 - x^2)^{-1/2}, \quad \tilde{E}_x(k_x) = \frac{-V_0}{2\pi} J_0(k_x g) \quad (2.9.7)$$

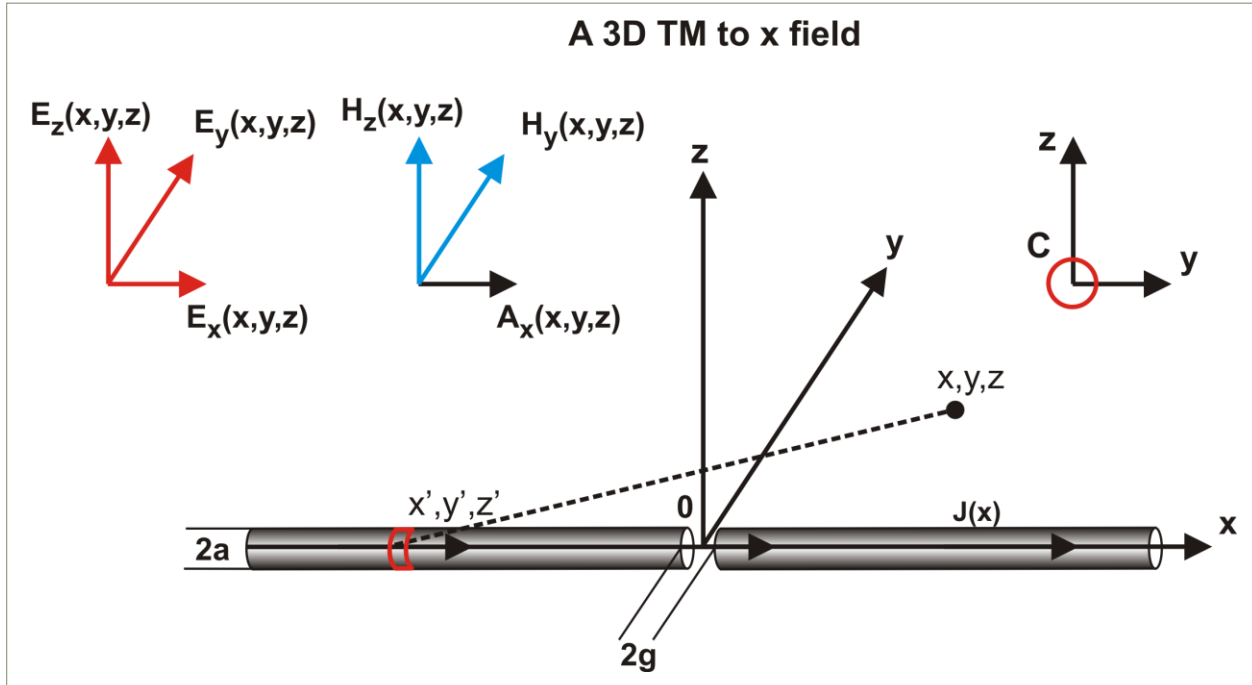


Figure 2-10. Single dipole configuration: an infinite dipole

Collinear and Planar Array

The key idea from VanKoughnett and Yen^{2.11} was to treat an infinite collinear 1D array as one infinitely long dipole with multiple feeds as shown in Figure 2-11^{2.33}:

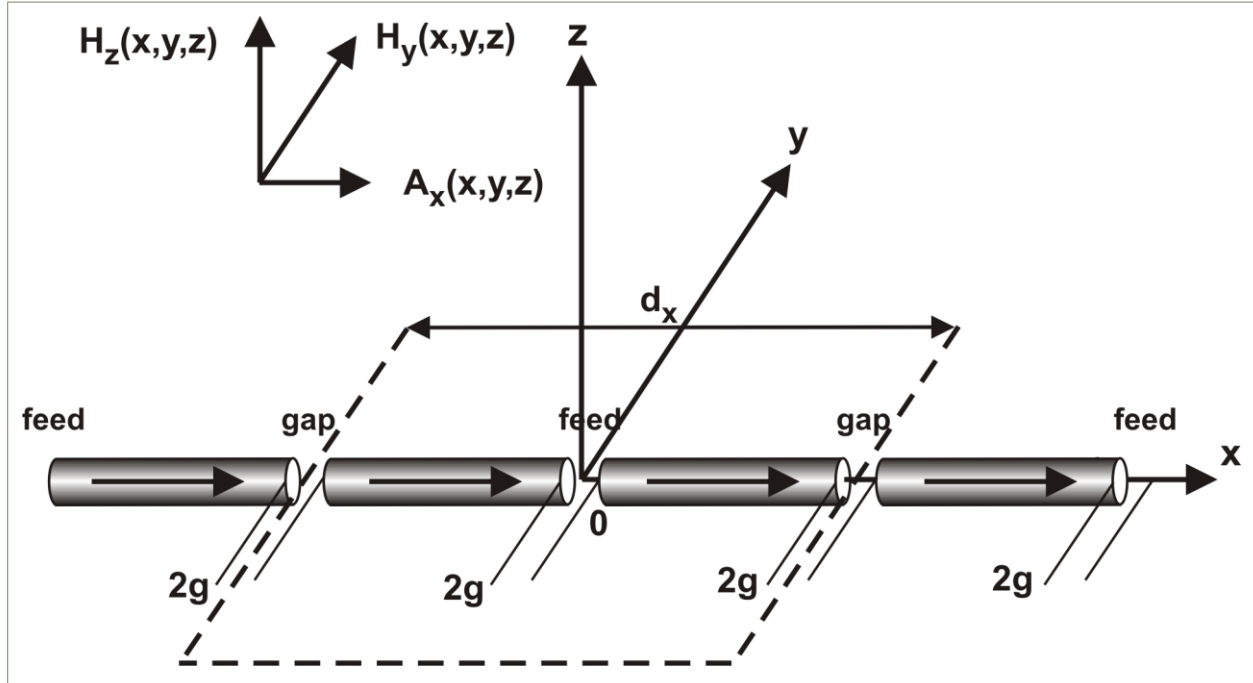


Figure 2-11. A collinear dipole array with feeding gaps equal to spacing gaps

Based on Figure 2-11, the authors write the feed voltage, gap voltage, and the current for the m -th array element:

$$V_m = V_0 \exp(-jk_{x0}d_x m), \quad m = 0, \pm 1, \pm 2, \dots \quad (2.9.8)$$

$$V'_m = V'_0 \exp(-jk_{x0}d_x (2m+1)/2), \quad m = 0, \pm 1, \pm 2, \dots \quad (2.9.9)$$

$$I_m = I(x - x_m) \exp(-jk_{x0}x), \quad m = 0, \pm 1, \pm 2, \dots \quad (2.9.10)$$

Note that $I(x)$ is a periodic function of x with period d_x ; equation 2.9.10 (14c in reference 2.1.10) is Floquet's theorem. The authors go on to formulate a total periodic current as a weighted sum of the currents in the gap and in the feed:

$$V_0 I(x) = V_0 I_S(x) + V'_0 I_S(x - d_x/2) \quad (2.9.11)$$

The next step is to excite the collinear array; the authors stress that the next critical part of the model concern the feed and gap excitation: "Two assumptions are made: one of a constant current

in the feed (gap), and another - of the same (to within a constant) field distribution within the feed and the gap, respectively.”^{2,34}

Excitation of the Collinear Array

We have the excitation field for an infinitely thin gap:

$$E_x(z) = -V_0 \sum_{m=-\infty}^{m=+\infty} \exp(-jk_{x0}d_x m) \delta(x - md_x), \quad \tilde{E}_x(k_x) = \frac{-V_0}{2\pi} \sum_{m=-\infty}^{m=+\infty} \exp(-j(k_{x0} - k_x)d_x m) \quad (2.9.12)$$

or, for a gap with a constant field:

$$\tilde{E}_x(k_x) = \frac{-V_0}{2\pi} \operatorname{sinc}\left(\frac{k_x g}{\pi}\right) \sum_{m=-\infty}^{m=+\infty} \exp(-j(k_{x0} - k_x)d_x m) \quad (2.9.13)$$

As the authors point out, the Fourier transformed electric field in gap has the form:

$$\tilde{E}_x(k_x) = \frac{-V_0}{2\pi} F(k_x) \sum_{m=-\infty}^{m=+\infty} \exp(-j(k_{x0} - k_x)d_x m) \quad (2.9.14)$$

where the feed function F is given by:

$$F(k_x) = 1, \quad \operatorname{sinc}\left(\frac{k_x g}{\pi}\right), \quad J_0(k_x g) \quad (2.9.15)$$

Each term for $F(k_x)$ represents one of the feed models given by expressions 2.9.5, 2.9.6 and 2.9.7 on page 71 above. Finally, the infinite sum of exponentials is replaced by the infinite sum of delta functions:

$$\tilde{E}_x(k_x) = \frac{-V_0}{d_x} F(k_x) \sum_{m=-\infty}^{m=+\infty} \delta\left(k_x - k_{x0} - \frac{2m\pi}{d_x}\right) \quad (2.9.16)$$

The authors go on to solve for the periodic component of the short-circuit array current, I_s , in equation 20d of the paper^{2,35}. We now examine two important sets of plots given in the paper:

1. Collinear Array of half wave dipoles- no ground plane;
2. Collinear Array of half wave dipoles- with ground plane

Collinear Array of Half Wave Dipoles – No Ground Plane

The behavior of the total current for the real and quadrature (imaginary) current due to the solution of equations 14c, 15b, 16 and 20d^{2.36} is shown in Figure 2-12:

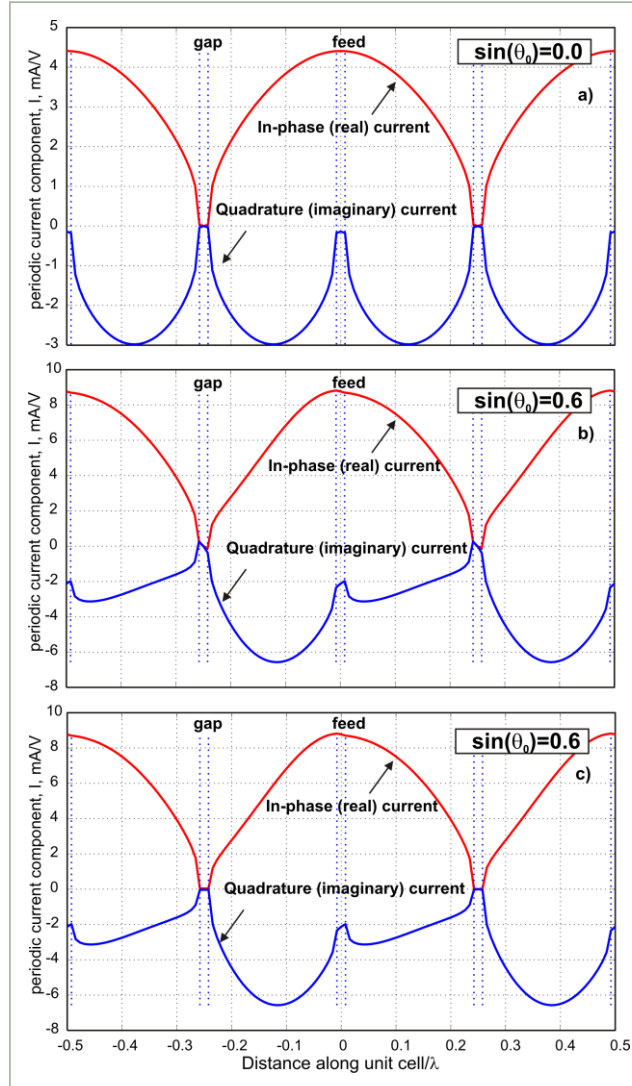


Figure 2-12. Distribution of the periodic current component, $I(x)$, for the half-lambda collinear array in echelon (no ground plane) at two different scan angles from zenith - 0 deg and 37 deg, respectively. Array parameters: $d_x = \lambda/2$, $ka = 0.08$, $g/a = 0.61$. a) – scan angle 0 deg, exact solution; b) – scan angle 37 deg, exact solution; c) – scan angle 37 deg, averaged gap current is used through the gap.

Collinear Array of Half Wave Dipoles – With Ground Plane

Interesting results are obtained by modifying equation 20d for a planar dipole array with ground plane shown in Figure 2-13:

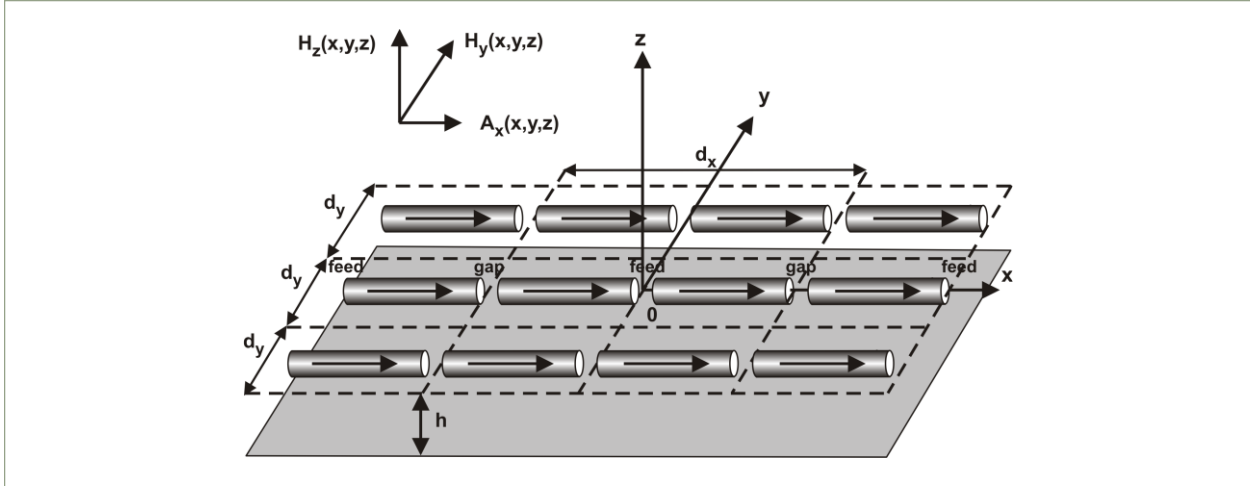


Figure 2-13. A planar dipole array with feeding gaps equal to spacing gaps

As shown in Figure 2-13, the authors model the planar array above a ground plane; this situation is similar to the strip-dipole array shown in Figure 2-2. The authors make two key limitations on the sinusoidal current model^{2,37}:

1. "...the current distribution is not really sinusoidal at any scan angle from zenith, and it is in addition asymmetric for nonzero scan angles from zenith";
2. "...the phase of the complex current is not constant through the dipole length; it changes with the position along the dipole and with the scan angle."

Next, the plots of the theory versus HFSS and CST in the E-, D- and H-planes are shown for three different planar dipole arrays with ground plane cases; the square-root feed model was used for the gap feed;

$$\tilde{E}_x(k_x) = \frac{-V_0}{d_x} J_0(k_x g) \sum_{m=-\infty}^{m=+\infty} \delta\left(k_x - k_{x0} - \frac{2m\pi}{d_x}\right) \quad (2.9.17)$$

Comparisons were between the analytical based scan impedance model and numerical solvers in the E-, D- and H-planes for 4 different dipole geometries:

- $ka = 0.04, 0.08$ and $g/a = 0.5, 1.0$

The scan impedance plots are shown on the next three pages for the E-, D- and H-Plane scans. The agreement between the analytical scan impedance model and HFSS and CST calculations for the E- and D-planes agreed very well. For the H-plane, the agreement was very good for scan angles up to 60 degrees.

The plots of the theory versus HFSS and CST in the E-, D- and H-planes are shown for three different dipole array cases^{2,38}:

1. $ka = 0.04, g/a = 0$;
2. $ka = 0.04, g/a = 1.0$;
3. $ka = 0.08, g/a = 1.0$

E-Plane

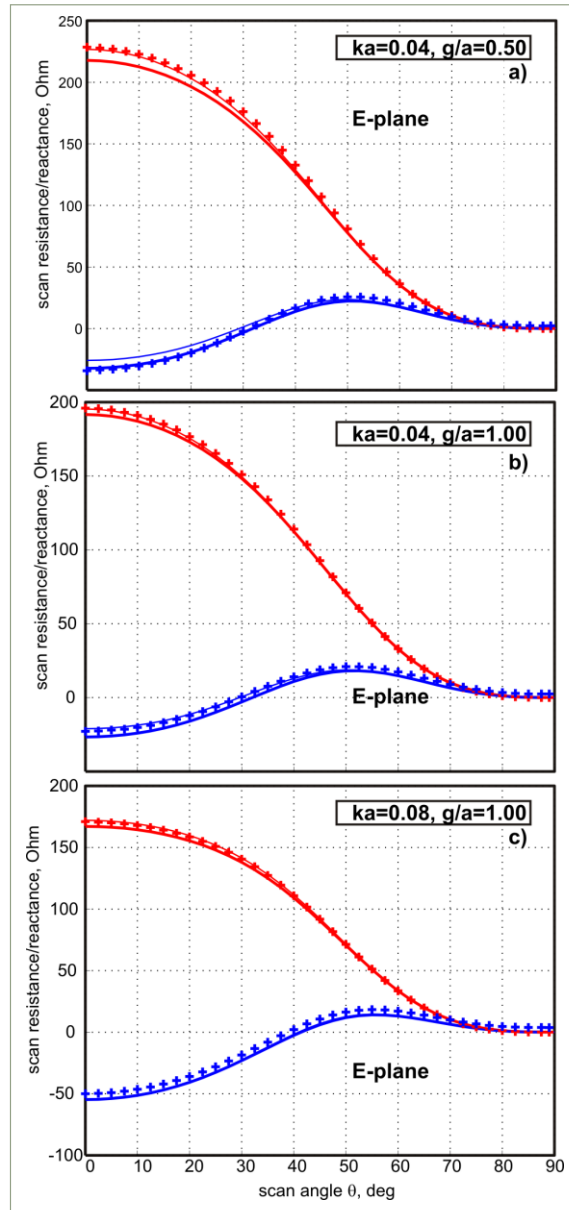


**Figure 2-14. Scan impedance in the E-plane. Scan resistance is marked red; reactance – blue
Thick curves - theory model; crosses - the Ansoft HFSS v.11 solution; thin curves - the CST
solution**

D-Plane

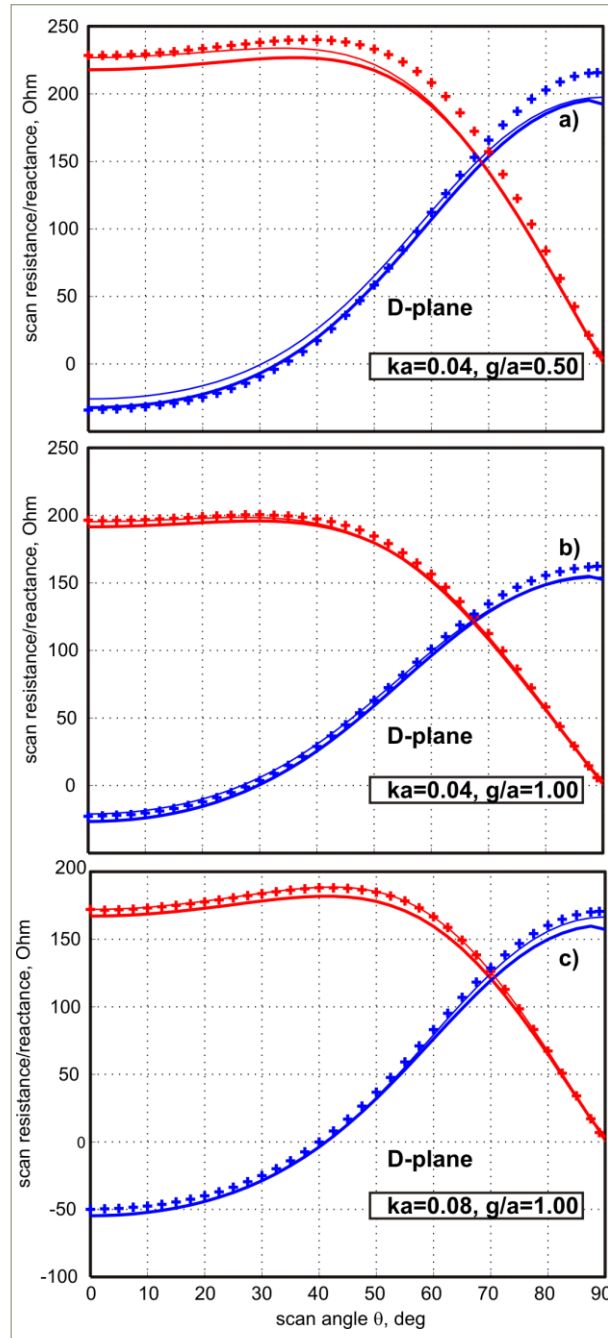


Figure 2-15. Scan impedance in the D-plane. Scan resistance is marked red; reactance – blue. Thick curves - theory model; crosses - the Ansoft HFSS v.11 solution; thin curves - the CST solution.

H-Plane

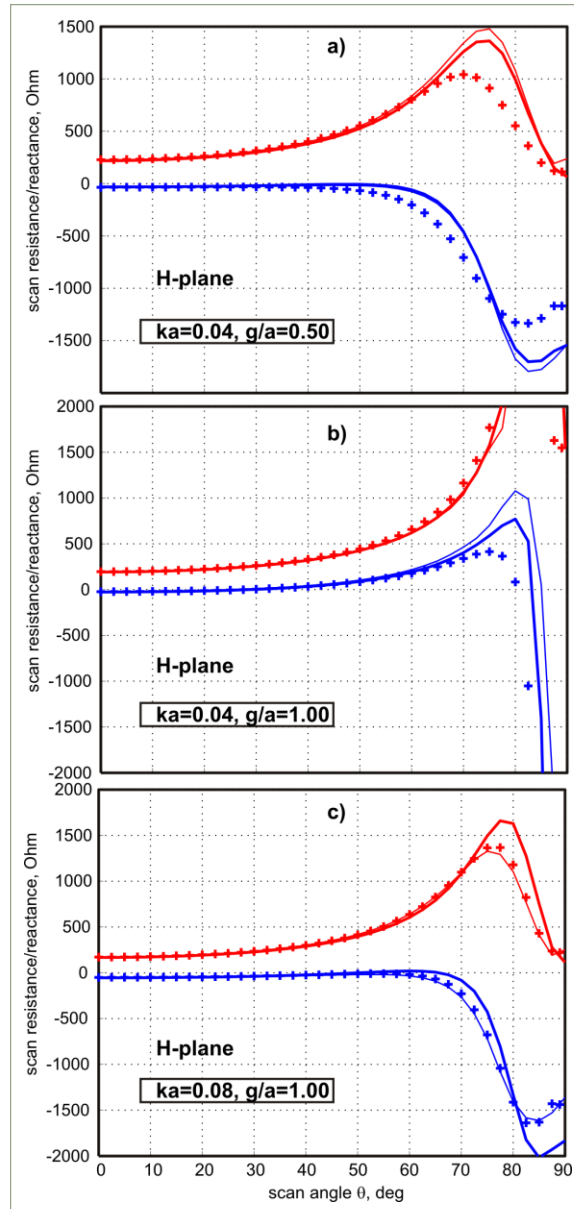


Figure 2-16. Scan impedance in the H-plane. Scan resistance is marked red; reactance – blue. Thick curves - theory model; crosses - the Ansoft HFSS v.11 solution; thin curves - the CST solution

The authors also make an interesting observation on the accuracy of the analytical model versus the numerical model for electrically thick antennas: possible angular asymmetry of the antenna current on thick antennas, which is not covered by Pocklington equation. Figure 2-17 presents an example of an HFSS model of the surface current distribution of a dipole with $ka=0.08$ and $g/a=0.5$, for a D-plane scan of 75 degrees. Figure 2-17 shows that in addition to the longitudinal

asymmetry of current distribution, there is clearly an angular asymmetry in the current distribution- this is not accounted for in the analytical model.

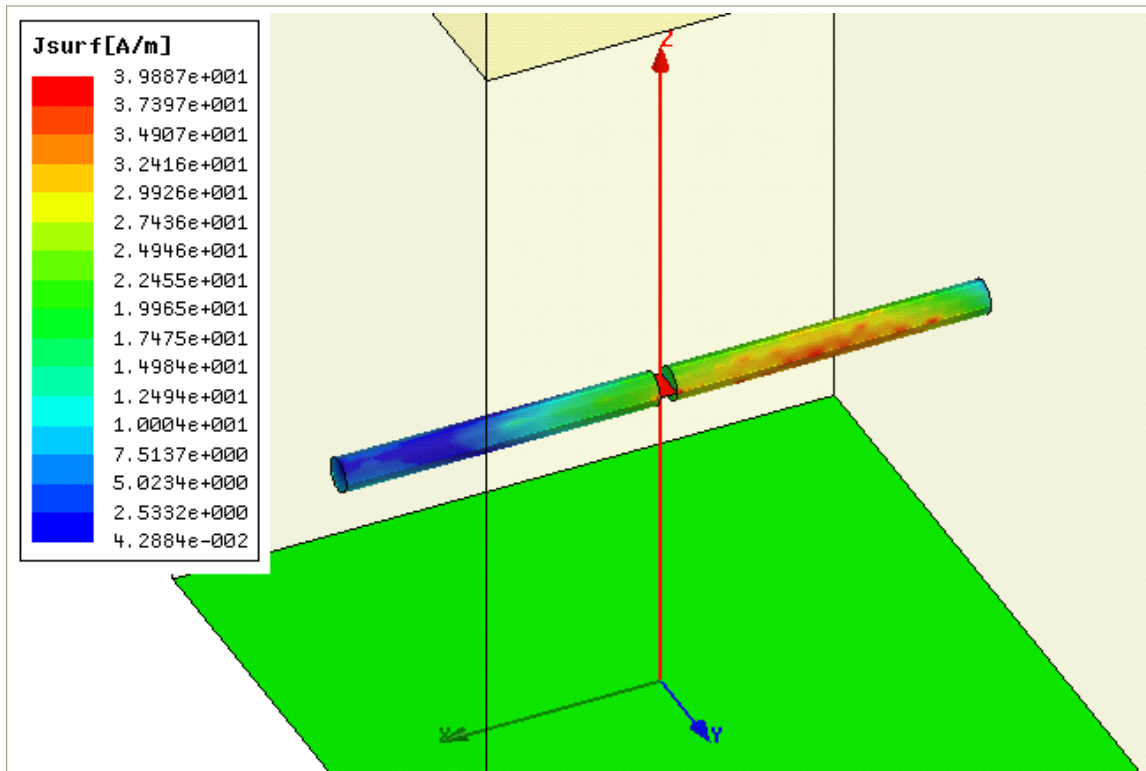


Figure 2-17. Surface current distribution in the D-plane at 75 degree scan angle for the dipole with $ka=0.08$, $g/a=0.5$ - Ansoft HFSS v. 11. Note longitudinal asymmetry of current distribution and angular asymmetry in the current distribution a) E-plane; b) D-plane ($\phi=45$ deg); c) H-plane

Summary

The authors, Makarov and Iyer have made a significant contribution towards obtaining excellent agreement between the extended analytical model for the infinite planar array of dipole antennas and the commercial antenna software packages: Ansoft HFSS v. 11 and CST Microwave Studio 2008.

The authors have extended the analytical model of VanKoughnett and Yen for the infinite planar array of dipole antennas by incorporating a finite feeding gap and a non-uniform field distribution in the gap; this approach has produced a more realistic scan impedance result in the E-, D- and H-planes that had excellent agreement with Ansoft HFSS v. 11 and CST Microwave Studio 2008. Finally, the authors note the angular asymmetry in the dipole current distribution that is not accounted for in the analytical model.

2.10 A Simplified Model for Multimode Solution Expansion

Following the Moment Method approach where the current distribution is modeled as a summation of sinusoidal current “modes”, the analytical Floquet approach developed in Sections 2.2 through 2.7 can be extended by adding higher order sinusoidal functions and using the spectral representation of the higher order sinusoidal functions in the representation of the current distribution $\vec{J}(x, y)$. This approach would be similar to the Periodic Moment Method (PMM) approach developed at Ohio State. PMM also uses a Floquet mode expansion approach for the electric or magnetic currents to generate the fields due to a doubly infinite array or dipoles or slots, respectively.

For example, the well-known “piecewise sinusoidal Galerkin Method” used in the Method of Moments formulation could be used in the Floquet approach. The idea is to simply partition the dipole strip into segments; the overlapping current segments approximate the total current on the dipole. The “shape” of the current distribution changes with array scan angle. Thus, the single mode current distribution for Cases A, B and C becomes less effective at representing the current distribution on the strip dipole versus scan angle. Figure 2-18 shows a strip dipole with 4 segments with modal current (in blue) and total current (yellow dotted line).

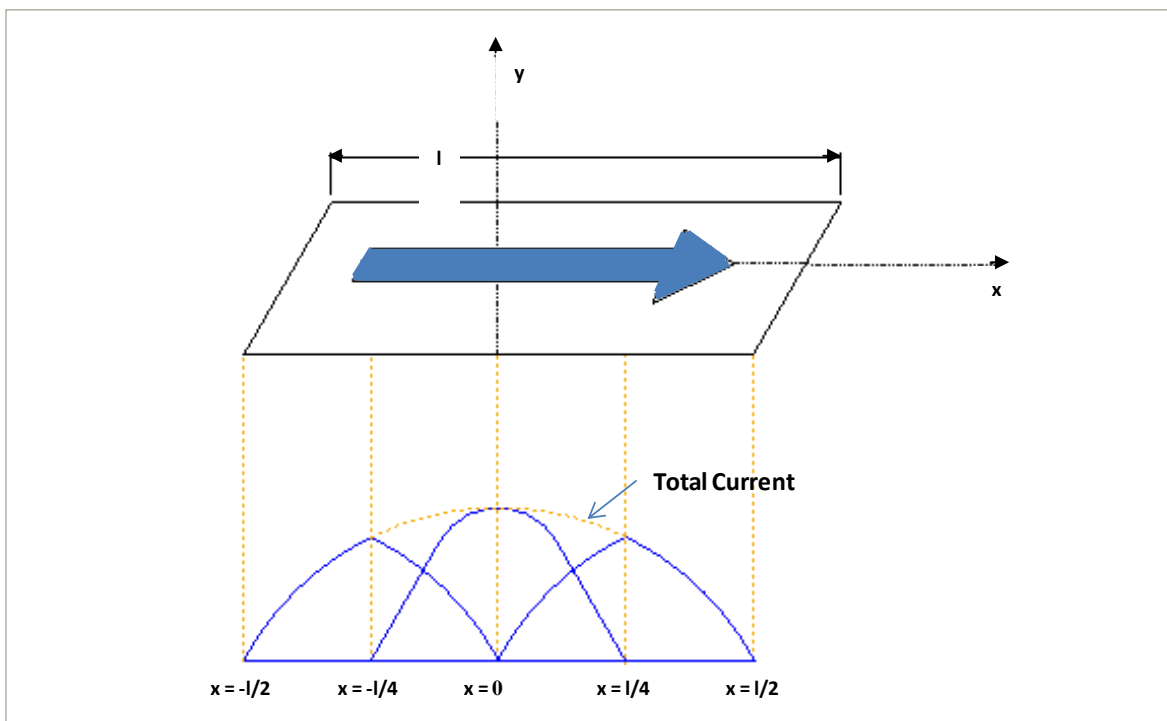


Figure 2-18. Strip dipole current approximated by sinusoidal current over each section

Applying “piecewise sinusoidal” method^{2,9}, the sinusoidal expansions for each segment in Figure 2-17 above is defined:

Case 1: Strip – Dipole Segment, $-l/2 \leq x \leq -l/4$.

$$f_1(x) = \frac{\sin[k_0(l/2 - |x|)]}{\sin(k_0l/4)} \quad (2.10.1)$$

Case 2: Strip – Dipole Segment, $-l/4 \leq x \leq 0$.

$$f_2(x) = \frac{\sin[k_0(l/4 - |x|)]}{\sin(k_0l/4)} + \frac{\sin[k_0|x|]}{\sin(k_0l/4)} \quad (2.10.2)$$

Case 3: Strip – Dipole Segment, $0 \leq x \leq l/4$.

$$f_3(x) = \frac{\sin[k_0(l/4 - x)]}{\sin(k_0l/4)} + \frac{\sin[k_0x]}{\sin(k_0l/4)} \quad (2.10.3)$$

Case 4: Strip – Dipole Segment, $l/4 \leq x \leq l/2$.

$$f_4(x) = \frac{\sin[k_0(l/2 - x)]}{\sin(k_0l/4)} \quad (2.10.4)$$

The current along the y-axis is not changed:

$$g(y) = \Pi\left(\frac{y}{t}\right) \quad (2.10.5)$$

Next, we calculate the spatial Fourier Transform of Cases 1 through 4.

Given the symmetry of the current expansions on the strip dipole, we start with Case 4 and then use a change of variable to derive the results for Case 1.

Spatial Fourier Transform: Case 4.

$$\tilde{f}_4(k_x) = \frac{1}{2\pi} \int_{l/4}^{l/2} f_4(x) \exp(jk_x x) dx$$

$$\tilde{f}_4(k_x) = \frac{1}{2\pi} \int_{l/4}^{l/2} \frac{\sin[k_0(l/2 - x)]}{\sin(k_0 l/4)} \exp(jk_x x) dx \quad (2.10.6)$$

Define:

$$\begin{aligned} I_4 &= \int_{l/4}^{l/2} \sin[k_0(l/2 - x)] \exp(jk_x x) dx \\ &= \frac{1}{2j} \left\{ \int_{l/4}^{l/2} \exp(jk_0 l/2) \exp[j(k_x - k_0)x] dx - \int_{l/4}^{l/2} \exp(-jk_0 l/2) \exp[j(k_x + k_0)x] dx \right\} \end{aligned} \quad (2.10.7)$$

using the trigonometric identity: $\sin(\theta) = [\exp(j\theta) - \exp(-j\theta)]/2j$.

$$\begin{aligned} I_4 &= \frac{-1}{2} \left\{ \frac{e^{jk_0 \frac{l}{2}} e^{j(k_x - k_0)x}}{(k_x - k_0)} \Big|_{l/4}^{l/2} - \frac{e^{-jk_0 \frac{l}{2}} e^{j(k_x + k_0)x}}{(k_x + k_0)} \Big|_{l/4}^{l/2} \right\} \\ &= \frac{-1}{2} \left\{ \frac{e^{jk_0 \frac{l}{2}} (e^{j(k_x - k_0) \frac{l}{2}} - e^{j(k_x - k_0) \frac{l}{4}})}{(k_x - k_0)} - \frac{e^{-jk_0 \frac{l}{2}} (e^{j(k_x + k_0) \frac{l}{2}} - e^{j(k_x + k_0) \frac{l}{4}})}{(k_x + k_0)} \right\} \\ &= \frac{-1}{2} \left\{ \frac{e^{jk_0 \frac{l}{2}} e^{j(k_x - k_0) \frac{l}{4}} (e^{j(k_x - k_0) \frac{l}{4}} - 1)}{(k_x - k_0)} - \frac{e^{-jk_0 \frac{l}{2}} e^{j(k_x + k_0) \frac{l}{4}} (e^{j(k_x + k_0) \frac{l}{4}} - 1)}{(k_x + k_0)} \right\} \end{aligned} \quad (2.10.8)$$

Thus,

$$I_4 = \frac{-1}{2} \left\{ \frac{e^{j(k_x + k_0) \frac{l}{4}} (e^{j(k_x - k_0) \frac{l}{4}} - 1)}{(k_x - k_0)} - \frac{e^{j(k_x - k_0) \frac{l}{4}} (e^{j(k_x + k_0) \frac{l}{4}} - 1)}{(k_x + k_0)} \right\}$$

Final result:

$$\tilde{f}_4(k_x) = \frac{I_4}{2\pi \sin(k_0 l/4)} \quad (2.10.9)$$

Spatial Fourier Transform: Case 1.

$$\tilde{f}_1(k_x) = \frac{1}{2\pi} \int_{-l/2}^{-l/4} f_1(x) \exp(jk_x x) dx \quad (2.10.10)$$

From the symmetry of the current expansion on the strip dipole: $f_1(x) = f_4(-x)$.

$$\tilde{f}_1(k_x) = \frac{1}{2\pi} \int_{-l/2}^{-l/4} f_4(-x) \exp(jk_x x) dx = \frac{-1}{2\pi} \int_{l/4}^{l/2} f_4(x) \exp(-jk_x x) dx \quad (2.10.11)$$

upon substituting $-x$ for x . We have:

$$\tilde{f}_1(k_x) = -\tilde{f}_4(-k_x) \quad (2.10.12)$$

We now use the results from Case 4; substituting $-k_x$ for k_x in the expression for I :

$$I_1 = \frac{-1}{2} \left\{ \frac{e^{j(k_0 - k_x)l/4} (1 - e^{-j(k_x + k_0)l/4})}{(k_x + k_0)} - \frac{e^{-j(k_x + k_0)l/4} (1 - e^{-j(k_x - k_0)l/4})}{(k_x - k_0)} \right\} \quad (2.10.13)$$

Final result:

$$\tilde{f}_1(k_x) = \frac{I_1}{2\pi \sin(k_0 l / 4)} \quad (2.10.14)$$

Spatial Fourier Transform: Case 2.

$$\tilde{f}_2(k_x) = \frac{1}{2\pi} \int_{-l/4}^0 f_2(x) \exp(jk_x x) dx \quad (2.10.15)$$

$$\tilde{f}_2(k_x) = \frac{1}{2\pi} \int_{-l/4}^0 \left\{ \frac{\sin[k_0(l/4 - |x|)]}{\sin(k_0 l / 4)} + \frac{\sin[k_0|x|]}{\sin(k_0 l / 4)} \right\} \exp(jk_x x) dx \quad (2.10.16)$$

Define:

$$I_{21} = \int_{-l/4}^0 \sin[k_0(l/4 - |x|)] \exp(jk_x x) dx \quad (2.10.17)$$

$$I_{22} = \int_{-l/4}^0 \sin[k_0|x|] \exp(jk_x x) dx \quad (2.10.18)$$

Evaluating I_{21} :

$$I_{21} = \int_{-l/4}^0 \sin[k_0(l/4 - |x|)] \exp(jk_x x) dx = \frac{1}{2j} \left\{ \int_{-l/4}^0 e^{jk_0(\frac{l}{4}+x)} e^{jk_x x} dx - \int_{-l/4}^0 e^{-jk_0(\frac{l}{4}+x)} e^{jk_x x} dx \right\} \quad (2.10.19)$$

again using the trigonometric identity: $\sin(\theta) = [\exp(j\theta) - \exp(-j\theta)]/2j$.

$$I_{21} = \frac{1}{2j} \left\{ \frac{e^{jk_0 \frac{l}{4}} e^{j(k_x+k_0)x}}{j(k_x+k_0)} \Big|_{-l/4}^0 - \frac{e^{-jk_0 \frac{l}{4}} e^{j(k_x-k_0)x}}{j(k_x-k_0)} \Big|_{-l/4}^0 \right\} \quad (2.10.20)$$

$$I_{21} = \frac{-1}{2} \left\{ \frac{e^{jk_0 \frac{l}{4}} (1 - e^{-j(k_x+k_0)\frac{l}{4}})}{(k_x+k_0)} - \frac{e^{-jk_0 \frac{l}{4}} (1 - e^{-j(k_x-k_0)\frac{l}{4}})}{(k_x-k_0)} \right\}$$

Evaluating I_{22} :

$$I_{22} = \int_{-l/4}^0 \sin[k_0|x|] \exp(jk_x x) dx = \frac{1}{2j} \left\{ \int_{-l/4}^0 e^{j(k_x+k_0)x} dx - \int_{-l/4}^0 e^{j(k_x-k_0)x} dx \right\}$$

$$= \frac{1}{2j} \left\{ \frac{e^{j(k_x+k_0)x}}{j(k_x+k_0)} \Big|_{-l/4}^0 - \frac{e^{j(k_x-k_0)x}}{j(k_x-k_0)} \Big|_{-l/4}^0 \right\} \quad (2.10.21)$$

$$I_{22} = \frac{-1}{2} \left\{ \frac{(1 - e^{-j(k_x+k_0)\frac{l}{4}})}{(k_x+k_0)} - \frac{(1 - e^{-j(k_x-k_0)\frac{l}{4}})}{(k_x-k_0)} \right\}$$

Final result:

$$\tilde{f}_2(k_x) = \frac{I_{21} - I_{22}}{2\pi \sin(k_0 l / 4)} \quad (2.10.22)$$

Spatial Fourier Transform:

Case 3.

$$\tilde{f}_3(k_x) = \frac{1}{2\pi} \int_0^{l/4} f_3(x) \exp(jk_x x) dx$$

$$\tilde{f}_3(k_x) = \frac{1}{2\pi} \int_{l/4}^0 \left\{ \frac{\sin[k_0(l/4 - x)]}{\sin(k_0 l/4)} + \frac{\sin[k_0 x]}{\sin(k_0 l/4)} \right\} \exp(jk_x x) dx \quad (2.10.23)$$

From the symmetry of the current expansion on the strip dipole: $f_3(x) = f_2(-x)$.

$$\begin{aligned} \tilde{f}_3(k_x) &= \frac{1}{2\pi} \int_0^{l/4} f_3(x) \exp(jk_x x) dx = \frac{1}{2\pi} \int_0^{l/4} f_2(-x) \exp(jk_x x) dx \\ &= \frac{-1}{2\pi} \int_{-l/4}^0 f_2(x) \exp(-jk_x x) dx \end{aligned} \quad (2.10.24)$$

upon substituting $-x$ for x . We have:

$$\tilde{f}_3(k_x) = -\tilde{f}_2(-k_x)$$

We now use the results from Case 2; substituting $-k_x$ for k_x in the expression for I_{31} and I_{32} :

$$I_{31} = \frac{-1}{2} \left\{ \frac{e^{jk_0 \frac{l}{4}} (1 - e^{-j(k_0 - k_x) \frac{l}{4}})}{(k_0 - k_x)} + \frac{e^{-jk_0 \frac{l}{4}} (1 - e^{j(k_x + k_0) \frac{l}{4}})}{(k_x + k_0)} \right\} \quad (2.10.25)$$

$$I_{32} = \frac{-1}{2} \left\{ \frac{(1 - e^{-j(k_0 - k_x) \frac{l}{4}})}{(k_0 - k_x)} - \frac{(1 - e^{j(k_x + k_0) \frac{l}{4}})}{(k_x + k_0)} \right\}$$

Final result:

$$\tilde{f}_3(k_x) = \frac{I_{31} - I_{32}}{2\pi \sin(k_0 l/4)} \quad (2.10.26)$$

The total spatial Fourier Transform for the piecewise sinusoidal current on the strip dipole is given by:

$$\tilde{f}_T(k_x) = \{\tilde{f}_1(k_x) + \tilde{f}_2(k_x) + \tilde{f}_3(k_x) + \tilde{f}_4(k_x)\} = \frac{1}{2\pi \sin(k_0 l / 4)} \{I_1 + (I_{21} - I_{22}) + (I_{31} - I_{32}) + I_4\}$$

(2.10.27)

The Floquet Series expansion for $\vec{J}(x, y, z)$ for the single mode current expansion was given by expression 2.3.3:

$$\vec{J}(x, y, z) = \bar{x} \frac{4\pi^2}{d_x d_y} J_0 \delta(z) \sum_{m=-\infty}^{m=+\infty} \sum_{n=-\infty}^{n=+\infty} \tilde{f}(k_{xmn}) \tilde{g}(k_{ymn}) e^{(-jk_{xmn}x - jk_{ymn}y)} \quad (2.10.28)$$

We now substitute $\tilde{f}_T(k_{xmn})$ in expression 2.10.26 for $\tilde{f}(k_{xmn})$ in expression 2.10.28 ($\tilde{g}(k_{ymn})$ is unchanged):

$$\vec{J}(x, y, z) = \bar{x} \frac{4\pi^2}{d_x d_y} J_0 \delta(z) \sum_{m=-\infty}^{m=+\infty} \sum_{n=-\infty}^{n=+\infty} \tilde{f}_T(k_{xmn}) \tilde{g}(k_{ymn}) e^{(-jk_{xmn}x - jk_{ymn}y)} \quad (2.10.29)$$

Expression 2.10.29 represents the new Floquet Series expansion for $\vec{J}(x, y, z)$ representing the piecewise sinusoidal current on the strip dipole; the radiated electric field and the scan impedance is written using $\tilde{f}_T(k_{xmn})$; the electric field is given by:

$$E_x = -\hat{x} \frac{2\pi^2 J_0}{d_x d_y \omega \epsilon_0} \sum_m \sum_n \frac{k_0^2 - k_{xmn}^2}{k_{zmn}} \tilde{f}_T(k_{xmn}) \tilde{g}(k_{ymn}) e^{(-jk_{xmn}x - jk_{ymn}y - jk_{zmn}z)} \quad (2.10.30)$$

$$E_y = \hat{y} \frac{2\pi^2 J_0}{d_x d_y \omega \epsilon_0} \sum_m \sum_n \frac{k_{xmn} k_{ymn}}{k_{zmn}} \tilde{f}_T(k_{xmn}) \tilde{g}(k_{ymn}) e^{(-jk_{xmn}x - jk_{ymn}y - jk_{zmn}z)} \quad (2.10.31)$$

$$E_z = \hat{z} \frac{2\pi^2 J_0}{d_x d_y \omega \epsilon_0} \sum_m \sum_n k_{ymn} \tilde{f}_T(k_{xmn}) \tilde{g}(k_{ymn}) e^{(-jk_{xmn}x - jk_{ymn}y - jk_{zmn}z)} \quad (2.10.32)$$

The scan impedance is given by:

$$Z_S = \frac{2\pi^2\eta}{t^2(D_x D_y)k_0^2} \sum_{m=-\infty}^{m=+\infty} \sum_{n=-\infty}^{n=+\infty} \frac{\left(1 - \frac{k_{xnm}^2}{k_0^2}\right)}{\frac{k_{znm}}{k_0}} \left|k_0 \tilde{f}_T(k_{xnm})\right|^2 \left|k_0 \tilde{g}(k_{ymn})\right|^2 \quad (2.10.33)$$

Having found the scan impedance for the piecewise sinusoidal current on the strip dipole, a Matlab script would be modified to add the calculation of $\tilde{f}_T(k_{xnm})$; define:

$$P(k_{xnm}, k_{ymn}) \equiv \tilde{f}_T(k_{xnm}) \tilde{g}(k_{ymn}) = \frac{t}{2\pi} \tilde{f}_T(k_{xnm}) \text{sinc}\left(\frac{k_{ymn} t}{2}\right) \quad (2.10.34)$$

2.11 Summary

An analytical approach based on a Floquet modal expansion of an array of printed dipoles was presented in Chapter 2 based on the paper ‘‘Scan Impedance for An Infinite Dipole Array: Hansen’s Formulas Compared with Ansoft HFSS Simulations’’. The analytical approach includes the effect of mutual coupling and was compared with the infinite array numerical solver HFSS; an extension of the analytical approach was developed to minimize the discrepancies in scan impedance between the infinite array solver and the Floquet modal approach.

The Floquet modal expansion approach is an elegant mathematical method to initially analyze the scan performance of a phased array of dipoles (or slots) and gives the designer an appreciation for the parameters that greatly influence the scan impedance. The value of the analytical Floquet approach presented in the paper, possibly augmented by higher order sinusoidal expansion terms presented in Section 2.9, provides a rapid estimation of antenna array performance over a frequency band of interest; the value of the numerical simulation tool HFSS is to make final adjustments to the model for optimal performance^{2.1}.

Section 2.9 introduced a multimodal Floquet approach that extended the analytical model of VanKoughnett and Yen for the infinite planar array of dipole antennas. In reference 2.1.10, the authors investigate the effects of the feed-gap voltage model including a non-uniform field distribution in the gap. The authors demonstrated how the real and imaginary current distribution on a linear array of dipoles changes as the scan direction is changed; also, the authors produced a more realistic scan impedance result in the E-, D- and H-planes that had excellent agreement with Ansoft HFSS v. 11 and CST Microwave Studio 2008.

Although the analytical approaches presented in this chapter are powerful and useful to understand the physics of the array problem, it is limited to simple radiator geometries and feed circuits. On the other hand, HFSS can handle very complex radiator and radiator feed geometries including anisotropic microwave materials (that is, the construction of most commercial microwave materials have a different dielectric constant and loss tangent in the z-axis relative to the x- and y-axes).

The next chapter will present a new phased array element and element feed: “Droopy bowtie radiator with integrated balun: Theory”

Chapter 4 presents “Practical realization and applications of droopy bowtie for finite arrays” that utilizes low cost manufacturing techniques, processes and assembly approach. Measured data for prototypes at L-Band and X-Band are also presented.

Chapter 3 – Droopy Bowtie Radiator with Integrated Balun: Theory

3.0 Introduction

The present challenge for array radiator and radiator feed design (between the active transmit/receive module and the radiator) is to combine excellent RF performance (bandwidth, scan volume, low cross-polarization) and low recurring and non – recurring engineering (NRE) cost. Radar requirements are driving towards higher range resolution to track smaller, stealthier targets which drives RF bandwidth and low cross-polarization. In addition to broadband RF performance, Active Electronically Scanned Antenna (AESA) designs demand polarization diversity with low cross-polarization and stable scan element pattern gain across the operating frequency band. The array radiator and radiator feed RF performance should include:

- Bandwidth: 50% RF bandwidth up to one octave RF bandwidth
- Polarization: Linear or dual linear
- Array Lattice: Rectangular lattice, triangular lattice, etc.
- Scan Volume: $\pm 45^\circ$ up to $\pm 60^\circ$ conical scan volume

Chapter 3 is based on the paper “Design and Manufacturing of an Injection-Molded Dual-Polarized X-Band Low-Cost Scanning Array”^{3.1} and US Patent “Droopy bowtie radiator with integrated balun”^{3.2}. Chapter 3 presents the theoretical model of the droopy bowtie radiator with integrated balun.

Section 3.1 reviews the phased array radiator selection approach. Section 3.2 develops the droopy bowtie Radiator simulation model; infinite array and isolated performance is presented. Section 3.3 examines cross-polarization performance. Section 3.4 presents the Feed and Balun approach. A novel quad line vertical feed that is made out of four individual transmission striplines around a common solid ground conductor is used as the RF feed for the two pairs of bow-tie antenna elements. Section 3.5 presents the complete antenna-transmission line model. Section 3.6 is a summary of Chapter 3; Chapter 4 presents prototype measurements and the manufacturing approach based on automated assembly of plated, injection molded parts, the quad line feed and a printed wiring board (PWB) carrier.

3.1 Phased Array Radiator Selection

The starting point for designing a low cost Active Electronically Scanned Array (AESA) is with the radiator and radiator feed architecture. Table 3-1 lists the qualitative criteria used to select a suitable radiator element and radiator feed for use in a phased array:

Table 3-1. Phased array radiator requirement

| Radiator Requirement | System Requirement |
|--|---|
| RF Performance | |
| 1. Broadband Radiator | Range resolution; multifunction radar |
| 2. Low cross-polarization | Target discrimination; clutter rejection |
| 3. Low directivity | Radar sensitivity: Low scan loss over large scan volume |
| 4. Low RF Loss | Radar sensitivity: Reduced Noise Figure |
| Mechanical Performance | |
| 1. Fit within a unit cell area of $\lambda_{\text{high}}/2$ by $\lambda_{\text{high}}/2$ | Wide band, large scan volume: Grating lobe free scan |
| | |
| Feed Performance | |
| 1. Low Loss | Radar sensitivity: Reduce Front-End Loss |
| 2. Polarization Diversity | Target discrimination; clutter rejection |

Recurring and non-recurring cost is treated as one of the critical design parameters; manufacturing cost for the new radiator and radiator feed design will be addressed:

- Fabrication Recurring Cost:
 - Radiator design should have a large supplier base; drive towards commodity based cost;
- Assembly Recurring Cost:
 - Maximize automated assembly; minimize touch labor;
- Non-Recurring Cost:
 - The modular design of the radiator and feed reduces design cycle time for re-scaling to different frequency bands or adjusting performance in an existing design.

Several potential radiator elements were considered for a wideband, low-cost, dual-polarized X-Band array; viable candidates included printed dipoles^{3.3, 3.4}; thick slot-fed microstrip patches^{3.5, 3.6}

and Vivaldi notch elements^{3.7, 3.8}. Non-resonant radiators such as a helix have broadband RF performance- typically one octave^{3.13}. However, the helix is not low profile and difficult to assemble into a large array and is not suitable for polarization diverse radar applications (e.g., switchable dual linear polarization or switchable circular polarization).

A bow-tie radiator^{3.9-3.12} was chosen because it had the potential to meet the RF criteria outlined in Table 3-2:

Table 3-2. Bowtie radiator vs. phased array radiator requirement

| Radiator Requirement | System Requirement | Bowtie Radiator |
|--|---|--|
| RF Performance | | |
| 1. Broadband Radiator | Range resolution; multifunction radar | Non-resonant radiator; high impedance bandwidth: Section 3.2, Appendix A |
| 2. Low cross-polarization | Target discrimination; clutter rejection | Excellent cross-pol for non-resonant radiator; Section 3.3 |
| 3. Low directivity | Radar sensitivity: Low scan loss over large scan volume | Section 3.2.1.2 |
| 4. Low RF Loss | Radar sensitivity: Reduced Noise Figure | Chapter 4 Simulations |
| Mechanical Performance | | |
| 1. Fit within a unit cell area of $\lambda_{\text{high}}/2$ by $\lambda_{\text{high}}/2$ | Wide band, large scan volume: Grating lobe free scan | Bend bowtie wings "Droopy" bowtie; Section 3.2 |
| Feed Performance | | |
| 1. Low Loss | Radar sensitivity: Reduce Front-End Loss | Novel, High Isolation Feed; Chapter 4 Simulations |
| 2. Polarization Diversity | Target discrimination; clutter rejection | Crossed bowties; Section 3.4 |

Appendix A outlines the time domain characteristics of a broadband antenna; it is shown that the bowtie antenna has inherently excellent RF bandwidth versus scan properties.

3.2 Droopy Bowtie Radiator Model

The droopy bowtie radiator is the baseline element to investigate how it meets the phased array system requirements outlined in Table 3-2. In addition, we will investigate the practical aspects of the bowtie radiator design towards the objective of low cost. Table 3-3 outlines the bowtie radiator design challenges and approaches that will be expanded upon in subsequent sections.

Table 3-3. Bowtie radiator design challenges vs. approach

| Radiator Requirement | Design Challenges | Approach |
|---------------------------|------------------------------------|---|
| RF Performance | | |
| 1. Broadband Radiator | Wideband Impedance Match | “Droopy” Bowtie Design; Section 3.2 |
| 2. Low cross-polarization | Wideband, High Isolation Balun | Novel Quad Line Balun Design; Section 3.4 |
| 3. Low directivity | Bowtie Radiator Mechanical Support | “Eggcrate” Cavity support; Chapter 4 |
| 4. Low RF Loss | Bowtie Radiator Fabrication | Plated, Injection Molded Part; Chapter 4 |

We briefly discuss each design challenge and proposed approach:

- Wideband Impedance Match: “Droopy” bowtie wings selected^{3.9-3.12}
 - Large impedance bandwidth;
 - Relatively low gain due to droopy wings^{3.14};
- Wideband high isolation Balun: quad line balun design
 - “Droopy” bowtie wings: inherently high isolation^{3.9-3.12};
- Bowtie radiator mechanical support: “Eggcrate” cavity support
 - “Eggcrate” cavity support: inexpensive, easily plated for unit cell to unit cell isolation; height easily adjusted for optimum radiator performance;
 - Options considered:
 - Syntactic foam support^{3.15}: inability to copper plate; fragile; expensive;
 - Printed wiring board (PWB) support: thick, heavy and expensive;

- Bowtie radiator fabrication: plated, injection molded part
 - Droopy bowtie: planar geometry amenable to commercial injection molding and plating processes.

The basic droopy bowtie model, using Ansoft High Frequency Structure Simulator (HFSS), is presented in Figure 3-1; with the arrangement of the bowtie wings, we call the radiator model: droopy bowtie “turnstile” radiator. The model in Figure 3-1 is constructed as two stacked blocks:

- A solid Teflon block support of height $2h_b$,
- A radiator Teflon block of height h .

The radiator Teflon block is shown turned upside-down in Figure 3-1 to highlight the hidden air cavity. The basic model begins to incorporate the low-cost design objectives:

- The support block simulates an injection molded support;
- The radiator Teflon block simulates a shaped injection mold with four surface-plated metal wings.

The geometry shown in Figure 3-1 allows the radiator to be covered with a protective dielectric layer (or radome).

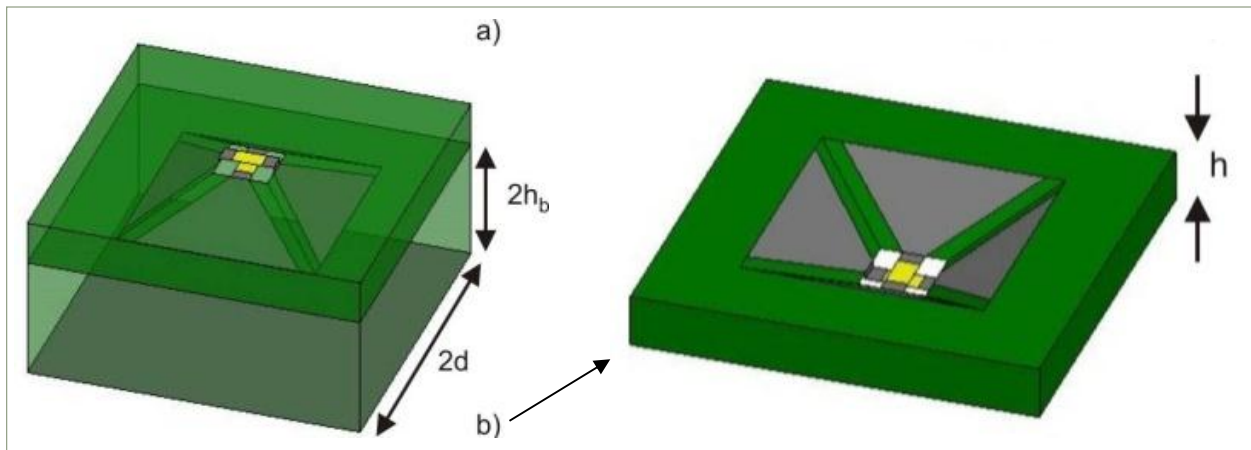


Figure 3-1. Model of the center-fed droopy bowtie turnstile radiator in Ansoft HFSS. Left: Full model; Right: Radiator block.

Figure 3-2 represents the parametric model used in HFSS; a “shape convexity factor”, Δ , has been introduced to control the shape of the bowtie wing for optimal RF bandwidth and scan performance.

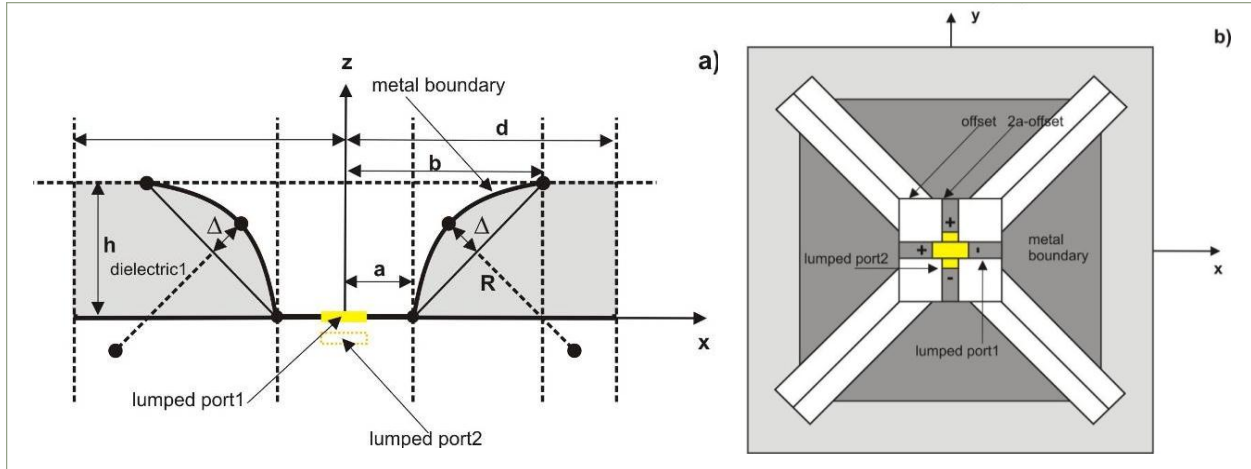


Figure 3-2. Parametric model of radiator block. Left: Side view of dimensioned droopy bowtie radiator. Right: Top view showing lumped port excitation.

Table 3-4 lists the dimensions of a baseline X-Band droopy bowtie radiator. The rectangular lattice has a unit cell size is 10.9mm (0.429in), which is slightly less than a free-space half-wavelength, $\lambda/2 = 12.5\text{mm}$ (0.492in) at the upper band frequency $f = 12\text{ GHz}$. The total element height from the ground plane to the top of the upper Teflon cover is $2h_b + h = 5.45\text{mm}$ (0.215in). The convexity factor was varied over the range $\pm 0.2\text{mm}$; the antenna scan impedance was not significantly affected over this range, but the simulation established acceptable mechanical tolerances for antenna manufacturing.

Table 3-4. Baseline X-band droopy bowtie radiator dimensions

| Quantity | Dimension | Description |
|----------|---------------------|------------------------------------|
| a | 0.9mm | Feed half-width |
| b | 3.25mm | Radiator half-width |
| d | 5.45mm | Unit cell half-size |
| h | 1.45mm | Height of the radiator top section |
| Δ | from 0.2 to -0.2 mm | Wing convexity factor |
| $2h_b$ | 4mm | Height of antenna support |

3.2.1 Droopy Bowtie Radiator Model: Infinite Array Modeled Results

Section 3.2.1 examines the baseline X-Band droopy bowtie radiator simulated performance in HFSS for the parameters given in Table 3-4:

- Infinite Array Simulation Performance
 - Figure 3-3a through Figure 3-5a. Scan Resistance
 - Figure 3-3b through Figure 3-5b. Scan Reactance
 - Figure 3-3c through Figure 3-5c. Scan Return Loss
- Isolated Element Pattern Performance
 - Figure 3-6a. Scan Resistance
 - Figure 3-6b. Scan Reactance
 - Figure 3-6c. Scan Return Loss
- Isolated Element Input Impedance and Return Loss Performance
 - Figure 3-7a. Input Impedance
 - Figure 3-7b. Return Loss

3.2.1.1 Infinite Array Simulation Performance: Scan Impedance and Return Loss

Section 3.2.1.1 examines the tradeoff in RF performance as the bowtie wing convexity factor is varied. Figure 3-3 through Figure 3-5 simulate the baseline X-Band droopy bowtie radiator scan resistance, scan reactance and scan return loss for three normalized wing convexity factors: $\Delta/b = 0.0, 0.06$ and -0.06 . Each curve in Figure 3-3 through Figure 3-5 corresponds to a discrete frequency from 8 – 12GHz; there are three azimuthal scan angles simulated at each frequency: $\varphi = 0^\circ, 45^\circ$ and 90° . The scan impedance was found using the unit-cell approach in HFSS, with two parametric sweeps over two variable scan angles^{3.1}. The center-fed bowtie antenna is matched to a 60 Ohm balun design. Examining Figure 3-3 through Figure 3-5, the scan return loss generally lies below -10 dB for elevation scan angles up to $\theta = 50^\circ$ and approaches approximately -6 dB for elevation scan angle of exactly $\theta = 60^\circ$. Based on the relative performance of all three normalized convexity factors, the simpler normalized convexity factor of $\Delta/b = 0.0$ is chosen for further investigation of RF performance.

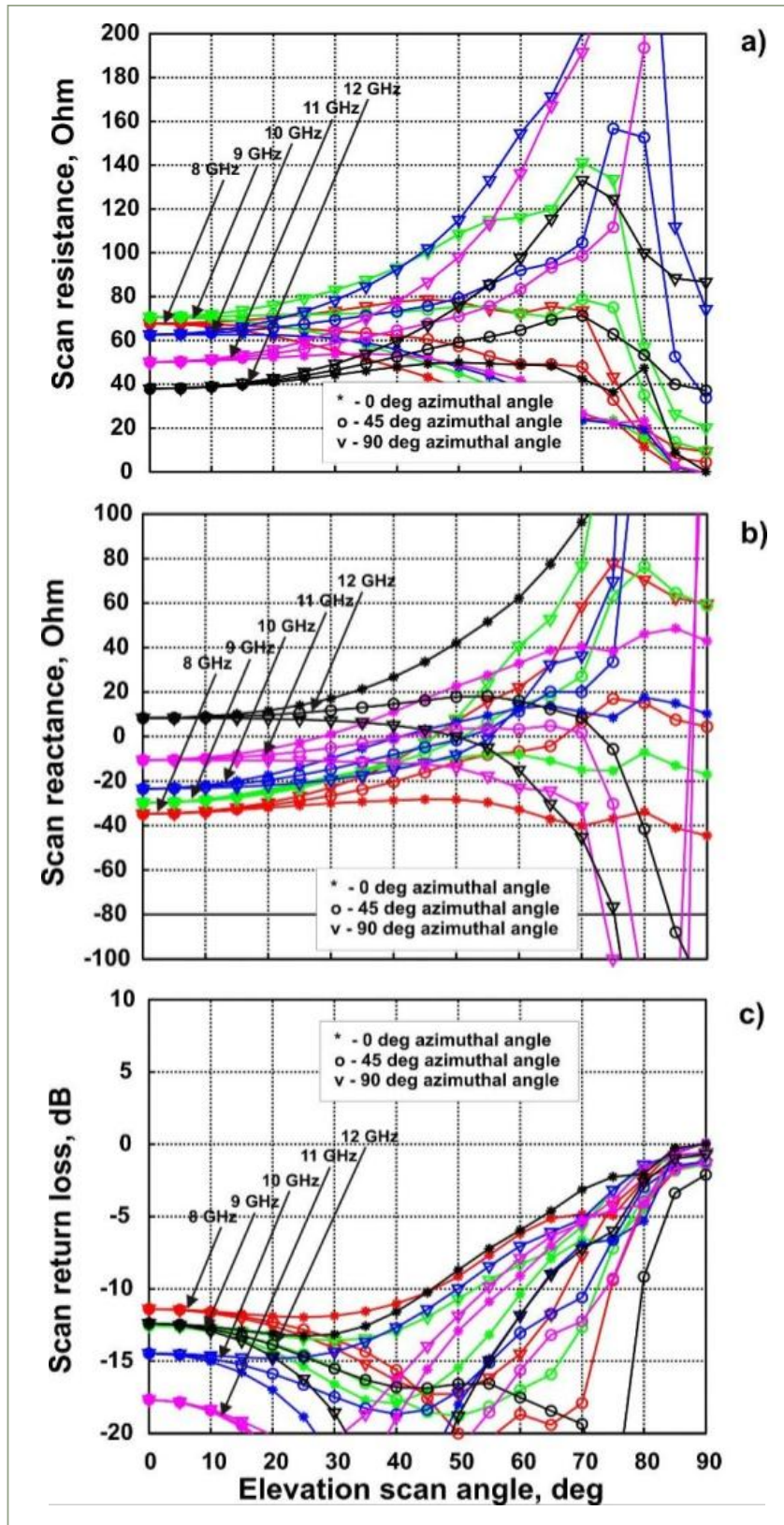


Figure 3-3. Baseline X-Band droopy bowtie radiator simulation a) Scan impedance, b) Scan reactance, c) Scan return loss. Dimensionless convexity factor $\Delta/b=0.0$

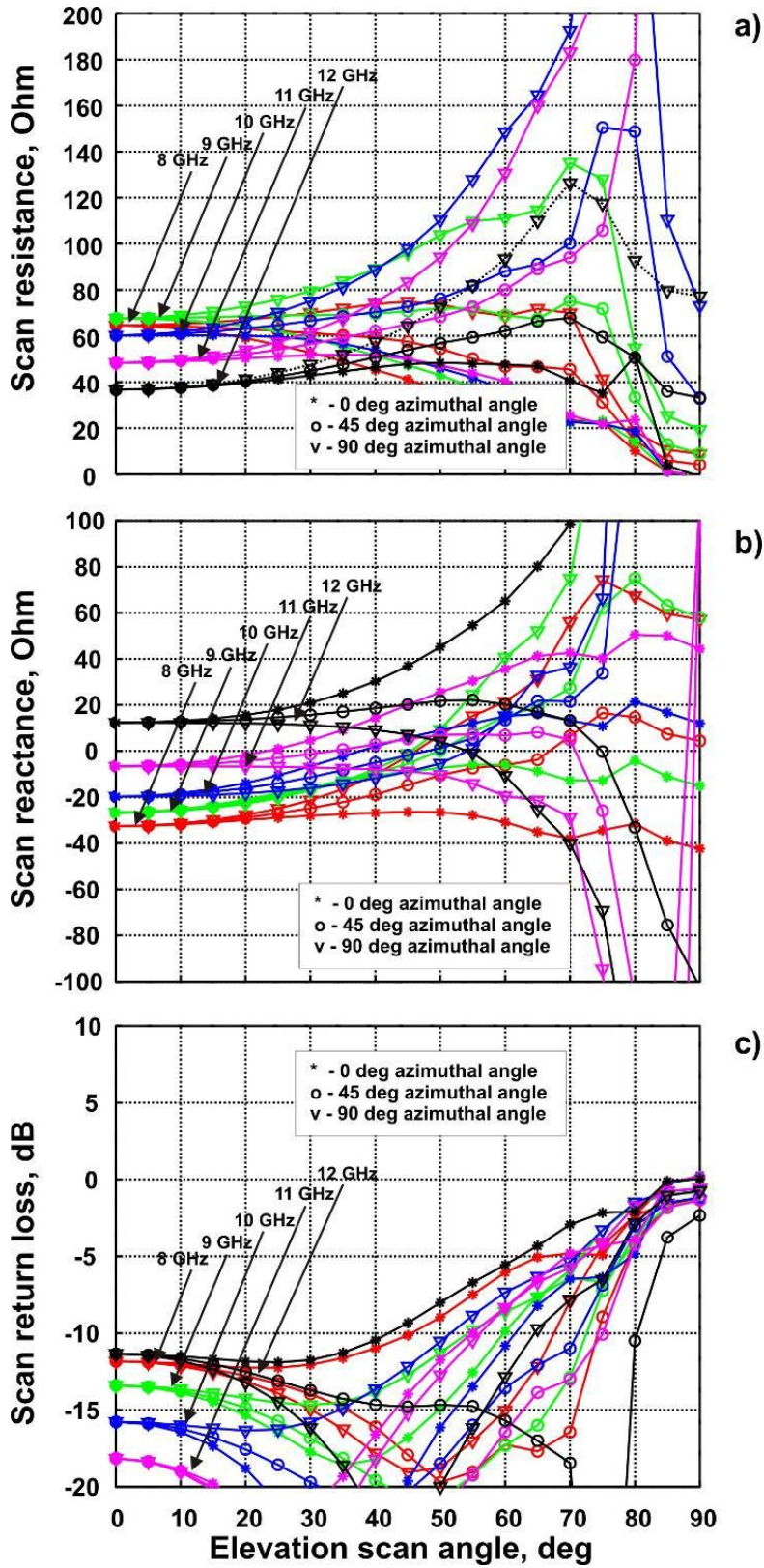


Figure 3-4. Baseline X-Band droopy bowtie radiator simulation a) Scan impedance, b) Scan reactance, c) Scan return loss. Dimensionless convexity factor $\Delta/b = +0.06$

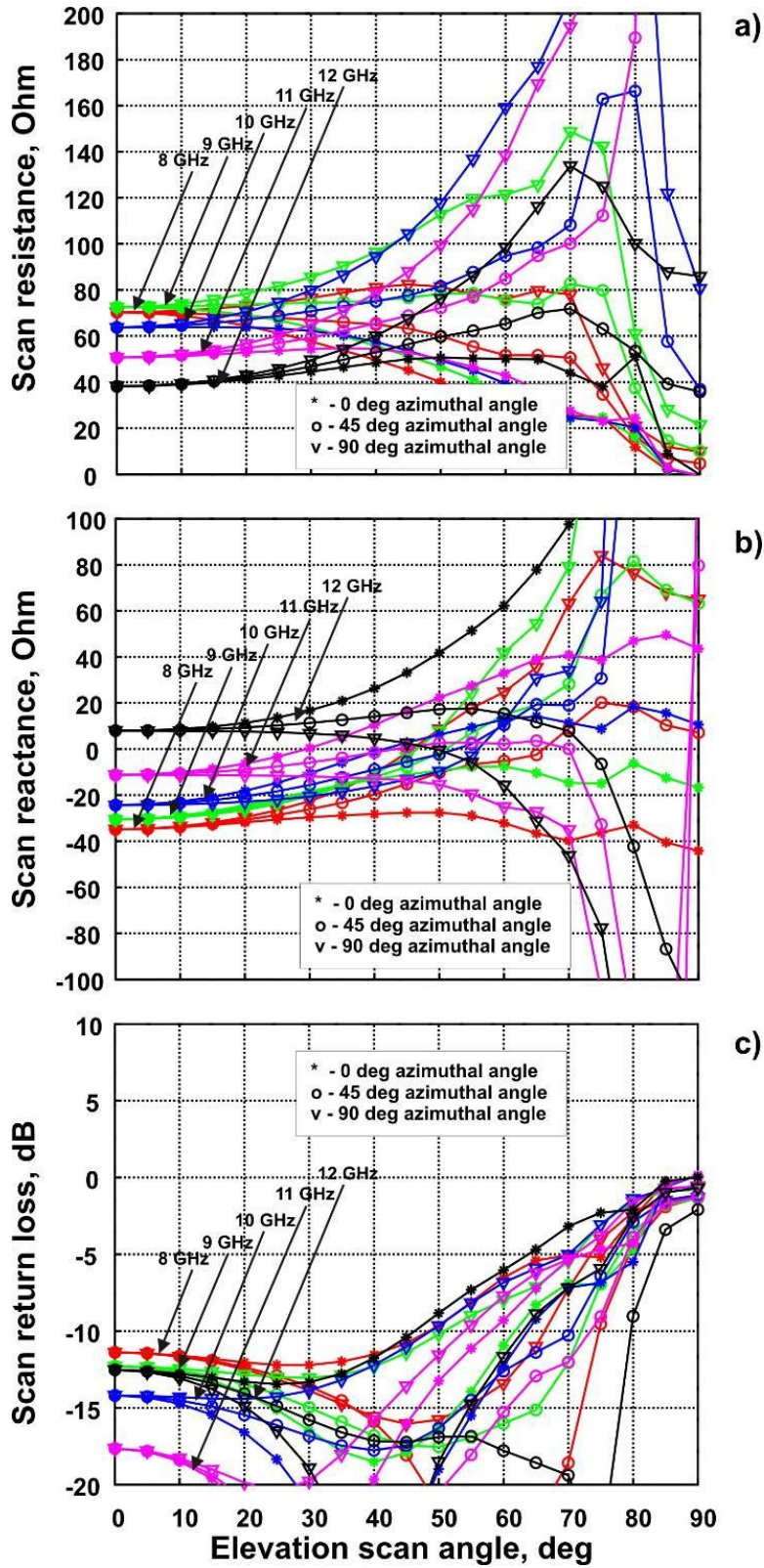


Figure 3-5. Baseline X-Band droopy bowtie radiator simulation a) Scan impedance, b) Scan reactance, c) Scan return loss. Dimensionless convexity factor $\Delta/b = -0.06$

3.2.1.2 Isolated Element Pattern Performance

The isolated droopy bowtie element pattern is simulated in HFSS and shown in Figure 3-6.

For phased arrays, low scan loss requires that the isolated element pattern have low directivity—that is, a broad pattern versus scan out to 90 degrees. Figure 3-6 shows that the droopy bowtie has relatively low scan loss from 8GHz to 12GHz. The isolated element pattern for one pair of droopy bowtie radiators is shown in Figure 3-6 for radiating boundary conditions and an infinite ground plane. Figure 3-6 gives the total directivity of an isolated element for three scan planes: a) E-plane; b) D-plane ($\phi=45$ deg); c) H-plane. One notes directivity and gain variation with frequency, which approximately follows the $4\pi A/\lambda^2$ law; this variation is nearly uniform over the elevation angles and provides a preliminary understanding of the scan performance of the droopy bowtie element.

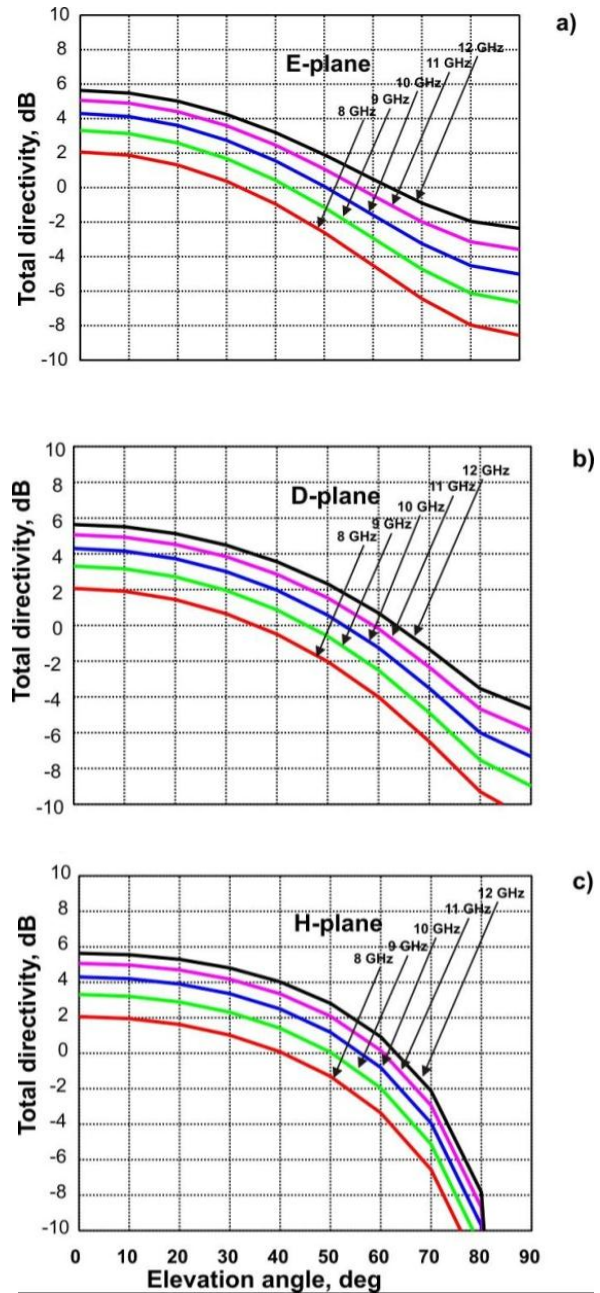


Figure 3-6. Total directivity of an isolated element over infinite ground plane –one bowtie pair is excited; radiator geometry is given in Table 3-2. a) E-plane; b) D-plane ($\phi=45$ deg); c) H-plane. Dimensionless convexity factor $\Delta/b= 0.0$

3.2.1.3 Isolated Element Input Impedance and Return Loss Performance

Figure 3-7 shows the input impedance and return loss (S11) for one pair of droopy bowtie radiators connected to a 50 Ohm transmission line without an impedance matching network; only one droopy bowtie pair is driven (the other droopy bowtie pair is terminated to a 50 Ohm load). The two droopy bowtie pairs of the turnstile form a simple two-port network that allows estimation of S11 for a single dipole and also the cross talk between two polarizations, S21.

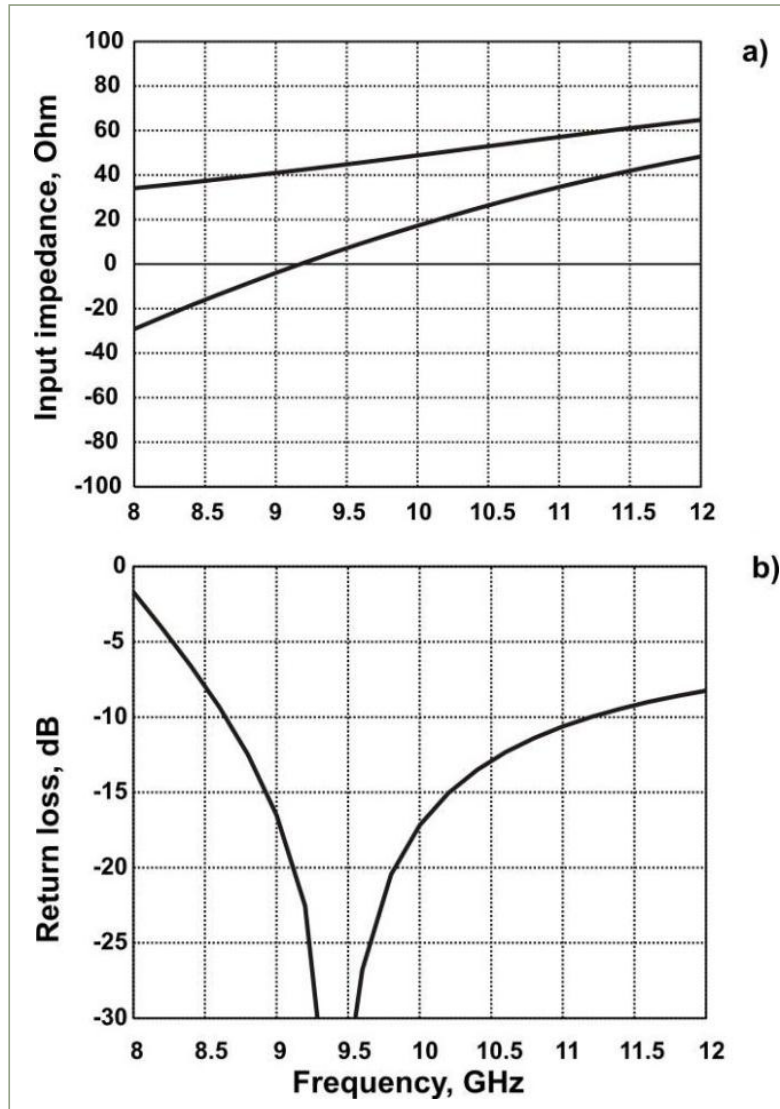


Figure 3-7. Input impedance (a) and return loss (b) for an isolated droopy bowtie over infinite ground plane. Dimensionless convexity factor $\Delta/b=0.0$

3.3 Cross-Polarization Performance

Low cross polarization for target discrimination and clutter rejection is a key phased array requirement for a linear polarized element or dual linear polarized element like the droopy bowtie turnstile radiator; low cross polarization is also important for circular polarization.

The key design goal for dual polarization antenna arrays is to obtain a high cross-polarization isolation^{3.16-3.21}; the challenge is to combine high cross-polarization isolation with a wide bandwidth radiator and radiator feed.

A brief overview is given below on the tradeoff between wide bandwidth and high cross-polarization isolation.

The tapered slot (Vivaldi element) bulky array is very broadband, but it produces high cross-polarization components in the principal planes, especially in the 45 degree diagonal plane^{3.20-3.21}. High cross-polarization components mainly arise from extensive surface currents flowing in the longitudinal direction along the element, and partly from unbalanced feed ports^{3.20}. Cross-polarization components can be partially reduced by using carefully designed balanced feeds, but that cannot eliminate the source of the problem, which is related to the long flare of the element^{3.21}.

The “bunny-ear” low-profile wideband dipole array introduced in gives better polarization isolation and simultaneously, possesses a relatively large bandwidth^{3.20}. A planar array of printed dipoles has excellent cross-polarization isolation – see^{3.18}; however, the dipole bandwidth typically has the narrowest bandwidth of operation. For the printed dipoles (and for any dipole-like array, including our droopy turnstiles), the cross-polarization effect is mostly dominant in the D-plane (at 45 degree azimuthal scan angle). As noted above, combining wideband RF performance and high cross-polarization isolation in a dual linear polarized radiator is a challenge^{3.16-3.21}. Figure 3-8 compares the cross polarization performance (identified in the figure as S21) of the droopy bowtie turnstile radiator in the array environment with the narrow band dipole radiator array^{3.18,3.22} and wide band “bunny-ear” or flared notch radiator array^{3.21}. Referring to Figure 3-8:

At boresite: the droopy bowtie has at -60dB cross-pol; the dipole is at -80dB and the “Bunny-Ear” is at -30dB;

E and H plane scans: the droopy bowtie is between -60dB and -70dB; “Bunny-Ear” is between -27dB and -30dB; data was not provided for the dipole in the E and H plane;

D-plane scan ($\varphi=45^\circ$): the cross polarization performance for all three radiators converges in the D-plane ($\varphi=45^\circ$): the cross polarization performance is worst in the D-plane due to mutual coupling for all three radiators. At $\theta=60^\circ$ scan, both the droopy bowtie turnstile radiator array and dipole array have the same cross polarization isolation of ≈ -10 dB.

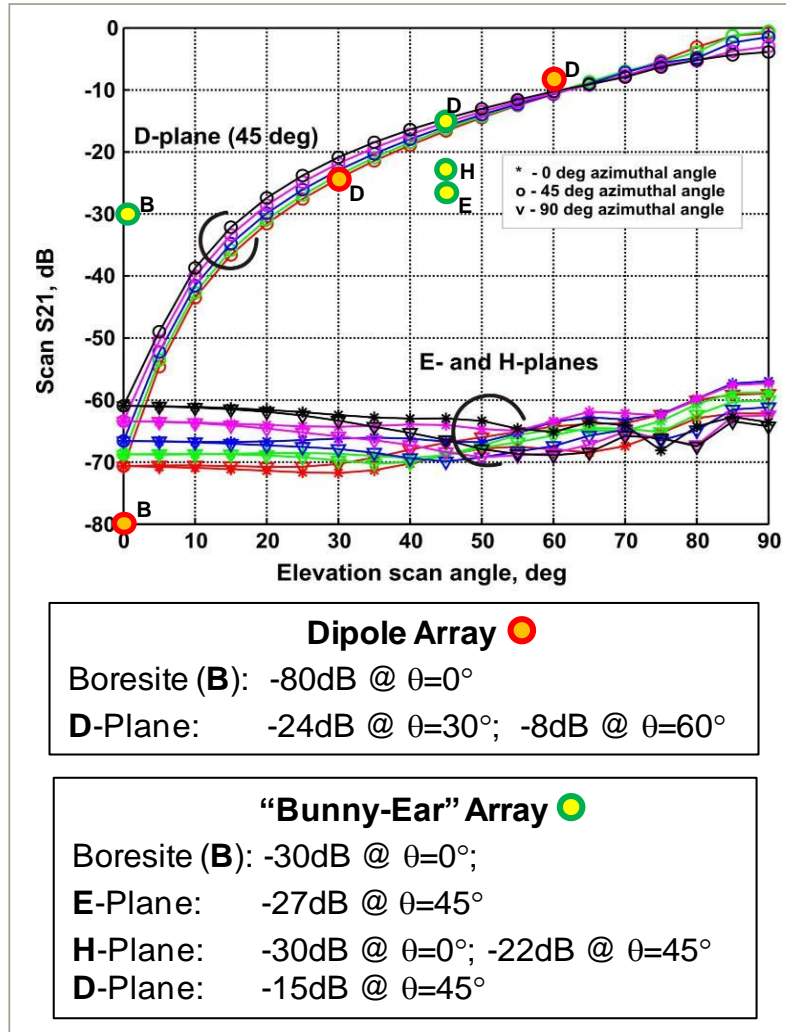


Figure 3-8. Cross polarization of droopy bowtie turnstile array radiators versus a dipole array and a "bunny-ear" array.

The droopy bowtie turnstile radiator has the best aggregate performance with respect to RF bandwidth and cross-polarization performance:

- $\text{dipole}_{\text{RF bandwidth}} < \text{droopy bowtie}_{\text{RF bandwidth}} < \text{Notch radiator}_{\text{RF bandwidth}}$
- $\text{Notch radiator}_{|\text{cross-pol}|} < \text{droopy bowtie}_{|\text{cross-pol}|} < \text{dipole}_{|\text{cross-pol}|}$

3.3.1 Axial Ratio for Circular Polarization

Cross-polarization is primarily responsible for poor axial ratio since the element patterns in all planes (E, H, and D) have nearly the same gain up to 60 degree scan. The RHCP polarization (or polarization *isolation*), ρ_c , is given by^{3.23}:

$$\rho_c = \frac{|E_A + jE_B|}{|E_A - jE_B|}, \text{ cross polarization} = 20 \log_{10} \rho_c \quad (3.3.1)$$

in every azimuthal plane; subscripts *A* and *B* denote two orthogonal dipoles. The axial ratio is given by^{3.23}:

$$\text{axial ratio} = 20 \log_{10} \left| \frac{\rho_c + 1}{\rho_c - 1} \right| \quad (3.3.2)$$

In particular, for RHCP polarization,

$$\rho_c = \frac{|2jE_B + \Delta|}{|\Delta|} \approx \frac{|2E_A|}{|\Delta|} = 2 \cdot 10^{-S_{21,dB}/20} \quad (3.3.3)$$

According to Figure 3-8, we should expect an axial ratio approaching 0dB in the E- and H-planes. The worst-case axial ratio is the 60 degree elevation scan angle in the D-plane, where $S_{21,dB} \approx -10\text{dB}$ according to Figure 3-8, resulting in a worst-case axial ratio value of ≈ 3 dB.

3.4 Feed and Balun

The feed and balun transmission line design is critical to achieving low RF loss and high cross-polarization isolation as outlined in Table 3-2. The feed and balun transmission line design must meet the following requirements:

- Low RF loss;
- High cross-polarization isolation;
- Coincident phase centers;
- Wideband performance;
- Low Cost.

3.4.1 Dyson Balun

For the development of droopy bow-tie turnstile array, the Dyson balun design was selected^{3.24-3.33}. The Dyson balun is widely used for standard dipoles and other symmetric antennas. The balun needs to provide a high isolation between two turnstile antenna elements since two pairs of feeding transmission lines are shielded; the phase center of two crossed dipoles remains the same. The Dyson balun has a considerably wider bandwidth compared to the split-coaxial balun (bandwidth of 20-25%^{3.34}). Another advantage of the Dyson balun is its direct applicability to a turnstile dipole element with two crossed dipoles or dipole-like antennas fed with two separate hybrids.

The Dyson balun is widely used as the feed/ balun for standard dipoles, crossed dipoles and other symmetric antennas^{3.24-3.35}; the Dyson balun is also amenable to printed wiring board fabrication techniques and is used as the feed/ balun for the droopy bowtie turnstile radiator array. Figure 3-9 shows the Dyson balun concept: each half of the dipole is fed 180 degrees out of phase with a separate coaxial line. The coaxial lines share the same outer ground- this ensures the proper balanced current distribution along the dipole.

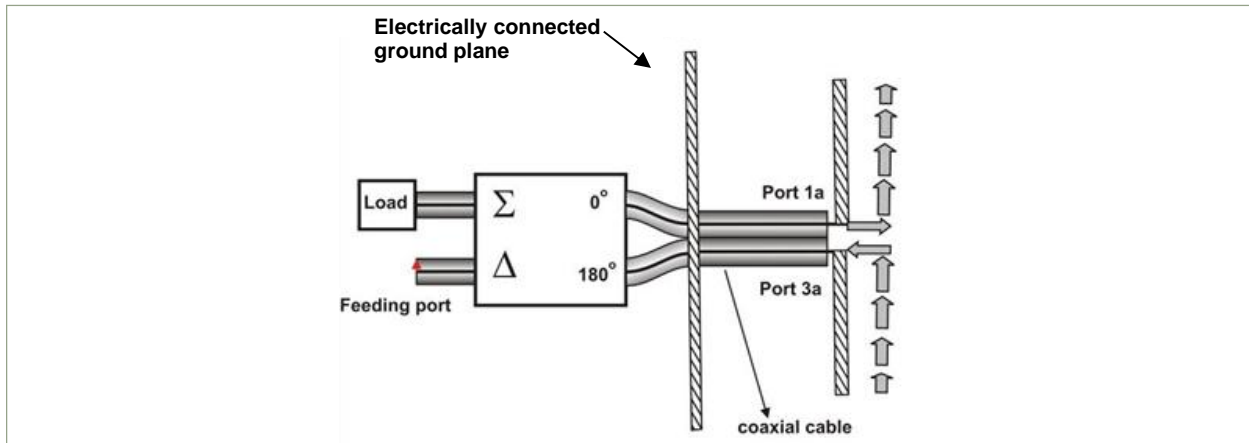


Figure 3-9. Dyson balun for single polarized dipole antenna.

3.4.2 Vertical Balun Column: The Quad line RF Transmission Line

To realize the Dyson balun for the droopy bowtie turnstile radiator, a new vertical rectangular transmission line, which is denoted as the “quad line”, is developed. Table 3-5 describes the features of the quad line. The quad line construction concept is shown in Figure 3-10 for three different frequency bands; fabrication and assembly is discussed in Chapter 4.

Table 3-5. Quad line features

| Feature | Function | Material | Comments |
|----------------------------|---|--|---|
| Central Conducting Post | Mechanical Support RF Ground | Nickel-Gold plated Aluminum Nickel-Gold plated Zinc Nickel-Gold plated plastic | Post is inserted into PWB during assembly – see Section 3.6.3 |
| Coplanar Transmission Line | RF transmission line feed for bowtie wing | Rogers RT/duroid 6010 PTFE Nominal, relative dielectric constant: 10.2 Nominal loss tangent: 0.0023 Standard thickness: 0.010 in., 0.025 in., 0.050 in. | High relative dielectric constant plus air gaps between coplanar lines provides high isolation between adjacent coplanar transmission line feeds Low loss tangent: Low RF loss |

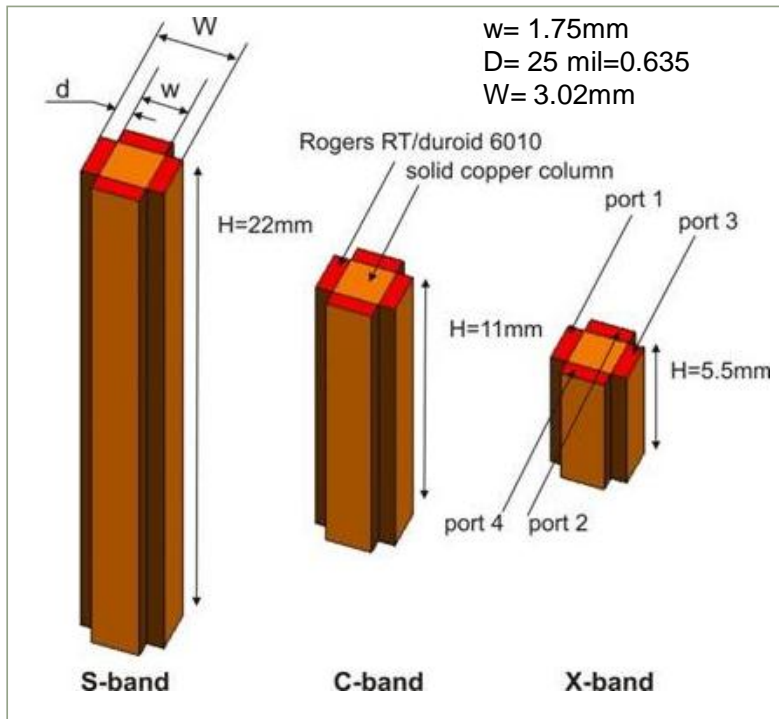


Figure 3-10. Quad line concept

Figure 3-11 shows the bowtie wing to quad line to printed wiring board (PWB) assembly concept. The outward facing conductor of the coplanar line is conductively attached to the bowtie wing; the inward facing conductor of the coplanar line is conductively bonded (soldered or conductive epoxy) to the central conducting post- the central conducting post is conductively bonded to RF ground.

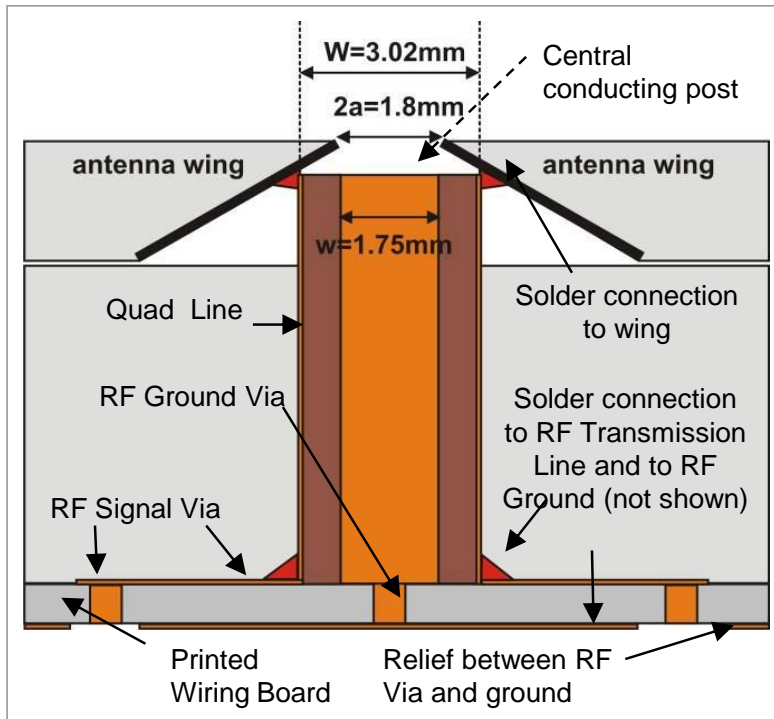


Figure 3-11. Bowtie wing to quad line to printed wiring board assembly

3.4.3 Transmission Line Parameters of the Quad Line Model

This section outlines the analytic modeling methods used to approximate the quad line characteristic impedance; this model serves as a starting point for the quad line dimensions and dielectric constant used in the HFSS model of the droopy bowtie turnstile radiator with quad line feed discussed in Chapter 4.

The quad line is composed of four dielectric-filled parallel-plate waveguide transmission lines. The complete quad line is an eight-port network; the approximate characteristic impedance of the dielectric-filled parallel-plate waveguide is given by^{3,36}:

$$Z_0 = \eta \frac{d}{w} = \frac{\eta_0}{\sqrt{\epsilon_r}} \frac{d}{w} \quad (3.4.1)$$

where:

- $Z_0 \equiv$ characteristic impedance of the dielectric-filled parallel-plate waveguide;
- $d \equiv$ spacing between plates;
- $w \equiv$ width of plates;

- $\eta_0 \equiv$ characteristic impedance of vacuum (~ 377 Ohm).
- $\epsilon_r \equiv$ relative dielectric constant;

The approximation in equation 3.4.1 does not take into account the finite waveguide size, interaction between waveguides, and does not distinguish between even and odd modes of propagation.

A more realistic approximation that takes into account quad line symmetry is shown in Figure 3-12. In Figure 3-12a, only one port (port 1) is driven and the structure has an infinite PEC ground plane. According to the method of images, this structure is equivalent to that in Figure 3-12b, with ports 1 and 3 driven out of phase (differential or odd mode) and with ports 2 and 4 shorted out. The characteristic impedance of port 1 in Figure 3-12a will thus be the characteristic impedance of one port in the differential mode (port 3 has the same impedance as port 1). Similarly, the propagation constant (effective dielectric constant) of the port is that of the odd mode.

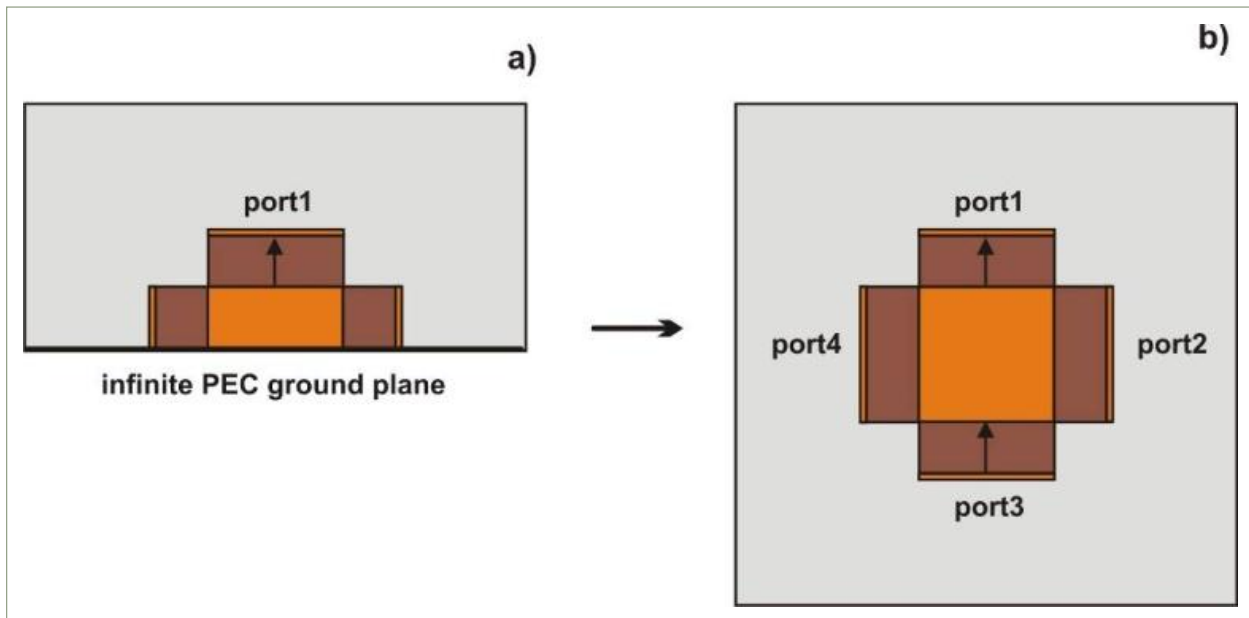


Figure 3-12. Calculation of odd mode characteristic impedance and propagation constant using the method of images over a PEC ground plane.

The model shown in Figure 3-12a was simulated in HFSS using two input/output wave ports and a perfect electric conductor (PEC) surrounding boundary. The line length was chosen to be $3\lambda/4$ at the center frequency. From the solution matrix data, HFSS automatically gives the characteristic impedance, Z_0 , and effective dielectric constant, ϵ_{eff} , of the line in the odd mode. The value of

characteristic impedance corresponding of the quad line, where $w/d = 0.365$ and $\epsilon_r = 10.85$ (Rogers RT/duroid 6010 material) is approximately 29.67 Ohm (compared to 41.23 Ohm when derived using the parallel-plate approximation); the corresponding effective dielectric constant is 6.74. The parallel-plate approximation of equation 3.4.1 may be refined:

$$Z_0 = \frac{\eta_0}{\sqrt{\epsilon_r}} \frac{d}{w} \left[1 + z_1 \left(\frac{d}{w} \right) + z_2 \left(\frac{1}{\sqrt{\epsilon_r}} \right) \right], \quad c_p = \frac{c_0}{\sqrt{\epsilon_r}} \left[1 + c_1 \left(\frac{d}{w} \right) + c_2 \left(\frac{1}{\sqrt{\epsilon_r}} \right) \right] \quad (3.4.2)$$

where c_p is the phase velocity in the dielectric; the constants z_1, z_2, c_1, c_2 can be found from the best fit to the full set of numerical data.

3.4.4 Mode Isolation of the Quad Line

As noted in Table 3-1, enhanced target discrimination in clutter drives the low cross-polarization requirement; this requires that the quad line feed have high isolation between parallel-plate waveguides. Figure 3-13 shows the HFSS model of the quad line and Figure 3-14 the modeled isolation between ports. The model confirms that the high dielectric, physically separated parallel-plate waveguides comprising the quad line have excellent isolation over a broad band ($f/f_0 = 2$).

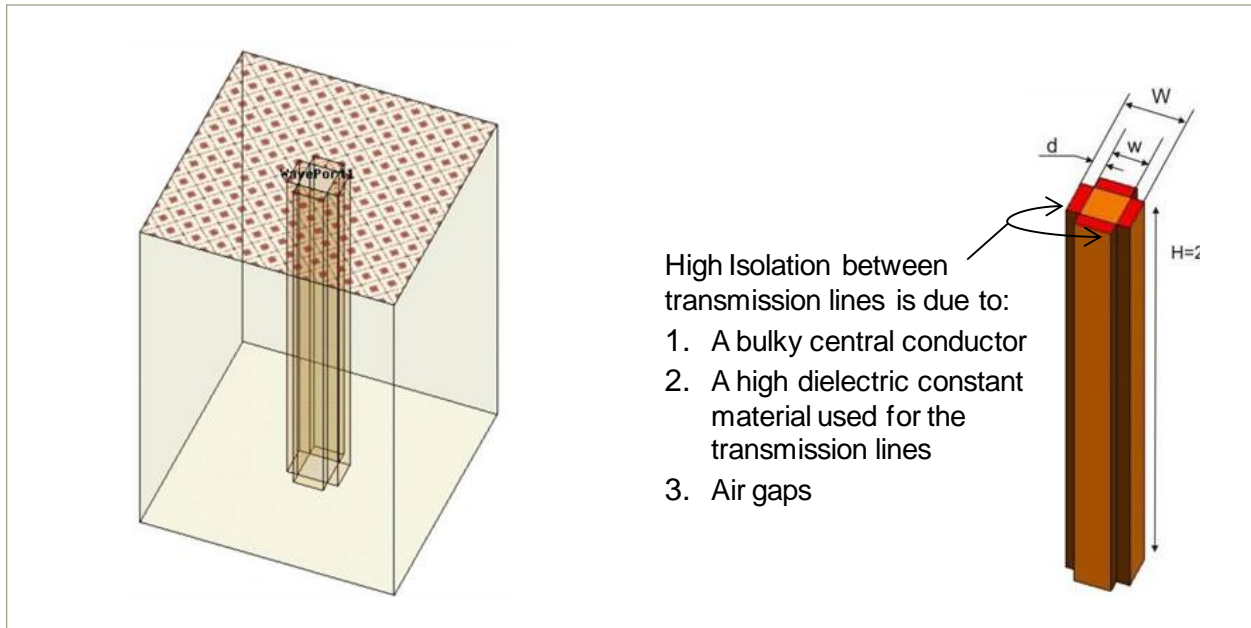


Figure 3-13. HFSS model of quad line (left); high isolation quad line (right)

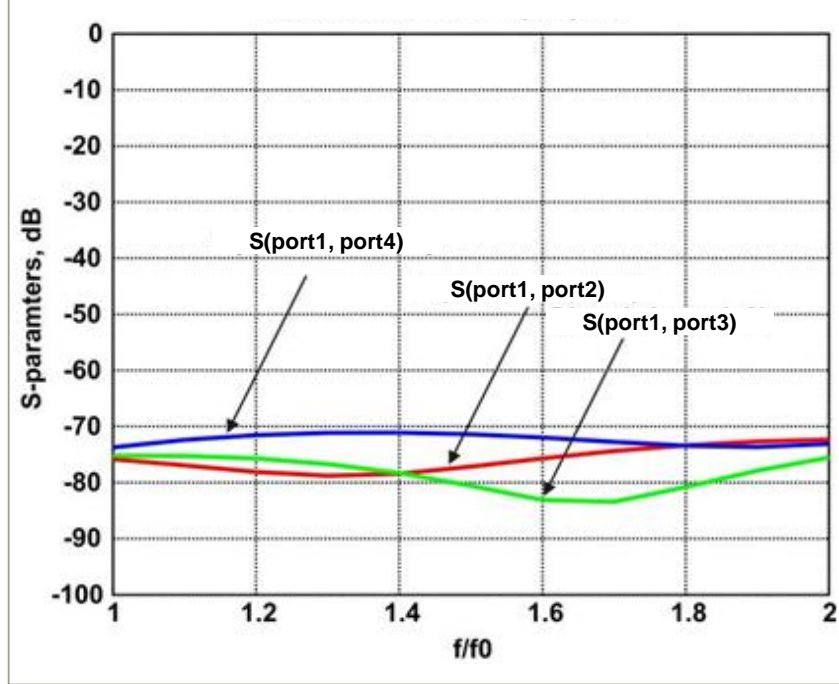


Figure 3-14. Isolation between parallel plate waveguides: HFSS calculated S-parameters

Summarizing the port-to-port isolation of quad line:

- The isolation between any two ports of the quad line is greater than 70dB over one octave bandwidth.

Because it is difficult to introduce eight independent ports in HFSS, we have introduced two ports (input and output), with four independent modes corresponding to four individual transmission lines per port; the software allows us to find the S-parameters for every mode and thus establish the complete 8×8 S-matrix. The resulting mode isolation is satisfactory; similar results have been obtained for the cross talk between input and output modes.

To check the differential mode isolation and also check the data for the line impedance, we terminated all modes of the output port into a matched load (lumped R-load); this was done for the case $w/d = 0.365$ and $\epsilon_r = 10.85$, which corresponds to the quad line shown in Figure 3-10. The resulting system then becomes the four-port, or rather, the “four-mode” network. The S-parameters for the differential mode can be found as:

$$S_{1,1}^D = \frac{V_D^{-I}}{V_D^{+I}} \Big|_{V_D^{+II}, V_C^{+I,II}=0} = \frac{V_1^- - V_3^-}{V_1^+ - V_3^+} = \frac{1}{2}(S_{11} + S_{33} - S_{13} - S_{31}) \quad (3.4.3)$$

$$S_{II,II}^D = \left. \frac{V_D^{-II}}{V_D^{+II}} \right|_{V_D^{+I}, V_C^{+I,II}=0} = \frac{V_2^- - V_4^-}{V_2^+ - V_4^+} = \frac{1}{2}(S_{22} + S_{44} - S_{24} - S_{42}) \quad (3.4.4)$$

$$S_{II,I}^D = \left. \frac{V_D^{-II}}{V_D^{+I}} \right|_{V_D^{+II}, V_C^{+I,II}=0} = \frac{V_2^- - V_4^-}{V_2^+ - V_4^+} = \frac{1}{2}(S_{12} - S_{14} - S_{32} + S_{34}) \quad (3.4.5)$$

Figure 3-15 shows the data from equations 3.4.3 through 3.4.5 for the differential mode:

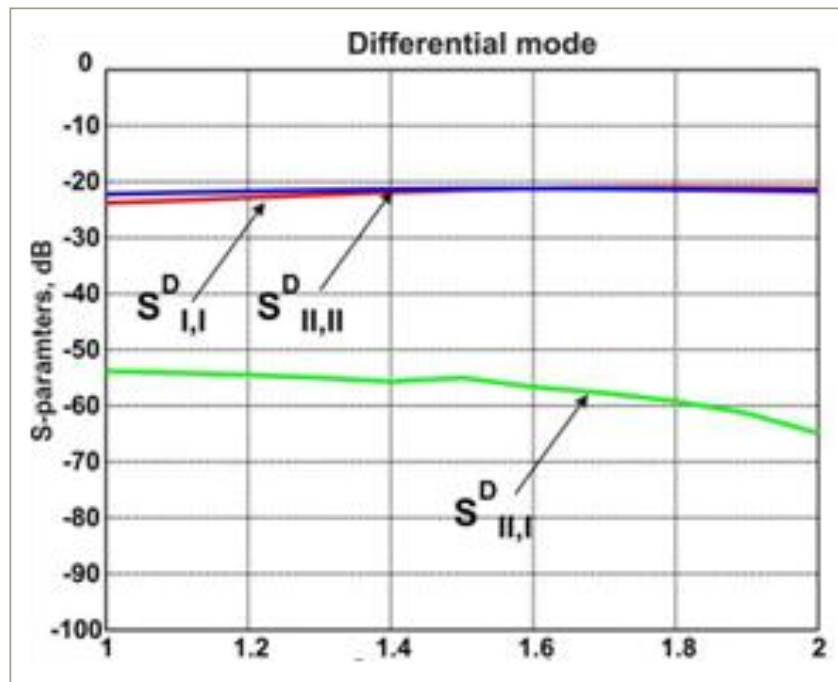


Figure 3-15. Differential-mode results for the terminated four-port quad line column

The isolation between two differential modes approaches about 60 dB, which confirms the high-isolation properties of the quad line. On the other hand, the return loss of individual modes remains rather high – approximately -22 dB; this may be due to the lumped-load approximation used or insufficient accuracy of the impedance data.

3.5 Complete Antenna-Transmission Line Model

The phased array requirement of a wideband radiator requires a wideband feed. The wideband, high isolation quad line was presented in Section 3.4.

The basic requirement for the droopy bowtie turnstile radiator is that each pair of bowties is fed with equal voltage with 180 degree phase shift between voltages- this ensures balanced current distribution along the bowtie. One approach that has been widely used to feed standard dipole antennas has been the Dyson balun^{3.37-3.42}; Section 3.5.2 presents the complete antenna-balun transmission line model for the droopy bowtie turnstile radiator with quad line feed.

3.5.1 Built-in Hybrid

A disadvantage of the Dyson balun is the necessity of a 180 degree wideband hybrid coupler. While there is no problem to purchase such a coupler at L- and S- band (e.g., from MiniCircuits), the commercial hybrid at X-band, or higher frequencies, is bulky and relatively expensive. It is preferred to have the hybrid implemented together with the antenna on a printed wiring board. One canonic setup is the rat-race coupler^{3.43}; three other simple setups are adopted from Refs.^{3.44-3.45}. At first sight, most inviting is the balun on the base of two band-pass filters with open or short quarter wave stubs^{3.44}. These dual filters are one-quarter wavelength long at band center and have the property that the image phase shift of the upper filter (with the pair of open-circuited stubs) – that is -90 deg – is always 180 degrees greater than that of the lower filter – +90 deg (with the pair of short-circuited strips). At the frequencies where the normalized image impedances of the coupled-strip-line filters are equal to unity, the input VSWR of the balun is also unity and the ratio of balanced to unbalanced voltage at the output ports is infinite^{3.44}. The theoretical balun bandwidth for 1.2 VSWR and for balanced-to-unbalanced voltage ratio in excess of 15 dB is on the order of 100% or higher^{3.44}; measured values have balanced-to-unbalanced voltage ratio about 12dB in the center of the band^{3.44}. However, a closer look at the design of reference 3.5.8 for our antenna element shows that the image impedances of the short-short coupled-line band pass filter are significantly different from those of the open-open section, at the same filter dimensions. Furthermore, it is difficult to realize the short-short section of the filter on a printed wiring board at X-Band, due to small gap size. Therefore, we eventually decided to abandon this design and turn back to a simpler $\lambda/2$ delay line with some broad-banding elements.

3.5.2 Antenna-Balun Transmission Line Model

Figure 3-16 shows the complete antenna-balun transmission line model for the droopy bowtie turnstile radiator for dual-linear polarization operation; the model shows excitation of one pair of droopy bowtie radiators with input impedance Z_D . Each section is described:

- 180 degree hybrid.
 - Power divider. Balanced power split realized in a printed wiring board by an equal power split Wilkinson divider^{3.45-3.49}; voltage imbalances at the two output ports resulting in reflected power are terminated in a resistor that is placed between the two output arms;
 - 180 degree phase shifter. A wide band stripline balun^{3.44} is used to connect the unbalanced stripline circuit (Wilkinson divider) to the balanced circuit (one pair of droopy bowtie radiators);
- Quad line balun column.
 - Connects the 180 degree hybrid outputs to each bowtie;
 - Provides a coincident phase center feed for the two polarizations

A complete antenna-balun model, assuming a dipole-like antenna with input impedance Z_D and coupling impedance Z_c can be derived from^{3.50}. For a symmetric antenna load with input impedance, Z_D , the antenna model can be simplified as shown in Figure 3-16. The power divider is either a T-divider or a Wilkinson power divider.

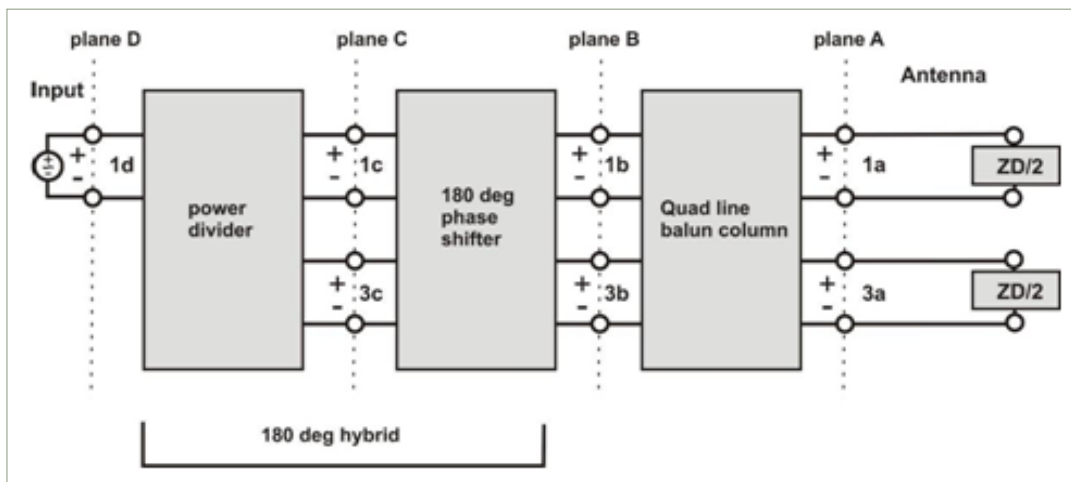


Figure 3-16. Complete Dyson balun-based antenna radiator with a symmetric antenna load. The balun for only one antenna element is shown.

Figure 3-17 illustrates where the quad line is inserted in the transmission line model.

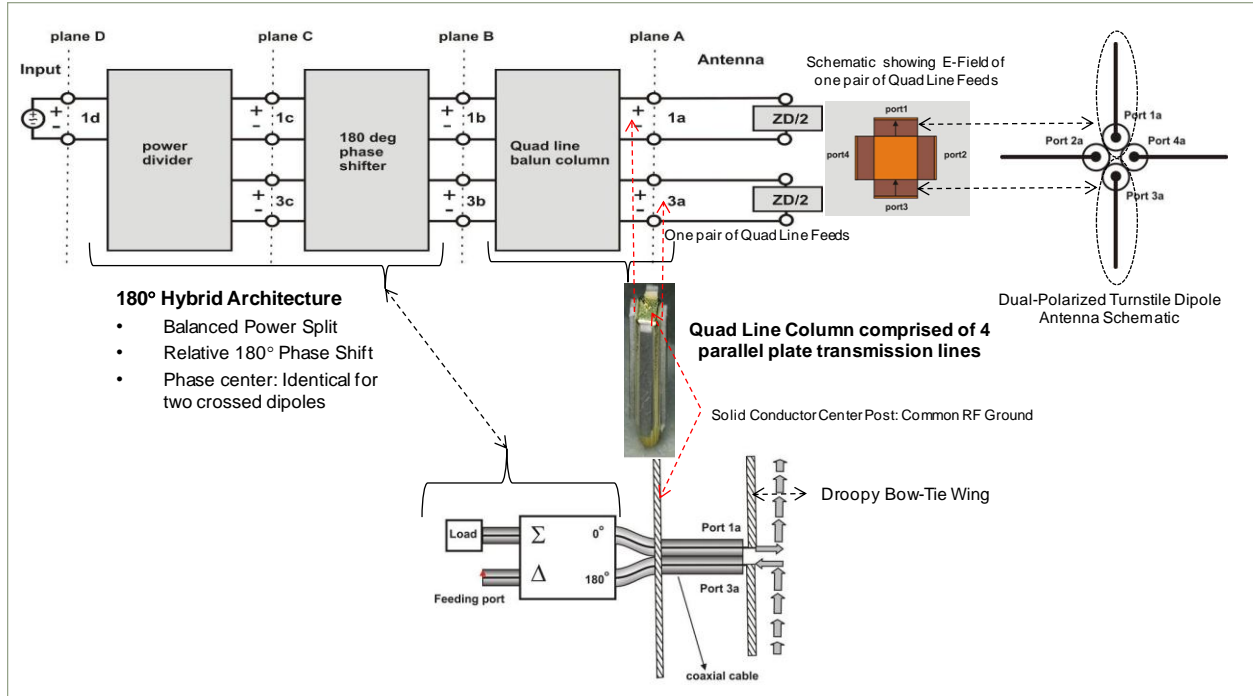


Figure 3-17. Antenna-balun transmission line model for the droopy bowtie turnstile radiator with quad line feed

The model of the quad line column is that of a transmission line with termination impedance $Z_T = Z_D / 2$. The transformed impedance is then given by^{3.51}:

$$Z_{in} = Z_0 \frac{Z_T + jZ_0 \tan \beta L}{Z_0 + jZ_T \tan \beta L} \quad (3.5.1)$$

where L is the quad line length. Similarly, the ratio of input to output voltage is found from the ABCD matrix of a two-port network, in the form,

$$\frac{V_{in}}{V_T} = \cos \beta L + j \frac{Z_0}{Z_T} \sin \beta L \quad (3.5.2)$$

For the phase shifter, we will use a simple $\lambda/2$ delay line. Note that using the delay line on one port already introduces asymmetry into the setup. The power divider model considered above is capable of taking this asymmetry into account. A transmission line model for coupled microstrips can be found in^{3.52-3.54}.

Power dividers vary widely with particular advantages and disadvantages^{3.55-3.57}. Multiple synthesis procedures for the Wilkinson power divider have been proposed and realized^{3.56-3.57}. Figure 3-18 shows one section of an axially symmetric Wilkinson power divider, represented as a four-port network, which includes two (generally uncoupled) symmetric transmission lines of length l , and an additional block with shunt conductance, G . For the first section, two input ports would be coupled so that their voltages are equal.

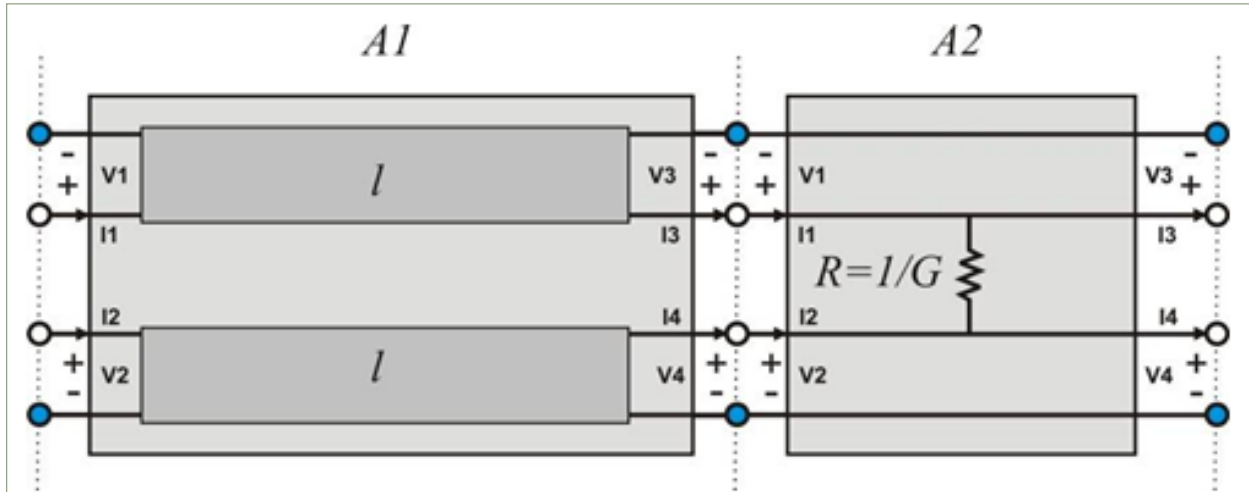


Figure 3-18. Four-port model of one section for the standard Wilkinson power divider

Cohn's two- and three-section power Wilkinson divider with $f_2/f_1=2$ are discussed in^{3.56} for a three-section power divider with high output port isolation of about 40 dB over the band – with all sections exactly quarter wavelength – we can observe that the high port isolation is not an issue in our case since one power divider is always feeding the same antenna (as a part of the Dyson balun), but not two different antennas. Therefore, a less involved two-section power divider may be used^{3.56}, with the same return loss bandwidth.

As far as power loss and phase transformation for the Wilkinson power divider is concerned, it is the odd mode in the power divider that is responsible for current flow and power loss in the shunt resistors. This mode will be excited if the termination impedances are not equal.

Note that the transmission line model for the T-divider is that for the Wilkinson divider, but without the second block A2 in Figure 3-18. The only meaningful blocks are two matching $\lambda/4$ transmission line sections for the input ports. They should match the impedance of the summing (output) port multiplied by two, to the impedance of each input port.

3.5.3 Power Divider Design

It is anticipated that the summing port of the divider must be matched to $Z_{in} = 50$ Ohm, but the input ports are to be matched to some different value, such as $Z_{in} = 30$ Ohm in the present case. For the T-divider, this problem is solved by introducing a characteristic impedance Z_0 of the matching $\lambda/4$ -sections in the form:

$$2Z_{in} = \frac{Z_0^2}{Z_m}, \quad Z_0 = \sqrt{2Z_{in}Z_m} \quad (3.5.3)$$

which gives us a conventional value of characteristic line impedance close to 50 Ohm for $Z_{in} = 50$ Ohm and $Z_{in} = 30$ Ohm, respectively.

A Wilkinson power divider with higher port isolation is not required since the divider drives two wings of the same antenna, and is a part of the balun to *one* antenna. The cross-polarization isolation between two antennas for two different polarizations is not affected by the power divider. The divider has to be only symmetric over the band. A simpler T-divider^{3.44-3.46}, with impedance matching between ports using a quarter wave transformer will perform the same function for a symmetric antenna and have simpler construction. On the other hand, for an asymmetrical antenna load, the Wilkinson power divider should still deliver the receiving power to the summing port instead of leakage to the second antenna wing.

3.6 Summary

Chapter 3 began with an outline of present and future radar requirements: increased sensitivity and significantly lower cost. Radar system requirements and cost pressure demand radiator and radiator RF feed designs that provide excellent, versatile RF performance and significantly lower recurring and non-recurring engineering (NRE) cost.

Chapter 3 developed a new radiator and radiator feed for phased arrays: the droopy bowtie turnstile radiator with quad line feed:

- The bowtie radiator was selected based on its inherent wideband RF performance and simple construction;

- A droopy bowtie radiator simulation model was developed and parameterized for HFSS analysis;
 - infinite array and isolated performance were presented;
- Cross-polarization performance of the droopy bowtie turnstile radiator was presented and compared with a dipole element and “Bunny Ear” element;
- The feed and balun approach was developed. A novel quad line balun column feed made out of four individual transmission striplines around a common solid ground conductor was presented and analyzed for its impedance and isolation properties;
- The complete antenna-transmission line model brought together the power divider network, the 180 degree hybrid, the quad line balun column and droopy bowtie turnstile radiator. This network model will be the basis for the practical construction of the droopy bowtie turnstile radiator with quad line feed presented in Chapter 4.

The following chapter will present manufacturing approach for the droopy bowtie turnstile radiator with quad line feed as well as measured data for prototypes at L-Band and X-Band.

Chapter 4 – Practical Realization and Applications of Droopy Bowtie for Finite Arrays

4.0 Introduction

Chapter 3 presented the driving requirements for present and future phased arrays and flowed down the high level requirements to the radiator and radiator feed requirements.

Chapter 3 developed the design and theory of a new radiator and radiator feed for phased arrays: the droopy bowtie turnstile radiator with quad line feed. The next step is the practical realization of the droopy bowtie turnstile radiator with quad line feed for applications in finite phased arrays^{4.1}.

Chapter 4 presents a low cost manufacturing and assembly approach applied to the droopy bowtie turnstile radiator with quad line feed that leverages commercial techniques, materials and automation that are used across industries such as the electronics industry and auto industry.

HFSS models for the “Gen 1.0” and “Gen 2.0” prototype droopy bowtie turnstile radiator with quad line feed are presented. Gen 2.0” prototype droopy bowtie turnstile radiator with quad line feed HFSS infinite array simulations of the return loss versus scan volume and frequency and embedded element pattern versus frequency are presented.

Measurements of a prototype L-Band droopy bowtie turnstile radiator with quad line feed and X-Band droopy bowtie turnstile radiator with quad line feed are presented. In the case of the X-Band droopy bowtie turnstile radiator with quad line feed, an injection molded and plated droopy bowtie is fabricated and tested for the first time.

4.1 Droopy Bowtie Radiator with Quad Line Feed: Manufacturing Approach

A key requirement for the droopy bowtie turnstile radiator with quad line feed is low recurring cost. Section 4.1 presents the low cost fabrication and assembly approach for the droopy bowtie turnstile radiator with quad line feed.

4.1.1 Approach

The radiator and feed RF design was approached by first considering low-cost manufacturing processes and robotic assembly techniques:

- Identify commercial industrial base that supports proposed manufacturing and assembly approach;
- Assembly based on automated pick-and-place of components
- Automated application of solder or conductive epoxy;

Figure 4-1 shows two concepts of an 8 x 16 droopy bowtie turnstile radiator array fabricated and assembled using the processes and techniques described in this chapter.

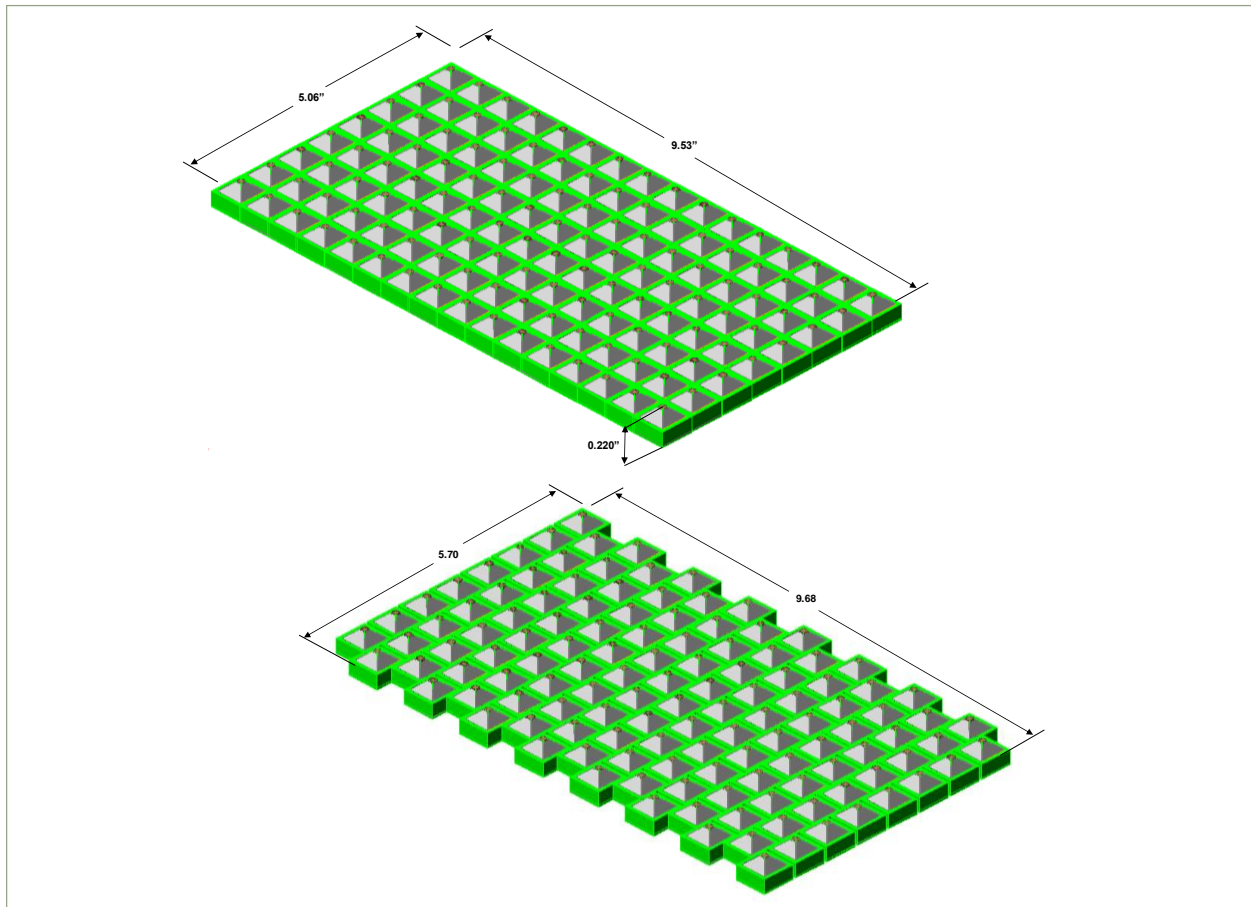


Figure 4-1. Injection Molded, 8 x 16 droopy bowtie turnstile radiator array: Top: rectangular lattice; Bottom: triangular lattice

4.1.2 Injection Molded Radiator

There is a large, commercial vendor base for supplying injection molded parts and for plating injection molded parts. The injection molded bowtie radiator is a three-dimensional structure that is copper plated to realize the bowtie radiator; an opening at the top allows the quad line feed assembly to be inserted. A brief description is given on the fabrication process:

- a) Injection Molded Part. Injection molding is a manufacturing process where heated molten plastic is forced into a mold cavity under pressure. A mold cavity is a negative of the part being produced, when the cavity is filled with plastic, it is cooled and the plastic becomes solid material resulting in a completed positive component. The most common material used for injection molds is Liquid Crystal Polymer (LCP); LCP is injected into the mold material^{4,2};
- b) Copper Plating. The bowtie wings are realized by copper plating; the copper may be selectively removed using a laser; or, copper is direct pattern plated on injection mold.

Figure 4-2 shows a Gen 1.0 prototype 2x6 element injection molded array; the radiator is integral with the egg-crate cavity. The square hole in the middle of each radiator is for assembly of the RF quad line feed. Figure 4-3 shows a prototype Gen 1.0 droopy bowtie radiator before and after laser etch.

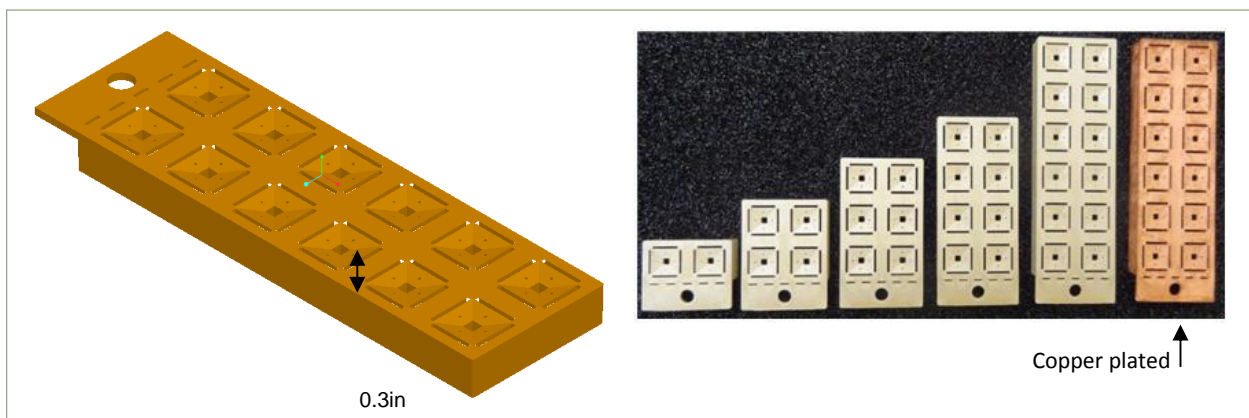


Figure 4-2. Injection Molded, Gen 1.0 droopy bowtie turnstile radiator array: Left: 2x6 drawing; Right: injection molded prototypes

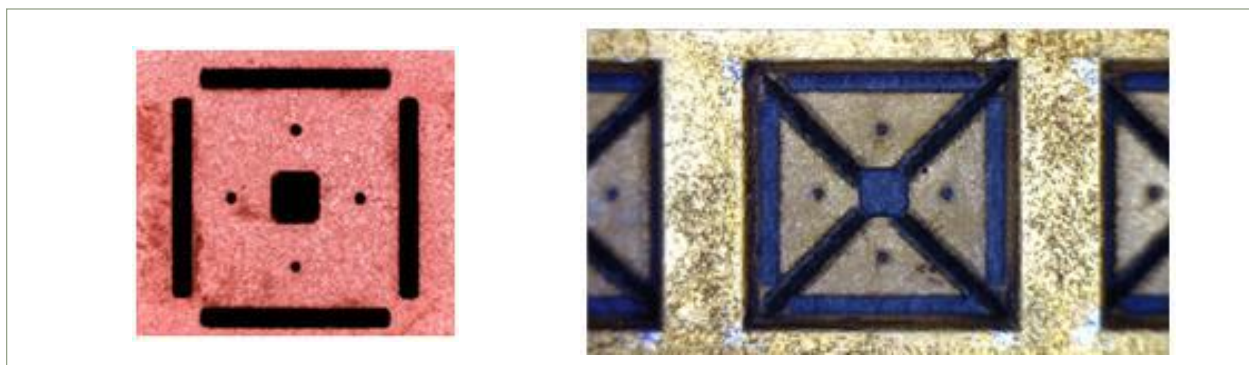


Figure 4-3. Right: injection molded, copper plated Gen 1.0 droopy bowtie radiator Left: Gen 1.0 droopy bowtie radiator after laser etch

Figure 4-4 shows the new, Gen 2.0 droopy bowtie radiator as a separate subassembly from the eggcrate base; this was done to facilitate assembly:

- Assembly. Each molded radiator is placed over each cavity of the egg-crate base; features on the radiator locate and align the radiator to the egg-crate base. An opening in the center of the radiator allows the RF feed assembly to be inserted.

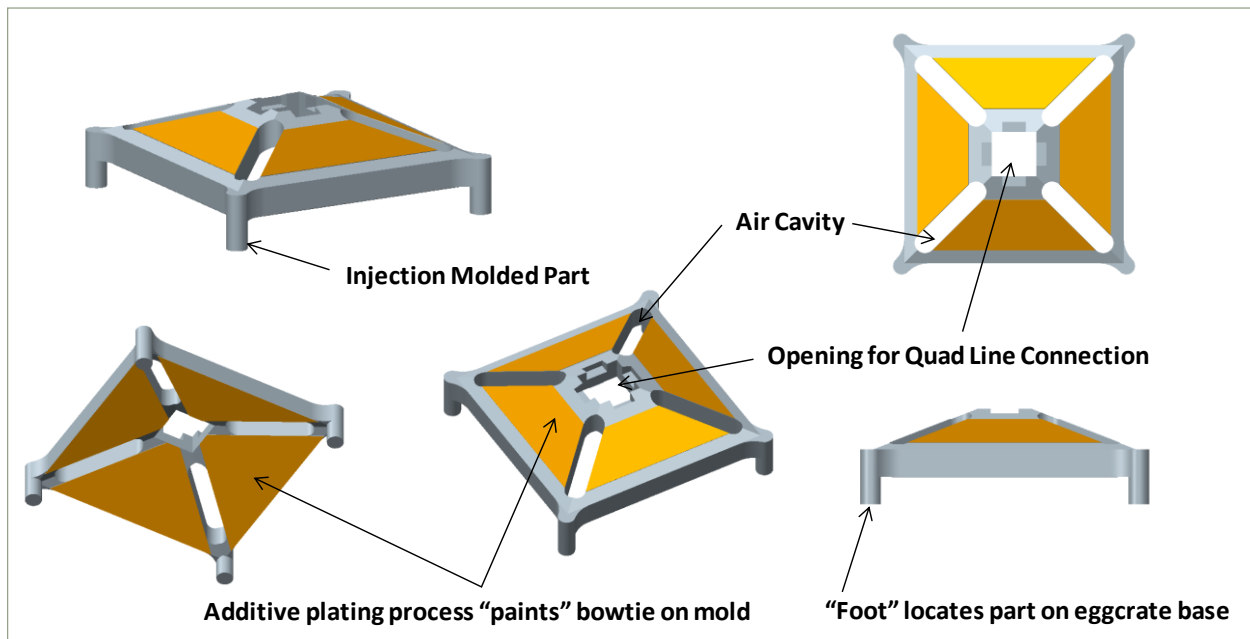


Figure 4-4. Injection molded, plated Gen 2.0 droopy bowtie radiator model

Figure 4-5 shows the prototype Gen 2.0 droopy bowtie radiator. The Gen 2.0 droopy bowtie radiator is an injection molded liquid crystal polymer. The first prototypes were silver epoxy spray coated; the edges and openings in the droopy bowtie radiator were masked and the excess silver epoxy was laser ablated. Note the following features in Figure 4-5: in the top view, there are 4 notches in the mold- this is where the conductive epoxy or nanosilver paste is applied to make electrical connection with the quad line feed; in the bottom view, the plating wraps around from the lower bowtie and into the notch area- the electrical connection is made between the lower bowtie and the quad line feed- the upper bowtie is parasitically coupled to enhance RF bandwidth.

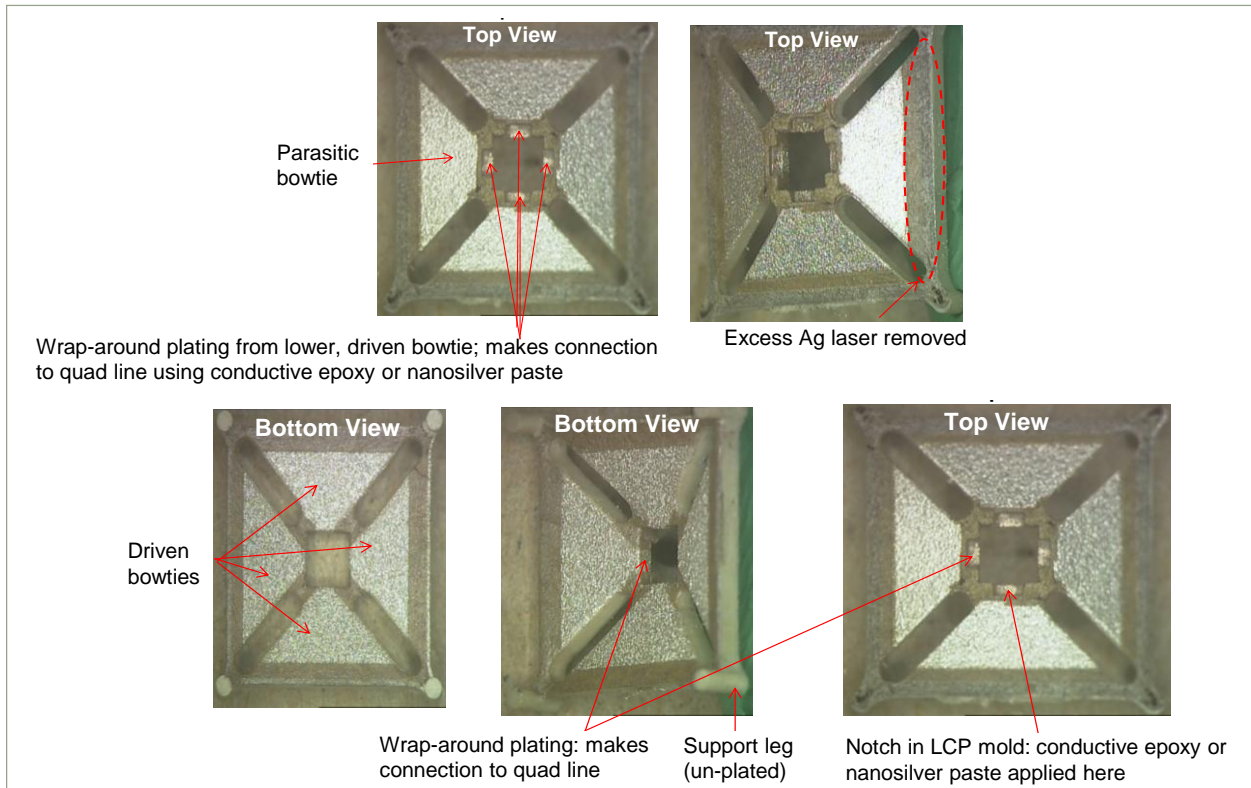


Figure 4-5. Injection molded, silver epoxy spray plated Gen 2.0 droopy bowtie radiator

Figure 4-6 provides an up close view of the bottom of the droopy bowtie.

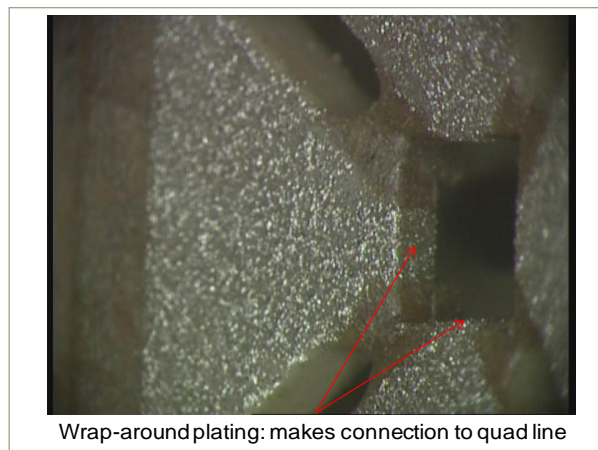


Figure 4-6. Close-up: injection molded, silver epoxy spray plated Gen 2.0 droopy bowtie radiator

The technical specifications of the silver epoxy are given in Table 4-1^{4.3}.

Table 4-1. Silver epoxy technical specifications

| Technical Specifications | |
|--------------------------|-------------------------|
| Material | Silver in epoxy |
| Shielding (@ 1GHz) | >90dB |
| Sheet Resistance | 13mΩ/sq |
| Density | 2.7gr/ cm3 |
| Salt Spray | Excellent after 1000hr |
| Thermal Shock | -65°C to + 200°C |
| Adhesion | ASTM D3359 Class 5 |
| Process Steps | Two (1) Spray, (2) Cure |

Figure 4-7 compares microstrip line insertion loss (dB/in) for copper, aluminum and the silver epoxy spray coating versus frequency^{4.4}.

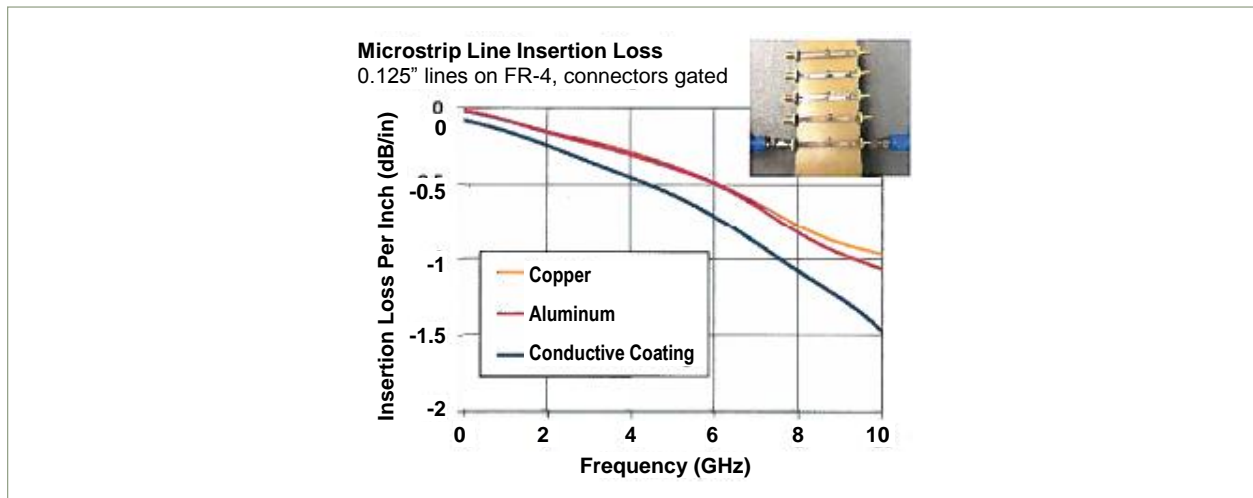


Figure 4-7. Microstrip line insertion loss: silver epoxy spray vs copper and aluminum

Figure 4-8 compares the efficiency of a copper conductor dipole versus a silver epoxy spray coated dipole^{4.5}.

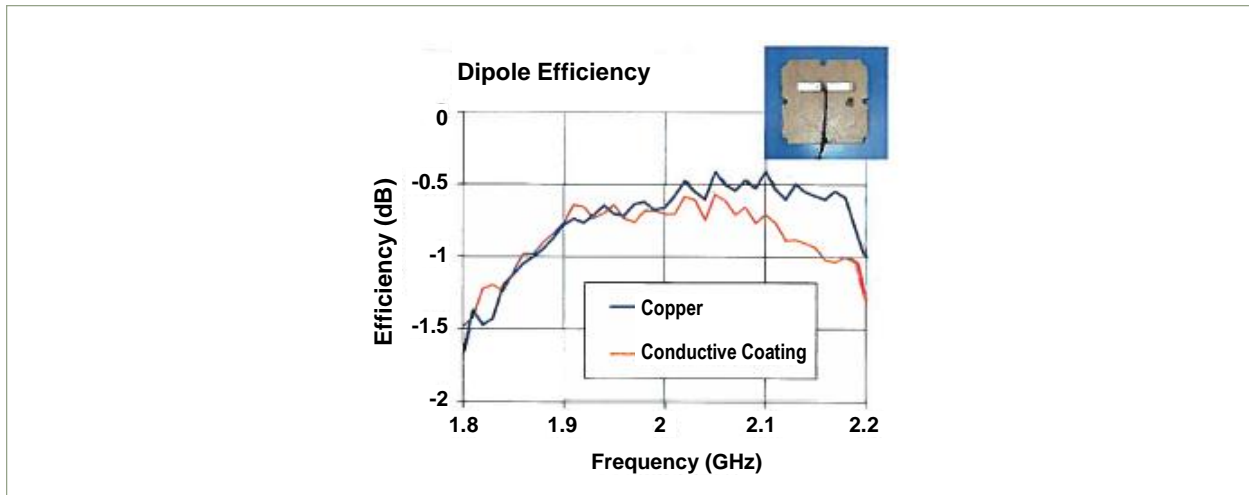


Figure 4-8. Dipole efficiency: silver epoxy spray vs copper

Overall, the silver epoxy spray is a cost effective 3-D metallization designed for harsh environments with good conductivity.

4.1.3 The Quad Line Feed Assembly

The quad line RF Feed Assembly consists of 4 RF transmission lines bonded to a metallic post; each part of the assembly optimizes RF performance or lowers fabrication and assembly cost:

- RF Performance. RF Material. Each parallel plate transmission is a double – copper sided printed wiring board strip made of Rogers RT/duroid 6010 PTFE; the 6010 material has a high dielectric constant, $\epsilon_r = 10.2$, and low loss tangent, 0.0023, ideal for a high isolation, low RF loss radiator feed;
- Assembly. Knurled part of post is inserted into the printed wiring board assembly during pick-and-place assembly process;
- Cost: The metallic balun column is low-cost: either a zinc-plated cast or plated-plastic molded part.

Figure 4-9 illustrates the quad line feed assembly concept; note the knurled post to secure the quad line feed into the printed wiring board during assembly.

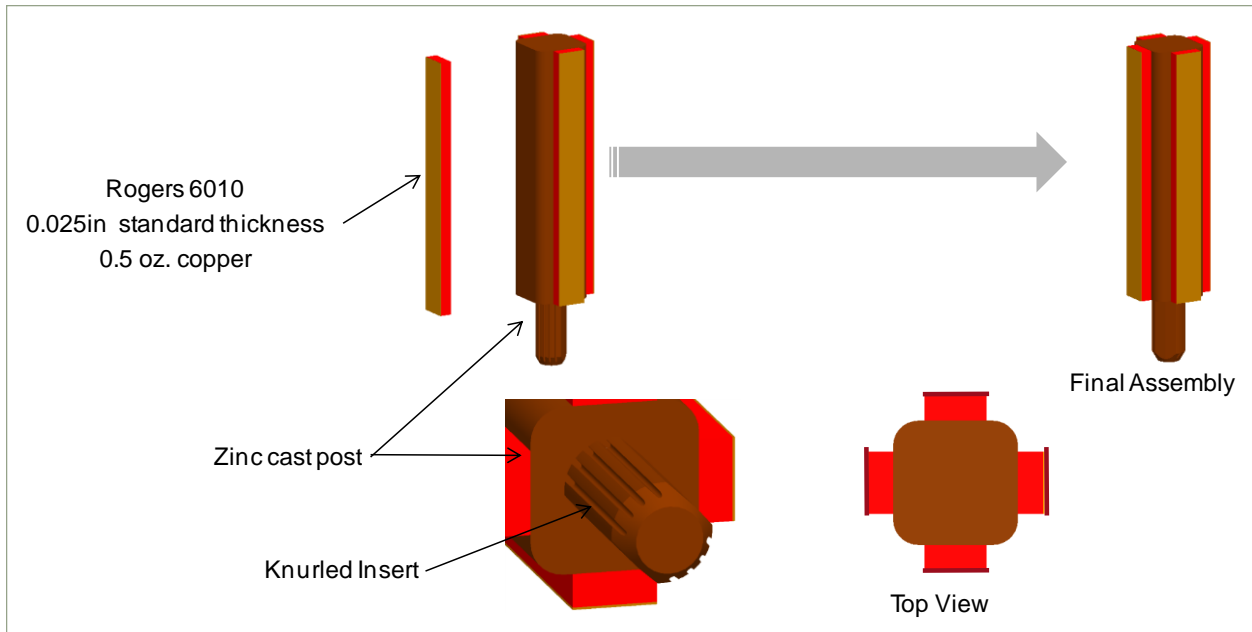


Figure 4-9. Quad line feed assembly concept

Figure 4-10 shows a prototype X-Band quad line feed assembly.

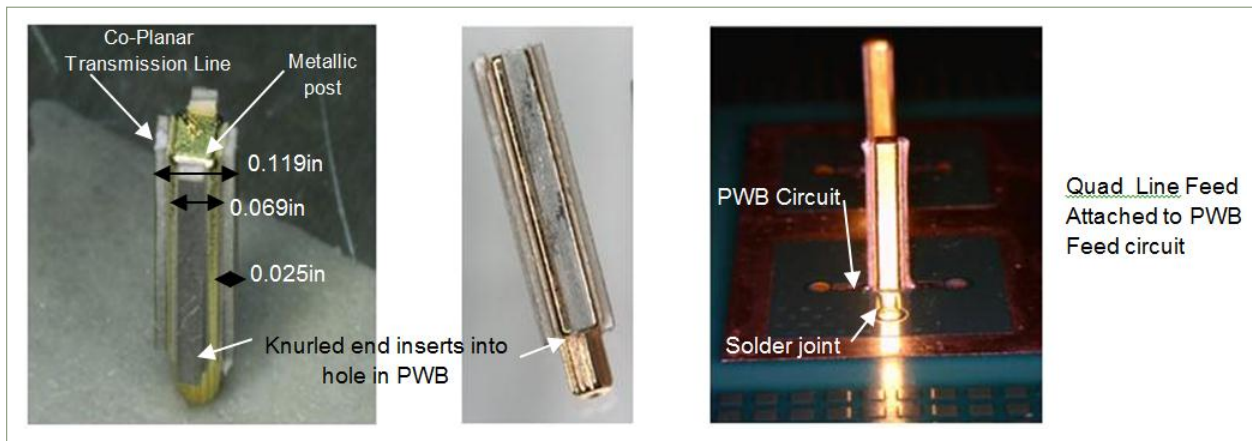


Figure 4-10. Quad line feed assembly

4.1.3.1 Quad Line Feed Assembly Process

The quad line feed assembly is made of two parts: 1) Injection zinc molded center post, nickel-gold plated and 2) Rogers RT/duroid 6010 PTFE double – copper sided parallel plate transmission line.

Figure 4-11 shows a printed wiring board sheet of Rogers RT/duroid 6010 with an array of strips; the sheet has 300 strips.

The double – copper sided parallel plate transmission lines are produced from a single printed wiring board sheet of Rogers RT/duroid 6010 as shown in Figure 4-11; each strip is copper etched to exact dimensions using fiducials on the printed wiring board; a laser is then used to route out the strip leaving two tabs The quad line feed assembly process is outlined in Figure 4-12:

- 1) Dispense conductive material onto quad line strips in pwb array;
- 2) Pick and place center post, within half mil tolerance, on quad line strips and cut tabs;
- 3) Die cut punch out first pass assemblies;
- 4) Repeat steps 3 through 4, 3 more times to produce finished quad line assembly

Figure 4-13 shows an example of batch process assembly of the quad line feed assembly.

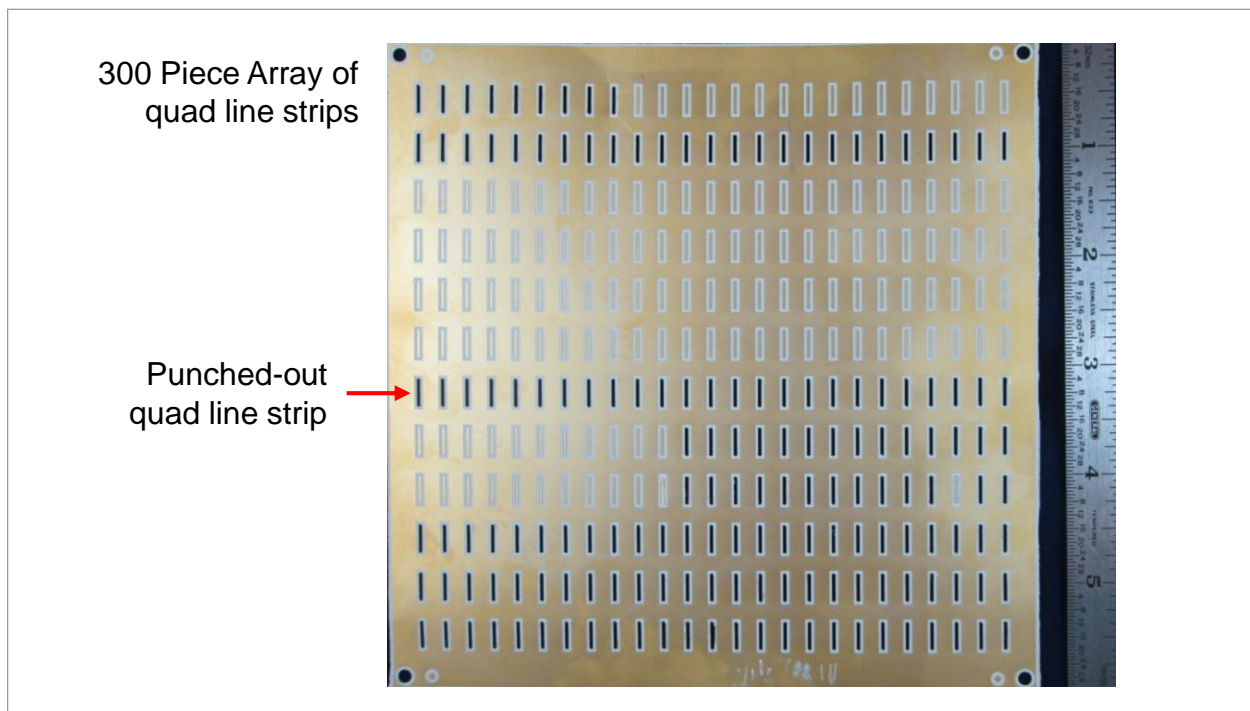


Figure 4-11. Printed wiring board array of quad line strips

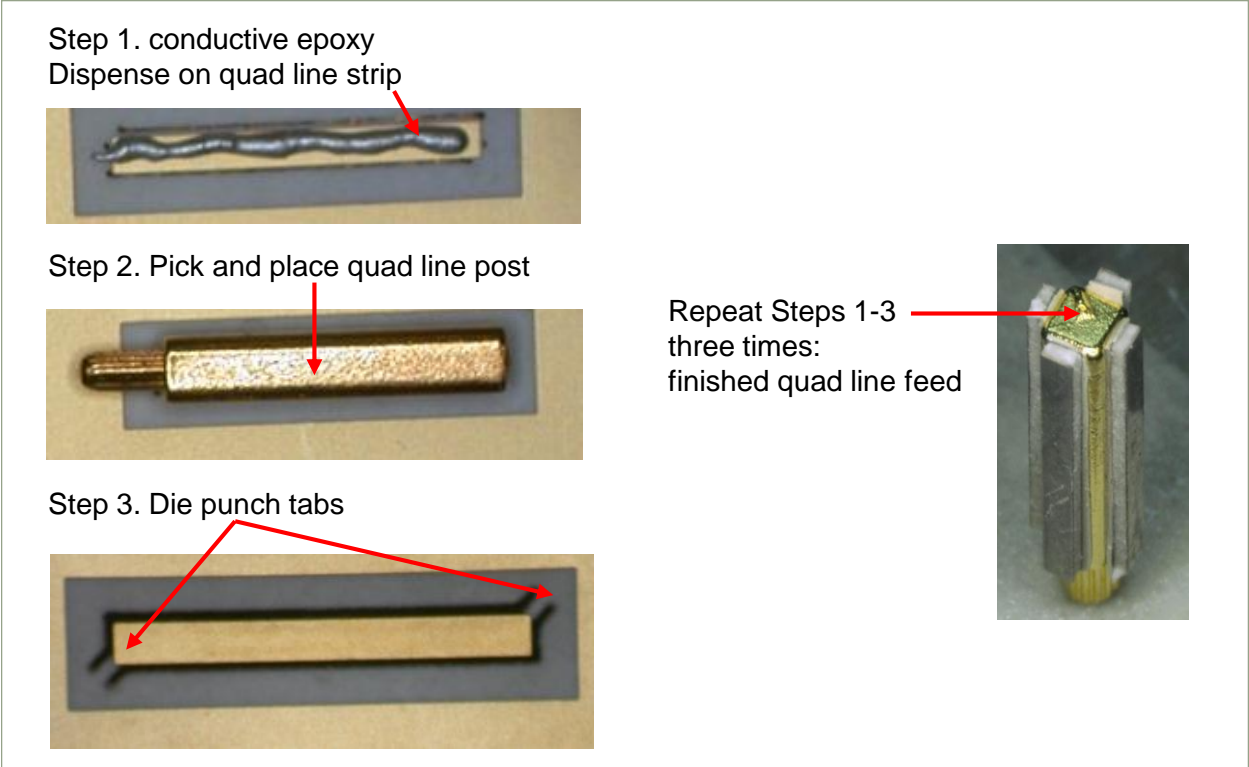


Figure 4-12. Semi-automated quad line feed assembly



Figure 4-13. Batch process: quad line feed assembly

4.1.3.2 Unit Cell Assembly Concept

Figure 4-14 shows a number of views of an assembled droopy bowtie radiator unit cell and summarizes the assembly concept of Section 4.1.3.

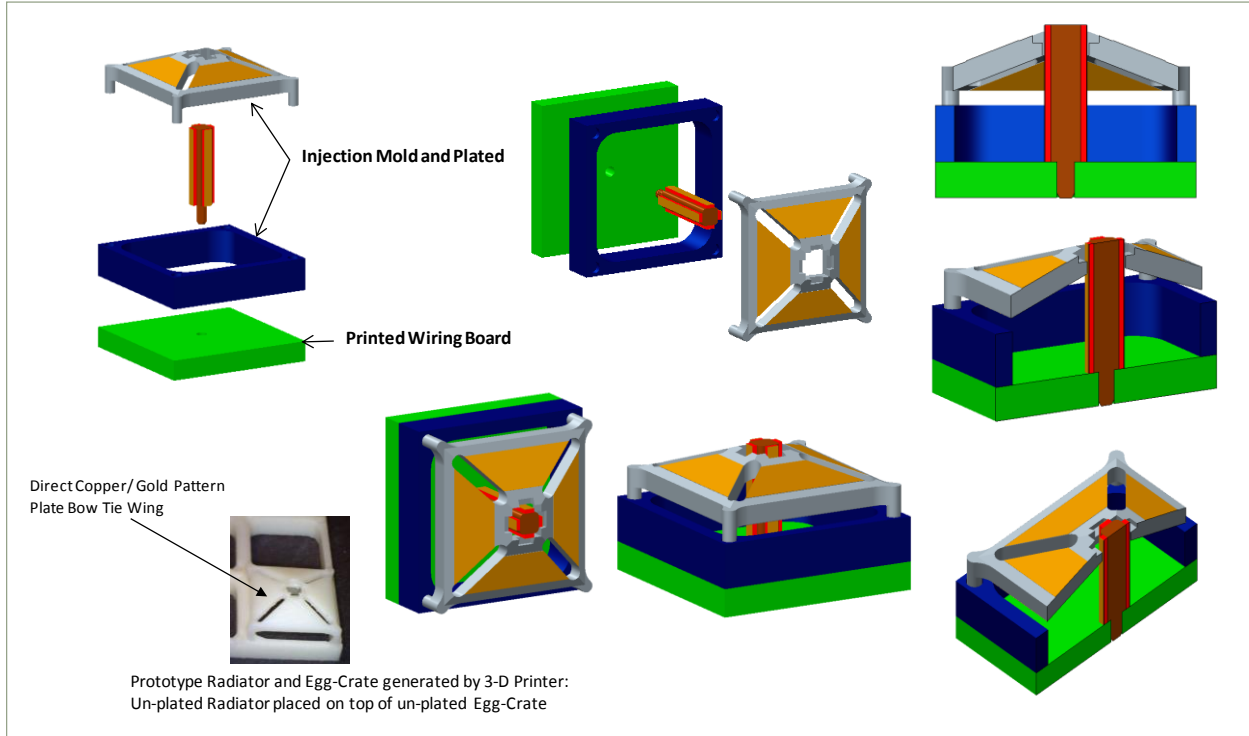


Figure 4-14. Droopy bowtie with quad line feed: unit cell assembly concept

4.2 Array Assembly

Array assembly for the Gen 1.0 and Gen 2.0 droopy bowtie and quad line feed arrays use commercial pick – and – place robots as shown in the Figure 4-15. The droopy bowtie and quad line feed subassemblies combine RF performance objectives with low cost manufacturing; the assembly steps for the droopy bowtie and quad line feed are outlined:

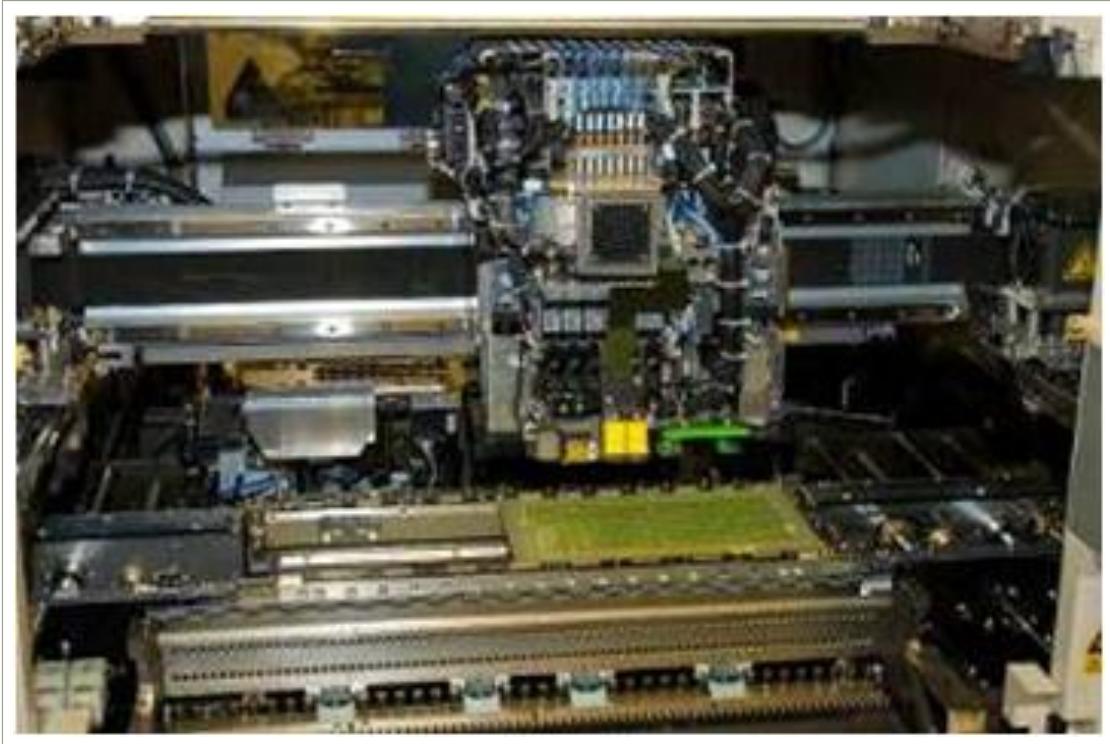


Figure 4-15. Pick-and-place robot

1. Start with standard printed wiring board (pwb) carrier. The pwb defines the basic building block of the droopy bowtie radiator with quad line feed. Figure 4-16 shows the prototype 2x6 Gen 2.0 pwb; the unit cell shows 4 co-planar transmission lines that are connected to the quad line feed with a conductive epoxy. The pad for each coplanar line transitions to a coaxial connector on the reverse side, shown in Figure 4-17, with a plated through hole via; there are also plated vias surrounding the pad and coplanar lines connecting the ground plane surrounding the coplanar lines and the ground plane on the coaxial connector side. The coaxial connectors are soldered on the pwb;
2. Quad line feed to printed wiring board assembly;
 - a. The quad line feed assemblies are pressfit into the printed wiring board. The concept is shown in Figure 4-18;
 - b. The fixture is pinned to the printed wiring board;
 - c. Each quad line feed is loaded into the alignment fixture and pressed into the printed wiring board in a single stroke with a top plate (not shown);

- d. After each quad line is inserted into the pwb carrier, conductive epoxy (or nanosilver paste) is automatically dispensed as the base of the quad line between the coplanar line and the outer conductor of the quad line.
3. Eggcrate to printed wiring board assembly: see Figure 4-19 and Figure 4-20.
 - a. Conductive epoxy is automatically dispensed on pwb;
 - b. Place eggcrate on pwb: alignment pins in pwb locate and secure eggcrate;
 - c. Epoxy cure cycle;
4. Droopy bowtie assembly to eggcrate
 - a. Autodispense adhesive on eggcrate; Pick and place droopy bowtie assembly on eggcrate; see Figure 4-21;
 - b. Features in eggcrate align droopy bowtie assembly and locates quad line feed Autodispense conductive epoxy to make final electrical connections between quad line feed and bowtie wings on underside of droopy bowtie assembly.
 - c. Epoxy cure cycle;
 - d. Final 2x6 droopy bowtie with quad line feed assembly; see Figure 4-22

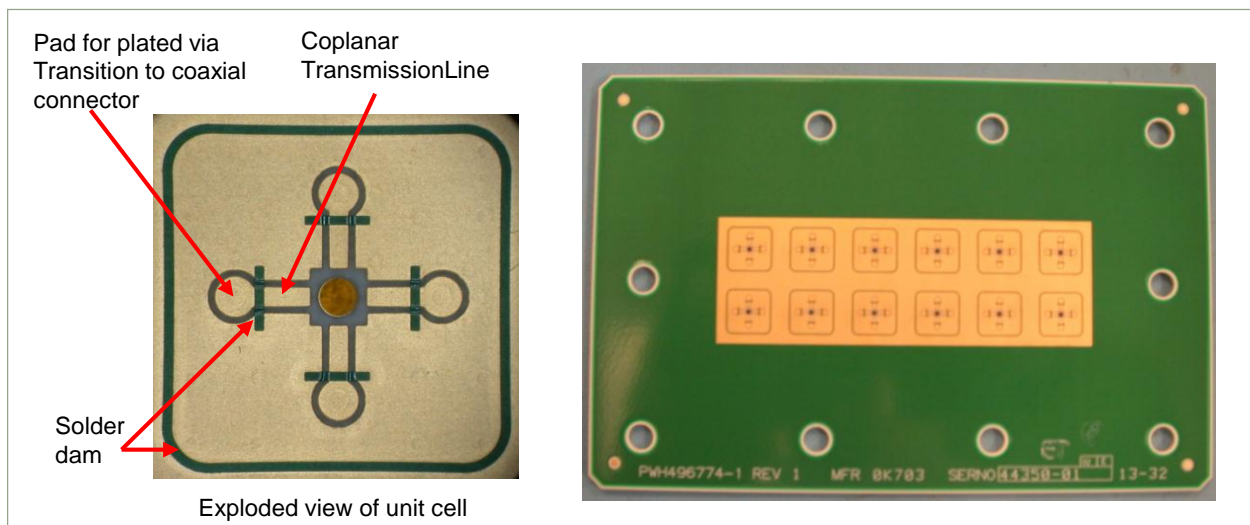


Figure 4-16. 2x6 Printed wiring board-radiator side

GPPO coaxial connector

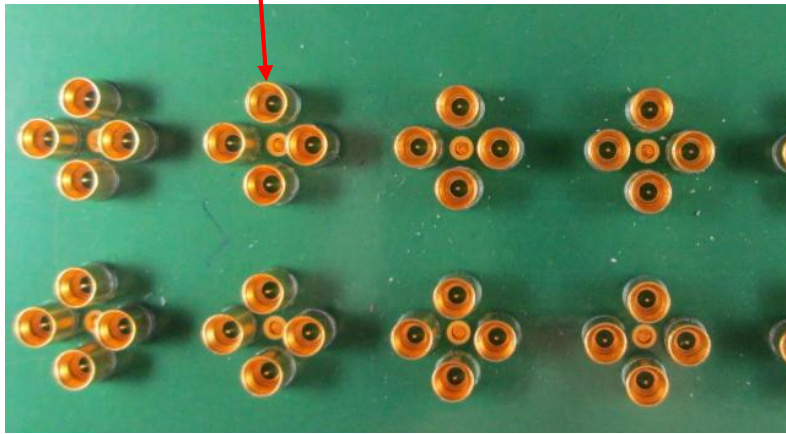


Figure 4-17. 2x6 Printed wiring board-connector side

Locating pins in pwb for fixture and eggcrate alignment

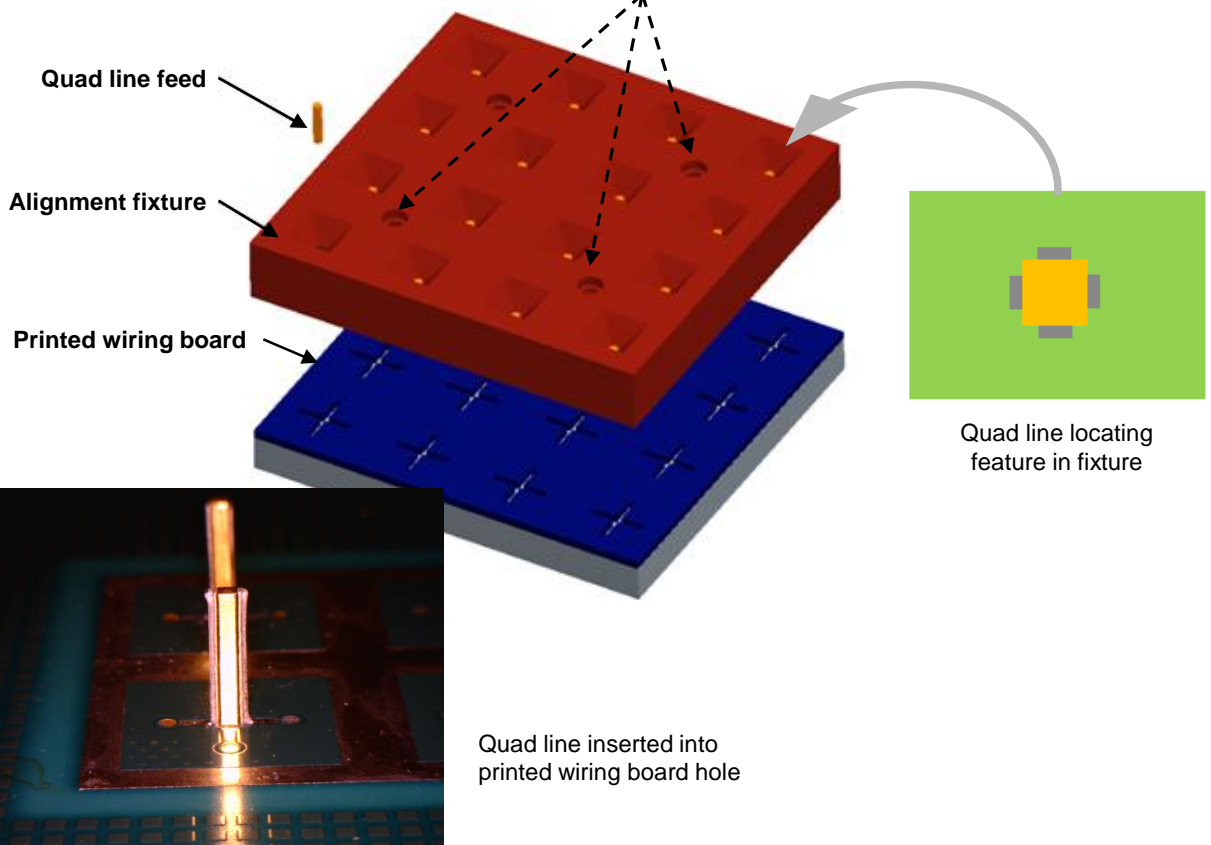


Figure 4-18. Quad line feed assembly process

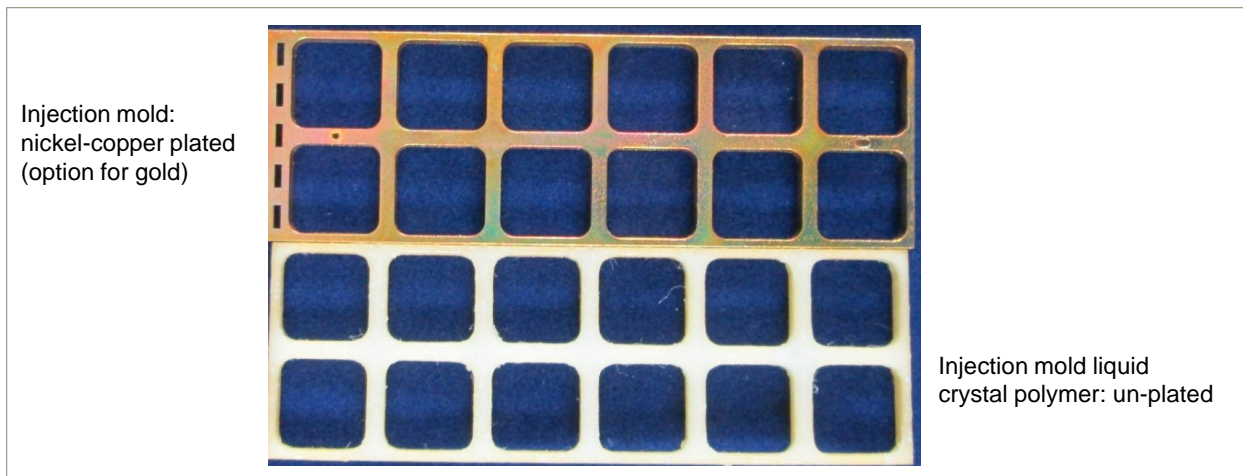


Figure 4-19. 2x6 eggcrate assembly

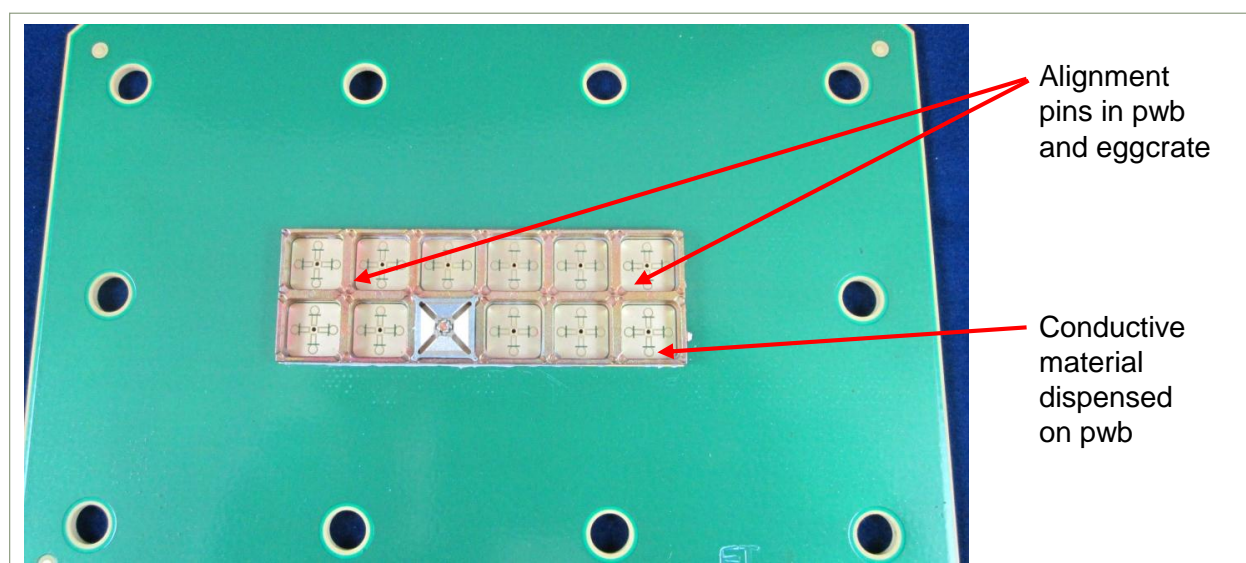


Figure 4-20. 2x6 eggcrate assembled to pwb carrier

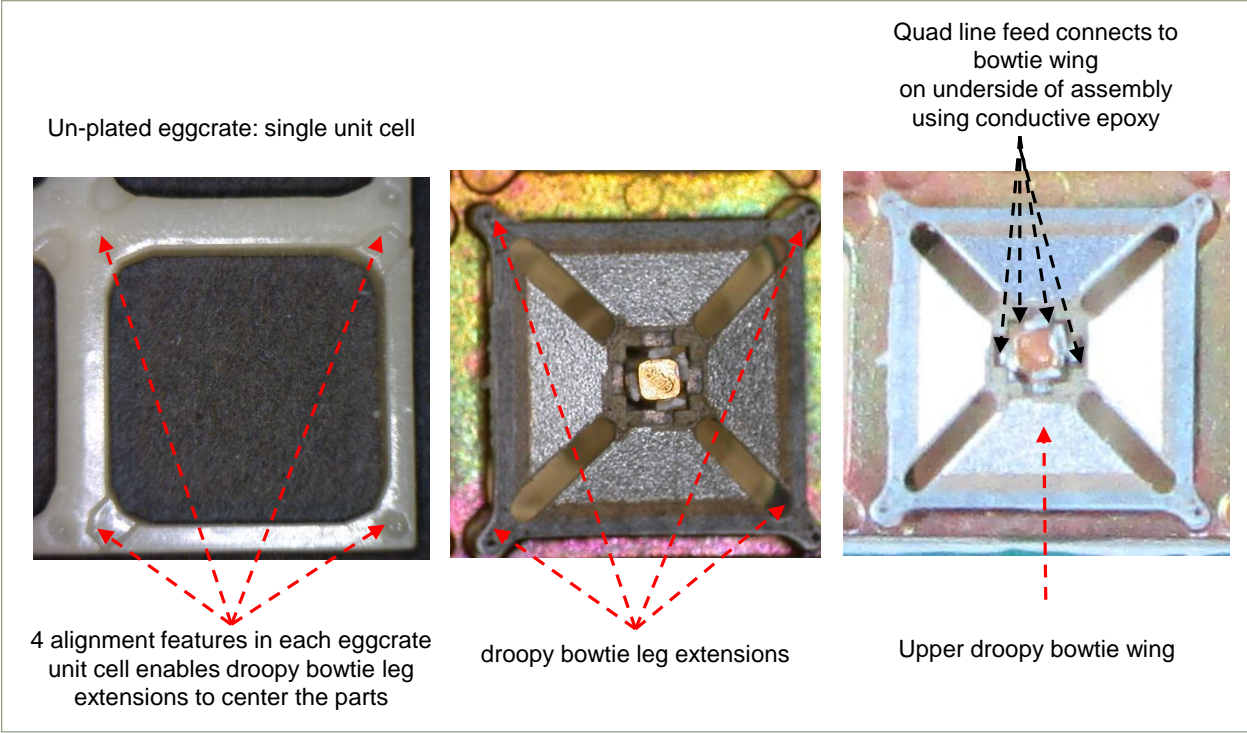


Figure 4-21. Droopy bowtie assembled to eggcrate unit cell

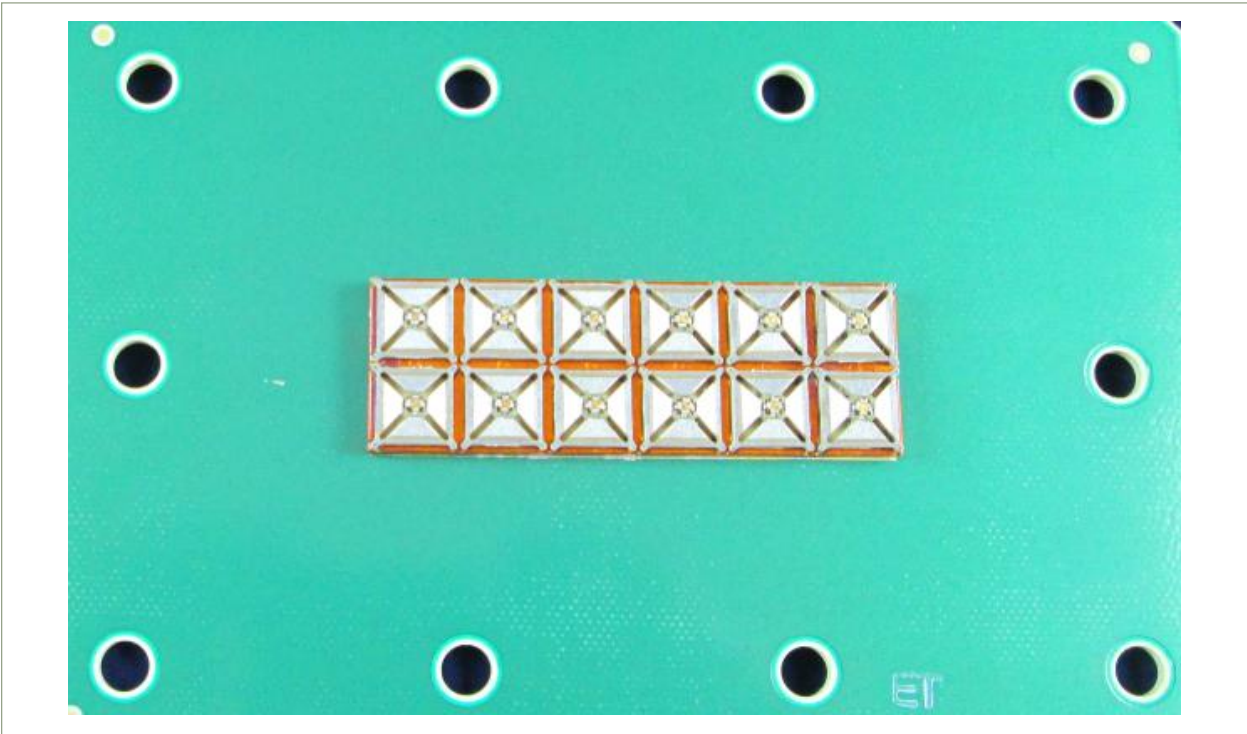


Figure 4-22. 2x6 Gen 2.0 X-Band droopy bowtie radiator with quad line feed

Figure 4-23 and Figure 4-24 summarize the assembly sequence for the example of a 2x6 array.

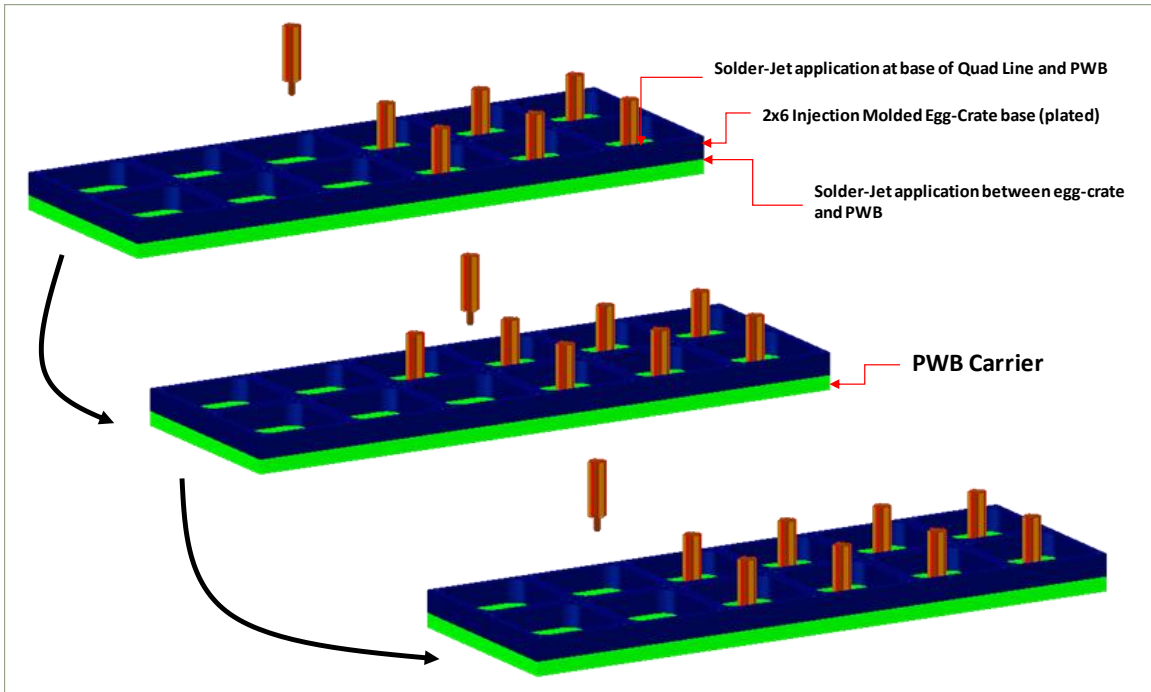


Figure 4-23. Assembly steps 1 - 4

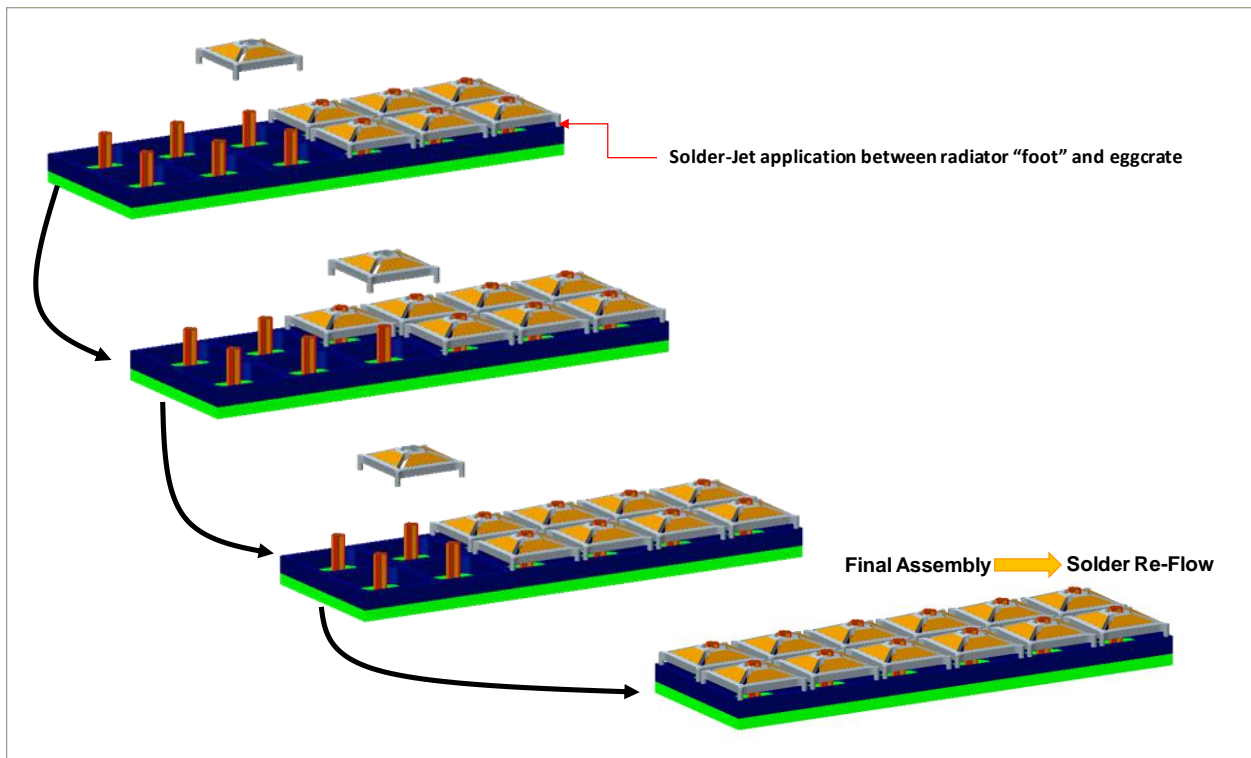


Figure 4-24. Assembly steps 5 - 6

Array Assembly Summary

Sections 4.1 and 4.2 outlined the manufacturing and assembly approach for the droopy bowtie and quad line feed. The ultimate objective is to show that a high performance RF assembly, such as the droopy bowtie and quad line feed, can be compatible with low cost manufacturing and assembly techniques.

Sections 4.3 and 4.3.1 present the HFSS models for the “Gen 1.0” prototype droopy bowtie radiator and quad line feed and Gen 2.0 droopy bowtie turnstile radiator and quad line feed, respectively. The objective of the “Gen 1.0” prototype was to implement low cost fabrication techniques- like injection molding and plating the droopy bowtie radiator; low cost assembly processes: fabricating the quad line feed and assembling the quad line feed to the droopy bowtie radiator. Lessons learned from fabricating and assembling Gen 1.0 are incorporated into Gen 2.0 with further RF optimization performed on Gen 2.0. Section 4.4 presents the Gen 2.0 droopy bowtie turnstile radiator with quad line feed HFSS infinite array simulations.

Section 4.5 presents measurements of a prototype L-Band droopy bowtie turnstile radiator and quad line feed. This assembly was basically hand-crafted and the bowtie wings were supported by Teflon blocks. However, the first objective was accomplished: the L-Band droopy bowtie turnstile radiator and quad line feed showed excellent return loss RF bandwidth and good isolation between bowtie wings. Section 4.6 presents X-Band Gen 1.0 droopy bowtie turnstile radiator and quad line feed measurements. The X-Band assembly used injection molded, plated droopy bowtie wings; the copper was etched using laser ablation and the assembly used a final solder re-flow operation to attach the quad line to the droopy bowtie wings as well as soldering the quad line to the printed wiring board. Return loss measurements are first presented followed by far-field element patterns. Section 4.7 presents the summary to Chapter 4.

4.3 HFSS Model: Gen 1.0

The objective of the Gen 1.0 model was to implement low cost manufacturing techniques:

- Injection mold manufacturing and plating processes: experiment and learn how to implement for the droopy bowtie radiator;
- Quad line feed: Develop fabrication and assembly process.

The balun approach implemented for the Gen 1.0 and Gen 2.0 X-Band models was a coaxial transmission line input to a coplanar transmission line feed; the coplanar transmission line then connects to the quad line feed. This approach was implemented because each transmission line is amenable to low cost manufacturing:

- Coaxial transmission line
 - pseudo-coaxial transmission lines are common in printed wiring boards (PWB) by a plated through hole via surrounded by a concentric ring of plated through hole vias;
 - Low RF loss, excellent isolation between pseudo-coaxial transmission lines;
- Coplanar transmission line
 - Uses standard PWB plating and etching techniques;
 - Materials: Rogers 4003C laminate and Rogers 4450F bonding adhesive;
 - Low RF loss, excellent isolation between pseudo-coaxial transmission lines.

The Gen 1.0 droopy bowtie turnstile radiator was a “wings-up” design to investigate RF performance relative to the baseline “wings-down”; prototype Gen 1.0 measured data is shown in Section 4.5.

Figure 4-25 shows the Gen 1.0 HFSS model; the unit cell lattice is 0.595in x 0.595in.

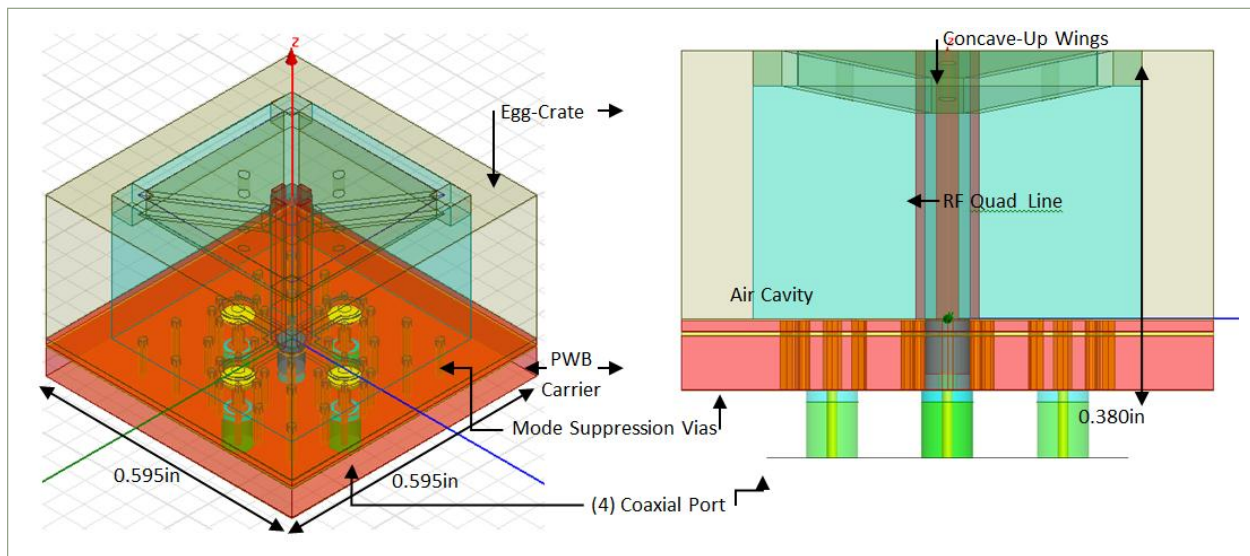


Figure 4-25. Gen 1.0 HFSS model

Figure 4-26 shows a Gen 1.0 solid model cutaway view and an assembled 2x6 X-Band array.

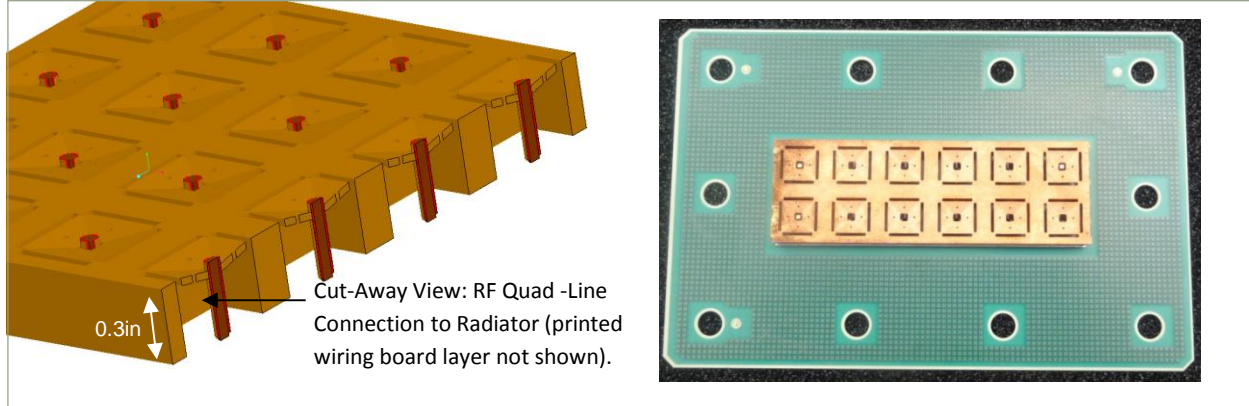


Figure 4-26. Gen 1.0 radiator and quad line feed assembly. Left: Pro-E model showing quad line; Right: fabricated 2x6 X-Band array

4.3.1 HFSS Model: Gen 2.0

The Gen 2.0 droopy bowtie turnstile radiator implements the “wings-down” approach. Fabrication and manufacturing improvements implemented in Gen 2.0:

- The droopy bowtie turnstile radiator is now a separate sub-assembly from the egg-crate base support; the enables robotic placement of the droopy bowtie turnstile radiator over each unit cell of the egg-crate base support;
 - Lesson learned: Gen 1.0 bowtie wings were part of the eggcrate assembly;
 - masking/ plating the assembly was difficult;
 - also: assembly with the quad line difficult
- The wings-down design enables solder-jet application between the bowtie wing and the quad line feed;
 - Lesson learned: Gen 1.0 “wings-up” bowtie wings;
 - Difficult to make solder connection between bowtie and quad line.

Figure 4-27 shows the Gen 2.0 HFSS model; the unit cell lattice is 0.440in x 0.440in. Section 4-4 presents the HFSS results for Gen 2.0. Figure 4-28 through Figure 4-37 present additional detail and dimensions for Gen 2.0.

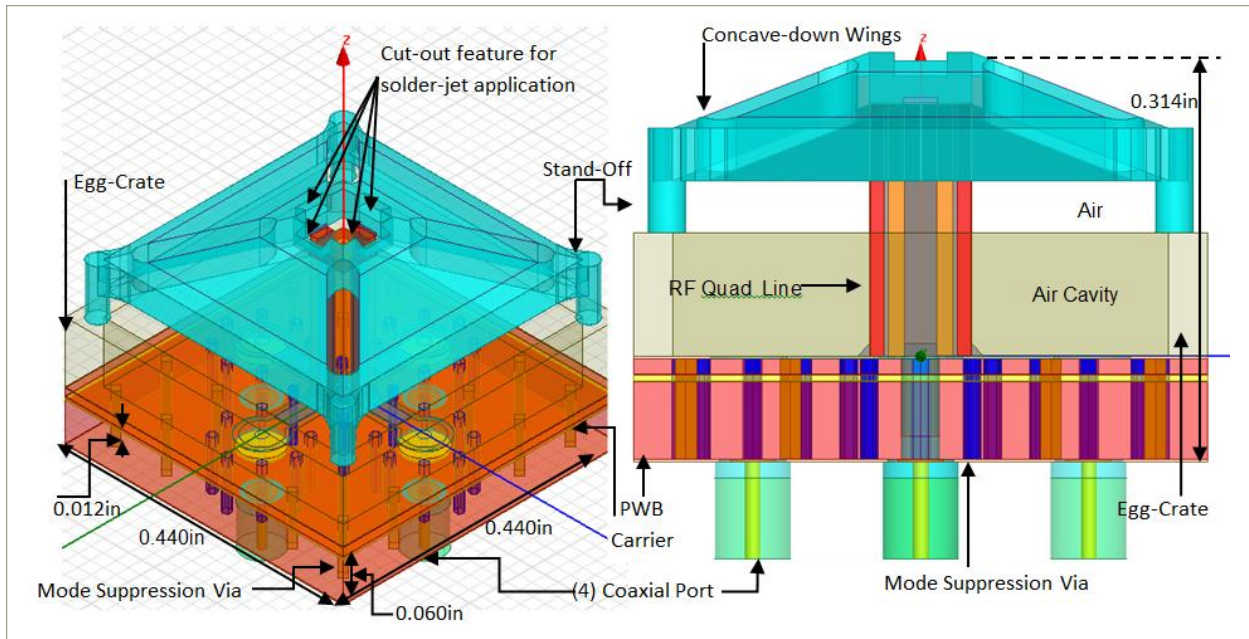


Figure 4-27. Gen 2.0 HFSS model

The next set of figures presents details for the Gen 2.0 X-Band droopy bowtie turnstile radiator and quad line feed HFSS model.

Droopy Bowtie Subassembly

Note in Figure 4-30: The topside and bottom side bowtie wings have a different final width; this “stacked” bowtie wing arrangement enhances RF bandwidth.

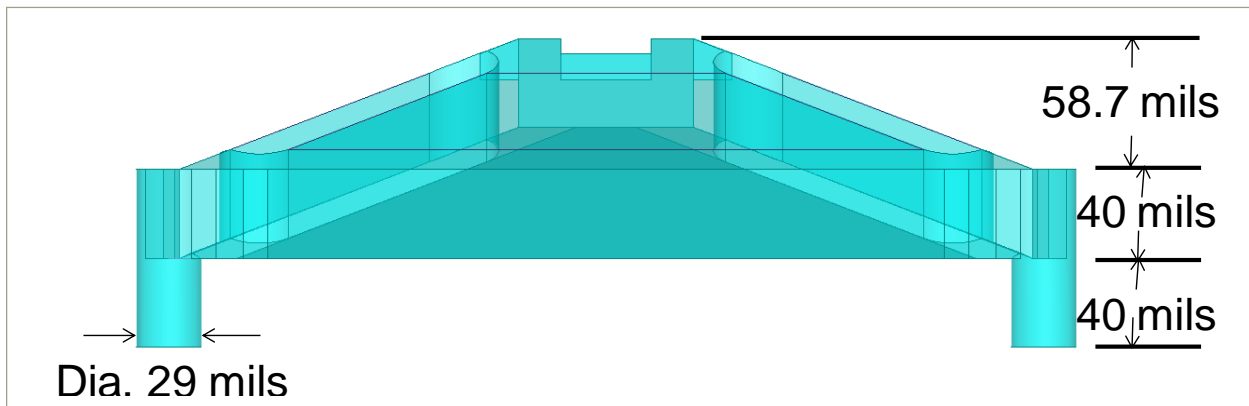


Figure 4-28. X-Band droopy bowtie subassembly: side view, unplated

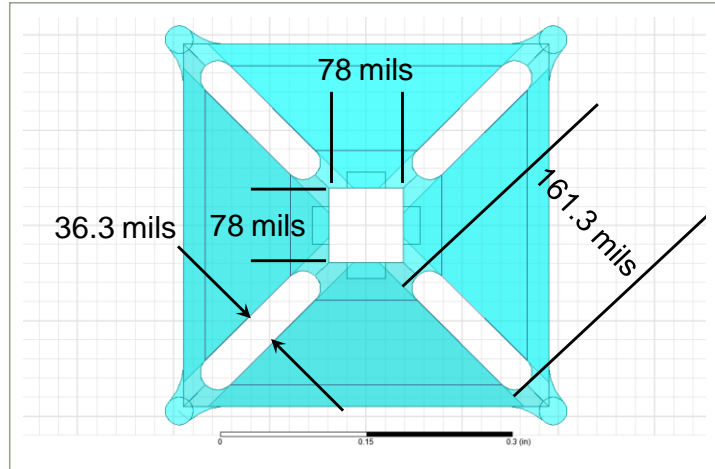


Figure 4-29. X-Band droopy bowtie subassembly: top view, unplated. Dimensions of openings in mold

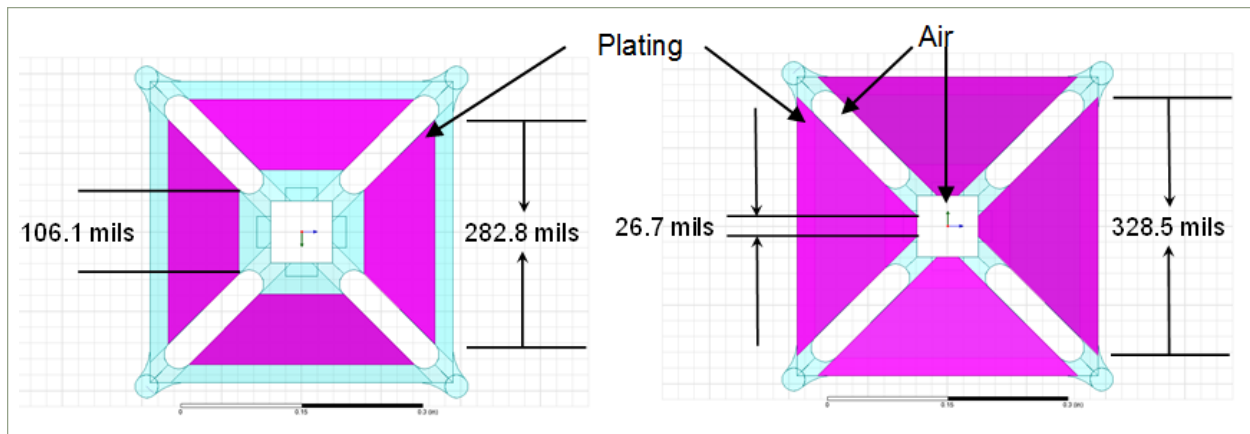


Figure 4-30. X-Band droopy bowtie subassembly: top view, plated. Left: topside plated wings; Right: bottom side plated wings

Quad Line Subassembly

Figure 4-31 and Figure 4-32 show the details of the quad line.

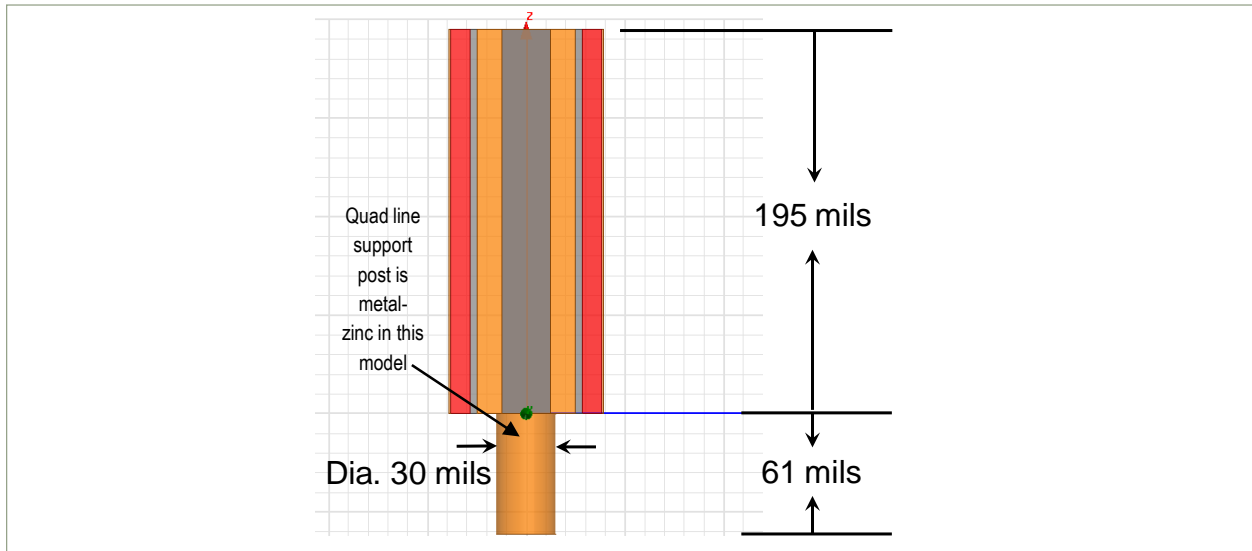


Figure 4-31. X-Band quad line, side view

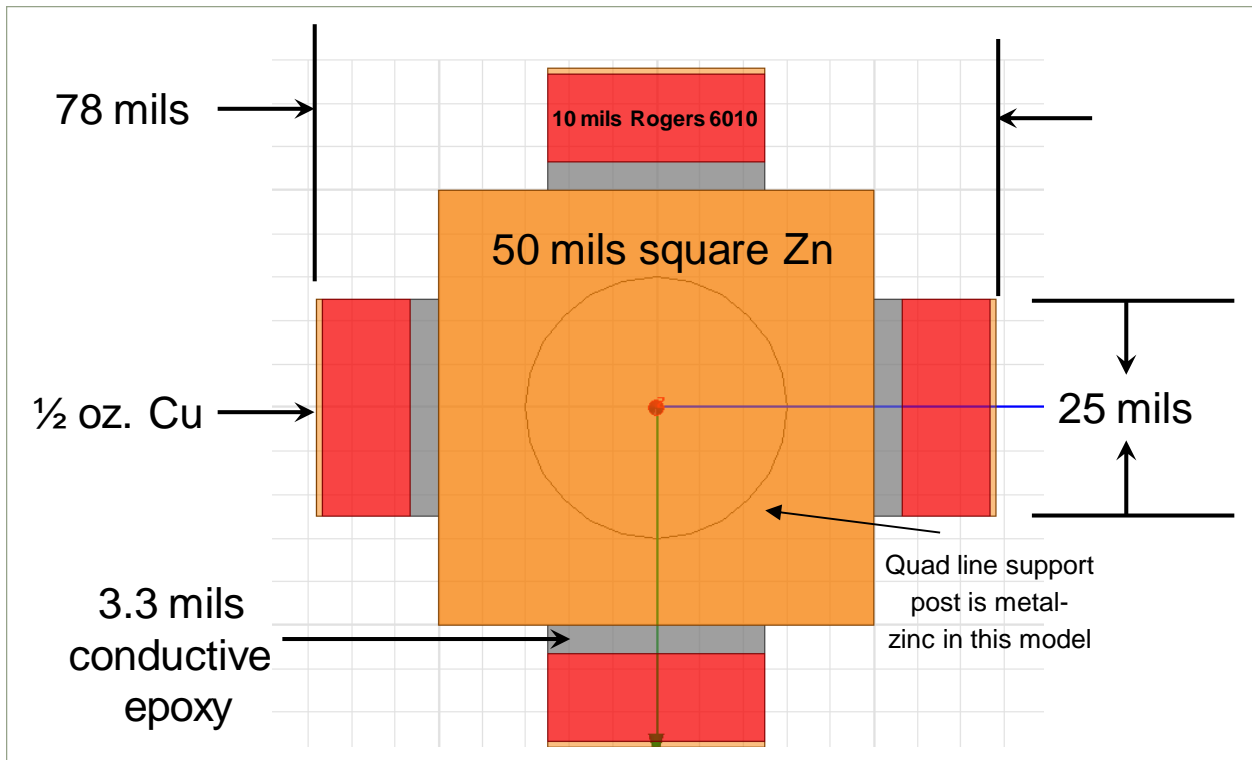


Figure 4-32. X-Band quad line, top view

Eggcrate Subassembly

Figure 4-33 and Figure 4-34 shows the details of the eggcrate subassembly. The eggcrate subassembly is modeled as a plated plastic.

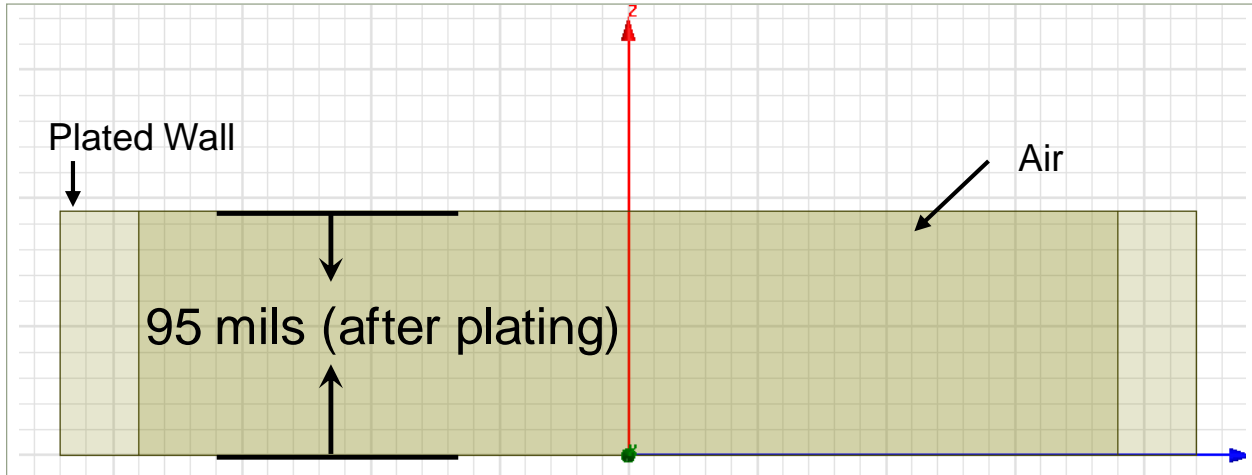


Figure 4-33. X-Band eggcrate subassembly, side view

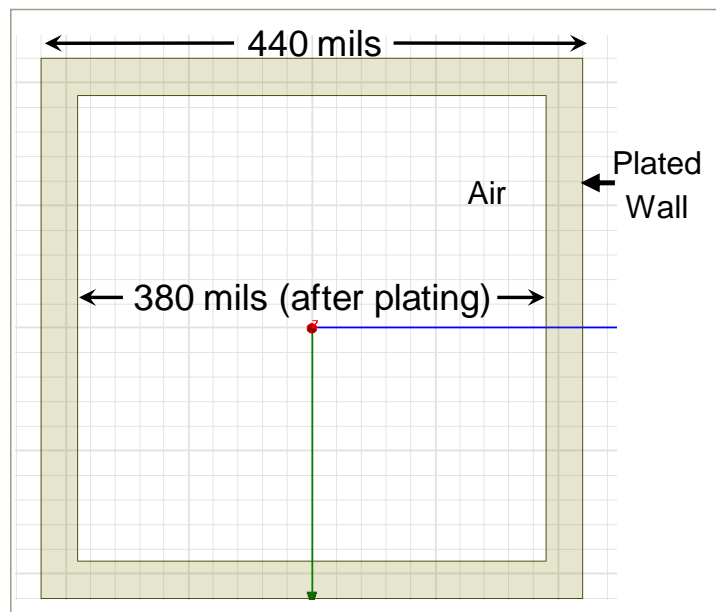


Figure 4-34. X-Band eggcrate subassembly, top view

Printed Wiring Board Subassembly

Figure 4-35 shows the detail of the printed wiring board (PWB) subassembly.

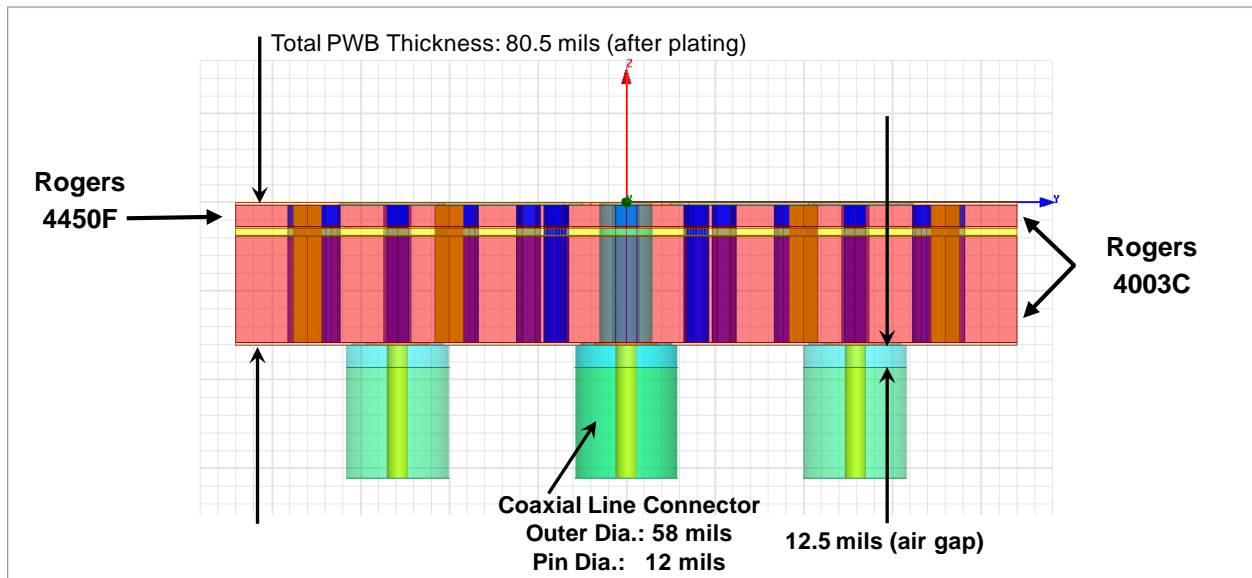


Figure 4-35. X-Band PWB subassembly, side view

Printed Wiring Board Subassembly

Figure 4-36 and Figure 4-37 shows the detail of the four coplanar transmission lines on the top side of the PWB subassembly.

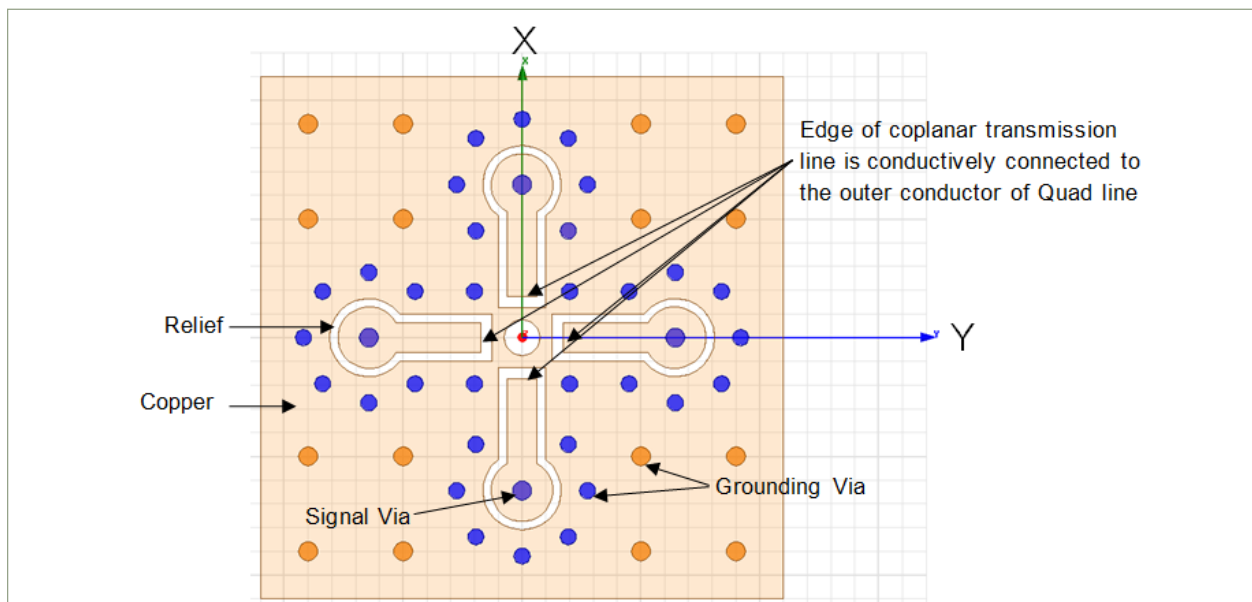


Figure 4-36. X-Band PWB subassembly, top view of coplanar line

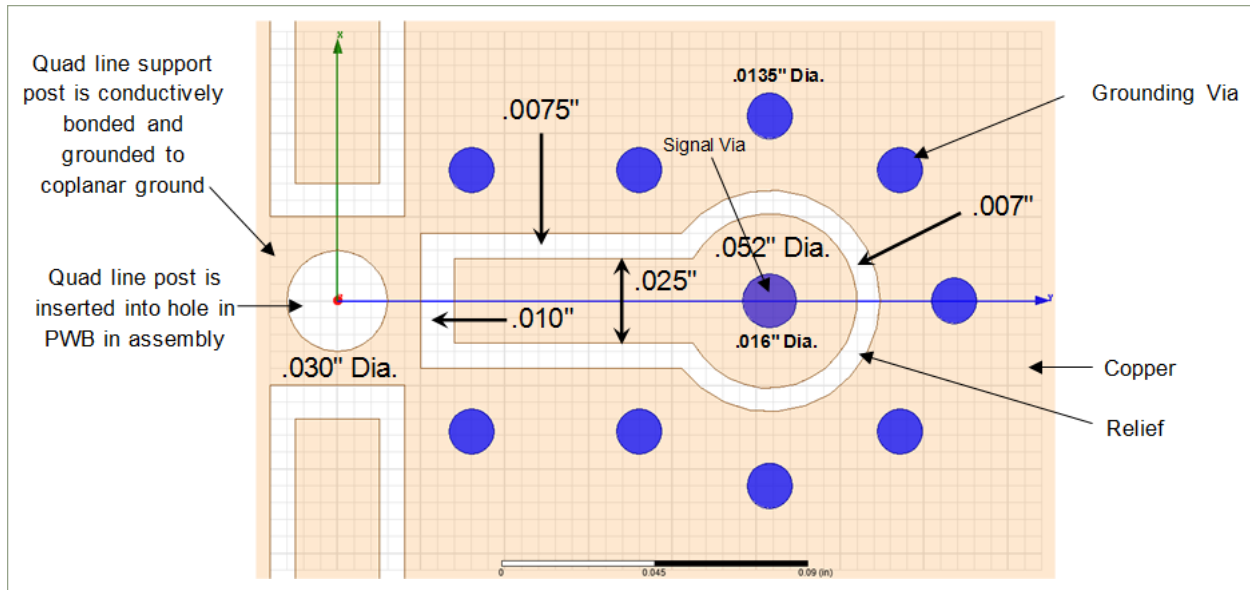


Figure 4-37. X-Band PWB subassembly. Detail of coplanar Line

4.4 HFSS Infinite Array Simulation Results

Section 4.4 presents the Gen 2.0 droopy bowtie turnstile radiator with quad line feed infinite array simulations.

The HFSS infinite array model used the following port definitions:

- Input coaxial ports.
 - Four coaxial ports feed the four coplanar transmission lines;
 - Each coaxial port has an “integration line” definition from inner to outer conductor.
- Output Radiation port.
 - The “perfectly matched layer” (PML) boundary condition was used.

Figure 4-38 shows the Gen 2.0 return loss versus frequency for 4 scan angles; Figure 4-39 shows the grating lobe plot at 12GHz and 15GHz.

HFSS infinite array execution times for droopy bowtie radiator and quad line feed are summarized:

- Raytheon HFSS run time: 13.75 hours includes 361 HFSS infinite array scans;
- Worcester Polytechnic Institute HFSS run time: 18 hours includes 361 HFSS infinite array scans.

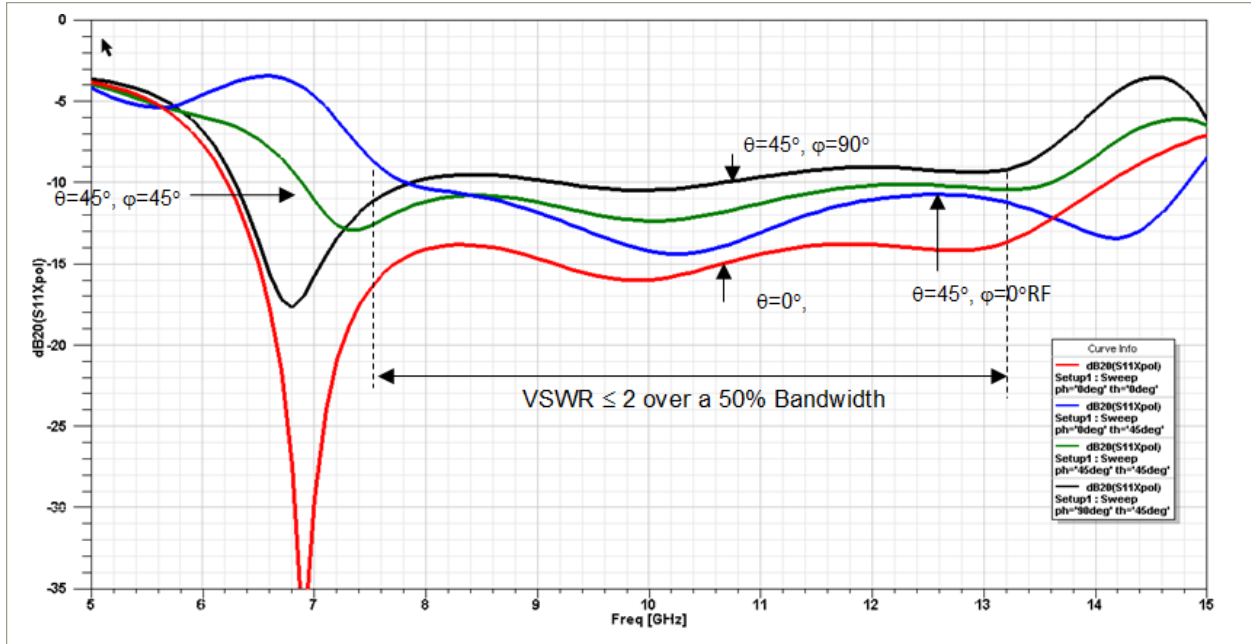


Figure 4-38. Gen 2.0 radiator and feed: return loss

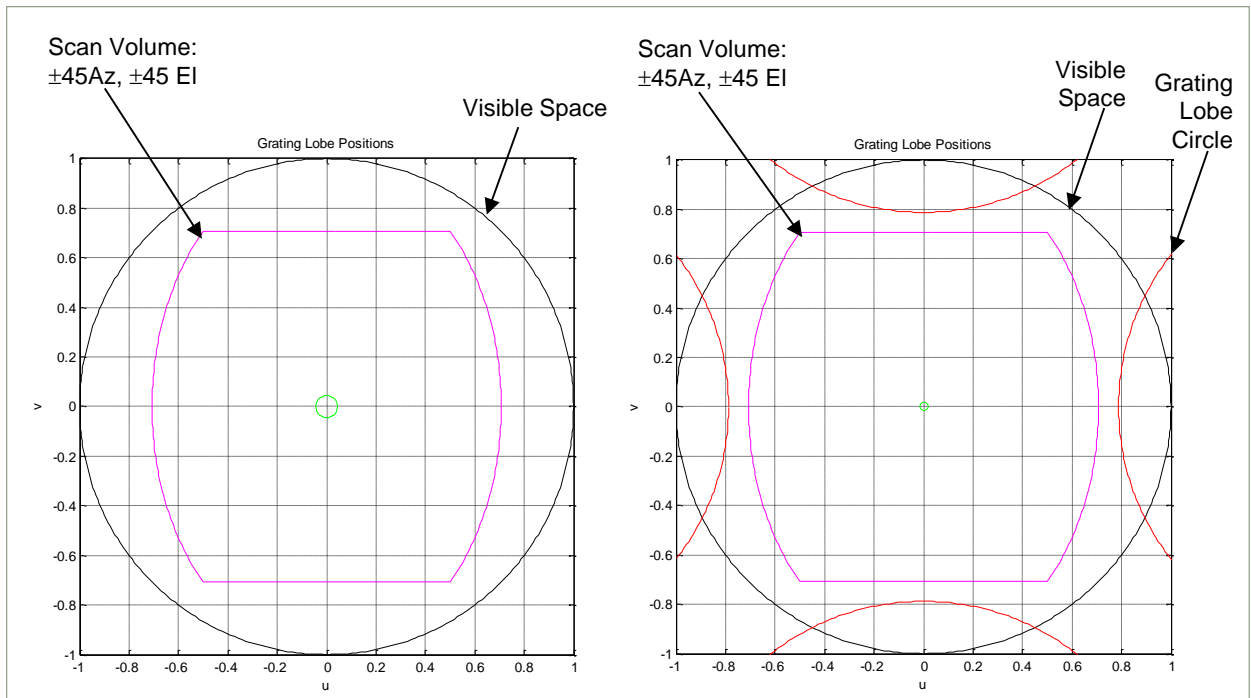


Figure 4-39. Gen 2.0 lattice grating lobe plot: 0.440in square lattice. Left: 12GHz; Right: 15GHz

Figure 4-40 shows the Gen 2.0 infinite array element patterns from 8GHz to 12GHz. The electric field polarization is shown in Figure 4-41. The x-axis in each plot is the polar scan angle, θ ; each curve represents a scan in a ϕ -cut plane. Note that the element pattern gain at boresite ($\theta=0^\circ$) includes the total front-end loss of the combined radiator, quad line feed and printed wiring board transmission line. Note that the simulated loss of the droopy bowtie and quad line feed is excellent: $<0.37\text{dB}$.

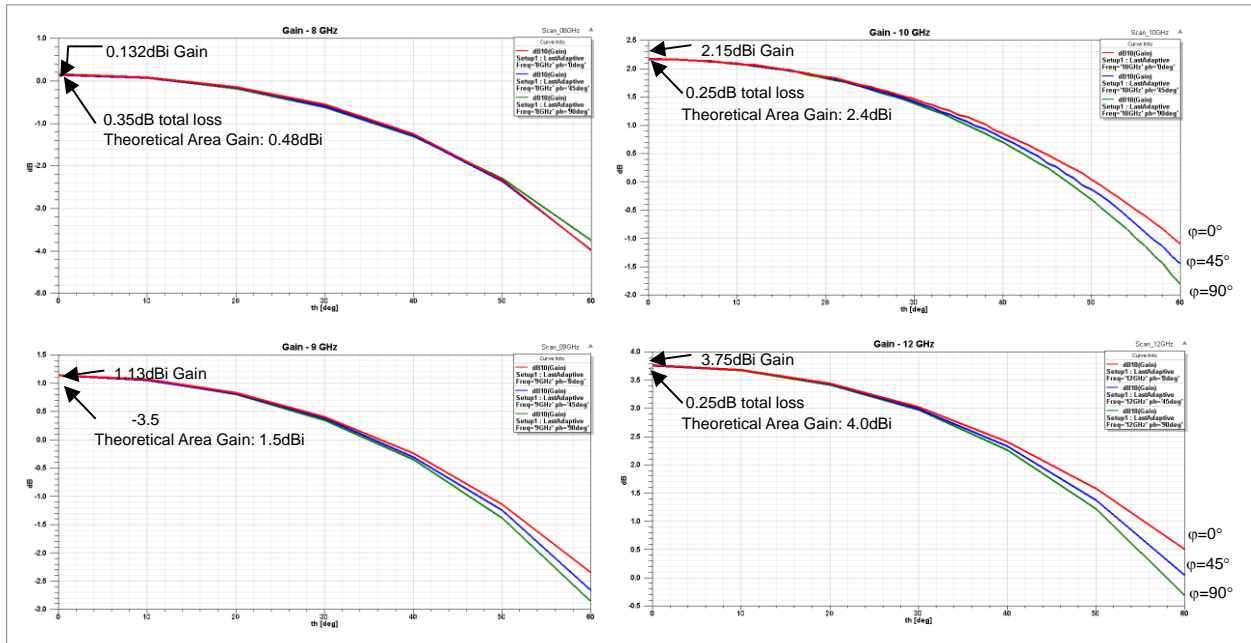


Figure 4-40. Gen 2.0 radiator and feed: infinite array embedded element patterns

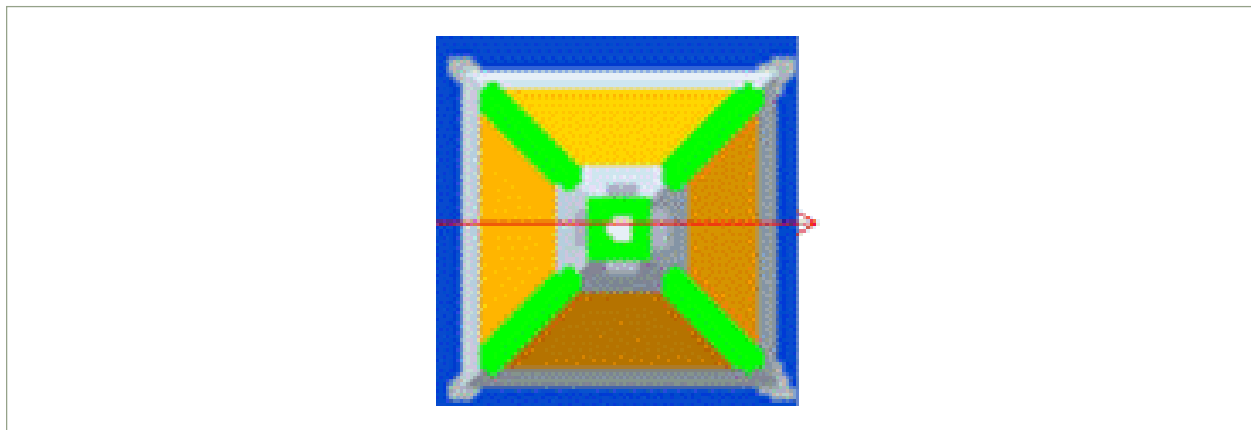


Figure 4-41. Droopy bowtie electric field polarization

4.5 L-Band Prototype Droopy Bowtie Turnstile with Quad Line Feed

Section 4.5 presents measurements of a prototype L-Band droopy bowtie turnstile radiator and quad line feed. Return loss and isolation measurements are presented on prototype units.

The objectives of the L-Band prototype were:

1. Construct the droopy bowtie turnstile radiator and quad line feed based on the antenna-balun transmission line model of Figure 4-42;
2. Measure input RF return loss radiating into free space.

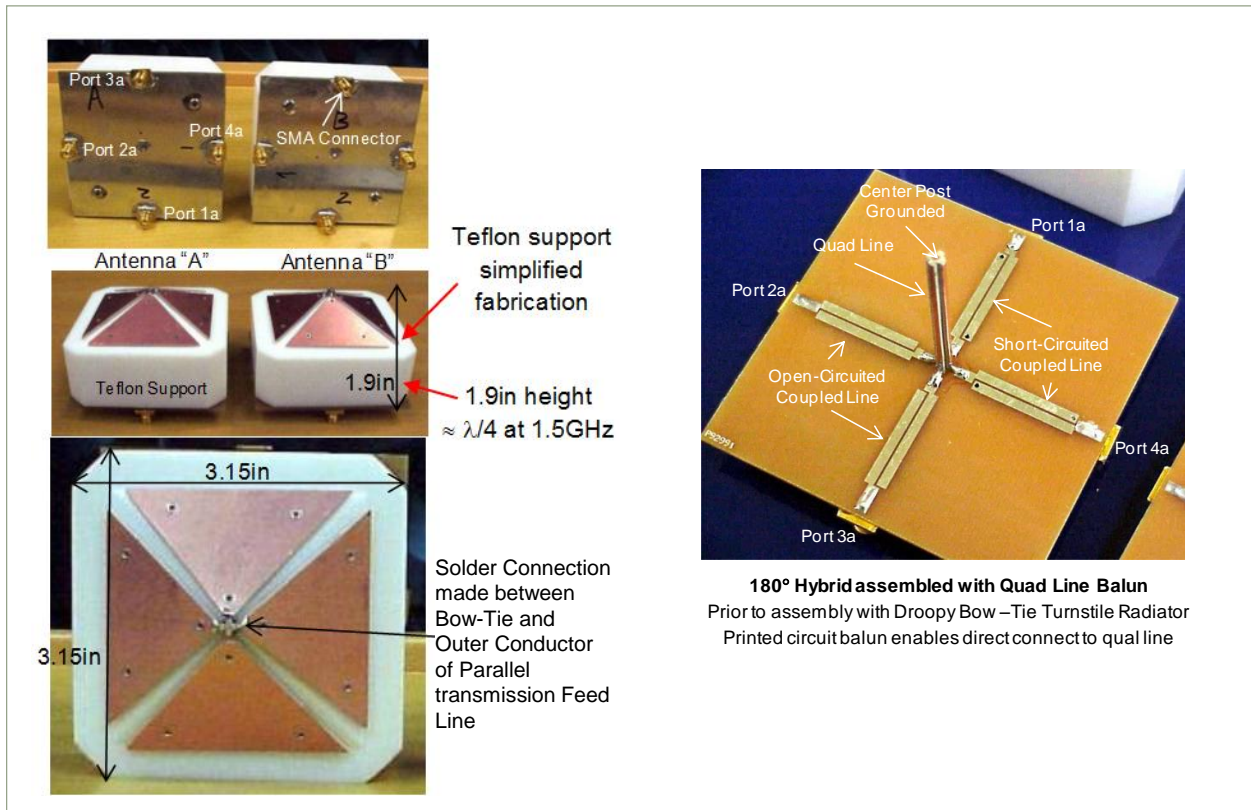


Figure 4-42. L-Band prototype assembly

4.5.1 Measurement Set-up

The L-Band return loss measurement set up is shown in Figure 4-43; Input return loss, S_{11} , and isolation, S_{21} , between the two droopy bowtie assemblies were measured.

The measurement equipment included:

- Agilent 7822 two-port Network Analyzer,
- Two 0-degree power splitters from Mini Circuits (ZAPD-20+, 700 MHz to 2 GHz, typical port isolation is 30-40 dB over the operating band),
- A set of SMA connectors.

The standard “Through-Reflect-Line” (TRL) method was used for calibration; the calibration is performed using short and load terminations and related S-parameter data for the power splitters with cables for S_{11} , and the throughput data between two sets of cables/power splitters for S_{21} .

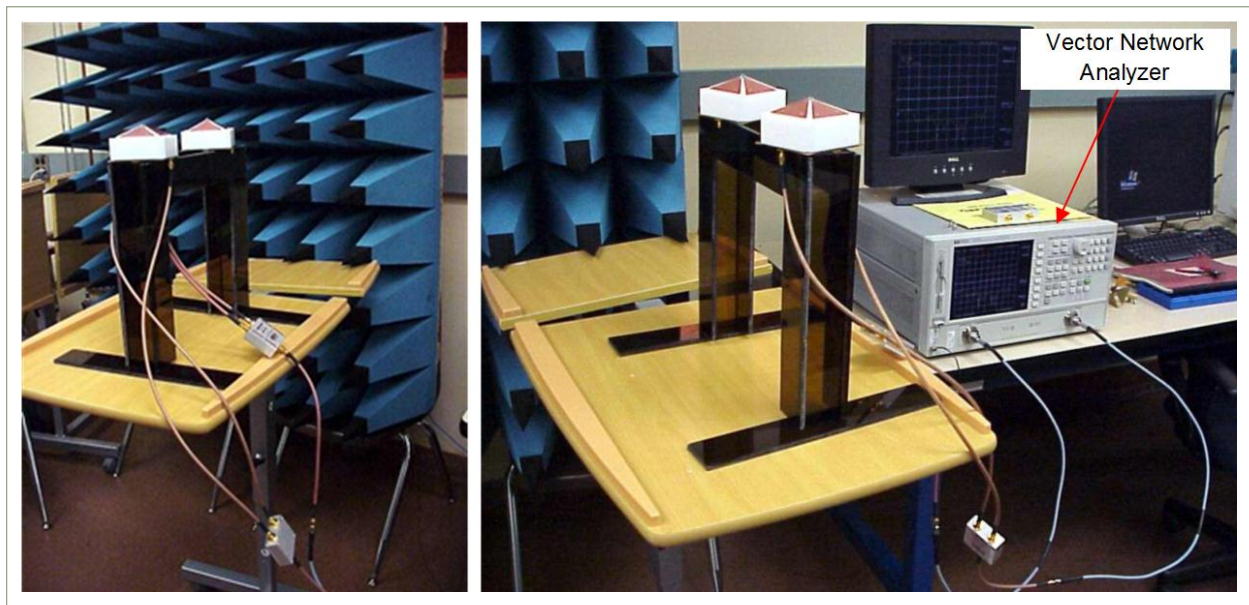


Figure 4-43. L-Band test measurement set up

4.5.2 Measurements

The isolation measurement, S_{21} , between two orthogonal polarizations using two power splitters is shown on the left in Figure 4-44. The measured isolation between two orthogonal polarizations is shown on the right: the isolation is 40dB from 1.5-1.8 GHz and better than 30dB isolation from 1.5-1.85GHz. This result is encouraging given that the power splitter isolation is limited to about 40dB in the measurement band.

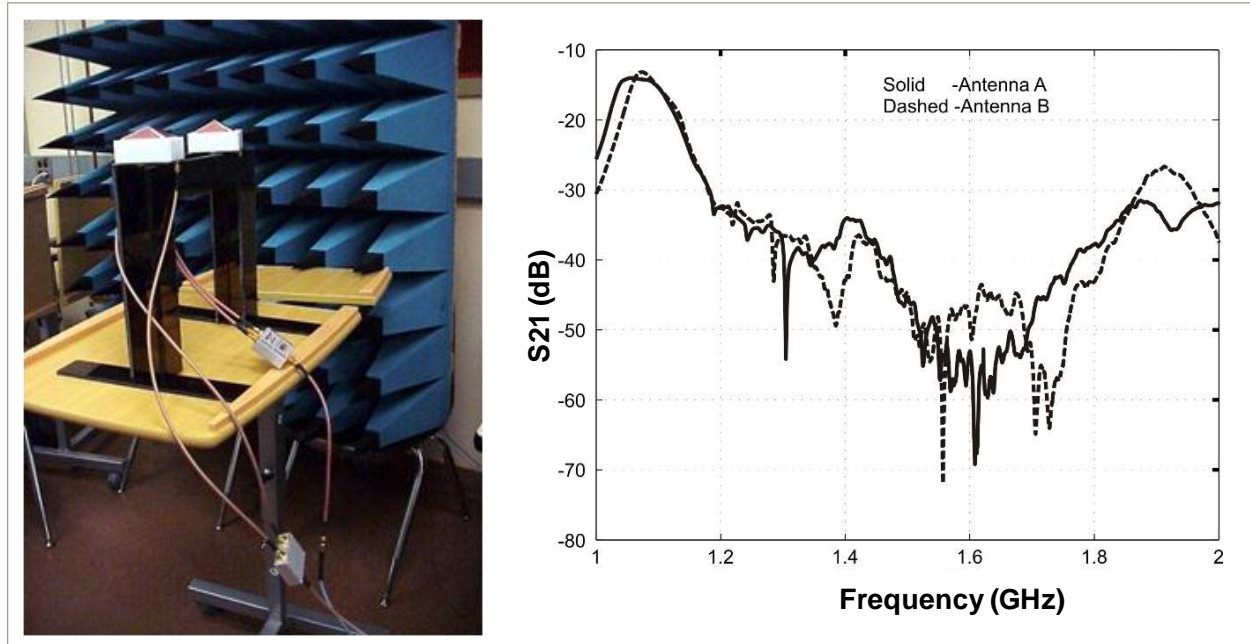


Figure 4-44. L-Band prototype. Measured isolation between the two prototype antennas setup (left); measured results (right)

Next, we present the return loss measurement. Return loss measurements are shown in Figure 4-45 for the four pairs of droopy bowtie antennas. For each pair of droopy bowtie antennas, the orthogonal pair of droopy bowtie antennas was terminated in a 50 Ohm load.

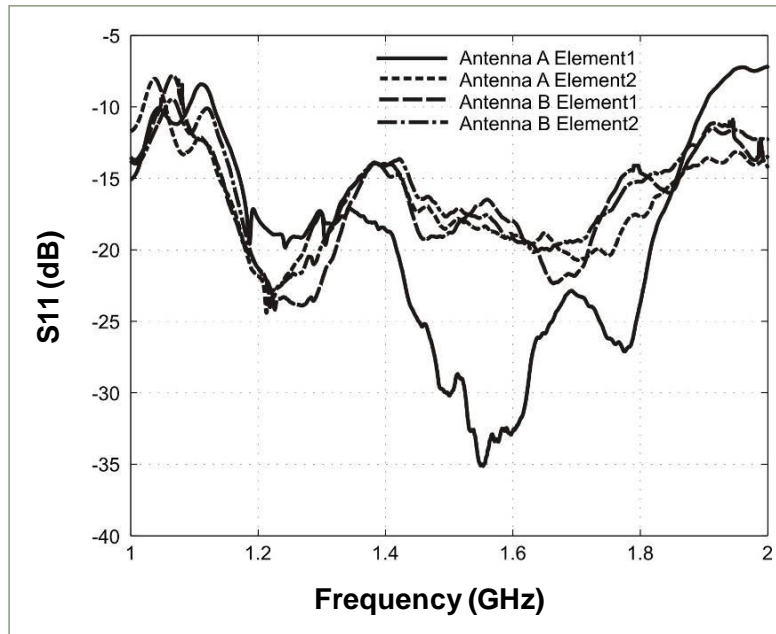


Figure 4-45. L-Band prototype. Measured return loss

4.5.3 Discussion: L-Band Prototype

Two prototype L-Band droopy bowtie turnstile radiator with quad line feed assemblies were fabricated, assembled and tested; RF performance is summarized:

- Return Loss: $\approx 2:1$ RF bandwidth for a $VSWR \leq 2:1$;
 - Note: the loss of the Wilkinson power divider over the band is about 2dB.
- Isolation: $> 30\text{dB}$ over most of the band (narrow-band commercial 3dB power divider used)
 - The data shown in Figure 4-44 confirms that the quad line has a sufficiently high isolation between adjacent transmission lines feeding the droopy bowtie wings.

The overall objective of demonstrating the manufacturing and assembly approach and the potential RF performance of the droopy bowtie turnstile radiator with quad line feed was also demonstrated.

4.6 X-Band Prototype Gen 1.0 Droopy Bowtie Turnstile with Quad Line Feed

Section 4.6 presents measurements of a prototype X-Band Gen 1.0 and Gen 2.0 droopy bowtie turnstile radiator and quad line feed.

4.6.1 Gen 1.0 Return Loss Measurement

Return loss measurements are first presented followed by far-field element patterns. The X-Band return loss measurement set up is shown in Figure 4-46; the prototype X-Band Gen 1.0 droopy bowtie turnstile radiator and quad line feed is shown in Figure 4-47.

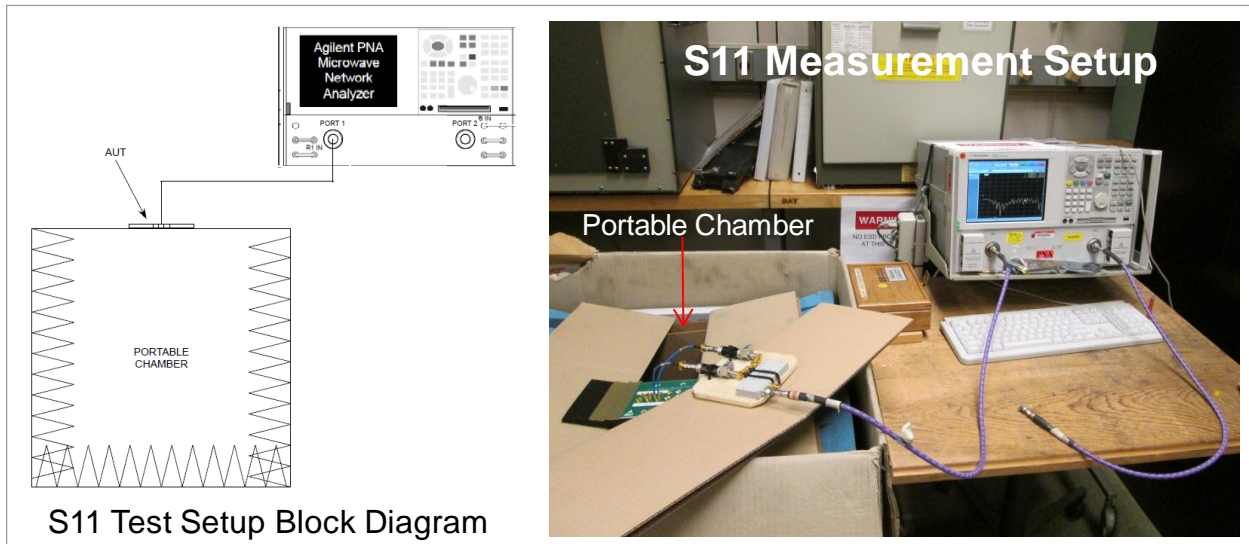


Figure 4-46. X-Band return loss measurement set up

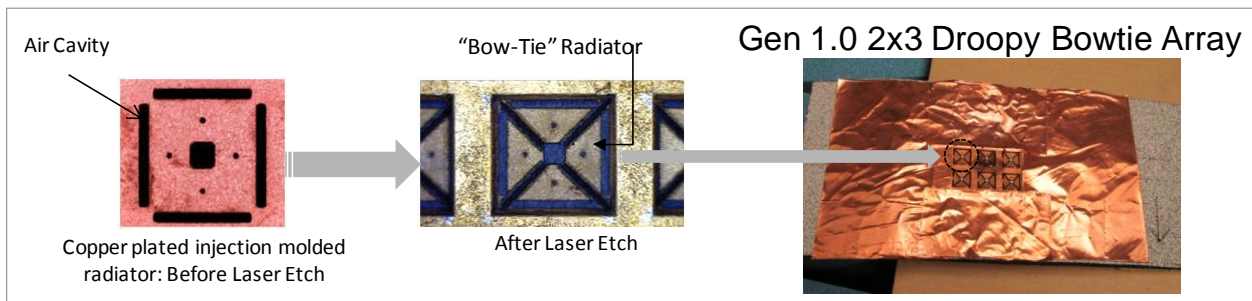


Figure 4-47. X-Band Gen 1.0 droopy bowtie turnstile radiator and quad line feed

The Gen 1.0 droopy bowtie turnstile radiator and quad line feed was fed by a commercial off-the-shelf hybrid feeding a pair of GPO coaxial connectors; the GPO coaxial connectors feed one pair of bowtie wings as shown in Figure 4-48.

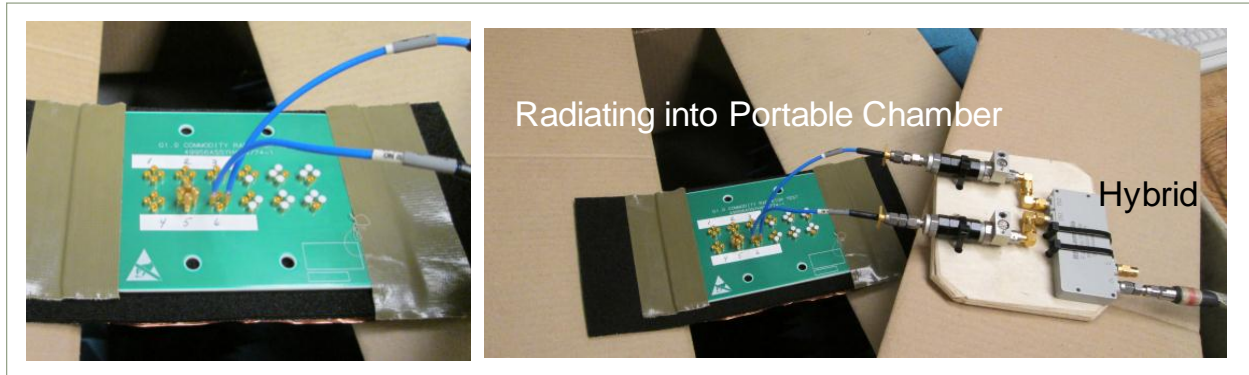


Figure 4-48. Unit under test

Return Loss Measurement

Figure 4-49 presents the return loss, S_{11} , for the horizontal and vertical polarization. The bandwidth for a $VSWR \leq 2:1$ is approximately 14%.

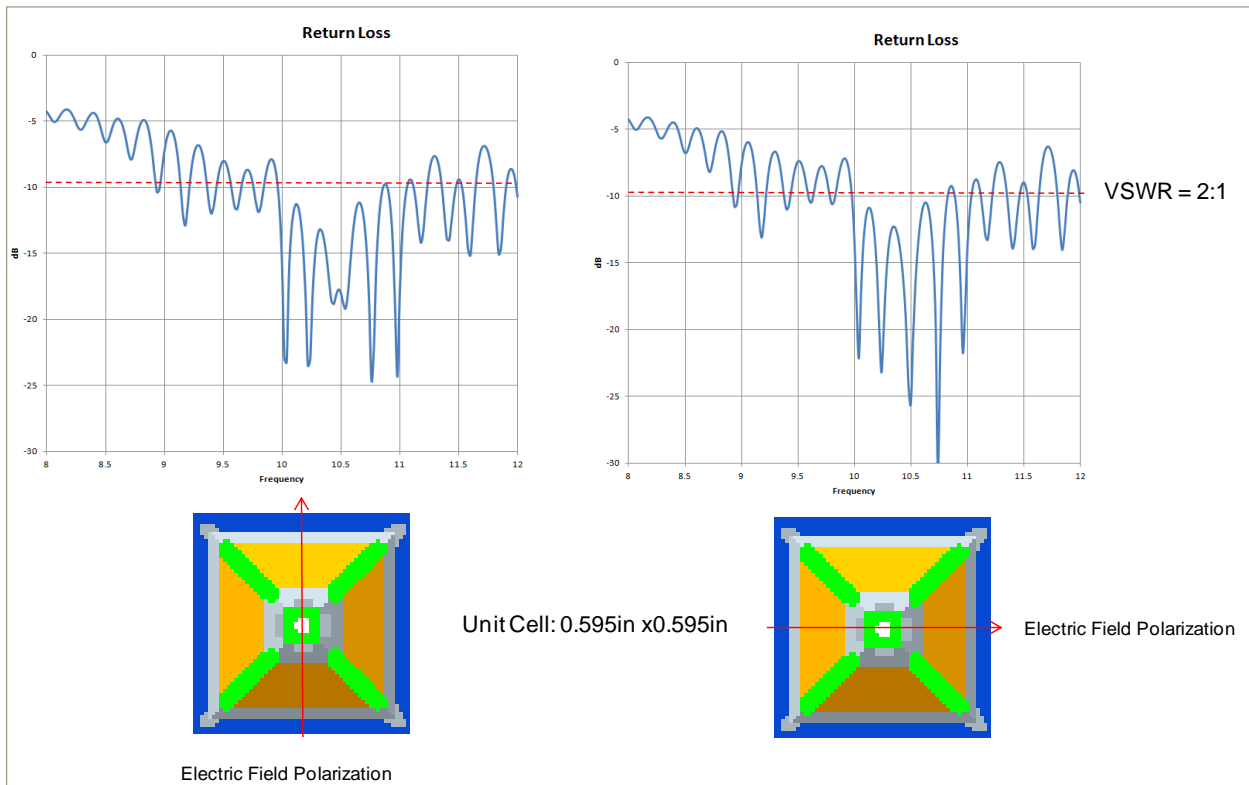


Figure 4-49. Return loss. Vertical polarization (left) and horizontal polarization (right)

4.6.2 Gen 1.0 Far-field Element Patterns

Figure 4-50 shows the test measurement setup; Figure 4-51 shows the unit under test in the far-field anechoic chamber.

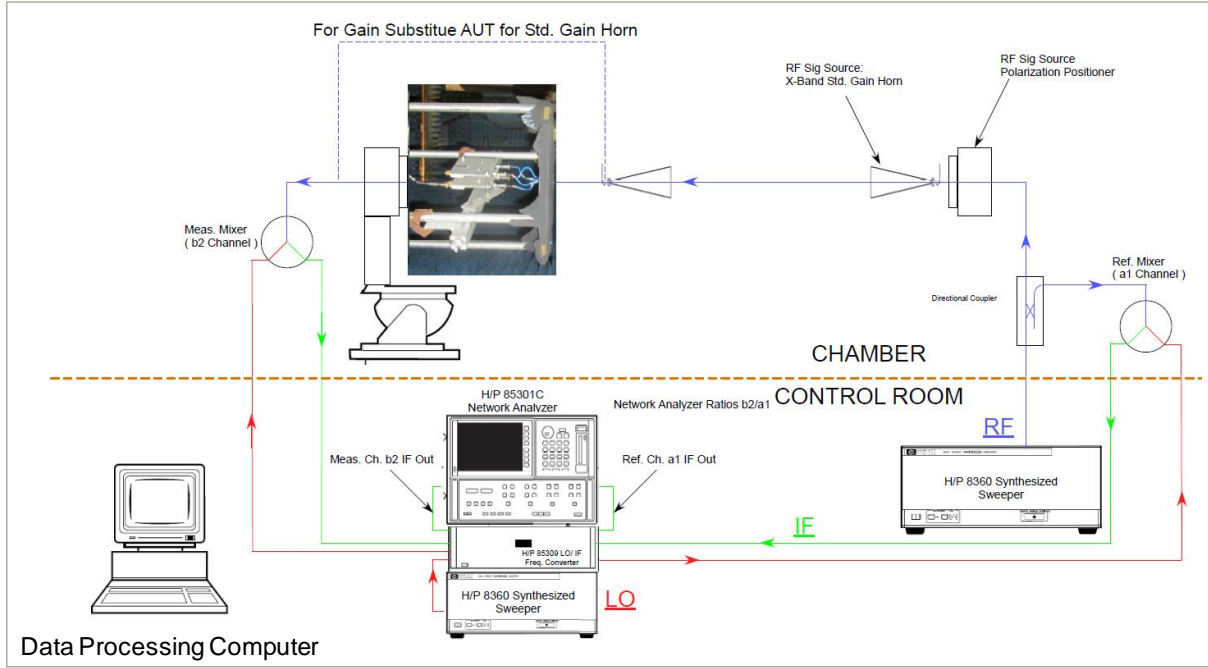


Figure 4-50. Far-field pattern test measurement set up

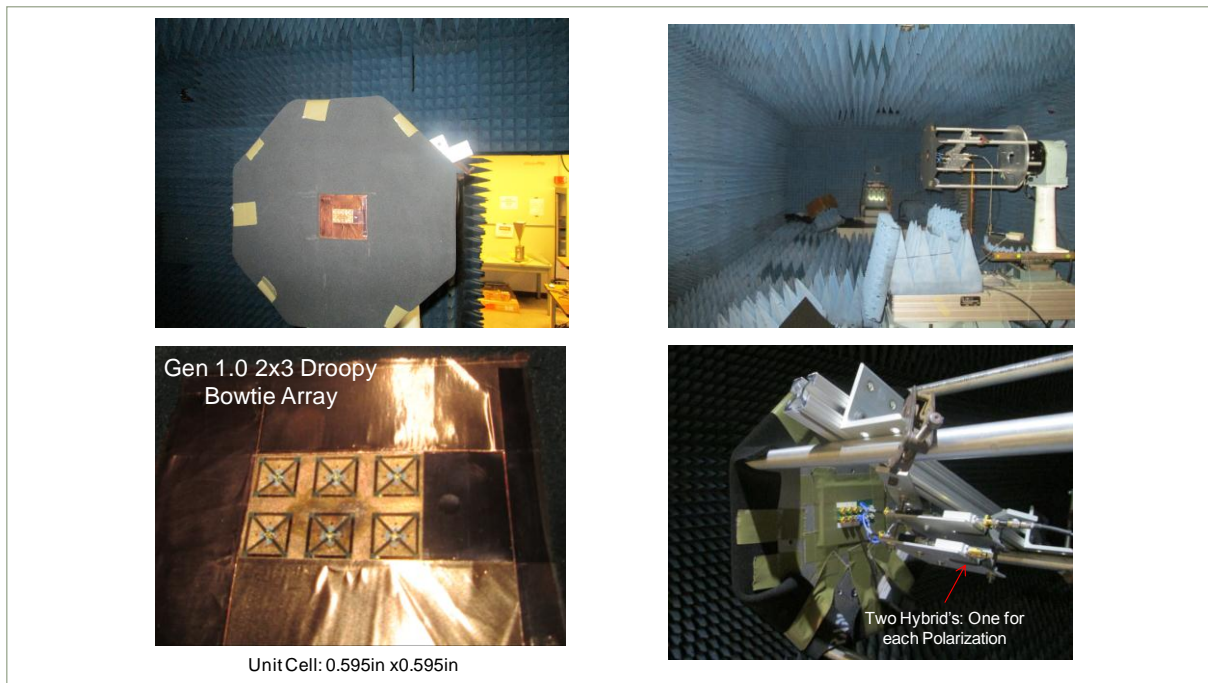


Figure 4-51. Unit under test in the far-field anechoic chamber

Far-field Element Patterns

Figure 4-52 presents the far-field element pattern E-plane cuts from 8GHz to 12GHz.

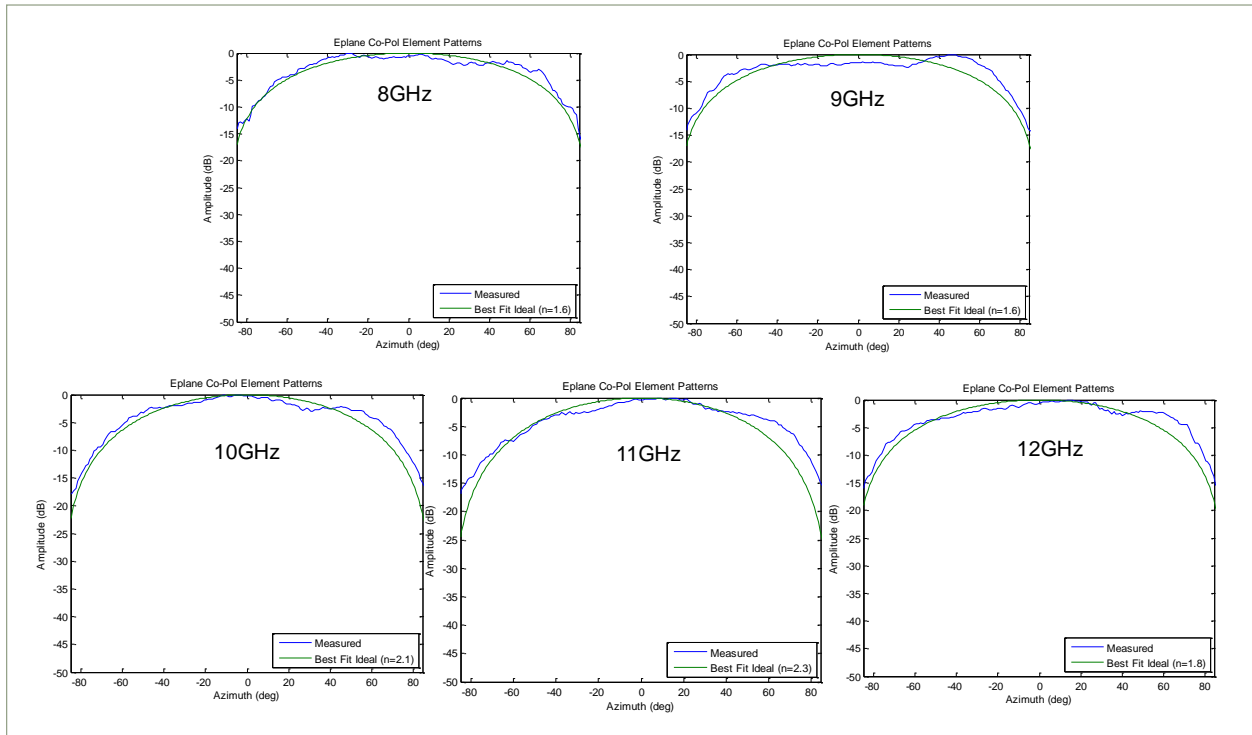


Figure 4-52. E-plane pattern cuts

Far-field Element Patterns

Figure 4-53 presents the far-field element pattern D-plane cuts from 8GHz to 12GHz.

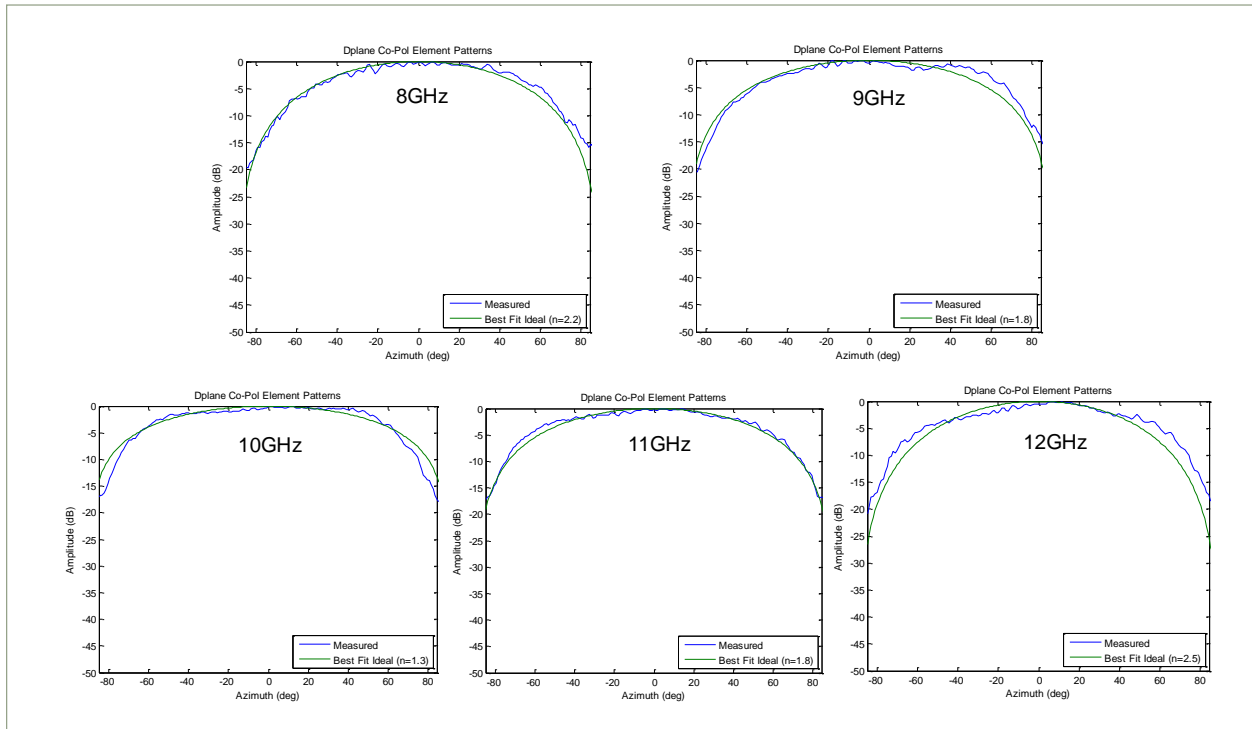


Figure 4-53. D-plane pattern cuts

Far-field Element Patterns

Figure 4-54 presents the far-field element pattern H-plane cuts from 8GHz to 12GHz.

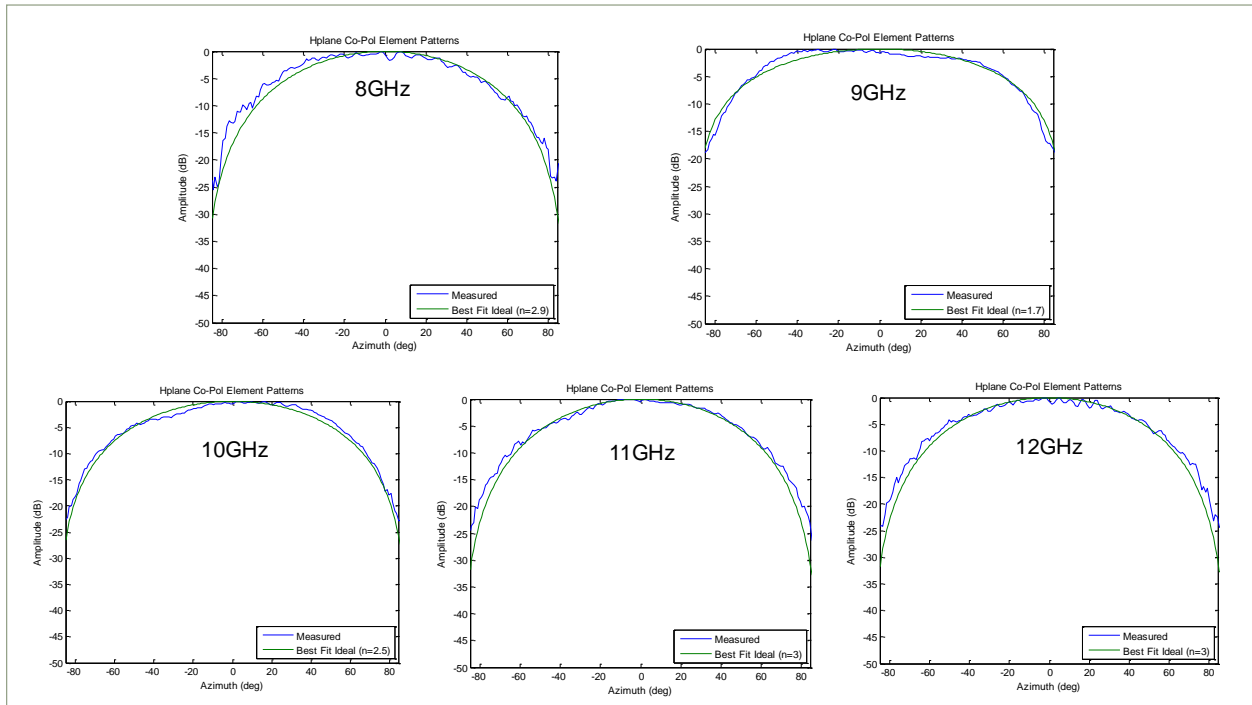


Figure 4-54. H-plane pattern cuts

4.6.3 Gen 2.0 RF Measurements

Return loss and isolation measurements are presented for the prototype Gen 2.0 droopy bowtie turnstile radiator with quad line feed. Figure 4-55 and Figure 4-56 present the measured and simulated return loss and measured and simulated isolation, respectively, for one of the unit cells in the 2x6 array shown in Figure 4-22. The infinite array simulated return loss is for the unit cell vertical and horizontal polarization. The measurement and simulation is at boresite scan.

The simulated RF bandwidth is 50% for a VSWR of 2:1, or better. The measured RF bandwidth for the Gen 2.0 prototype, 28% for a VSWR of 2:1, is excellent for a radiator and feed in a compact 0.44in x 0.44in unit cell; the return loss for both vertical and horizontal polarization are very similar. Given that the Gen 2.0 is fabricated and assembled with the techniques described in sections 4.1 and 4.2 for the first time, the measured results are very good and will improve as the fabrication and assembly processes mature.

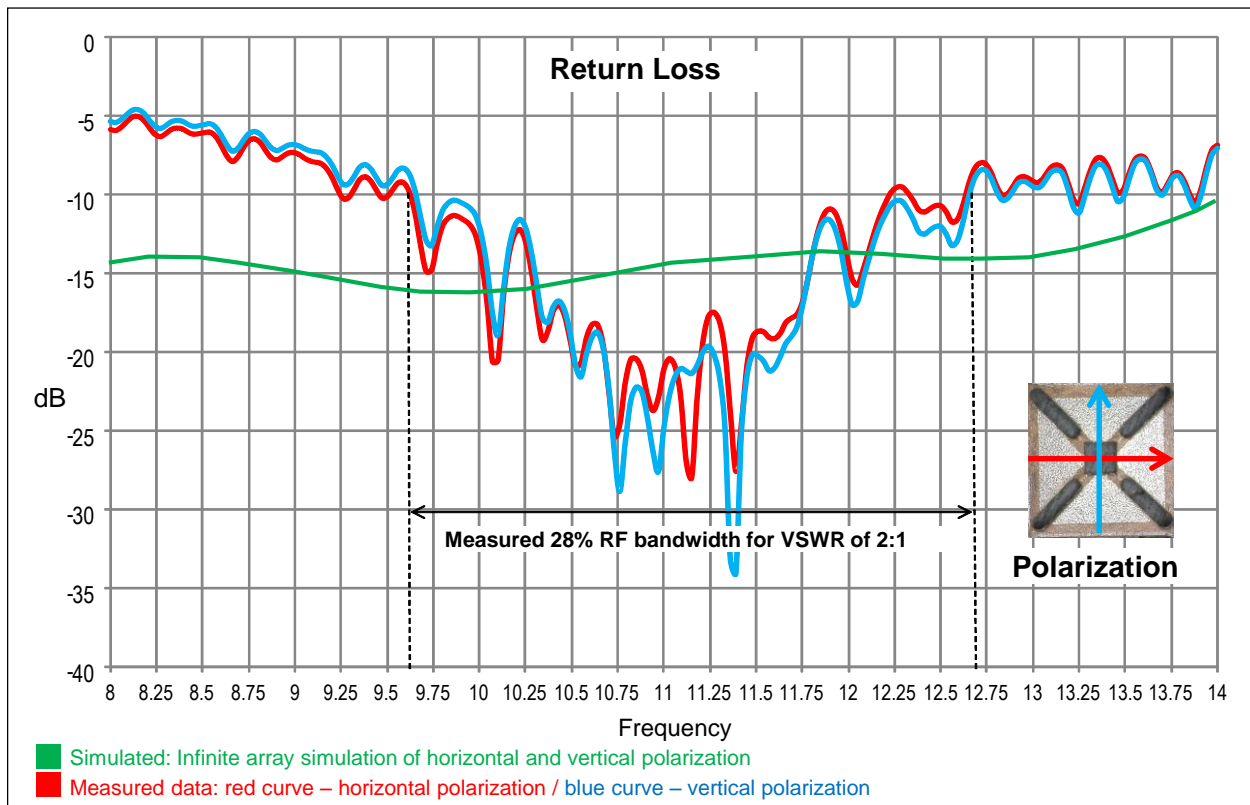


Figure 4-55. Gen 2.0 X-Band droopy bowtie radiator with quad line feed: Return loss for vertical and horizontal polarization for a single element (measurement) and an embedded array element at boresite (simulation).

In Figure 4-56, the measured unit cell isolation between the vertical and horizontal polarization is better than 35dB from 8GHz to 14GHz; the infinite array simulation unit cell isolation between the vertical and horizontal polarization is 60dB, or better, from 8GHz to 14GHz. Again, the Gen 2.0 measurement is very good and encouraging given the maturity of the fabrication and assembly process of the quad line feed and the droopy bowtie- the worst case axial ratio (assuming perfect phase quadrature between vertical and horizontal polarization) would be 0.31dB for the measured Gen 2.0 droopy bowtie and quad line feed.

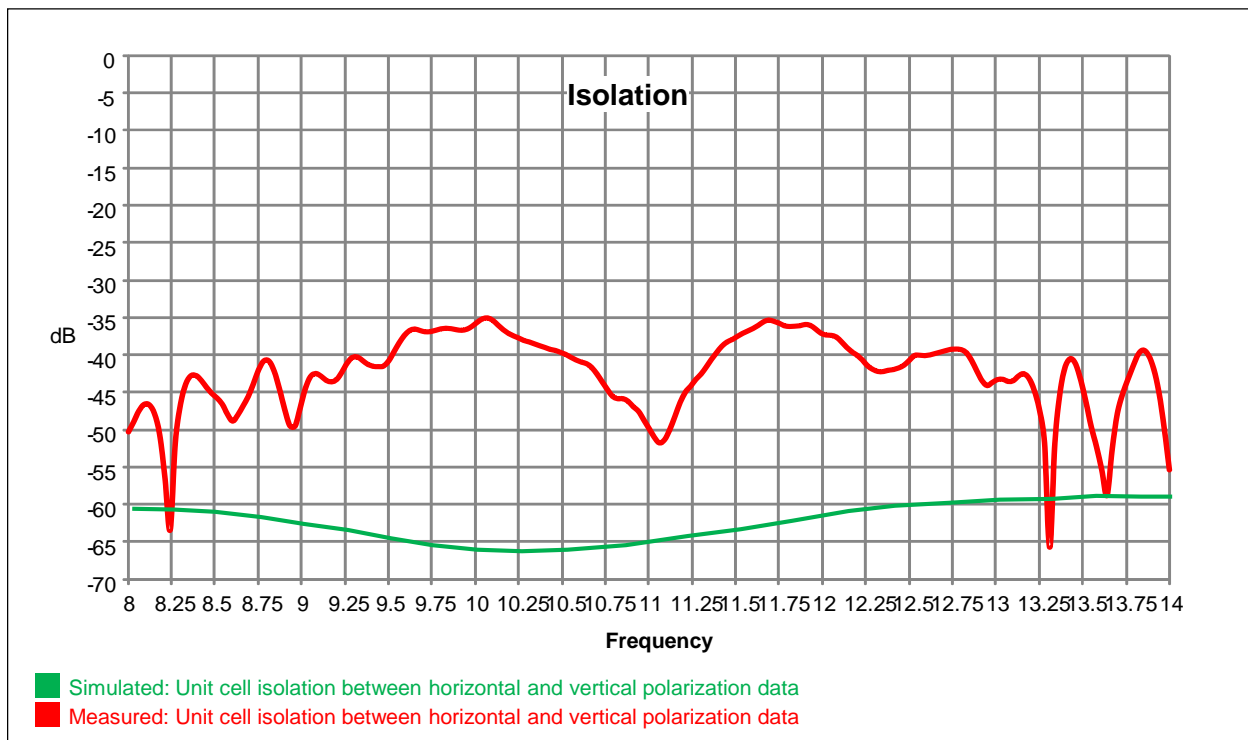


Figure 4-56. Gen 2.0 X-Band droopy bowtie radiator with quad line feed: isolation between vertical and horizontal polarization for a single element (measurement) and embedded array element at boresite (simulation).

4.7 Summary

The objective of Chapter 4, “Practical Realization and Application” was to develop prototype droopy bowtie turnstile radiator with quad line feed assemblies and measure against RF performance goals set out in Chapter 3 and begin to incorporate the manufacturing and assembly approaches aimed at low cost that were presented in Sections 4.1 and 4.2.

Low Cost Manufacturing Techniques

Sections 4.1 through 4.2 discussed and illustrated how low cost fabrication and assembly techniques could be used on the Droopy bowtie turnstile radiator with quad line feed; the modular construction of the droopy bowtie turnstile radiator with quad line feed enables:

- Injection molded radiator. Conventional plating or direct-patterned copper application; HFSS modeling has shown that RF performance of the bowtie is not degraded for standard injection mold tolerances of ± 0.005 in on all dimensions.
- Egg-crate base. Plated plastic or plated injection molded part.
- PWB Base. Use standard printed wiring board material and fabrication techniques.
- Automated pick – and – place assembly.

HFSS Prototype X-Band Models

Sections 4.3 and 4.3.1 presented the detailed “Gen 1.0” and “Gen 2.0” prototype X-Band droopy bowtie radiator and quad line feed HFSS models. Section 4.4 presented HFSS infinite array simulations of the return loss versus scan volume and frequency and embedded element pattern versus frequency.

Gen 2.0 modeled infinite array performance is summarized from Section 4.4:

- 50% RF bandwidth versus scan angle:
 - Exceptional packing efficiency: 0.44in x 0.44in lattice;
 - Octave bandwidth possible with further optimization;
 - Loss at boresite from 8GHz to 12GHz ranged from 0.35dB to 0.25dB.

Prototype RF Measurements

The return loss measurements for the L-Band and X-Band prototypes are discussed. L-Band. Figure 4-45 presented the measured results:

- Return Loss: $\approx 2:1$ RF bandwidth for a $VSWR \leq 2:1$;
- Isolation: > 30 dB over most of the band;
- X-Band. Figure 4-49 presented the measured return loss results:
 - Gen 1.0 droopy bowtie turnstile radiator and quad line feed
 - A 14% bandwidth for a $VSWR \leq 2:1$ for vertical and horizontal polarization;

- Summarizing the element pattern cuts in terms of $\cos^n\theta$ from Figure 4-52 through Figure 4-53:
 - o E-Plane Cut: Scan loss ranges from $\cos^{1.6}(\theta)$ to $\cos^{2.3}(\theta)$ from 8GHz to 12GHz;
 - o D-Plane Cut: Scan loss ranges from $\cos^{1.8}(\theta)$ to $\cos^{2.5}(\theta)$ from 8GHz to 12GHz;
 - o H-Plane Cut: Scan loss ranges from $\cos^{1.7}(\theta)$ to $\cos^{3.0}(\theta)$ from 8GHz to 12GHz;

The X-Band return loss plots had ripples as the frequency band was swept; this is indicative of multiple reflections between two points in the transmission line- typically the largest reflection being at the input to the feed and the first RF transition in the structure. However, the plots do show an overall wideband trend and, with an improved input match, the $VSWR \leq 2:1$ could be extended from 9GHz to 12GHz- the upper part of the band limited by the grating lobe for the Gen 1.0 lattice.

- Gen 2.0 droopy bowtie turnstile radiator and quad line feed.
 - Measured and simulated return loss results presented in Figure 4-55.
 - o Measured: A 28% bandwidth for a $VSWR \leq 2:1$ for vertical and horizontal polarization;
 - Simulated: $\approx 15\text{dB}$ return loss from 8GHz – 10.75GHz; $\approx 14\text{dB}$ return loss from 10.75GHz – 12.75GHz; return loss linearly decreasing from 14dB to 10dB from 12.75GHz to 14GHz.
- Measured and simulated unit cell isolation results presented in Figure 4-56.
 - Measured: Isolation $\geq 35\text{dB}$ from 8GHz to 12GHz.
 - Simulated: Isolation $\geq 60\text{dB}$ from 8GHz to 12GHz.

Although the simulations for return loss and isolation between orthogonal linear polarizations are, overall, better than the prototype Gen 2.0 droopy bowtie turnstile radiator and quad line feed measurements, the Gen 2.0 has already doubled the RF bandwidth from 14% to 28% for a $VSWR \leq 2:1$ compared to Gen 1.0; this is impressive given the early stages of manufacturing and assembly of the Gen 2.0 design:

- Gen 2.0 lattice is 0.440in by 0.440in compared to the Gen 1.0 lattice of 0.595in by 0.595in;

- Rogers 6002 was used for the quad line feed strips instead of Rogers 6010; this caused a higher level of mismatch between the quad line feed and the droopy bowtie wings and degraded isolation between the orthogonal polarizations;
- Automated epoxy dispense. This process needs further refinement since excessive epoxy could further exacerbate the impedance mismatch between the quad line feed and the coplanar transmission line feed on one end and the droopy bowtie wings on the other end. Other conductive bond materials are being investigated including nano silver paste.

With further improvements in manufacturing and assembly, the modeled goal of 50% RF bandwidth for a $VSWR \leq 2:1$ is achievable with the Gen 2.0 design.

In summary:

- The L-Band prototype showed the potential for wideband RF operation and high isolation between the two orthogonal droopy bowtie wings;
- The prototype X-Band Gen 2.0 droopy bowtie turnstile radiator and quad line feed showed the potential for combining excellent RF performance with a low cost manufacturing and assembly process.

Conclusions

The objectives of this thesis were to develop a new, high performance radiator and radiator feed amenable to low cost manufacturing and assembly for advanced phased arrays. This objective was achieved and validated through measurements of prototype hardware and simulations performed on measured finite arrays of the new high performance radiator.

I defend:

New, high performance integrated radiator and feed design for phased arrays including:

- A. dual linear polarization
- B. potential octave bandwidth with wide scan volume
- C. coincident phase center feed
- D. high polarization isolation
- E. very low simulated front end loss

The design is based upon:

- A. theoretical and numerical modeling
- B. hardware fabrication and assembly
- C. finite-array prototype measurement results

A brief review is given of each chapter in the thesis:

Chapter 1 reviewed basic phased array concepts and mathematical expressions to calculate simple phased array patterns and predict their shape as the beam was scanned. Chapter 1 also established terminology that facilitated the development of the droopy bowtie radiator and, later, the new method to analyze finite planar arrays.

Chapter 2 developed an analytical approach based on a Floquet modal expansion of an array of printed dipoles and included the effect of mutual coupling. The analytical approach presented is powerful and insightful but limited to radiator and feed geometries that can be analytically modeled in closed form.

Chapter 3 developed the theory for a new radiator and radiator feed for phased arrays: the droopy bowtie turnstile radiator with quad line feed.

Chapter 4 presented the “Practical Realization and Application” of the droopy bowtie turnstile radiator with quad line feed with prototype measurements. Also, Chapter 4 presented low cost fabrication techniques for the droopy bowtie turnstile radiator with quad line feed and automated assembly using the modular construction of the droopy bowtie turnstile radiator with quad line feed. Chapter 4 presented measured prototype RF measurements at L-Band and X-Band that showed potential for wideband RF operation combined with low cost manufacturing techniques:

- L-Band. Teflon supported droopy bowtie wings.
 - Return Loss: $\approx 2:1$ RF bandwidth for a $VSWR \leq 2:1$;
 - Isolation: $> 30\text{dB}$ over most of the band.
- X-Band. Injection molded and plated droopy bowtie wings.
 - Gen 1.0: 14% bandwidth for a $VSWR \leq 2:1$ for vertical and horizontal polarization;
 - Gen 2.0: 28% bandwidth for a $VSWR \leq 2:1$ for vertical and horizontal polarization

The HFSS infinite array simulations of the X-band droopy bowtie turnstile radiator with quad line feed showed excellent RF bandwidth and low cross-polarization in a dual-linear polarized. Summarizing Gen 2.0 simulated RF performance:

- Bandwidth
 - Goal: 50% RF bandwidth up to one octave RF bandwidth
 - Gen 2.0: 30% RF bandwidth
- Polarization (for polarization isolation see Chapter 4)
 - Goal: Linear or dual linear
 - Gen 2.0: Dual linear performance
- Scan Volume
 - Goal: $\pm 45^\circ$ up to $\pm 60^\circ$ conical scan volume
 - Gen 2.0: $\pm 45^\circ$ from 7GHz to 15GHz

Also, X-band droopy bowtie turnstile radiator with quad line feed indicated excellent simulated low loss performance of 0.37dB maximum up to 12GHz; typically, the average radiator and radiator feed loss is 0.5dB over a similar bandwidth.

Future Impact

Finally, design and cost is not only important for military use of phased arrays but, increasing, for commercial uses of phased arrays. Biomedical applications^{CC.1} using phased array antennas are an area of intense research in analyzing printed antennas for electrically small antenna arrays; two examples:

- Brain Cancer Detection^{CC.2}. A growing area of biomedical research over the past several years has been in the area of microwave imaging based cancer detection. The present design could be combined with a printed version of the bowtie antenna to quickly model a compact array at X-Band for this specific area of research.
- Hyperthermia therapy for cancer^{CC.3}. Phased array focusing antennas used to heat cancerous tumors is another active area of research. There is a critical need to better understand and model the electrically small antenna array pattern in order to improve non-invasive monitoring and control of the heat applied to the tumor.

Future Work

Future work will focus on manufacturing and assembly techniques discussed in Chapter 4 and more RF testing of droopy bowtie turnstile radiator with quad line feed arrays.

Key focus areas of manufacturing and assembly include:

- Refining the injection mold process for the droopy bowtie.
- Plating injection molded droopy bowtie. Several techniques are under investigation:
 - Direct pattern plating;
 - Laser ablation of plated part.
- Investigation of 3-D printed droopy bowties;
- Automated assembly of quad line subassembly;
- Automated assembly of droopy bowtie turnstile radiator with quad line feed.

Specifically, I intend to

1. Fabricate and test a Gen 2.0 droopy bowtie turnstile radiator with quad line feed using injection molded droopy bowtie for:
 - a. 2x6 array
 - b. 6x6 array
 - c. 12x12 array
2. Fabricate a prototype 3-D printed droopy bowtie and test
 - a. 2x6 array
 - b. 6x6 array
 - c. 12x12 array

Appendix A: Time Domain Approach to Characterizing Antenna Radiation

Analyzing the time domain impulse response of an antenna provides an insightful method to analyze the relationship between bandwidth and radiation efficiency.

An ideal broadband antenna has a radiated field impulse response consisting of a single “delta function” and would deliver equal power at all frequencies. Narrow-Band Antennas are characterized by a time domain response where multiple reflections between antenna boundary and feed point produce a sum of “delayed delta functions” which reduces bandwidth^{3.58}. We shall see that the impulse response of the bow-tie antenna results in a relatively wideband radiation response.

An Antenna Element can be modeled as a Linear System:

The utility of the linear systems approach is that the system being analyzed can be modeled as a “black box” (see Figure A-1): we are only interested in the system response to an arbitrary input stimulus. First, find the impulse response, $h(t)$, of the system to a delta function input stimulus; then, using the superposition property of a linear system, the system response to an arbitrary input is the superposition of delta function responses of the system.

A Linear operator T has the following properties^{3.59}:

- $T \{ x_1(t) \} = y_1(t)$ and $T \{ x_2(t) \} = y_2(t)$
- $T \{ ax_1(t) + bx_2(t) \} = ay_1(t) + by_2(t)$, where a and b are constants.

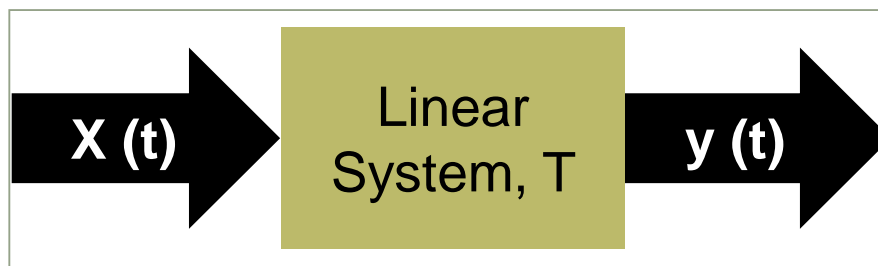


Figure A-1. Linear system block diagram

We now proceed to give a brief mathematical background on the output response of a linear system to an arbitrary input signal.

The impulse response of a linear system, $h(t)$, is defined as the response to a delta function input:

$$h(t) \equiv T\{\delta(t)\} \quad (\text{A.1})$$

where T represents the linear operator (or, transfer function operation) of the linear system. For a time delayed delta function input, we have:

$$h(t-t') \equiv T\{\delta(t-t')\} \quad (\text{A.2})$$

Now, we can express an arbitrary input, $x(t)$, as a weighted sum of delta functions:

$$x(t) = \int_{-\infty}^{\infty} x(t')\delta(t-t')dt' \quad (\text{A.3})$$

Thus, the output response of a linear system to an arbitrary input is given by the convolution integral:

$$y(t) = \int_{-\infty}^{\infty} x(t')h(t-t')dt' \quad (\text{A.4})$$

The convolution integral is the key to understanding the radiation mechanism of an antenna and provides insight into the selection of an array radiator that meets the requirements outlined in Table 3-3:

- 1) wideband operation,
- 2) stable input impedance,
- 3) “packing efficiency” (i.e., tight lattice spacing) for wideband and wide scan angle performance.

Matching to a wideband frequency antenna is difficult; current waves arriving back at the feed port of the antenna are partially absorbed and partially reflected back down the antenna structure. This cycle of reflections occurs “ n ” times until all the energy is radiated to free space and absorbed by the feed. We can model this process as a finite sum of delta functions^{3,58}:

$$h(t) = \sum_{m=0}^n r^m \delta(t-m\tau) \quad (\text{A.5})$$

where “ r ” represents the current attenuation (due to radiation and/ or absorption) factor along the length of the antenna and $|r|<1$; and $t \equiv$ transit time between radiation points (e.g., any discontinuity) on the antenna.

Representing the input, $x(t)$, as a phasor, $e^{i\omega t}$, the resulting output signal is given by the convolution:

$$y(\tau) = \sum_{m=0}^{n-1} r^m \delta(t - m\tau) e^{i\omega t} = 1 + r e^{i\omega t} + r^2 e^{i2\omega t} + r^3 e^{i3\omega t} + \dots + r^{n-1} e^{i(n-1)\omega t} \quad (\text{A.6})$$

Let $z = r e^{i\omega \tau}$; then, expression A.6 becomes:

$$y(\tau) = 1 + z + z^2 + z^3 + \dots + z^{n-1} \quad (\text{A.7})$$

Since $|r|<1$, expression A.7 is a geometric series; the magnitude of the geometric series represents the magnitude of the radiated field:

$$|H(\omega)| = \left| \frac{1 - z^n}{1 - z} \right| \quad (\text{A.8})$$

As the number of radiation terms, n , in expression A.8 increases, the resonance peak increases (higher efficiency) and becomes sharper (less RF bandwidth)^{3,58}.

We now utilize expression A.8 to provide a qualitative examination of the RF bandwidth of an antenna based on its impulse response.

Case 1. Impulse Response of dipole antenna.

Suppose the current attenuation is $|r|=0.9$; this value means that only 10% of the incident signal is radiated for one cycle along the antenna structure. This value of r may be representative of a dipole radiator. Figure A-2 plots the impulse response given by expression A.8; each curve in Figure A-2 represents a radiation term, n , in expression A.8.

After $n = 10$ radiation cycles, the radiated field peak is 6.5; however, the bandwidth in terms of relative wavelength is 0.85 to 1.25 (using a radiated field of “1” as the metric) or approximately a 1.5:1 bandwidth- not a broadband radiator.

Clearly, this qualitative example provides a key insight to designing wideband antennas: reduce r in order to broaden the impulse response and, therefore, the RF bandwidth of the antenna radiator.

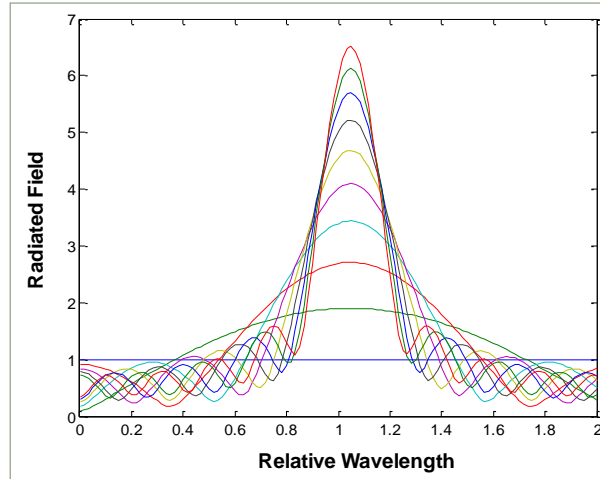


Figure A-2. Impulse response for $r=0.9$

Figure A-2 shows that for $n = 10$ radiation cycles, the total radiated field has begun to reach its maximum; this is characteristic of narrow band radiators.

Next, we examine the impulse response of a bowtie antenna. The bowtie antenna is a flat plane version of the wideband bi-conical antenna^{3,61}. The bowtie antenna has the current distributed over a relatively large surface; the “spreading out” of current over the surface is effective in dissipating the current into a radiated field. The magnitude of the current is greatly diminished before it reaches the physical end of the bowtie; thus, the bowtie is classified as a non-resonant structure^{3,60}.

We present four cases for the bowtie antenna modeled in HFSS as an infinite array of bowties spaced one-half free space wavelength apart in the x and y coordinate; each case corresponds to a spherical scan angle:

- Case 1. ($\varphi=0^\circ, \theta=0^\circ$)
- Case 2. ($\varphi=0^\circ, \theta=45^\circ$)
- Case 3. ($\varphi=45^\circ, \theta=45^\circ$)
- Case 4. ($\varphi=90^\circ, \theta=45^\circ$)

All four cases will show that the currents on the surface of the bowtie significantly attenuate before reaching the edge of the bowtie and, hence, have a broadband frequency radiation over a large scan volume.

Case 1. Scan Angle: $\varphi=0^\circ, \theta=0^\circ$; Frequency = 10 GHz

Figure A-3 shows the magnitude of the surface current density on the bowtie. The current attenuation is $|r| = (10\text{A/m})/(200\text{A/m}) = 0.05$; this value means that about 95% of the incident signal is radiated for one cycle along the antenna structure. Figure A-4 shows the plot of the impulse response, $|H(\omega)|$, for $|r| = 0.05$; for $n = 3$ radiation cycles the total radiated field has reached its maximum; this is characteristic of wide band radiators.

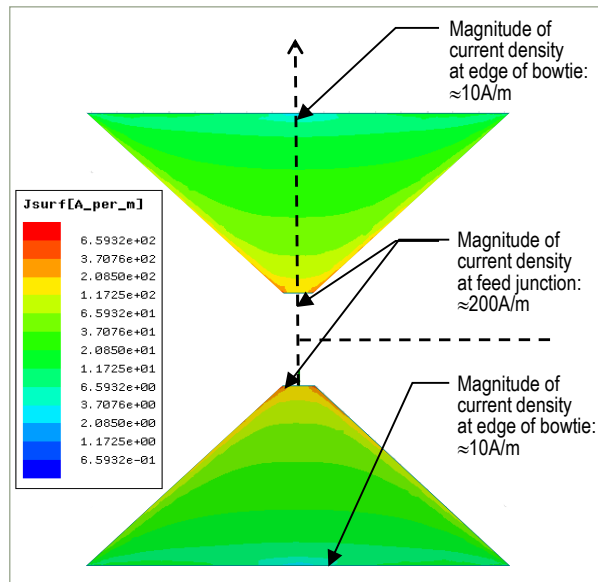


Figure A-3. Single unit cell bowtie surface currents

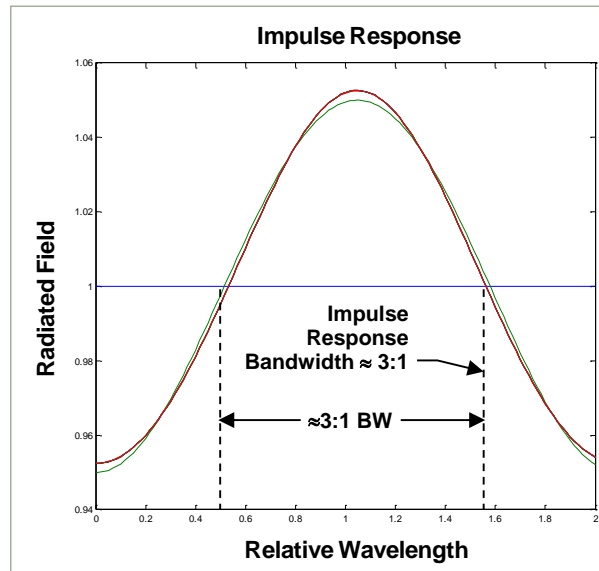


Figure A-4. Impulse response $|H(\omega)|$ for $|r| = 0.05$; $n = 3$

Case 2. Scan Angle: $\varphi=0^\circ$, $\theta=45^\circ$; Frequency = 10 GHz

Figure A-5 shows the magnitude of the surface current density on the bowtie. The current attenuation is $|r| = (7A/m)/(200A/m) = 0.035$; this value means that about 96.5% of the incident signal is radiated for one cycle along the antenna structure. Figure A-6 shows the plot of the impulse response, $|H(\omega)|$, for $|r| = 0.035$; for $n = 3$ radiation cycles the total radiated field has reached its maximum; this is characteristic of wide band radiators.

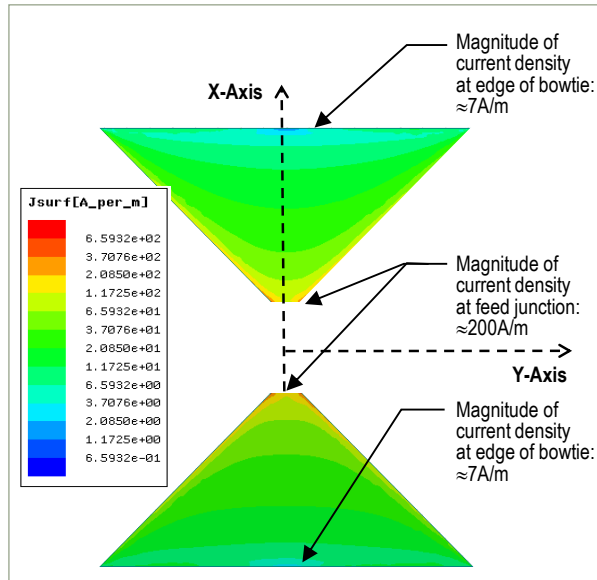


Figure A-5. Single unit cell bowtie surface currents

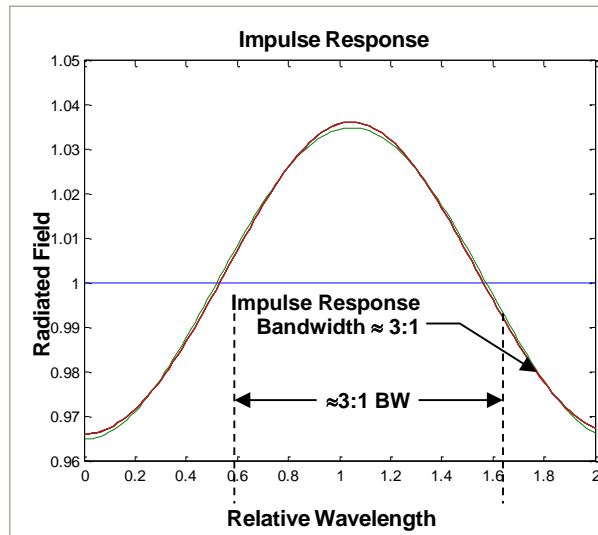


Figure A-6. Impulse response $|H(\omega)|$ for $|r| = 0.035$; $n = 3$

Case 3. Scan Angle: $\varphi=45^\circ$, $\theta=45^\circ$; Frequency = 10 GHz

Figure A-7 shows the magnitude of the surface current density on the bowtie. The current attenuation is $|r| = (12\text{A/m})/(200\text{A/m}) = 0.06$; this value means that about 94% of the incident signal is radiated for one cycle along the antenna structure. Figure A-8 shows the plot of the impulse response, $|H(\omega)|$, for $|r| = 0.06$; for $n = 3$ radiation cycles the total radiated field has reached its maximum; this is characteristic of wide band radiators.

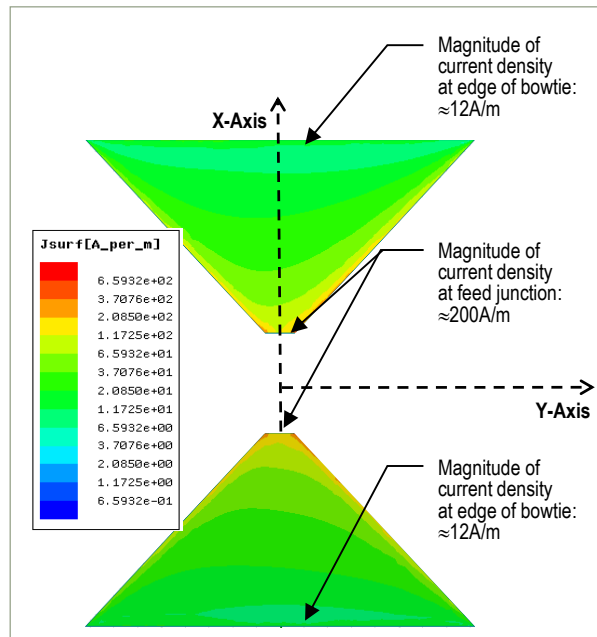


Figure A-7. Single unit cell bowtie surface currents

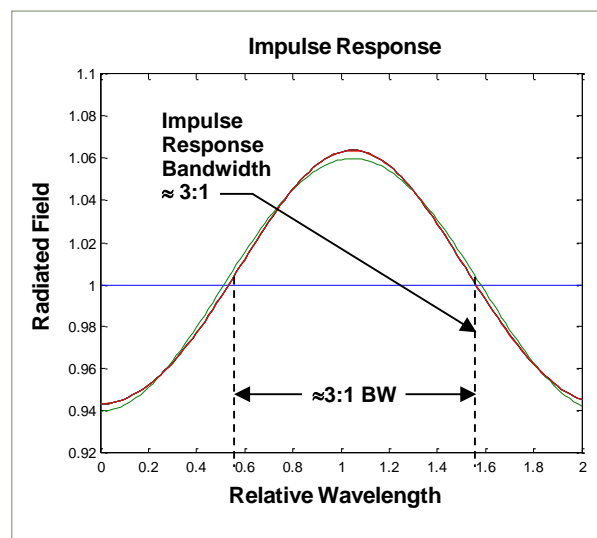


Figure A-8. Impulse response $|H(\omega)|$ for $|r| = 0.06$; $n = 3$

Case 4. Scan Angle: $\varphi=90^\circ$, $\theta=45^\circ$; Frequency = 10 GHz

Figure A-9 shows the magnitude of the surface current density on the bowtie. The current attenuation is $|r| = (20\text{A/m})/(200\text{A/m}) = 0.1$; this value means that about 90% of the incident signal is radiated for one cycle along the antenna structure. Figure A-10 shows the plot of the impulse response, $|H(\omega)|$, for $|r| = 0.1$; for $n = 3$ radiation cycles the total radiated field has reached its maximum; this is characteristic of wide band radiators.

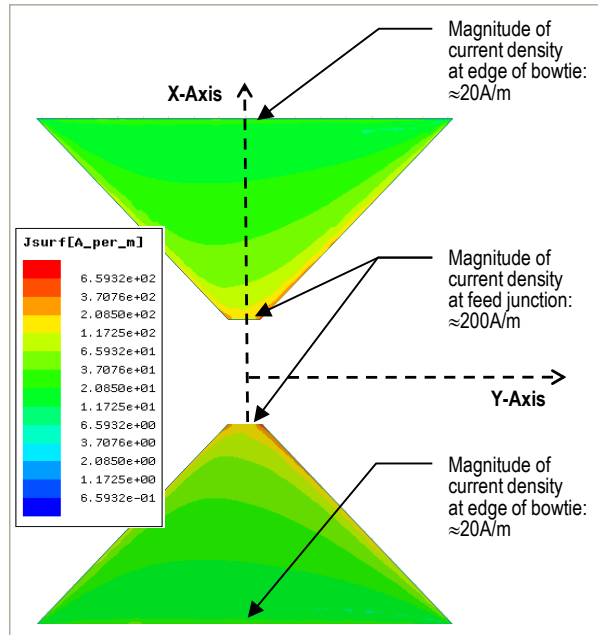


Figure A-9. Single unit cell bowtie surface currents

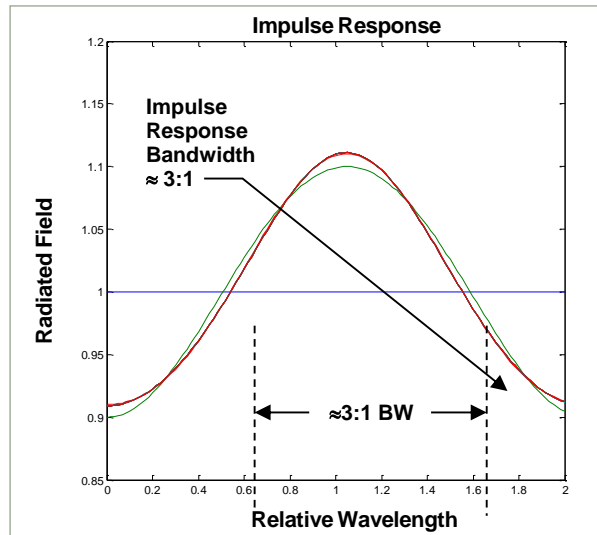


Figure A-10. Impulse response $|H(\omega)|$ for $|r| = 0.1$; $n = 3$

Summary

A time-domain approach to qualitatively assess the potential for wideband RF performance has been discussed. The bowtie radiator was modeled in HFSS in an infinite array simulation; the estimated impulse response bandwidth over a large scan volume (up to 45 deg) was 3:1. Thus, the geometrically simple bowtie radiator has the characteristics of a non-resonant radiator. The combination of a simple geometry and relatively large RF bandwidth makes the bowtie radiator a suitable candidate for a low cost, phased array antenna element.

References

Chapter 1

- 1.1 Brown, Arik D., Electronically Scanned Arrays, CRC Press, 2012, pg. 5.
- 1.2 Young and Freeman, University Physics, Pearson/ Addison Wesley, 12th Edition, pp. 1237.
- 1.3 Stutzman, Warren L., Thiele, Gary A., Antenna Theory and Design, John Wiley and Sons, New York, 1981, pg. 125.
- 1.4 Brown, Arik D., Electronically Scanned Arrays, CRC Press, 2012, Ch 1.
- 1.5 Visser, Hubregt J., Array and Phased Array Antenna Basics, John Wiley and Sons, 2005, Ch 11.
- 1.6 Mailloux, Robert J., Electronically Scanned Arrays, Morgan and Claypool, 2007, Ch 2.
- 1.7 Brown, Arik D., Electronically Scanned Arrays, CRC Press, 2012, Ch 1.
- 1.8 *ibid*, Ch 1.

Chapter 2

- 2.1 S. N. Makarov and A. Puzella, "Scan Impedance for An Infinite Dipole Array: Hansen's Formulas Compared with Ansoft HFSS Simulations", IEEE Antennas and Propagation Magazine, Vol 49, No. 4, August 2007.
- 2.2 Stutzman, Warren L., Thiele, Gary A., Antenna Theory and Design, John Wiley and Sons, New York, 1981, Ch. 3.
- 2.3 Bhattacharyya, Arun K., Phased Array Antennas, Wiley-Interscience, 2006, Ch. 2.
- 2.4 Hansen, R. C., Phased Array Antennas, John Wiley and Sons, New York, 1998, pg. 237.
- 2.5 Harrington, R. F., Time Harmonic Electromagnetic Fields, McGraw-Hill, New York, 1961, pg. 349.
- 2.6 Hansen, R. C., Microwave Scanning Antennas, Academic Press, New York, 1966, pg. 286.
- 2.7 *ibid*, pg. 247.
- 2.8 *ibid*, pg. 245.

- 2.9 Stutzman, Warren L., Thiele, Gary A., Antenna Theory and Design, John Wiley and Sons, New York, 1981, Ch. 7.
- 2.10 S. N. Makarov and V. Iyer, "Scan Impedance for An Infinite Dipole Array: Accurate Theoretical Model Versus Numerical Software", *IEEE Antennas and Propagation Magazine*, Vol. 50, No. 6, 2008, pg. 132-149.
- 2.11 A. L. VanKoughnett and J. L. Yen, "Properties of a cylindrical antenna in an infinite planar or collinear array," *IEEE Trans. Antennas Prop.*, vol. AP-15, no. 6, Nov. 1967, pp. 750-757.
- 2.12 J. A. Stratton and L. J. Chu, "Steady-state solutions of electromagnetic field problems. I. Forced oscillations of a cylindrical conductor," *J. Appl. Phys.*, vol. 12, 1941, pp. 231-235.
- 2.13 S. A. Schelkunoff, "Theory of antennas of arbitrary size and shape," *Proc. IRE*, vol. 29, 1941, pp. 493-521.
- 2.14 E. Hallen, "Properties of a long antenna," *J. Appl. Phys.*, vol. 19, 1948, pp. 1140-1147.
- 2.15 E. Hallen, "Exact treatment of antenna current wave reflection at the end of a tube-shaped cylindrical antenna," *IEEE Trans. Antennas Prop.*, vol. 4, no. 3, July 1956, pp. 479-491.
- 2.1 L. A. Vainshtein, "Waves of current in a thin cylindrical conductor," I. Current and impedance of a transmitting antenna," *Soviet. Phys. Tech. Physics*, vol. 4, 1959, pp. 601-615.
- 2.17 L. A. Vainshtein, "Waves of current in a thin cylindrical conductor," II. The current in a passive oscillator and the radiation of a transmitting antenna," *Soviet. Phys. Tech. Physics*, vol. 4, 1959, pp. 617-626.
- 2.18 J. R. Wait, *Electromagnetic Radiation from Cylinder Structures*, Pergamon Press, 1959.
- 2.19 R. H. Duncan and F. A. Hinchey, "Cylindrical antenna theory," *J. Research NBS (D-Radio Prop.)*, vol. 64D, 1960, pp. 569-584.
- 2.20 T. T. Wu, "Theory of the dipole antenna and the two-wire transmission line," *J. Math. Phys.*, vol. 2, 1961, pp. 550-574.

- 2.21 R. H. Duncan, "Theory of the infinite cylindrical antenna including the feedpoint singularity in antenna current," J. Research NBS (D-Radio Prop.), vol. 66D, no. 2, 1962, pp. 181-188.
- 2.22 Y. M. Chen and J. B. Keller, "Current on and input impedance of a cylindrical antenna," J. Research NBS (D-Radio Prop.), vol. 66D, no. 1, Jan.-Feb. 1962, pp. 15-21.
- 2.23 R. L. Fante, "On the admittance of the infinite cylindrical antenna," Radio Science, vol. 1, no. 9, Sep. 1966, pp. 1041-1044.
- 2.24 R. W. P. King and T. T. Wu, "The imperfectly conducting cylindrical transmitting antenna," IEEE Trans. Antennas Prop., vol. AP-14, no. 5, Sep. 1966, pp. 524-534.
- 2.25 E. K. Miller, "Admittance dependence of the infinite cylindrical antenna upon exciting gap thickness," Radio Science, vol. 2, no. 12, Dec. 1967, pp. 1431-1435.
- 2.26 R. W. P. King, "The linear antenna - eighty years of progress," Proceedings of the IEEE, vol. 55, no. 1, Jan. 1967, pp. 2-16.
- 2.27 R. A. Hurd and J. Jacobsen, "Admittance of an infinite cylindrical antenna with realistic gap feed," Electronics Letters, vol. 4, no. 19, Sep. 1968, pp. 420-421.
- 2.28 L.-C. Shen, T. T. Wu, and R. W. P. King, "A simple formula of current in dipole antennas," IEEE Trans. Antennas Prop., vol. AP-16, no. 5, Sep. 1968, pp. 542-547.
- 2.29 S. N. Makarov and V. Iyer, "Scan Impedance for An Infinite Dipole Array: Accurate Theoretical Model Versus Numerical Software", IEEE Antennas and Propagation Magazine, Vol. 50, No. 6, 2008, Pg. 2.
- 2.30 Stutzman, Warren L., Thiele, Gary A., Antenna Theory and Design, John Wiley and Sons, New York, 1981, pg. 306.
- 2.31 S. N. Makarov and V. Iyer, "Scan Impedance for An Infinite Dipole Array: Accurate Theoretical Model Versus Numerical Software", IEEE Antennas and Propagation Magazine, Vol. 50, No. 6, 2008, Pg. 5.
- 2.32 *ibid*, pg. 4.
- 2.33 *ibid*, pg. 13.

- 2.34 *ibid*, pg.14.
- 2.35 *ibid*, pg.15.
- 2.36 *ibid*, pg.16.
- 2.37 *ibid*, pg.21.
- 2.38 *ibid*, pg.25-27.

Chapter 3

- 3.1 A. Puzella, F. Sciré-Scappuzzo, S. N. Makarov, “Design and Manufacturing of an Injection-Molded Dual-Polarized X-Band Low-Cost Scanning Array”, 2013 Antenna Applications Symposium, Robert Allerton Park, Monticello, Illinois.
- 3.2 U.S. Patent. “Droopy bowtie Radiator with Integrated Balun”, US 2011/0291907, Pu No. 8581801 (B2), Angelo M. Puzella, Sergey Makarov and Patrick Morrison.
- 3.3 D. M. Pozar and D. H. Schaubert, “Scan blindness in infinite phased array of printed dipoles,” *IEEE Trans. Antennas and Propagation*, vol. AP-32, no. 6, June 1984, pp. 602-610.
- 3.4 J.-P. R. Bayard, M. Cooley, and D. H. Schaubert, “Analysis of infinite arrays of printed dipoles on dielectric sheets perpendicular to the ground plane,” *IEEE Trans. Antennas and Propagation*, vol. AP-39, no. 12, Dec. 1991, pp. 1722-1732.
- 3.5 A. K. Bhattacharyya, *Phased Array Antennas: Floquet Analysis, Synthesis, and Active Array Systems*, Wiley, New York, 2006.
- 3.6 D. M. Pozar and D. H. Schaubert, “Analysis of an infinite array of rectangular microstrip patches with idealized probe feeds,” *IEEE Trans. Antennas and Propagation*, vol. AP-32, no. 10, Oct. 1984, pp. 1101-1107.
- 3.7 M. W. Elsallal and D. H. Schaubert, “High performance phased arrays of doubly mirrored balanced antipodal Vivaldi antenna (DmBAVA): Current development and future considerations,” *Proc. 2007 Antenna Applications Symposium*, Allerton Park, Monticello, Illinois, Sep. 18-20 2007, pp. 148-159.

- 3.8 W. R. Pickles and W.M. Dorsey, "Proposed coincident phase center orthogonal dipoles," *2007 Antenna Applications Symposium Proc.*, Monticello, IL, Sep. 2007, pp. 106-124.
- 3.9 A. Kerkhoff, and S. Ellingson, "A wideband planar dipole antenna for use in the long wavelength demonstrator array (LWDA)," *IEEE AP-S International Symposium*, July 2005, vol. 1B, pp. 553-556.
- 3.10 S. Ellingson and A. Kerkhoff, "Comparison of two candidate elements for a 30-90 MHz radio telescope array," *IEEE AP-S International Symposium*, July 2005, vol. 1A, pp. 590-593.
- 3.11 M. S. Gatti and D. J. Nybakken, "A circularly polarized crossed drooping dipole antenna", *IEEE AP-S International Symposium*, May 1990, vol. 1, pp. 254-257.
- 3.12 D. E. Ping, J. T. Shaffer, L. U. Brown, and R. B. Dybdal, "A broadband rolled edged cavity antenna," *IEEE AP-S International Symposium*, June 2004, vol. 1, pp. 787-790.
- 3.13 Kraus, John D., Antennas for All Applications, McGraw-Hill, New York, 2002.
- 3.14 S. Makarov and F. Scire' Scappuzzo, "Multipath rejection by virtue of a choke ring for a broadband droopy turnstile antenna," *2007 Antenna Applications Symposium Proc.*, Monticello, IL, Sep. 2007, pp. 467-507.
- 3.15 P. G. Elliot, "Octave Bandwidth Microwave Scanning Array", *1995 Antenna Applications Symposium Proc.*, Monticello, IL, Sep. 1995, p.19.
- 3.16 A. Hoorfar, K. C. Gupta, and D. C. Chang, "Cross-polarization level in radiation from a microstrip dipole antenna," *Electromagn. Lab. Dept. Elec. Comput. Eng., Univ. Colorado*, Boulder, Sci. Rep. 83, July 1985.
- 3.17 A. Hoorfar, K. C. Gupta, and D. C. Chang, "Cross-polarization level in radiation from a microstrip dipole antenna," *IEEE Trans. Antennas and Propagation*, vol. AP-36, no. 9, Sep. 1988, pp. 1197-1203.
- 3.18 N. K. Das and A. Mohanty, "Characteristics of printed antennas and arrays covered with a layer of printed strip-grating for suppression of cross-polarization," *IEEE AP-S International Symposium*, July 1993, vol. 2, pp. 634-637.

- 3.19 K. Woelder and J. Granholm, "Cross-polarization and sidelobe suppression in dual linear polarization antenna arrays," *IEEE Trans. Antennas and Propagation*, vol. AP-45, no. 12, Dec. 1997, pp. 1727-1740.
- 3.20 J. J. Lee, S. Livingston, and R. Koenig, "Performance of a wideband (3-14 GHz) dual-pol array," *IEEE AP-S International Symposium*, June 2004, vol. 2, pp. 551-554.
- 3.21 J. J. Lee, S. Livingstone, and R. Koenig, "A low-profile wide-band (5:1) dual-pol array," *IEEE Antennas and Wireless Propagation Letter*, vol. 2, 2003, pp. 46-49.
- 3.22 Zhong Shun-Shi, Yang Xue-Xia, Gao Shi-Chang, and Cui Jun-Hai, "Corner-fed microstrip antenna element and arrays for dual-polarization operation," *IEEE Trans. Antennas and Propagation*, vol. AP-50, no. 10, Oct. 2002, pp. 1473-1480.
- 3.23 T. A. Milligan, *Modern Antenna Design*, Wiley-IEEE Press, NY, 2005, 2nd ed.
- 3.24 D. F. Bowman and E. F. Kuester, in: J. L. Volakis, Ed., *Antenna Engineering Handbook*, McGraw Hill, New York, 2007, fourth edition, Ch. 52, pp. 52-26, 52-27.
- 3.25 J. D. Dyson, "Balanced transmission-line measurements using coaxial equipment," *IEEE Trans. Microwave Theory Techniques*, pp. 94-96, Jan. 1971.
- 3.26 J. D. Dyson, "Measurement of near fields of antennas and scatterers," *IEEE Trans. Antennas Propagat.*, vol. AP-21, no. 4, pp. 446-460, July 1973.
- 3.27 R. G. Fitzgerrell, "Standard linear antennas, 30 to 1000 MHz," *IEEE Trans. Antennas Propagat.*, vol. AP-34, pp. 1425-1429, Dec. 1986.
- 3.28 Z. Chen and A. Cook, "Low uncertainty broadband EMC measurement using calculable precision biconical antennas," in *Proc. IEEE Int. Symp. Electromagnetic Compatibility*, vol. 2, 2000, pp. 505-510.
- 3.29 J. S. McLean, "Balancing networks for symmetric antennas. I. Classification and fundamental operation," *IEEE Trans. Electromagnetic Compatibility*, vol. 44, no. 4, Nov. 2002, pp. 503-514.
- 3.30 Seong-Youp Suh, W. L. Stutzman, and W. A. Davis, "Low-profile, dual-polarized broadband antennas," *2003 IEEE Antennas and Propagation Society International Symposium*, vol. 2, June 2003, pp. 256 - 259.

- 3.31 Seong-Youp Suh, W. Stutzman, W. Davis, A. Waltho, K. Skeba, and J. Schiffer, "A novel low-profile, dual-polarization, multi-band base-station antenna element – the Fourpoint Antenna," *2004 IEEE 60th Vehicular Technology Conference*, 2004. VTC2004-Fall, vol. 1, 26-29 Sept. 2004, pp. 225 – 229.
- 3.32 Seong-Youp Suh, W. Stutzman, W. Davis, A. Waltho, K. Skeba, and J. Schiffer, "Bandwidth improvement for crossed-dipole type antennas using a tuning plate," *2005 IEEE Antennas and Propagation Society International Symposium*, vol. 2A, July 2005, pp. 487 – 490.
- 3.33 W. R. Pickles and W.M. Dorsey, "Proposed coincident phase center orthogonal dipoles," *2007 Antenna Applications Symposium Proc.*, Monticello, IL, Sep. 2007, pp. 106-124.
- 3.34 S. Makarov and R. Ludwig, "Analytical model of the split-coaxial balun and its application to a wire dipole or a CP turnstile," *IEEE Trans. Antennas and Propagation*, vol. AP-56, no. 5, July 2007, pp. 1909-1918.
- 3.35 J. S. McLean, "Balancing networks for symmetric antennas. II. Practical implementation and modeling," *IEEE Trans. Electromagnetic Compatibility*, vol. 46, no. 1, Feb. 2004, pp. 24-32.
- 3.36 D. M. Pozar, *Microwave Engineering*, Wiley, New York, 2005, 3rd edition.
- 3.37 J. D. Dyson, "Balanced transmission-line measurements using coaxial equipment," *IEEE Trans. Microwave Theory Techniques*, pp. 94–96, Jan. 1971.
- 3.38 J. D. Dyson, "Measurement of near fields of antennas and scatterers," *IEEE Trans. Antennas Propagat.*, vol. AP-21, no. 4, pp. 446–460, July 1973.
- 3.39 R. G. Fitzgerrell, "Standard linear antennas, 30 to 1000 MHz," *IEEE Trans. Antennas Propagat.*, vol. AP-34, pp. 1425–1429, Dec. 1986.
- 3.40 Z. Chen and A. Cook, "Low uncertainty broadband EMC measurement using calculable precision biconical antennas," in *Proc. IEEE Int. Symp. Electromagnetic Compatibility*, vol. 2, 2000, pp. 505–510.

- 3.41 J. S. McLean, "Balancing networks for symmetric antennas. I. Classification and fundamental operation," *IEEE Trans. Electromagnetic Compatibility*, vol. 44, no. 4, Nov. 2002, pp. 503-514.
- 3.42 J. S. McLean, "Balancing networks for symmetric antennas. II. Practical implementation and modeling," *IEEE Trans. Electromagnetic Compatibility*, vol. 46, no. 1, Feb. 2004, pp. 24-32.
- 3.43 D. M. Pozar, *Microwave Engineering*, Wiley, New York, 2005, 3rd edition.
- 3.44 E. M. T. Jones and J. K. Shimizu, "A wide-band strip-line balun," *IRE Trans. Microwave Theory Techniques*, pp. 94-96, Jan. 1959.
- 3.45 Yong-Xin Guo, Kah-Wee Khoo, and Ling Chuen Ong, "Wideband dual-polarized patch antenna with broadband baluns," *IEEE Trans. Antennas and Propagation*, vol. AP-55, no. 1, pp. 78-83, Jan. 2007.
- 3.46 E. Wilkinson, "An N-way hybrid power divider," *IRE Trans. Microw. Theory Tech.*, vol. MTT-8, no. 1, pp. 116-118, Jan. 1960.
- 3.47 S. B. Cohn, "A class of broadband three port TEM-mode hybrids," *IEEE Trans. Microw. Theory Tech.*, vol. MTT-16, no. 2, pp. 110-116, Feb, 1968.
- 3.48 S. W. Lee, C. S. Kim, and K. S. Choi, "A general design formula of multi-section power divider based on singly terminated filter design theory," in *IEEE MTT-S Int. Microw. Symp. Dig.*, 2001, pp. 1297-1300.
- 3.49 H. Oraizi and Ali-Reza Sharifi, "Design and optimization of broadband asymmetrical multisection Wilkinson power divider," *IEEE Trans. Microw. Theory Tech.*, vol. MTT-54, no. 5, pp. 2220-2231, May, 2006.
- 3.50 Seong-Youp Suh, W. Stutzman, W. Davis, A. Waltho, K. Skeba, and J. Schiffer, "A novel low-profile, dual-polarization, multi-band base-station antenna element – the Fourpoint Antenna," *2004 IEEE 60th Vehicular Technology Conference*, 2004. VTC2004-Fall, vol. 1, 26-29 Sept. 2004, pp. 225 – 229.
- 3.51 D. M. Pozar, *Microwave Engineering*, Wiley, New York, 2005, 3rd edition.

- 3.52 E. Hammerstad and O. Jensen, “Accurate models for microstrip computer-aided design,” in IEEE MTT-S Inter. Microwave Symp. Dig., Wash., DC, 1980, p.407-9.
- 3.53 M. Kirschning and R. H. Jansen, “Accurate wide-range design equations for the frequency-dependent characteristic of parallel coupled microstrip lines,” IEEE Trans. Microwave Theory and Techniques, vol. MTT-32, pp. 83-89, 1984, with corrections in vol. MTT-33, p. 288, 1985.
- 3.54 Ch. Wan, “Analytically and accurately determined quasi-static parameters of coupled microstrip lines,” IEEE Trans. Microwave Theory and Techniques, vol. 44, no. 1, Jan. 1996, pp. 75 – 80.
- 3.55 E. Wilkinson, “An N-way hybrid power divider,” IRE Trans. Microw. Theory Tech., vol. MTT-8, no. 1, pp. 116–118, Jan. 1960.
- 3.56 S. B. Cohn, “A class of broadband three port TEM-mode hybrids,” IEEE Trans. Microw. Theory Tech., vol. MTT-16, no. 2, pp. 110–116, Feb, 1968.
- 3.57 H. Oraizi and Ali-Reza Sharifi, “Design and optimization of broadband asymmetrical multisection Wilkinson power divider,” IEEE Trans. Microw. Theory Tech., vol. MTT-54, no. 5, pp. 2220–2231, May, 2006.
- 3.58 Cloude, Shane, An Introduction to Electromagnetic Wave Propagation and Antennas, Springer, 1995, Ch. 3.
- 3.59 Fante, Ronald L., Signal Analysis and Estimation, John Wiley and Sons, 1988, Ch 3.
- 3.60 Makarov, Sergey N., Antenna and EM Modeling with Matlab, John Wiley and Sons, New York, pg. 169.
- 3.61 Kraus, John D., Antennas for All Applications, McGraw-Hill, New York, 2002.

Chapter 4

- 4.1 U.S. Patent. “Droopy bowtie Radiator with Integrated Balun”, US 2011/0291907, Pu No. 8581801 (B2), Angelo M. Puzella, Sergey Makarov and Patrick Morrison.
- 4.2 <http://www.vpmi.com/tech-basics.htm>

4.3 TE Connectivity Technical Data Sheet, 303 Constitution Drive, MS R32-1A, Menlo Park, CA 94024

4.4 *ibid*, 4.3

4.5 *ibid*, 4.3

Conclusion Chapter

CC.1 Sabban, Albert, “Comprehensive Study of Printed Antennas on Human Body for Medical Applications,” *International Journal of Advance in Medical Science (AMS)* Volume 1 Issue 1, February 2013.

CC.2 Haoyu Zhang, Ahmed O. El-Rayis, Nakul Haridas, Nurul H. Noordin, Ahmet T. Erdogan, Tughrul Arslan, “A Smart Antenna Array for Brain Cancer Detection,” *International Journal of Advance in Medical Science (AMS)* Volume 1 Issue 1, February 2013.

CC.3 P.R. Stauffer and P.F. Maccarini, “Evolution of Antenna Performance for Applications in Thermal Medicine”.